

ELEKTROTEHNI^KI FAKULTET
UNIVERZITETA U BAWALUCI

*FACULTY OF ELECTRICAL ENGINEERING
UNIVERSITY OF BANJALUKA*

ELEKTRONIKA

ELECTRONICS

YU ISSN 1450-5843

GODIŠTE 7, BROJ 2, DECEMBAR 2003. VOLUME 7, NUMBER 2, DECEMBER 2003.

FACULTY OF ELECTRICAL ENGINEERING UNIVERSITY OF BANJALUKA

Address: Patre 5, 78000 Banjaluka, Republic of Srpska, Bosnia and Herzegovina

Phone: + 387 51 211-408, + 387 51 221-820

Fax: + 387 51 211-408

ELECTRONICS

e-mail: elektronika@etfbl.net

Editor: Prof. Branko L. Dokić, Ph. D.
Faculty of Electrical Engineering
University of Banjaluka, Republic of Srpska
e-mail: bdokic@etfbl.net

Program Committee:

- Nikolaos Uzunoglu, National Technical University of Athens, Greece
- Barry Jefferies, University of Hertfordshire, UK
- Vojin Oklobdžija, University of California, Davis, USA
- Bratislav Milovanović, Faculty of Electronics Niš, FR Yugoslavia
- Milić Stojić, Faculty of Electrical Engineering Beograd, FR Yugoslavia
- Vojislav Aranđelović, Institute "Vinča" Beograd, FR Yugoslavia
- Veljko Milutinović, Faculty of Electrical Engineering Beograd, FR Yugoslavia
- Ilija Stojanović, SANU Beograd, FR Yugoslavia
- Vladimir Katić, Faculty of Technical Sciences Novi Sad, FR Yugoslavia
- Aleksandar Ilišković, Faculty of Electrical Engineering Banjaluka, RS
- Milorad Božić, Faculty of Electrical Engineering Banjaluka, RS

Secretary: Petar Matić, M.Sc.
e-mail: pero@etfbl.net,
Faculty of Electrical Engineering
University of Banjaluka, Republic of Srpska

Publisher: Faculty of Electrical Engineering
University of Banjaluka, Republic of Srpska
Address: Patre 5, 78000 Banjaluka, Republic of Srpska, Bosnia and Herzegovina
Phone: + 387 51 211-408, + 387 51 221-820
Fax: + 387 51 211-408
<http://www.etfbl.net>

Number of printed copies: 150

Часопис "Електроника" у издању Електротехничког факултета у Бањој Луци ослобођен је плаћања пореза на промет на основу мишљења Министарства науке и културе Републике Српске, број 06-75/97 од 20. новембра 1997. године.

BIOGRAPHY OF PROF. DR VLADAN VUČKOVIĆ



Vladan Vučković (Vladdan Vuchkovich), born 1928 in Kragujevac (Serbia, Yugoslavia), holds a Ph.D. degree from University of Belgrade, Department of Electrical Engineering (1964). Now retired, he was full professor in University of Belgrade (Faculty of Electrical Engineering), in University of Novi Sad (Faculty of Technical Sciences) and in University of Niš (Electronic Faculty). During his 40-years university career he has established and taught numerous fundamental courses, as for example, Magnetic Amplifiers, Transient Phenomena in Electrical Machines, Power Electronics, Theory of Electrical Machines, Electrical Drives, Control of Electrical Drives, Microcomputers in Power Electronics.

Parallel to this assignment, he was about 30 years Manager of Control Department in Electrical Engineering Institute "Nikola Tesla" in Belgrade, where he and his team have developed a series of different devices in the field of power electronics, electrical drives and analog and digital automatic control.

He has published over 80 scientific papers and articles in national and international professional publications and conference proceedings, as well as two monographs ("Generalized Theory of Electrical Machines" and "Electrical Drives").

BIOGRAPHY OF PROF. DR VLADIMIR KATIĆ



Prof. Dr. Vladimir A. Katić was born in Novi Sad, Serbia & Montenegro in 1954. He received B.Sc. degree from University of Novi Sad in 1978, and M.Sc. and Ph.D. degrees from University of Belgrade in 1981 and 1991, respectively, all in electrical engineering. From 1978 he is with Institute for Power, Electronics & Communication Engineering of the Faculty of Technical Sciences, University of Novi Sad, where he is currently Professor and Head of Power Electronics and Converters Group.

From 1993 to 1998 he was the Director of the Institute of Power, Electronics and Telecommunication Engineering and from 1998 - now the Vice-Dean of the Faculty of Technical Sciences.

The main fields of scientific and research interest of Prof. Katić are power quality, modelling of power electronics converters and standardization in electrical engineering.

He is the author of several books: "Electric Power Quality - Harmonics" (2002), "Power Electronics – Laboratory Practice" (2000), "Power Electronics - Worked Problems" (1998), and the editor of the book "Modern Aspects of Power Engineering" (1995).

He is the author or co-author of more than 210 scientific papers published in international and national monographs, journals or conferences proceedings. He is also reviewer, member of international programme committees and session chairman of many international or national journals and conferences.

He is also the Vice Chair of IEEE Yugoslavia Section, Chairman of the IEEE Joint Chapter on Industrial Electronics/Power Electronics/Industry Application Soc. and Senior Member of IEEE. He is president of the Power Electronic Society (Serbia & Montenegro), observer Member at CIGRE SC36 (Paris), Member of International and National Committees of CIGRE and National Committees of CIRED and ETRAN.

THIRTY YEARS OF SYMPOSIUM

Vladan Vučković, "Nikola Tesla" Institute, Belgrade, SERBIA AND MONTENEGRO

Thirty years ago, more precisely in June 1973, first symposium on power electronics in our country was held in the organization of Institute "Nikola Tesla" from Belgrade and Serbian Academy of Sciences and Arts. The event took place in Belgrade, in the building of Academy, in Knez Mihajlova street.

Many scientific, expert, educational and production centres in former Yugoslavia showed interest, already at the first symposium, for gatherings of this kind. Next reunion was held in two years, again in Belgrade, but since that time, as suggested by the colleagues from Croatia, Slovenia, and Bosnia and Herzegovina, it was planned for the event to take place each time in some other Yugoslav city, under the same name, symbols and attributes. Thus Third symposium took place in 1978, in Zagreb, in the organization of that time second biggest research centre, after the Institute "Nikola Tesla" in Belgrade, electrical engineering institute "Rade Končar", supported by the Yugoslav Academy of Sciences and Arts, and in cooperation with School of Electrical Engineering in Zagreb. Fourth symposium was in Sarajevo in 1981, where organizers were School of Electrical Engineering and "Energoinvest" company, Fifth symposium took place in Ljubljana in 1984, co-sponsored by "Iskra", School of Engineering in Ljubljana, "Elektrotehniška zveza" and in very close cooperation with School of Engineering in Maribor, and Sixth symposium took place in Subotica, in 1986, supported of "Sever" company and Institute of Power Engineering and Electronics of the Faculty of Technical Sciences in Novi Sad. All the events were supervised by the Counsel made of all Academies of Sciences and Arts of former Yugoslavia, so besides Serbian Academy from Belgrade and Yugoslav Academy in Zagreb, academies in Ljubljana and Sarajevo should also be mentioned as active participants and organizers.

Tour de Yugoslavie ended in October 1988, in Belgrade, at Sava Centre, where Seventh symposium in the organization of founders and organizers of first symposiums 15 years earlier, took place. At the time nobody could imagine it will be the last event after many years. New round of symposiums was planned to start in the same order, followed by the preparations organized by colleagues in Zagreb, for spring 1991. War conflict which soon broke out, was not the reason which obstructed the prolongation of this tradition. Conference was simply postponed for some other reasons. "Rade Končar" factory found itself in the middle of profound reorganization (usually called "transition", the newly introduced expression), and it's Institute, which hosted some of the major founders of the organization, started to fall apart. Some ideas and negotiations put an effort for the event to take place in Sarajevo, which at the time, though it seems strange and unbelievable today, was a safe place. After some time, many colleagues we used to work together at this, found themselves on the other side, inaccessible to us.

At initial meeting of the Institute for Power Engineering and Electronics, in January 1995, we had a dilemma whether we should go on and continue without

these people. As is evident today, desire to continue with the tradition prevailed, since these reunions started here and were violently interrupted at the same place. We continued with the eighth symposium, and here we are after eight years at the twelfth.

At the first symposium of the new round in autumn 1995, the number of participants was significantly decreased compared to the previous one, held in Sava Centre in 1988, in former big Yugoslavia. Number of papers decreased from 109 to only 79. However, thanks to the participation of foreign guests, that number was continuously increasing, reaching the amount of sent papers at 11th symposium in 2001, of 107 submitted works. That encouraged us to establish our reunion as an international event, what we also had in mind at our last meeting, while still together in 1988. At last symposium 45% of the papers were from abroad, coming from 16 countries. English language, together with Serbian, was introduced as official, and the program board was expanded by renowned foreign experts. Domestic authors were advised to write and send their papers in English, what resulted in 55% of all papers submitted, being sent in that language.

Further innovations introduced were possibilities for improved and more efficient correspondence and publishing. Papers were initially sent on floppy diskettes, and later by e-mail. Proceedings and other printed publications were copied to compact-disks (CD) which each participant received together with conference program. However, proceedings exist in both printed and electronic form. We also went out to the internet, with updated information accessible from any part of the world. Recently, our previous sponsors Serbian Academy of Sciences and Arts and Ministry for Science and Technology of Republic of Serbia were accompanied by the American institute IEEE (Yugoslav Joint Chapter).

Power electronics, as a scientific and technological field, was accepted in our country soon after its appearance in the world. Petar Miljanić, at the time researcher at the "Nikola Tesla" Institute in Belgrade, came out on 31 January, 1961 with his patent of subsynchronous (or Scherbius) cascade for induction motor speed control using thyristor inverter in the rotor circuit, later named throughpass inverter. Two years later, during his stay at NRC Institute in Canada, he made first experimental cascade, while the description of that pioneer work, with initial theoretical fundamentals, were published in IEEE Transactions in 1965, and is still quoted in literature. First thyristor in the form of screw with unusual head, which he brought to Belgrade in 1962, motivated researchers at "Nikola Tesla" Institute to start reflecting on substitution of magnetic amplifiers, at the time, with these little devices. Research study, on semiconductor application in drives based on induction motor was conducted at the Institute already in 1965, and in 1966 were made first controlled rectifiers for accumulator loading and parallel operation

with consumers, based on thyristor use. The same year was designed at the Institute, first subsynchronous cascade with thyristor inverter for induction motor of 3.5 kW power, and two years later a series of these devices were made, reaching the power of 125 kW, which was constructed and implanted in "Prva petoletka" in Trstenik, serving the purpose of pump testing, being produced in this company. Among the merits of the Institute was also their role in estimation of Soviet project for the plant system of six large synchronous 200 kVA generators, at new hydro plant on Đerdap in 1968, forcing Soviet distributors to remodel entire plant system project, which was previously based at mercury rectifiers, and incorporate thyristor rectifiers. First 3-phase thyristor inverter of bigger power (60 kVA), within the system rectifier-inverter, was made and put into operation by the "Nikola Tesla" Institute in the Federal Bureau of Statistics in 1968, as their original and proper solution, and first complete system for continuous supply (UPS) was designed by the same Institute at the Dispatcher Centre in Belgrade, in 1970, also as a result of their own research. In 1989 Slovenian company "Iskra" with the licence of "Nikola Tesla" Institute, made and delivered dozens of 250kVA large systems for continuous supply (UPS), intended for power dispatcher centres in our country and in Soviet Union.

This belgradian Institute was the only research centre in the country for the long time. At the time, "Rade Končar" factory was in the middle of opening their plant for the production of controlled rectifiers based on mercury. Moved by the worldwide development, they have soon introduced thyristor technology, but pursuing somewhat different approach: instead of designing their own solutions, mostly they were buying complete thyristor equipment from abroad and incorporating into their regulation systems. At first symposium on power electronics in Belgrade, in 1973, the researchers from this factory submitted papers on their new systems for continuous supply, electrical drives for DC current, plant systems etc. For that occasion, we received several papers from the faculty in Ljubljana, Slovenia, which dealt on the development of new technology. In the upcoming years appears the designer and company "Iskra" from Novo Mesto with licensed thyristor rectifiers. The period until the end of seventies was marked by the presence of some significant manufacturers, like "Energoinvest" from Sarajevo, "Uljanik" from Pula, "Sever" from Subotica and others, but most of them working with licenses of foreign companies AEG, Siemens, ASEA, BBC etc. and with very little original research work. That expansion was evident from the migration of our symposium on power electronics from Belgrade to Zagreb, later to Sarajevo, Ljubljana and Subotica.

Concerning the university courses at the time, Vladan Vučković was teaching magnetic amplifiers as an optional course. In 1965 he substituted content devoted exclusively to transducers, amplifiers and other devices which based their operation on magnetic saturation, with materials on thyristors and semiconductor converters. Ilija Volčkov was teaching optional course named "Mutators", on converter technology. In the regular curriculum power electronics appeared in 1976 with the course "Power

converters", initiated and taught during many years by Petar Miljanić. Vučković initiated and taught courses in power electronics at the faculty of electronics in Niš, starting from 1977, and later since 1981, at the Faculty of technical sciences in Novi Sad.

Usually, as the beginning of the power electronics era, is considered the appearance of silicon controlled rectifiers (SCR), later named thyristors, produced by the end of the fifties in the laboratories of American company "General Electric". In the next several years, these semiconductor devices made a true revolution in the development of rectifiers, inverters, frequency converters, and in electric energy converting technology in general, similar to the one made by transistors in information technology. Easiness and speed of control, significantly decreased loss, high reliability and longer lifetime of these electric current ventiles caused a massive breakthrough of converting technology into industry and into other aspects of production and research. At present time, thanks to the integration with information technology (based at transistors, integrated circuits and microprocessors) and automation theory, a series of power devices with advanced characteristics was made.

Nevertheless, as far as theory and application of power converters (rectifiers, inverters, etc.) is concerned, the invention of four-layered semiconductor ventiles presents a quantitative progress, significant enough to introduce a new notion of quality. Various configurations e.d. schemes, methods of control, commutation principles, and theory of power converters in general were elaborated and known decades earlier. Controllable ventiles in the form of mercury rectifiers with the net, tiratrons, ignitrons, excitrons and other so-called ionic devices, were different, similar to the use of electronic tubes in the field of information and telecommunication electronics. In 1930, AEG company made a so-called controlled tiratron motor at the power of 500 kW. Energy for the supply of metro and locomotions was conveyed through large mercury based rectifiers, and from Volgograd to Siberia was realized a remote high power DC transmission, which encompassed not only powerful high-voltage rectifiers, but inverters as well. Semiconductor ventiles are modern contactless fast switches, with significantly improved quantitative characteristics. It is not irrelevant whether ventile voltage in the permeable state is 20V or 1V, whether for the ventile transition into permeable state 100 mW or 10 W is enough, is the ventile recuperation time after turn-off several hundred miliseconds or several microseconds, and is the ventile lifetime around two years or it is practically infinite.

Seen from this aspect, term power electronics could have been used for earlier, ionic technology, as well. At the time electronics (frequently called low-current technology, according to German expression Schwachstromtechnik), as a branch of electrical engineering dealing with signal control (in its general meaning), had as its basic element for device realization electronic tubes, triodes, pentodes, etc. – similar to power engineering (or high current technique, according to German expression Starkstromtechnik), as a branch dealing with energy control had on disposal ionic tubes for high current interception. Interesting fact is that since the word

electronics was introduced into this high current technique, with the appearance of semiconductor ventiles, sometimes it is debated whether it is a field of electronics dealing with power engineering, or field of power engineering dealing with electronics.

Assuming the use, domain of power electronics is not limited to power converters and their immediate surrounding. Power converter is essential component of more or less controlled system which consists of elements belonging to other technologies. Modern controlled electromotor drive, for example, contains apart from converter and its immediate surrounding, electrical machine, digital regulation system realized with the use of microcomputers, measuring elements, supervising and controlling computers, telecommunication buses for group command in concordance with the requirements of technological process etc. To the previously mentioned may be added the necessity for the application of new methods for analysis and synthesis of regulated systems in general, based on the achievements of modern control theory, and application of computers for the design, acquisition of measurement data and simulation. This implied a new joint of not only power engineers and electronics engineers, but of engineers coming from different branches too. Eventually, entire power engineering, and not only its part dealing with energy conversion and its control is going nowadays through the same.

Therefore the programs of today scientific reunions, which in their title contain the name of power electronics, are being expanded to other fields of engineering. And vice versa, many magazines and meetings not containing this name in their title, like industrial electronics, industrial applications, electrical machines and systems, electrical drives, control and measurement in industry etc. implicitly contain power electronics, and in official programs, it appears even explicitly.

In accordance with the above mentioned, our program for the current symposium was expanded, and as is known, topics were classified into three groups. First one, under the name power converters, is the core of power electronics - converters, with their immediate application. In the second group, one of its widest applications is emphasized and excerpted - electrical drives. The classification was done not only for the more uniform distribution of submitted papers, but because we are in a need for some expert group of this kind, in recent years. Same is valid for the third group electrical machines. Fourth group, control and measurements in power engineering, comprises papers which regard system as an entity or its control, apropos measurement part. And finally, lately introduced fifth group under the name power electronics in telecommunications, appears due to the increased professional interest in this branch of engineering.

Brief historical review of development of power electronics in our country, given in the introduction of this exposure, relates to its beginning exclusively. In the past two decades, this field of engineering and its related fields were marked by new achievements. Invention of powerful transistors and other semiconductor ventiles, which pushed out thyristors to the power of several hundred kW. Regulation of immediate AC values at the output of inverter, due to the very fast interruption of transistors. Invention and further realization of vector control of induction motor, which finally becomes a motor controlled equally good as a DC current machine. Development of electronic commutator used in synchronous motor with permanent magnets to become DC current machine without brushes and lamina. Introduction of switching reluctant motor, by its nature suitable for the control of electronic ventiles. Application of microprocessors, microcomputers and digital signal processors in the control of power systems and direct control of converters. Digital realization of the principles of modern control theory, like state regulators, output regulators, observers, estimators, adaptive systems, etc. Substantial minituarization and decrease in prices of elements and devices, contributed to the significant expansion of the market.

And after all those events, we find ourselves at the beginning of the new encounter.

HIGH PRECISION CALIBRATION OF AC CURRENT TO VOLTAGE CONVERTERS

Petar Miljanić, Pushkin 9, Belgrade, Serbia and Montenegro

Abstract: A two stage transformer, built as a current comparator with shielded magnetic core, was used to make a novel ac bridge for the calibration of ac shunts, for large currents or other ac current to voltage converters. A reference fine adjustable transresistances is made by current transformation and a non-reactive precision resistor connected in the secondary. By using an auxiliary transformer and resistor, all four two stage transformer secondary terminals are brought to the ground potential and consequently both magnetizing and capacitive errors kept below 1ppm.

Key Words: I/U Converters, Calibration, High Precision

1. INTRODUCTION

High precision measuring of AC currents is obtained from digital data, of immediate voltage values, proportional to measured current. Appropriate electric circuits for synchronous and asynchronous sampling of AC voltage, were developed for such measurements. This way of measurement is suitable for measurement data acquisition: calculating effective current value, determining active and reactive power, distortion measuring, etc. All the indicators show that the digitalization of measuring processes will find wide application in power installations and industry.

The best known current to voltage converter is shunt: low-ohmic resistor made of metal alloy, which has low temperature coefficient of resistance variation and high stability in time. Shunt has two current and two voltage terminals. For the measurement of alternating current is used a transformer with a known resistor connected to its secondary. Assuming it is easier to construct a reliable resistor for smaller currents, using a transformer current measurement has its advantages. Besides, mentioned measurement galvanically separates part of the circuit where current is being measured from the instrumentation, what provides measurement of the current in the power mains of high voltage. Also it should be mentioned that exist transformer systems which enable measurements of not only alternating, but direct component of the current, as well (servo-systems which maintain zero flux in magnetic circuit).

Measurement current to voltage converter is displayed on figure 1. Having four terminals: two terminals for current and two for voltage. Single current terminal may, or may not be brought into connection with single voltage terminal. In the case of absence of galvanic connections, it is accustomed with precise measuring to place electrostatic shielding between above mentioned terminals. Assuming the low capacity between primary and shield it may be concluded that the current at on primary terminal equals the current at another terminal. However, having very precise measurements and high potential differences between circuits, this conclusion should be checked and reconsidered several times. Outgoing impedance with voltage signals is several tens of mili-Ohms, with shunts several tens of mili-Ohms at current to voltage transformer converters. Assuming large input impedance of modern A/D converters, outgoing

impedance may be neglected. Moreover, calibration of current to voltage converters can be done with attached electronics for sampling, and thereby take into account voltage alterations due to load and outgoing converter impedance.

Probing of low-ohmic shunts for alternating current was conducted using Maxwell-Wien's bridge and its variations. Measuring was based at known characteristics of reference shunt and auxiliary resistor and capacitor black boxes. It was not possible to accomplish high-precision measurements due to many difficulties. To mention just the problem of high currents in the bridge, connecting current and voltage connectors, stability of reference shunt, problem of auto-heating and swirling currents.

Low-ohmic shunts and transformer AC current to voltage converters can be directly compared to etalon for AC current to voltage converter, if the galvanic isolation of primary is accomplished, and capacitors between current input and voltage output are being driven to a negligible value. Simplified scheme of such etalon is displayed on Figure 2.

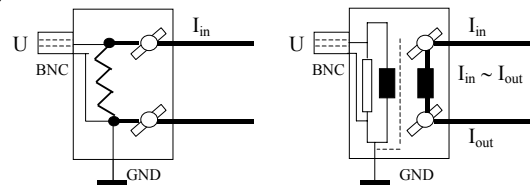


Fig.1

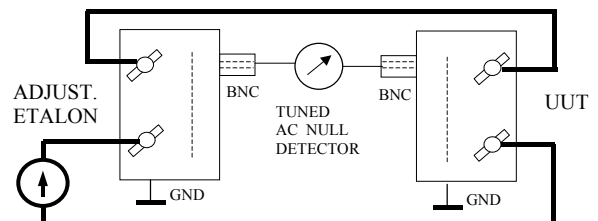


Fig.2

2. TWO STAGE CURRENT TRANSFORMER

If the goal is to accomplish measuring precision better than 0.01%, even the best current transformers yield unacceptably big errors. Theory of current comparators [1], which appeared in 1962, found its application in instruments for high-precision measuring, first at alternating, and later at direct currents.

Technology of current comparators enabled construction of high precision two stage current transformers[2]. Figure 3. shows the design, and figure 4. pictures equivalent scheme of these transformers. Important novelty with the design of high precision current transformers is that toroidal magnetic core of the first transformer has a cavity where another secondary and its toroidal core are placed. Assuming that dispersed lines of the magnetic field can not pierce into interior core, magnetic flux in all intersections of the interior core has the same value, what enables precise definition of such magnetic circuit and

well-known theoretical relations for magnetic circuits ($\Psi = \Sigma NI / \Theta$).

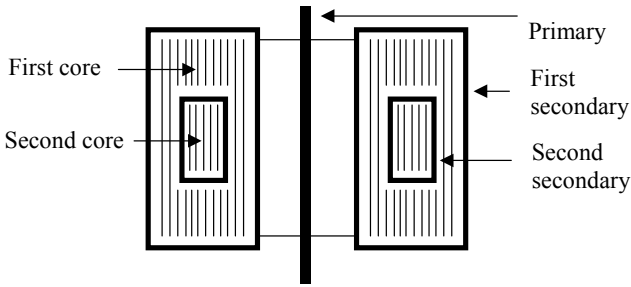


Fig. 3.

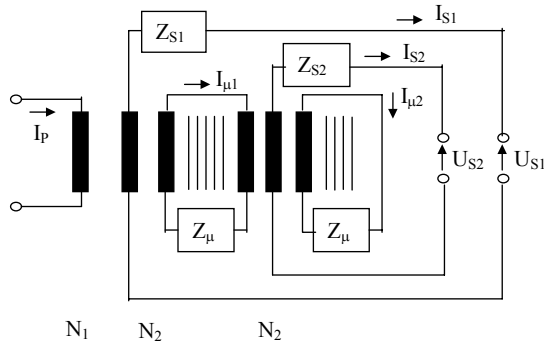


Fig. 4.

Assuming that by the use of magnetic shielding, in other words, placing magnetic circuit of the second core inside the cavity of the first, enabled further application of the law where magnetic flux is proportional to the difference of total ampercoils, following equations may be written:

$$N_1 I_1 = N_2 (I_{S1} + I_{\mu 1}) + e_m \quad (1)$$

$$N_1 I_1 - N_2 I_{S1} = N_2 (I_{S2} + I_{\mu 2}) \quad (2)$$

$$U_{S1} = Z_{\mu 1} I_{\mu 1} + Z_{\mu 2} I_{\mu 2} - Z_{S1} I_{S1} \quad (3)$$

$$U_{S2} = Z_{\mu 2} I_{\mu 2} - Z_{S2} I_{S2} \quad (4)$$

Value e_m acknowledges the fact that the concept of ideal magnetic circuit could not be adopted for magnetic circuit of first order, due to the absence of magnetic shielding. Other values are in conformity with equivalent scheme shown at Figure 2.

Errors of two stage current transformer are:

1) *Magnetic circuit idealization error.* Concept of magnetic circuit assumes that magnetic flux is of the same value in every intersection what enables the definition of magnetic every resistance and the rule that the flux of magnetic circuit equals magnetomotor force divided by the mentioned resistance ($\Psi = \Sigma NI / \Theta$). Though because of dispersing magnetic lines this simple relation cannot be applied, therefore equation (1) introduces error e_m . To approximate the ideal situation where flux in all intersections of magnetic circuit is constant, circuit is being placed in the cavity of magnetic shielding [1] of a toroidal form (Figure 3.). This novelty is essential for the construction of current comparators and for the construction of high precision two stage current transformers. It was established that if the magnetic circuit is protected like this, it is possible to diminish the error, which appears due to dispersing fluxes,

below 1 ppm. Examining the precision of current to voltage converter with the measuring uncertainty of order 1ppm, idealization error of magnetic circuit of second order may be neglected (equation 2).

2) *Error due to magnetizing currents of magnetic circuits of first and second order.* Neglecting errors of higher order in equations (1) - (4) yields the error of two stage current transformer

$$\begin{aligned} \varepsilon &= \frac{N_2 (I_{S1} + I_{S2})}{N_1 I_1} = \quad (5) \\ &= - \frac{Z_{S1} Z_{S2}}{Z_{\mu 1} Z_{\mu 2}} - e_m \frac{Z_{S2}}{Z_{\mu 2}} - \frac{Z_{S2}}{Z_{\mu 1} Z_{\mu 2}} \frac{U_{S1}}{(I_{S1} + I_{S2})} - \frac{1}{Z_{\mu 2}} \frac{U_{S2}}{(I_{S1} + I_{S2})} \end{aligned}$$

This error depends on voltages at terminals of first and second secondary and on magnetizing impedances and impedances of interior coils. If some auxiliary calibration reduces voltages U_{S1} and U_{S2} to zero value, error equals

$$\varepsilon = \frac{N_2 (I_{S1} + I_{S2})}{N_1 I_1} = - \frac{Z_{S1} Z_{S2}}{Z_{\mu 1} Z_{\mu 2}} - e_m \frac{Z_{S2}}{Z_{\mu 2}} \quad (6)$$

Assuming the impedances of the coil equal the order of several Ohms, magnetizing impedances are of order several thousand Ohm, and that low imperfection of magnetic circuit of first order is usually diminished by the quotient $Z_{S2} / Z_{\mu 2}$, this error is of order below 1 ppm. If voltages U_{S1} and U_{S2} are close to zero, error due to voltage U_{S1} is negligible, and error due to remaining voltage U_{S2} is below 1 ppm too.

3) *Capacitive currents error.* Between the coils of solenoid, between solenoids and between coils and electrostatic screen, exist capacitive feedbacks. These capacities are inevitable, their value though equals several tens or hundreds of pF, may seriously corrupt the precision of measurement. Besides the existence of capacity, the flow of capacitive current requires the presence of AC voltage at the terminals of these capacitors. Assuming the symmetry of the coil at toroidal cores and under assumption that voltage at the terminals of these coils is zero it is concluded that there is no potential difference at any place in the transformer, therefore there are neither capacitive currents, nor capacitive error. What is actually going on? Inside the cores, especially in the first core or magnetic shielding exists a change of magnetic flux, yielding electromotor force that induces the current in the coil. But locally in each coil, of both first and second secondary, that induced electromotor force is locally used to surmount ohmic and induction fall of voltage along the solenoid. Effect is the absence of potential difference in the solenoid, and thereby there are no capacitive currents. This leads to the conclusion that if the voltages on first and second secondaries are close to zero and if all four terminals of these solenoids find themselves at the same potential, close to the potential of electrostatic shield, there are no capacitive currents, and therefore there is no capacitive currents error. This fact was used in the instrumentation exposed in this paper.

3. ADJUSTABLE ETALON CURRENT TO VOLTAGE CONVERTER

Figure 5. shows current to voltage converter with a precision and sensibility based on the precise resistor $R_{ref} = 100 \Omega$ and two stage current transformer with $N_2 = 1000$

coils in the secondary and an opening to place one or more solenoids in the primary.

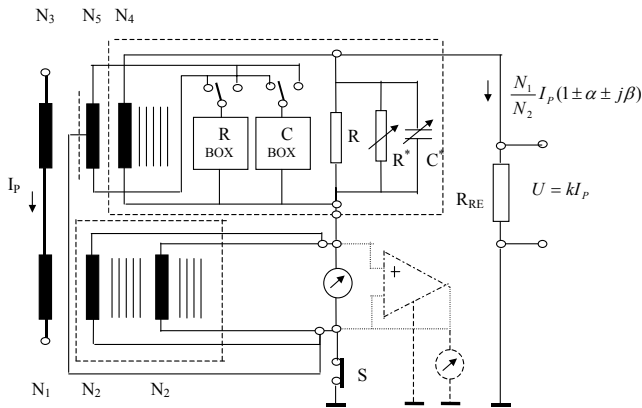


Fig. 5.

This converter and the instrument from the Figure 2. can be used for the calibration of shunts or transformer current to voltage converters with effective values 0.1, 0.2, 0.5 and 1 Ω . Assuming that the diameter of the copper wire used to make first and second secondary is $d = 1$ mm, substituting reference resistor with the 10 Ω resistor, would enable the shunts' calibration of 0.01, 0.02, 0.05 and 0.1 Ω effective values.

4. OPERATING PRINCIPLES

To abandon the use of two stage transformer for the transfer of power, and employ it as a measuring element only, and auxiliary transformer, whose secondary current is two times bigger than the secondary current of the two stage transformer. So, for instance, with primary current of 10 ampercoils (2 coils per 5 A) and 1000 coils in the secondary, secondary current of the two stage transformer is 10 mA. Assuming that $N_2/N_1 = 2 N_4/N_3$ (Figure 5), auxiliary transformer gives 20mA current. Resistor R_1 is approximately equal to the reference resistor R_{ref} so, having in mind that the current is 20 mA - 10 mA = 10 mA, voltage at this resistor is equal to the voltage at the reference resistor R_{ref} . When these two voltages become equal, calibrating resistor R^* and capacitor C^* , there will be no voltage at the terminals of the secondary of two stage transformer, what all gives a high precision of total secondary current, since the error coming from the magnetizing current and capacitive error are minimized.

Assuming the electrostatic screening of the auxiliary transformer, overall current of the two stage current transformer flows through the reference resistor R_{ref} and determines the output voltage which is precisely given by the relation $U = R_{ref} I_p N_2/N_1$. In above example for the measured current of 5 A and $R_{ref} = 100 \Omega$ it would result in an output voltage of 1 V, e.d. transresistance of 0.2 Ω . If the desired value for the effective voltage value, with the current of 5A, is 0.8 V, and the goal is a better adaptation to the measuring range of digital voltmeter for the measurement range up to 1.2 V ($\sqrt{2} * 0.8$), reference resistor should equal $R_{ref} = 80 \Omega$, or the number of coils on the secondary needs to be changed to $N_2 = 1250$, and $R_{ref} = 100 \Omega$ should remain unchanged.

If the application of electronic regulation circuits becomes widely accepted, zero indicator may be substituted by the electronic buffer with an output current of 10 mA, and thereby voltage at the secondaries of the two stage transformer will become negligible. It can be achieved by the opening of the switch S and inserting the circuit displayed by dashes on the figure. Certainly, buffer needs to be a complex circuit with very high input impedance and DC stabilization.

As a goal to obtain precise calibration of transresistance at the auxiliary transformer, solenoid N_3 which hosts the induced voltage proportional to the output voltage, is placed. Output may be precisely corrected by this voltage and with the help of resistor black box and capacitor black box, and thereby this circuit will be converted into an AC bridge intended for the calibration of AC I-U converters (shunts) according to Figure 2.

5. CONCLUSION

New method for AC current to voltage converter calibration was theoretically and experimentally shown and tested. Measurement instability was estimated at 1ppm. Top national measurement laboratories face a difficult task to estimate the precision of this equipment, having in mind that all known methods for measuring transresistance (shunts), with the use of bridge, and under AC currents of a precision which ranges from several amperes to several hundred amperes of less precision.

6. REFERENCES

- [1] P.N.Miljanic, N.L.Kusters, and W.J.M.Moore, "The development of the current comparator, a high accuracy ac ratio measuring device", Trans. AIEE (Commun.Electron.), vol.81, pp.359-368, 1962.
- [2] W.J.M.Moore and P.N.Miljanic, "The current comparator", Inst. Elect. Eng., Electrical Measurement Series, vol.4. London U.K. Peregrinus, 1988.

VECTOR-CONTROLLED MULTI-PHASE MULTI-MOTOR DRIVE SYSTEMS WITH A SINGLE INVERTER SUPPLY*

Emil Levi, Atif Iqbal*, Slobodan N. Vukosavic**, V. Vasic***

Liverpool John Moores University, School of Engineering, Liverpool, UK e.levi@livjm.ac.uk

**Liverpool John Moores University, School of Engineering, Liverpool, UK*

***Faculty of Electrical Engineering, Beograd, Serbia & Montenegro*

****University of Novi Sad, Faculty of Technical Sciences, Novi Sad, Serbia & Montenegro*

Abstract: *The paper discusses foundations of a novel multi-phase multi-motor drive system, in which a set of multi-phase machines is controlled independently while supplying the whole drive from a single multi-phase current-controlled inverter. Realisation of such a drive system requires series connection of stator windings, with an appropriate phase transposition. The concept is applicable to any ac machine type with sinusoidal field distribution and different can be mixed within the same multi-motor drive system. The idea is introduced for an arbitrary phase number and machine connectivity and the number of connectable machines are examined for all possible phase numbers. Connection diagrams are shown for selected phase numbers and decoupling of the flux/torque producing currents of one machine from flux/torque producing currents of all the other machines is proved by steady state calculations. The approach to the multi-motor series-connected drive system d - q modelling is illustrated using the five-phase case as an example. Detailed simulation studies are finally performed for the two-motor five-phase drive and the full dynamic decoupling of flux/torque control of one machine from the other machine in the group is verified.*

Key Words: *Multi-phase Machines, Multi-motor Drives, Vector Control, Phase Transposition.*

1. INTRODUCTION

Multi-phase machines ($n > 3$) offer a number of advantages when compared to three-phase machines. The most important ones are the possibility of achieving a higher torque density through injection of higher stator current harmonics and utilisation of higher spatial field harmonics, fail-safe operation in redundancy mode, and reduction of the required per-phase inverter rating for the same output power [1,2]. It should be noted that the first two advantages of multi-phase machines will not exist in the multi-phase multi-motor drive system elaborated in this paper. This is so since the additional degrees of freedom, which exist in multi-phase-machines and can be used to increase torque density and for fail-safe operation, will be used here for the control of other machines of the multi-motor group.

The basic idea behind the concept presented in the paper relies on the fact that, regardless of the number of phases, only two stator currents are required for decoupled dynamic flux and torque control (vector control) of an n -phase ac machine. This means that the remaining currents

can be used to control the other machines, provided that the stator windings of all the machines are connected in series. However, in order to enable decoupled flux/torque control of one machine from all the other machines in the group, it is necessary that flux/torque producing currents of one machine do not produce a rotating field in all the other machines. This requires introduction of an appropriate phase transposition in the series connection of stator windings.

The concept of the multi-phase multi-motor drive system developed in detail in this paper was for the first time proposed in [3], where the idea was introduced for a two-motor five-phase drive using the notion of an n -dimensional space for an n -phase machine. An entirely different approach, based on the general theory of electrical machines [4,5], is adopted here. The rules for establishing the necessary connection diagram within a multi-motor group are developed by analysing the properties of the decoupling (Clark's) transformation matrix. The numbers of connectable machines are examined for both odd and even phase numbers. It is shown, using a simple steady-state analysis, that flux/torque producing currents of one machine do not produce flux and torque in the other machines when the appropriate phase transposition is introduced in the series connection. Modelling procedure is illustrated for the case of the two-motor five-phase drive. Dynamics of the multi-phase multi-motor drive system are examined by simulation, for the five-phase two-motor drive with induction machines, and the existence of fully decoupled dynamic control is verified. More detailed analysis of various aspects covered in the paper is available in [6-8].

2. MODELLING OF MULTI-PHASE MACHINES

An n -phase machine, such that the spatial displacement between any two consecutive stator phases equals $\alpha = 2\pi/n$, is under consideration. The type of the ac machine is irrelevant as long as the field distribution can be regarded as sinusoidal and the machine can be either an induction or a synchronous (any type) motor. It is therefore assumed that the spatial distribution of the flux is sinusoidal, since the intention is to control torque production due to fundamental harmonic only. All the other standard assumptions of the general theory of electrical machines apply, including the one related to the linearity of the magnetic circuit.

The phase number can be in general either an odd or an even number. Let the phase number be taken initially as an

* This paper is dedicated to Professor dr. Vladan Vuckovic, the founding father of the general theory of electrical machines in South-East Europe, and to the memory of Assistant Professor dr. Radisa Jevremovic, who suddenly passed away in May 2003.

even number. It is important to note that only the true n -phase machines (n being an even number) are discussed here. This means that the m^{th} phase and the $(n/2 + m)^{\text{th}}$ phase are positioned 180 degrees apart and are supplied with currents in phase opposition. Each such an n -phase winding can be reconfigured into semi n -phase winding, with an effective number of phases equal to $n/2$. If the original even phase number n is such that $n/2$ is a prime number, semi n -phase winding becomes a winding with an odd number of phases (these phase numbers are encompassed by the paper). If the original phase number n is a power of two, reconfiguration into a semi n -phase winding requires a neutral conductor. This case is therefore excluded from the analysis.

The machine model in phase variable form can be transformed using decoupling (Clark's) transformation matrix [4,5]. Decoupling transformation substitutes the original set of n phase currents with a new set of n transformed currents. Decoupling transformation matrix for an arbitrary even phase number can be given in power invariant form with (1).

The first two rows in (1) define stator current components that will lead to fundamental flux and torque production (α - β components; stator to rotor coupling appears only in the equations for α - β components), while the last two rows define the two zero sequence components. In between, there are $(n-4)/2$ pairs of rows which define $(n-4)/2$ pairs of stator current components, termed further on x-y components. As will be shown shortly, x-y pairs of current components will play an important role in realising independent control of the machines connected in series.

$$\mathbf{C} = \sqrt{\frac{2}{n}} \begin{bmatrix} \alpha & 1 & \cos \alpha & \cos 2\alpha & \cos 3\alpha & \dots & \cos 3\alpha & \cos 2\alpha & \cos \alpha \\ \beta & 0 & \sin \alpha & \sin 2\alpha & \sin 3\alpha & \dots & -\sin 3\alpha & -\sin 2\alpha & -\sin \alpha \\ x_1 & 1 & \cos 2\alpha & \cos 4\alpha & \cos 6\alpha & \dots & \cos 6\alpha & \cos 4\alpha & \cos 2\alpha \\ y_1 & 0 & \sin 2\alpha & \sin 4\alpha & \sin 6\alpha & \dots & -\sin 6\alpha & -\sin 4\alpha & -\sin 2\alpha \\ x_2 & 1 & \cos 3\alpha & \cos 6\alpha & \cos 9\alpha & \dots & \cos 9\alpha & \cos 6\alpha & \cos 3\alpha \\ y_2 & 0 & \sin 3\alpha & \sin 6\alpha & \sin 9\alpha & \dots & -\sin 9\alpha & -\sin 6\alpha & -\sin 3\alpha \\ \dots & \dots \\ x_{\frac{n-4}{2}} & 1 & \cos\left(\frac{n-2}{2}\alpha\right) & \cos 2\left(\frac{n-2}{2}\alpha\right) & \cos 3\left(\frac{n-2}{2}\alpha\right) & \dots & \cos 3\left(\frac{n-2}{2}\alpha\right) & \cos 2\left(\frac{n-2}{2}\alpha\right) & \cos\left(\frac{n-2}{2}\alpha\right) \\ y_{\frac{n-4}{2}} & 0 & \sin\left(\frac{n-2}{2}\alpha\right) & \sin 2\left(\frac{n-2}{2}\alpha\right) & \sin 3\left(\frac{n-2}{2}\alpha\right) & \dots & -\sin 3\left(\frac{n-2}{2}\alpha\right) & -\sin 2\left(\frac{n-2}{2}\alpha\right) & -\sin\left(\frac{n-2}{2}\alpha\right) \\ 0_+ & 1/\sqrt{2} & 1/\sqrt{2} & 1/\sqrt{2} & 1/\sqrt{2} & \dots & 1/\sqrt{2} & 1/\sqrt{2} & 1/\sqrt{2} \\ 0_- & 1/\sqrt{2} & -1/\sqrt{2} & 1/\sqrt{2} & -1/\sqrt{2} & \dots & -1/\sqrt{2} & 1/\sqrt{2} & -1/\sqrt{2} \end{bmatrix} \quad (1)$$

However, even phase numbers do have a certain advantage for some specific phase numbers, as will be shown later on.

Since stator-to-rotor coupling appears only in the equations for α - β components regardless of the machine type, and since the torque production due to fundamental field component is entirely governed by α - β components only, rotational transformation is applied to α - β equations only. Assuming transformation into an arbitrary common reference frame ($\theta_s = \int \omega_a dt$), the transformation matrix for stator is given with

Equations for pairs of x-y components are completely decoupled from all the other components and stator to rotor coupling does not appear either. These components do not contribute to torque production when sinusoidal distribution of the flux is assumed. Zero sequence components will not exist in any star-connected multi-phase system without neutral conductor. Since any multi-phase machine requires only two stator current components for flux and torque production, this means that at most $(n-2)/2$ machines can be connected in series. In order to do so it is necessary to ensure that the flux/torque producing currents of one machine do not produce flux and torque in all the other machines of the group. A simple series connection of stator windings is obviously not going to achieve this goal. An appropriate phase transposition is therefore required when connecting the windings in series, as discussed shortly.

If the phase number n is an odd number, the last row of (1) does not exist and there is only one zero-sequence component. In between the flux/torque producing components and the zero sequence component there are $(n-3)/2$ pairs of rows, which define $(n-3)/2$ pairs of stator current x-y components. The maximum number of connectable machines is therefore $(n-1)/2$. Hence the number of x-y pairs of current components is the same for an odd number of phases n and the subsequent even number of phases $(n+1)$. This immediately indicates that an odd number of phases and the subsequent even number of phases will lead to the possibility of connecting at most the same number of machines in series. It is therefore advantageous to utilize machines with an odd phase number as far as the number of inverter legs (phases) is concerned.

$$\underline{D}_s = \begin{bmatrix} \cos \theta_s & \sin \theta_s & & & \\ -\sin \theta_s & \cos \theta_s & & & \\ & & 1 & & \\ & & & \dots & \\ & & & & 1 \end{bmatrix} \quad (2)$$

As the decoupled flux and torque control for any particular machine will be achieved using the principles of rotor flux oriented control (regardless of the machine type), the angle of transformation in (2) will equal the instantaneous rotor flux space vector position. Application

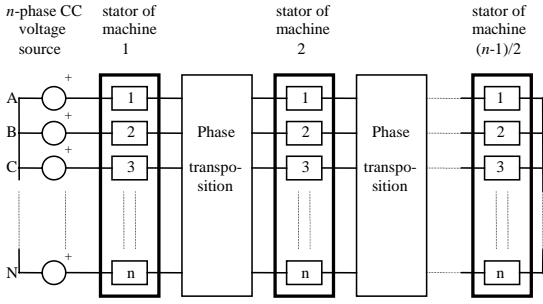


Fig. 1. Supply of $(n-1)/2$ machine stator windings, connected in series, from an n -phase current-controlled voltage source (odd phase number assumed).

case, while solid line is the box for the thirteen-phase case. If a number in the table, obtained by substituting $a=1$, $b=2$, $c=3$, $d=4$, etc., is greater than the number of phases n , resetting is performed by deducting $j \times n$ ($j = 1, 2, 3, \dots$) from the number so that the resulting number belongs to the set $[1, n]$.

4. CONNECTION DIAGRAMS AND CONNECTIVITY MATRICES FOR VARIOUS PHASE NUMBERS

Using the connectivity matrix and the connection diagram for the general n -phase case, given in Fig. 1 and Table 1, corresponding diagrams and matrices are obtained for any specified number of phases. A couple of cases are selected here, with the aim of facilitating the discussion of the number of connectable machines in the next Section.

Connectivity matrix and the connection diagram for the five-phase case are given in Table 2 and Fig. 2, respectively. It is possible to use two machines connected in series and supply them using five inverter legs, instead of six required in a customary two-motor three-phase drive system. The seven-phase case is illustrated in Table 3 and Fig. 3. Three machines can now be controlled with a seven-phase inverter, enabling a saving of two inverter legs with respect to the standard three-phase three-motor system.

The minimum even number of phases that will enable series connection is $n = 6$. The corresponding connectivity matrix, obtained on the basis of the given procedure, is given in Table 4. As can be seen from the last row of this matrix, only phases 1,3 and 5 of the second machine are utilised. As spatial displacement between these phases is 120° , it follows that the second machine is a three-phase machine rather than a six-phase machine. The corresponding connection diagram is given in Fig. 4. Note that the flux/torque producing currents of the six-phase machine mutually cancel at the connection points with the three-phase machine. This means that the three-phase machine will not suffer from any adverse effects due to the series connection with the six-phase machine (this of course does not hold true for the six-phase machine). This is a potential advantage of an even phase number when compared to the previous odd phase number. On the other hand, the six-phase case requires one more inverter leg than the five-phase case, while allowing series connection of the same number of machines (only two).

Table 2. Connectivity matrix, five-phase case.

	A	B	C	D	E
M1	1	2	3	4	5

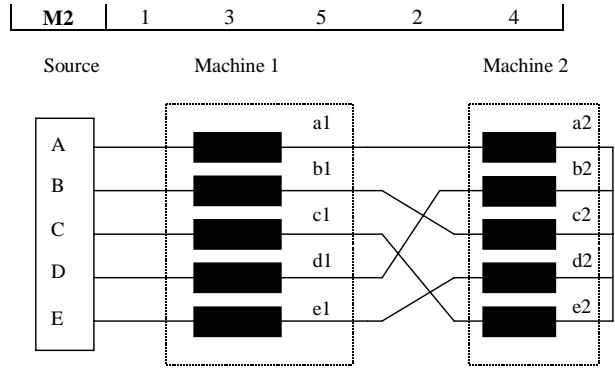


Fig. 2. Connection diagram for two five-phase machines.

Table 3. Connectivity matrix, seven-phase case.

	A	B	C	D	E	F	G
M1	1	2	3	4	5	6	7
M2	1	3	5	7	2	4	6
M3	1	4	7	3	6	2	5

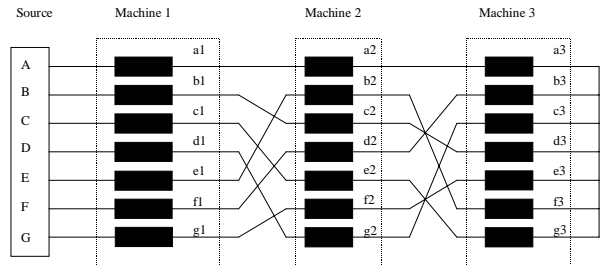


Fig. 3. Connection diagram for the seven-phase system.

Table 4. Connectivity matrix - the six-phase drive.

	A	B	C	D	E	F
M1	1	2	3	4	5	6
M2	1	3	5	1	3	5

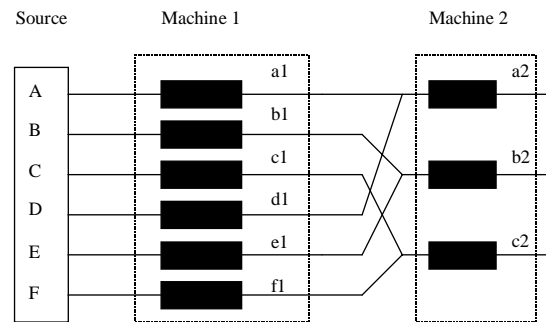


Fig. 4. Six-phase two-motor system.

In the case of an eight-phase system it is possible to connect three machines in series, this being the same as for the seven-phase case. The connectivity matrix is the one given in Table 5. The first and the third machine are eight-phase, however the second machine is four-phase since only phases 1,3,5,7 are utilised (and spatial displacement is therefore 90°). It is important to note that, when connecting the machines in series to the source, all the machines with the highest phase number must come first. This means that the actual sequence of connection of the three machines to the source has to be M1, M3, M2, as shown in the connection diagram in Fig. 5. This is so since flux/torque

producing currents of the machine with a higher phase number cancel when entering the machine with the lower phase number (for example, in the six-phase drive of Fig. 4 phase currents a_1 and d_1 of the six-phase machine are in phase opposition, so that their sum at the point of entry into phase a_2 of the second machine is zero).

In all the cases illustrated so far it was possible to connect in series the maximum possible number $k = (n - 1)/2$ (or $k = (n-2)/2$ for even phase numbers) of machines. Indeed, for any odd or even phase number one expects, on the basis of the considerations given so far, that the number of connectable machines will be $k = (n-1)/2$ or $k = (n-2)/2$. This is however not always the case. For all the phase numbers that require connection of machines with different phase numbers n_1, n_2, n_3 etc. the number of connectable machines will be the maximum one if and only if the ratios $n_1/n_2, n_2/n_3, n_3/n_4$ etc. are all integers. If this condition is not satisfied the number of connectable machines is smaller than the maximum number. For example, a twelve-phase system allows series connection of at most four machines instead of the expected maximum number of five machines. Similarly, a fifteen-phase system will allow series connection of at most six machines instead of the expected

seven machines. This means that some phase numbers are more advantageous than the others. The number of connectable machines is considered next for all the possible phase numbers.

5. NUMBER OF CONNECTABLE MACHINES

Depending on the properties of the phase number n , different situations may arise with respect to the number of connectable machines and their individual phase numbers. Let the phase number be at first an odd number. The following three situations may then be identified:

a) Let the number of phases n be a prime number. The number of machines that can be connected in series with phase transposition then equals

$$k = (n-1)/2 \tag{4}$$

Table 5. Connectivity matrix for the eight-phase drive.

	A	B	C	D	E	F	G	H
M1	1	2	3	4	5	6	7	8
M2	1	3	5	7	1	3	5	7
M3	1	4	7	2	5	8	3	6

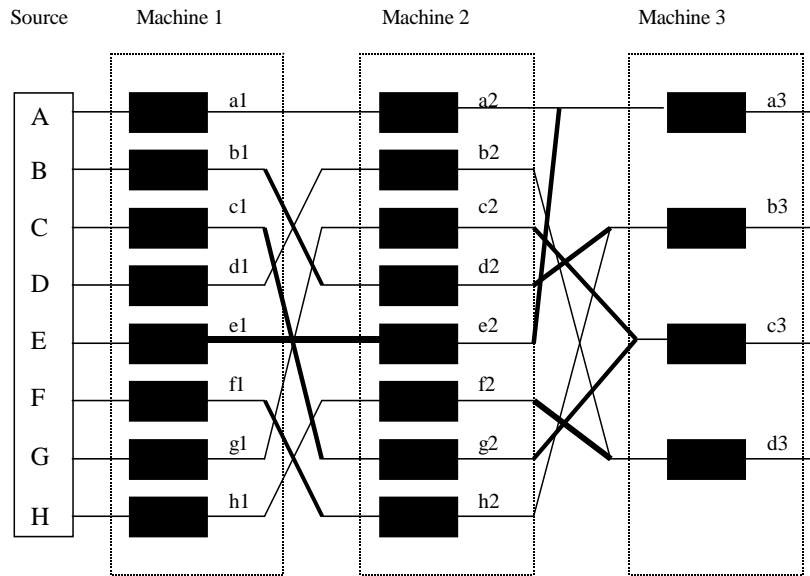


Fig. 5. Connection diagram for the eight-phase drive system.

since there are $(n - 1)/2$ pairs of current components that can be used for independent flux and torque control in this multi-phase machine set. All the machines are of the same number of phases equal to n . The phase numbers belonging to this category are $n = 3, 5, 7, 11, 13, 17, 19$, etc.

b) Consider next the number of phases n that is not a prime number, but it satisfies the condition

$$n = l^m, \quad m = 2, 3, 4, \dots \tag{5}$$

The number of machines that can be connected remains to be given with (4), i.e. $k = (n-1)/2$. However, not all k machines are now of the phase number equal to n . For example, in the case of $n = 27$ ($l=m=3$) a total of $k = 13$ machines can be connected in series: one three-phase machine, three nine-phase machines and nine 27-phase

machines. Hence for the general case of $m > 1$ the phase numbers of the machines that can be connected are

$$n, n/l, n/l^2, \dots, n/l^{m-1} \tag{6}$$

Phase numbers in this category are: $n = 9, 25, 27$, etc.

c) The third possible case arises when n is not a prime number and is not divisible by l^m . However, n is divisible by two or more prime numbers. Let these prime numbers be denoted as n_1, n_2, n_3 , etc. The number of machines that can be connected is now

$$k < (n-1)/2 \tag{7}$$

Ordering of machines in series connection has to be as follows: all the n -phase machines are at first connected in series to the source, with phase transposition. Next follow the machines with the largest prime number value out of n_1 ,

n_2, n_3, \dots (say, n_1). This should be followed by connection of all the machines with the second largest prime number, say n_2 , etc. This rule has to be observed, since its violation makes operation of a higher phase number machine, connected after a lower phase number machine, impossible. One thus reaches the stage where one n_1 phase machine is to be connected to a machine with n_2 phases. This is not possible since the ratio n_1/n_2 is not an integer. An attempt to connect machines of phase numbers equal to different prime numbers leads to the short-circuiting of terminals.

Among these k machines only a certain number will be with n phases. The other machines that should be connectable in the multi-drive system will have phase numbers equal to n_1, n_2, n_3, \dots . In general, the group will be composed of machines with the phase numbers equal to n and one of the prime numbers n_1, n_2, n_3, \dots :

$$n, n_1 \text{ or } n, n_2 \text{ or } n, n_3 \dots \text{ or } n, n_j \quad (8)$$

$$\text{where } n = n_1 \cdot n_2 \cdot n_3 \cdot \dots \cdot n_j.$$

This class of odd phase numbers encompasses the situation where some of the numbers $n_1, n_2, n_3, \dots, n_j$ may be the same prime number, but there is at least one other prime number in the sequence. That is, $n = n_1 \cdot n_2 \cdot \dots \cdot n_j \cdot l^m$, $m = 2, 3, 4, \dots$ is included. The phase numbers belonging to this category are 15, 21, 33, 35, 39, 45, 51, 55, 57, 63, 65, 69, 75, 77, etc.

Categories b) and c) can be regarded as sub-categories of a more general case for which n is not a prime number. They have in common that two or more phase numbers appear in the series connection with phase transposition of the multi-phase machines. However, the total number of connectable machines is not the same, as given by (4) and (7). A summary of all possible situations that can arise for odd numbers of phases is given in Table 6.

Consider next even system phase numbers. Again, there are three possible situations, depending on the properties of the system phase number.

a) Let the number $n/2$ be a prime number. The number of connectable machines equals

$$k = (n-2)/2 \quad (9)$$

The number of phases of individual k machines will be as follows: $k/2$ machines will be n -phase and $k/2$ machines will be $n/2$ -phase. Since the ordering of machines has to

follow the rule that higher number of phases comes first, the first $k/2$ machines are n -phase, while the subsequent $k/2$ machines are $n/2$ -phase. This means that one half of the machines are with an even number of phase, while the rest are with an odd number of phases. The phase numbers belonging to this category are $n = 6, 10, 14, 22, 26, 34, 38, 46, 58, 62, 74$ etc.

b) Consider next the number of phases n such that $n/2$ is not a prime number, but it satisfies the condition

$$n = 2^m, \quad m = 3, 4, 5, \dots \quad (10)$$

The number of machines that can be connected remains to be given with (9). Once again not all k machines are of the phase number equal to n . In the example illustrated previously $n = 8, k = 3$. However, only two machines are eight-phase, while the third one is four-phase. Hence for the general case of $m \geq 3$ the phase numbers of the machines that can be connected in series will be:

$$n, n/2, n/2^2, \dots, n/2^{m-2} \quad (11)$$

This case arises when the phase number of the multi-drive system takes values of $n = 8, 16, 32, 64$, etc.

c) The third possible case arises for all the other even n . The number of connectable machines is

$$k < (n-2)/2 \quad (12)$$

Series connection of machines whose phase number ratio is not an integer is not possible. Again, among these k machines only a certain number is with n phases. The other machines have phase numbers equal to $n/2, n/3, n/4, \dots$ as appropriate. There are at least three different phase numbers among the multi-machine set. Phase numbers that belong to this group are 12, 18, 20, 24, 28, etc.

Cases b) and c) can be again regarded as sub-cases of a more general case for which $n/2$ is not a prime number. The total number of connectable machines is however not the same, ((9) and (12), respectively). A summary of all possible situations for even numbers of phases is provided in Table 7. Of potential practical value are obviously only those phase numbers that enable series connection of the maximum number of connectable machines (i.e. cases a) and b) for both odd and even system phase numbers).

Table 6. Possible situations with odd phase numbers.

$n = \text{an odd number, } \geq 5$			
		Number of connectable machines	Number of phases of machines
$n = \text{prime number}$	$n = 5, 7, 11, 13, \dots$	$k = (n-1)/2$	N
$n \neq \text{prime number}$	$n = l^m, \quad m = 2, 3, 4, \dots$	$k = \frac{n-1}{2}$	$n, \frac{n}{l}, \frac{n}{l^2}, \dots, \frac{n}{l^{m-1}}$
	$n = n_1 \cdot n_2 \cdot n_3 \cdot \dots \cdot n_j$	$k < \frac{n-1}{2}$	$n, n_1 \text{ or } n, n_2 \dots \text{ or } n, n_j$
	$n = n_1 \cdot n_2 \cdot \dots \cdot n_j \cdot l^m, \quad m = 2, 3, 4, \dots$	$k < \frac{n-1}{2}$	$n, n_1 \text{ or } n, n_2 \dots \text{ or } n, n_j$ or $n, n/l, n/l^2 \dots n/l^{m-1}$

Table 7. Number of connectable machines and their phase order for an even system phase number.

$n = \text{an even number, } \geq 6$			
		Number of connectable machines	Number of phases of machines
$n/2 = \text{prime number}$		$k = \frac{n-2}{2}$	$K/2$ ARE N -PHASE AND $K/2$ ARE $N/2$ -PHASE
$n/2 \neq \text{prime number}$	$n = 2^m, m = 3,4,5,\dots$	$k = \frac{n-2}{2}$	$n, \frac{n}{2}, \frac{n}{2^2}, \dots, \frac{n}{2^{m-2}}$
	all other even numbers	$k < \frac{n-2}{2}$	$n, n/2, n/3, n/4,\dots$ as appropriate

6. VECTOR CONTROL OF MULTI-MOTOR DRIVES

The standard method of achieving rotor flux oriented control of a current-fed ac machine (indirect rotor flux oriented control) is considered. It is assumed that there is a rotor position sensor attached to each machine. The basic form of the vector controller is the same as for a three-phase machine of the same type and the only difference is in the co-ordinate transformation, where n phase current references are generated by using the co-ordinate transformation of (1) and (2), instead of three. The vector controller for operation in the base speed (constant flux) region is illustrated in Fig. 6 for n -phase induction and synchronous machines. Phase current references are built for each individual machine first, according to Fig. 6:

$$i_1^{*(Mj)} = \sqrt{\frac{2}{n}} [i_{ds}^{*(Mj)} \cos \phi_r^{(Mj)} - i_{qs}^{*(Mj)} \sin \phi_r^{(Mj)}]$$

$$i_2^{*(Mj)} = \sqrt{\frac{2}{n}} [i_{ds}^{*(Mj)} \cos(\phi_r^{(Mj)} - \alpha) - i_{qs}^{*(Mj)} \sin(\phi_r^{(Mj)} - \alpha)]$$

$$i_n^{*(Mj)} = \sqrt{\frac{2}{n}} [i_{ds}^{*(Mj)} \cos(\phi_r^{(Mj)} - (n-1)\alpha) - i_{qs}^{*(Mj)} \sin(\phi_r^{(Mj)} - (n-1)\alpha)]$$

(13)

where the system phase number is taken as an odd number and superscript Mj stands for the machine under consideration ($M1\dots Mk$). Inverter reference currents are further built, respecting the appropriate connection diagram for the given number of inverter phases. If the phase number n is a prime number, this is a simple summation. If not, the inverter current references are obtained in a slightly more complicated manner.

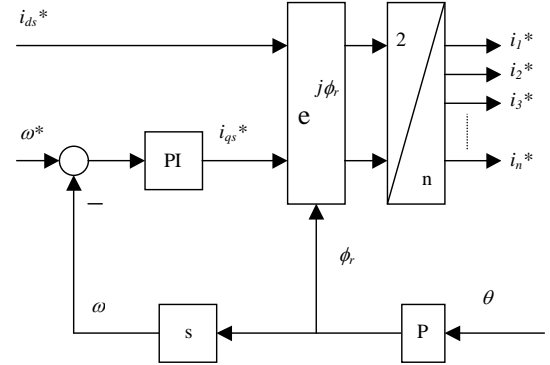
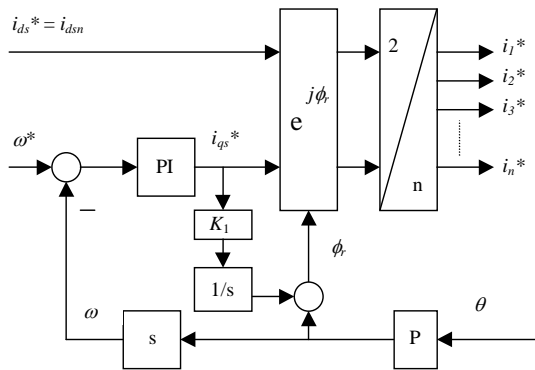


Fig. 6. Indirect vector controller for an n -phase induction and synchronous motor (for permanent magnet machine with surface mounted magnets $i_{ds}^* = 0$; for synchronous reluctance machine, using constant current along d -axis control, $i_{ds}^* = i_{dsn}$), respectively. Index n denotes rated values and $K_1 = 1/(T_r i_{dsn})$.

Taking as an example the seven-phase case of Fig. 3 and Table 3, the inverter current references are built as

$$\begin{aligned} i_A^* &= i_{a1}^* + i_{a2}^* + i_{a3}^* & i_B^* &= i_{b1}^* + i_{c2}^* + i_{d3}^* \\ i_C^* &= i_{c1}^* + i_{e2}^* + i_{g3}^* & i_D^* &= i_{d1}^* + i_{g2}^* + i_{c3}^* \\ i_E^* &= i_{e1}^* + i_{b2}^* + i_{f3}^* & i_F^* &= i_{f1}^* + i_{d2}^* + i_{b3}^* \\ i_G^* &= i_{g1}^* + i_{f2}^* + i_{e3}^* \end{aligned}$$

(14)

In the case of the six-phase system of Fig. 4 and Table 4 the inverter current references are given with

$$\begin{aligned} i_A^* &= i_{a1}^* + 0.5i_{a2}^* & i_B^* &= i_{b1}^* + 0.5i_{b2}^* \\ i_C^* &= i_{c1}^* + 0.5i_{c2}^* & i_D^* &= i_{d1}^* + 0.5i_{a2}^* \\ i_E^* &= i_{e1}^* + 0.5i_{b2}^* & i_F^* &= i_{f1}^* + 0.5i_{c2}^* \end{aligned}$$

(15)

Inverter current references can be built in this way for any system phase number.

The relationship between inverter output phase-to-neutral voltages and phase voltages of individual machines is again governed with the connection diagram. For example, for the five-phase case of Fig. 2 and Table 2,

$$\begin{aligned} v_A &= v_{a1} + v_{a2} & v_B &= v_{b1} + v_{c2} \\ v_C &= v_{c1} + v_{e2} & & \\ v_D &= v_{d1} + v_{b2} & v_E &= v_{e1} + v_{d2} \end{aligned}$$

(16)

while in the six-phase drive system of Fig. 4 and Table 4

$$\begin{aligned} v_A &= v_{a1} + v_{a2} & v_B &= v_{b1} + v_{b2} & v_C &= v_{c1} + v_{c2} \\ v_D &= v_{d1} + v_{a2} & v_E &= v_{e1} + v_{b2} & v_F &= v_{f1} + v_{c2} \end{aligned}$$

(17)

7. STEADY STATE CONSIDERATIONS

In order to verify the concept, steady state operation with ideal sinusoidal currents is analysed first. Let us assume that the machine 1 of the five-phase two-motor drive of Fig. 2 is supplied for the purposes of torque and flux production with ideal sinusoidal currents of RMS value and angular frequency equal to I_1, ω_1 . Similarly, machine 2 is supplied with a flux and torque producing set of currents of RMS value and frequency I_2, ω_2 . According to the connection diagram in Fig. 2, source currents are simultaneously corresponding phase currents for machine 1:

$$\begin{aligned} i_A &= i_{a1} = \sqrt{2}I_1 \sin(\omega_1 t) + \sqrt{2}I_2 \sin(\omega_2 t) \\ i_B &= i_{b1} = \sqrt{2}I_1 \sin(\omega_1 t - \alpha) + \sqrt{2}I_2 \sin(\omega_2 t - 2\alpha) \\ i_C &= i_{c1} = \sqrt{2}I_1 \sin(\omega_1 t - 2\alpha) + \sqrt{2}I_2 \sin(\omega_2 t - 4\alpha) \quad (18) \\ i_D &= i_{d1} = \sqrt{2}I_1 \sin(\omega_1 t - 3\alpha) + \sqrt{2}I_2 \sin(\omega_2 t - \alpha) \\ i_E &= i_{e1} = \sqrt{2}I_1 \sin(\omega_1 t - 4\alpha) + \sqrt{2}I_2 \sin(\omega_2 t - 3\alpha) \end{aligned}$$

Machine 2 is connected to the source via the "phase transposition", so that

$$\begin{aligned} i_{a2} &= i_A = \sqrt{2}I_1 \sin(\omega_1 t) + \sqrt{2}I_2 \sin(\omega_2 t) \\ i_{b2} &= i_D = \sqrt{2}I_1 \sin(\omega_1 t - 3\alpha) + \sqrt{2}I_2 \sin(\omega_2 t - \alpha) \\ i_{c2} &= i_B = \sqrt{2}I_1 \sin(\omega_1 t - \alpha) + \sqrt{2}I_2 \sin(\omega_2 t - 2\alpha) \quad (19) \\ i_{d2} &= i_E = \sqrt{2}I_1 \sin(\omega_1 t - 4\alpha) + \sqrt{2}I_2 \sin(\omega_2 t - 3\alpha) \\ i_{e2} &= i_C = \sqrt{2}I_1 \sin(\omega_1 t - 2\alpha) + \sqrt{2}I_2 \sin(\omega_2 t - 4\alpha) \end{aligned}$$

Application of the transformation matrix (1) on stator currents of the two machines given with (18)-(19) produces results summarised in Table 8. From Table 8 it is evident that, due to phase transposition in the series connection of the two machines, flux/torque producing currents of machine 1 produce α - β current components in machine 1, while they produce x-y current components in machine 2, and vice versa. It therefore follows that the currents of the second machine create a resultant mmf of overall zero value in any instant in time in machine 1, and vice versa. Hence it is possible to independently control the two five-phase machines while supplying them from a single five-phase inverter.

Consider next the six-phase system of Fig. 4 and Table 4 and let I_1, ω_1 and I_2, ω_2 now stand for the peak values and angular frequencies of sinusoidal flux/torque producing currents of the six-phase and the three-phase machine, respectively. Using the same procedure, results given in Table 9 are obtained (space vector form is given and zero sequence components, being equal to zero, are omitted). In principle, the same conclusions apply as for the five-phase case. It is to be noted that the three-phase machine is not affected in any adverse manner by the series connection to the six-phase machine.

8. D-Q MODELLING OF THE FIVE-PHASE TWO-MOTOR DRIVE SYSTEM

The modelling procedure and the resulting equations for the five-phase two-motor drive are given in this Section.

Table 8. Steady state current components of the two-machine five-phase drive system.

Current components	M1	M2
α	$\sqrt{5}I_1 \sin \omega_1 t$	$\sqrt{5}I_2 \sin \omega_2 t$
β	$-\sqrt{5}I_1 \cos \omega_1 t$	$-\sqrt{5}I_2 \cos \omega_2 t$
x1	$\sqrt{5}I_2 \sin \omega_2 t$	$\sqrt{5}I_1 \sin \omega_1 t$
y1	$-\sqrt{5}I_2 \cos \omega_2 t$	$\sqrt{5}I_1 \cos \omega_1 t$
0	0	0

Table 9. Steady state current components of the two-machine six-phase drive system.

Currents in supply phases	M1 – six-phase machine	M2 – three-phase machine
I_1, ω_1	$\frac{\alpha-\beta}{\sqrt{2}} I_1 e^{j(\omega_1 t - \pi/2)}$	—
$\frac{1}{2} I_2, \omega_2$	$\frac{x1-y1}{\sqrt{2}} \frac{I_2}{2} e^{j(\omega_2 t - \pi/2)}$	$\frac{\alpha-\beta}{\sqrt{2}} I_2 e^{j(\omega_2 t - \pi/2)}$

The same approach can be used for any system phase number. It is assumed that the two machines are both induction machines. Voltage equilibrium is given by (16), while the supply currents and individual motor currents are related through

$$\begin{aligned} i_A &= i_{a1} = i_{a2} \\ i_B &= i_{b1} = i_{c2} \\ i_C &= i_{c1} = i_{e2} \\ i_D &= i_{d1} = i_{b2} \\ i_E &= i_{e1} = i_{d2} \end{aligned} \quad (20)$$

Application of (1) in conjunction with inverter voltages of (16) yields axis components of the inverter voltages, which can be further expressed using correlation with individual machine phase voltages in (16), as functions of the voltage axis components of the two machines

$$\begin{bmatrix} v_\alpha^{INV} \\ v_\beta^{INV} \\ v_x^{INV} \\ v_y^{INV} \\ v_0^{INV} \end{bmatrix} = \underline{C} \begin{bmatrix} v_A \\ v_B \\ v_C \\ v_D \\ v_E \end{bmatrix} = \underline{C} \begin{bmatrix} v_{a1} + v_{a2} \\ v_{b1} + v_{c2} \\ v_{c1} + v_{e2} \\ v_{d1} + v_{b2} \\ v_{e1} + v_{d2} \end{bmatrix} = \begin{bmatrix} v_{\alpha s1} + v_{\alpha s2} \\ v_{\beta s1} - v_{\beta s2} \\ v_{x s1} + v_{\alpha s2} \\ v_{y s1} + v_{\beta s2} \\ 0 \end{bmatrix} \quad (21)$$

Due to the absence of the neutral conductor inverter zero sequence voltage component must equal zero. The correlation between inverter voltage axis components and

individual machine's voltage axis components implies series connection between appropriate α - β and x-y circuits of the two machines. A corresponding correlation between inverter output currents and α - β and x-y current components of the two machines is obtained by using (1) and (20),

$$\begin{aligned} i_{\alpha}^{INV} &= i_{\alpha s1} = i_{x s2} \\ i_{\beta}^{INV} &= i_{\beta s1} = -i_{y s2} \\ i_x^{INV} &= i_{x s1} = i_{\alpha s2} \\ i_y^{INV} &= i_{y s1} = i_{\beta s2} \end{aligned} \quad (22)$$

The zero sequence component is omitted due to the star connection of the system without neutral conductor.

Rotational transformation is executed next. Stationary reference frame is selected for the illustration of the resulting model of the five-phase two-motor drive system. The four inverter equations are obtained in the following form:

$$\begin{aligned} v_d^{INV} &= R_{s1}i_d^{INV} + (L_{ls1} + L_{m1})\frac{di_d^{INV}}{dt} + L_{m1}\frac{di_{dr1}}{dt} + R_{s2}i_d^{INV} + L_{ls2}\frac{di_d^{INV}}{dt} \\ v_q^{INV} &= R_{s1}i_q^{INV} + (L_{ls1} + L_{m1})\frac{di_q^{INV}}{dt} + L_{m1}\frac{di_{qr1}}{dt} + R_{s2}i_q^{INV} + L_{ls2}\frac{di_q^{INV}}{dt} \\ v_x^{INV} &= R_{s1}i_x^{INV} + L_{ls1}\frac{di_x^{INV}}{dt} + R_{s2}i_x^{INV} + (L_{ls2} + L_{m2})\frac{di_x^{INV}}{dt} + L_{m2}\frac{di_{dr2}}{dt} \\ v_y^{INV} &= R_{s1}i_y^{INV} + L_{ls1}\frac{di_y^{INV}}{dt} + R_{s2}i_y^{INV} + (L_{ls2} + L_{m2})\frac{di_y^{INV}}{dt} + L_{m2}\frac{di_{qr2}}{dt} \end{aligned} \quad (23)$$

Rotor voltage equilibrium equations are

$$\begin{aligned} 0 &= R_{r1}i_{dr1} + L_{m1}\frac{di_d^{INV}}{dt} + (L_{lr1} + L_{m1})\frac{di_{dr1}}{dt} + \omega_1(L_{m1}i_q^{INV} + (L_{lr1} + L_{m1})i_{qr1}) \\ 0 &= R_{r1}i_{qr1} + L_{m1}\frac{di_q^{INV}}{dt} + (L_{lr1} + L_{m1})\frac{di_{qr1}}{dt} - \omega_1(L_{m1}i_d^{INV} + (L_{lr1} + L_{m1})i_{dr1}) \\ 0 &= R_{r2}i_{dr2} + L_{m2}\frac{di_x^{INV}}{dt} + (L_{lr2} + L_{m2})\frac{di_{dr2}}{dt} + \omega_2(L_{m2}i_y^{INV} + (L_{lr2} + L_{m2})i_{qr2}) \\ 0 &= R_{r2}i_{qr2} + L_{m2}\frac{di_y^{INV}}{dt} + (L_{lr2} + L_{m2})\frac{di_{qr2}}{dt} - \omega_2(L_{m2}i_x^{INV} + (L_{lr2} + L_{m2})i_{dr2}) \end{aligned} \quad (24)$$

$$\begin{aligned} 0 &= R_{r2}i_{dr2} + L_{m2}\frac{di_x^{INV}}{dt} + (L_{lr2} + L_{m2})\frac{di_{dr2}}{dt} + \omega_2(L_{m2}i_y^{INV} + (L_{lr2} + L_{m2})i_{qr2}) \\ 0 &= R_{r2}i_{qr2} + L_{m2}\frac{di_y^{INV}}{dt} + (L_{lr2} + L_{m2})\frac{di_{qr2}}{dt} - \omega_2(L_{m2}i_x^{INV} + (L_{lr2} + L_{m2})i_{dr2}) \end{aligned} \quad (25)$$

Finally, torque equations of the two series-connected machines are given in terms of inverter current axis components with

$$\begin{aligned} T_{e1} &= P_1 L_{m1} [i_{dr1}i_q^{INV} - i_d^{INV}i_{qr1}] \\ T_{e2} &= P_2 L_{m2} [i_{dr2}i_y^{INV} - i_x^{INV}i_{qr2}] \end{aligned} \quad (26)$$

9. PERFORMANCE OF THE FIVE-PHASE TWO-MOTOR DRIVE SYSTEM

The concept of the multi-phase multi-motor drive system, described in the paper, is verified by simulating the two-motor five-phase drive system of Fig. 2. The two induction machines are assumed to be identical (per-phase parameters and ratings are given in the Appendix). Inverter is included in the simulation and hysteresis current control is

utilized. The simulated series of transients consists of the excitation transient, acceleration transient under no-load conditions, step load torque application and speed reversal (total simulation time of 2 s). Torque limit is set to twice the rated motor torque (i.e. 16.67 Nm).

Stator d-axis current reference (rotor flux reference) is initially ramped to twice the rated value and is after 0.05 seconds ramped down to the rated value. It is further kept unchanged. Speed command of 1500 rpm is applied to IM1 at 0.3 s, while a 750 rpm speed command is given to IM2 at 0.40 s (all speed commands have a ramp of 0.05 s). Next, rated load torque (8.33 Nm) is applied to IM1 at 1 s and load torque of 50% of the rated value (4.165 Nm) is applied to IM2 at 1.1 s. Finally, speed reversal to -1500 rpm is initiated for IM1 at 1.25 s, while IM2 is reversed to -750 rpm at 1.3 s.

Rotor flux reference and the actual rotor flux in the two machines are shown in Fig. 7 for the complete duration of the sequence of transients. As can be seen from Fig. 7, rotor flux builds up independently in the two machines and, after attaining rated value in less than 0.1 second, remains further on unchanged regardless of what happens to any of the two machines. This indicates that rotor flux control in any of the two machines is completely decoupled from torque control of both machines. Such a situation is confirmed in Fig. 8, where torque and speed responses of the two machines are shown for the initial accelerations (up to 0.9 s). Torque variation in one machine does not affect torque of the other machine and vice versa, so that both machines accelerate with the torque in the limit. One notices the

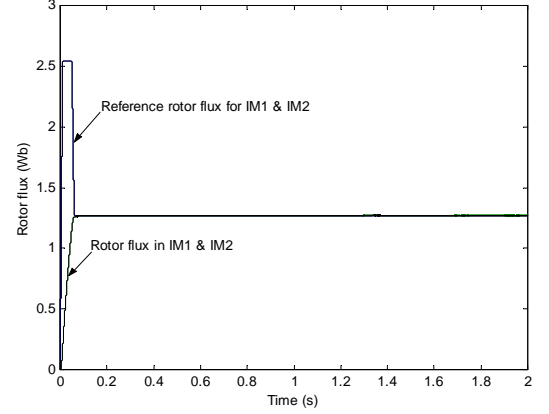
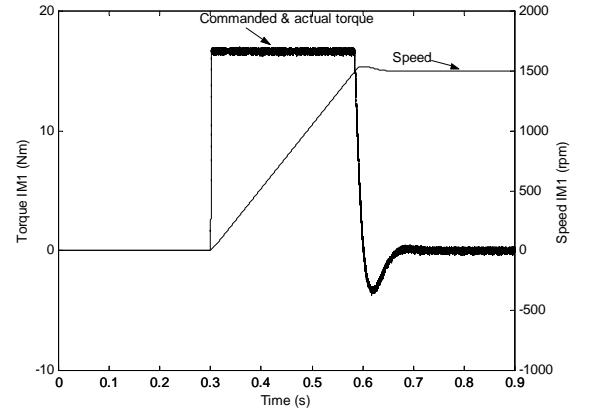


Fig. 7. Rotor flux reference and rotor flux in the two series-connected machines.



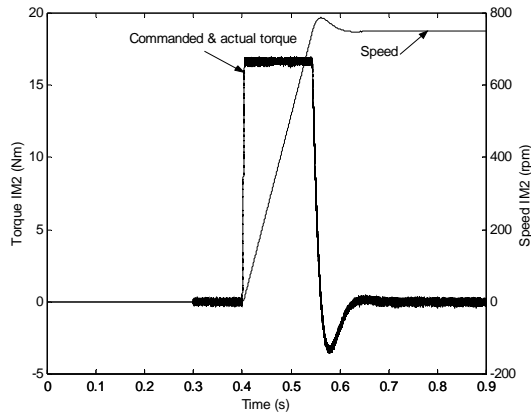


Fig. 8. Torque and speed response of the two five-phase induction motors connected in series.

appearance of the torque ripple in IM2 prior to the application of the speed command to it (time interval 0.3 to 0.4 s). This is a consequence of the inverter current higher harmonics and is an expected consequence of the non-ideal nature of the inverter.

Stator phase 'a' current references, as well as the inverter phase 'a' current reference and actual current, are shown in Fig. 9 for the same time interval. While the individual phase current references have the familiar waveform and are sinusoidal functions in final steady state, the inverter current references (and hence the actual inverter output currents as well) are highly distorted due to the summation, which involves phase transposition. In final steady state of Fig. 9 inverter current references are sums of two sinusoidal functions, of 50 Hz and 25 Hz frequency, respectively.

Stator phase 'a' voltages of the two machines and the total inverter phase 'a' output voltage are illustrated in Fig. 10. The inverter phase 'a' voltage is a sum of the stator phase 'a' voltages of the two machines, as given with (16). Due to the PWM nature of the waveforms in Fig. 10, no other viable conclusion can be drawn. However, it can be shown using Fourier analysis that all the voltages in Fig. 10 contain harmonic components at both 25 Hz and 50 Hz, of appropriate values.

Torque and speed responses following the step application of the load torque are illustrated in Fig. 11. Since the rotor flux remains undisturbed (Fig. 7), torque responses are the quickest possible, leading to a rapid compensation of the speed dip, caused by the load torque application. Reversing transient is illustrated in Figs. 12 (speed and torque responses) and 13 (stator phase 'a' current references and inverter phase 'a' current reference and actual current). Fully decoupled flux and torque control, as well as a fully independent control of the two machines, is again evident.

Simulation study, illustrated in Figs. 7-13, fully verifies the concept and confirms the feasibility of vector controlled multi-phase multi-motor drive systems with a single inverter supply and current control in the stationary reference frame. The principal advantage of such systems is a saving in the number of inverter legs, compared to an equivalent three-phase system with the same number of machines.

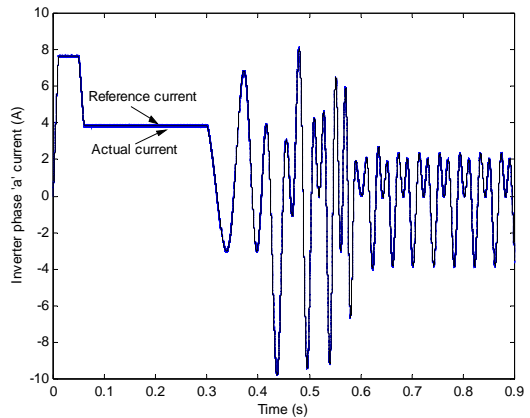
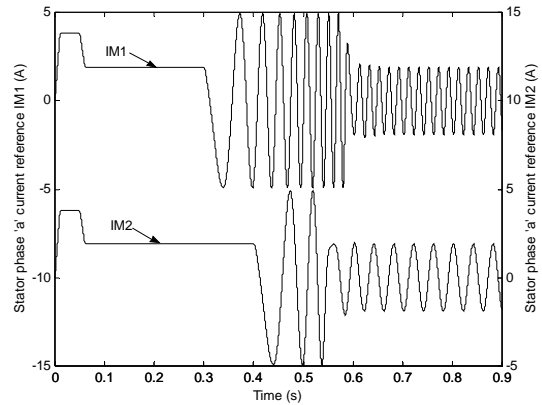


Fig. 9. Stator phase 'a' current references and reference and actual inverter phase 'a' current.

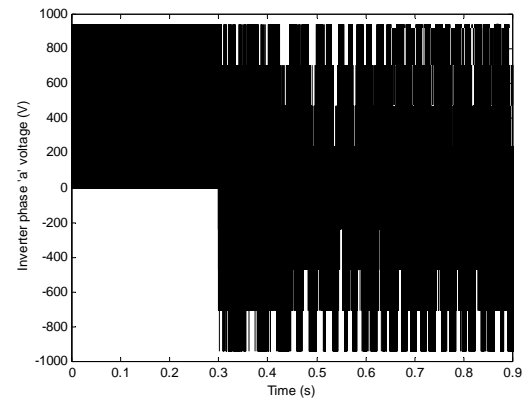
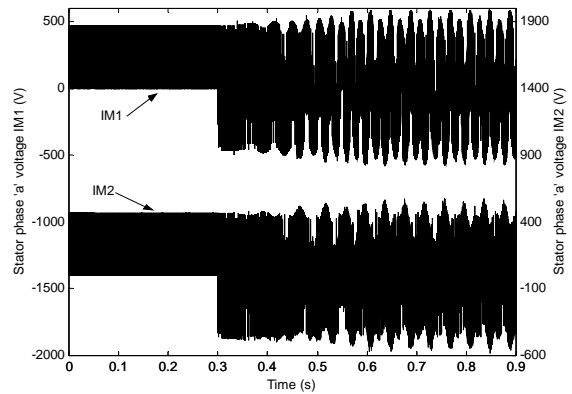


Fig. 10. Stator phase 'a' voltages of the two machines and inverter phase-to-neutral (phase 'a') output voltage.

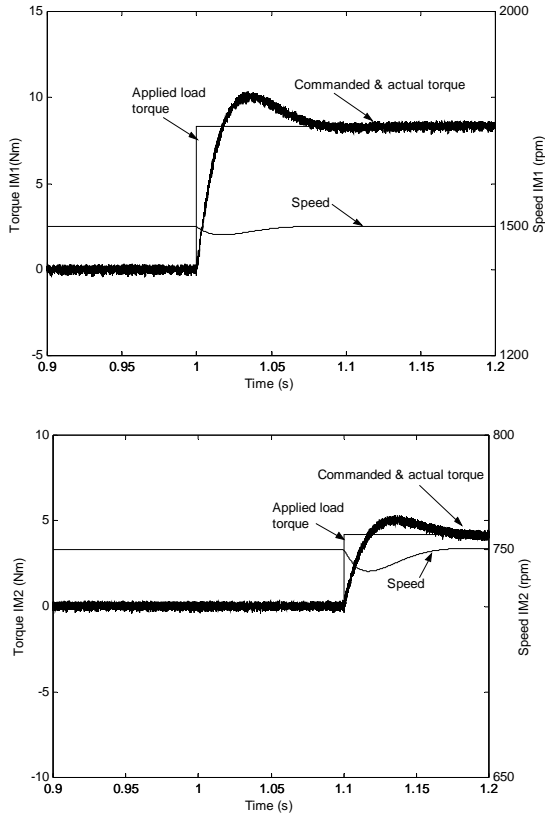


Fig. 11. Torque and speed responses following step load torque applications in the two machines.

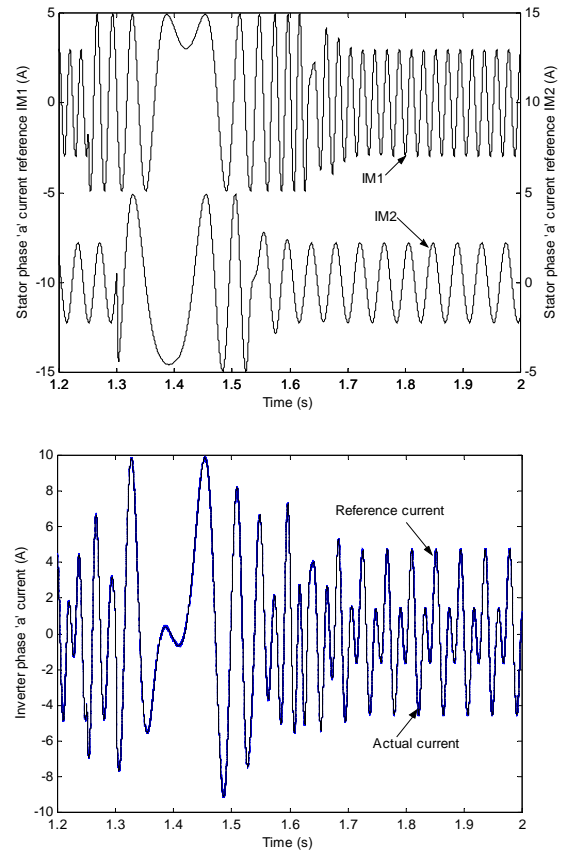


Fig. 13. Stator phase 'a' current references of IM1 and IM2 and inverter phase 'a' current during speed reversals.

10. CONCLUSION

The paper sets forth foundations of a novel concept for a multi-phase multi-motor drive system, which enables independent vector control of all the machines within the group although only a single current-controlled voltage source multi-phase inverter is used. The stator multi-phase windings have to be connected in series with an appropriate phase transposition, in order to achieve the independent control of the individual machines in the system. The concept is developed in a systematic manner, using general theory of electrical machines, and is valid regardless of the type of the ac machine, so that different machine types can be used within the same multi-motor drive system. The necessary pre-requisite for the application of the concept in presented form is that the inverter current control is performed in the stationary reference frame, using total inverter phase currents. The concept is applicable to any phase number greater than or equal to five.

Classification of all the possible odd and even phase numbers is performed, with regard to the maximum number of machines that can be connected in series and phase numbers of individual machines. A couple of characteristic phase numbers ($n = 5, 6, 7$ and 8) are illustrated with appropriate connection diagrams and a vector control algorithm is presented for the general n -phase case. A detailed presentation of the d-q modeling procedure for a five-phase two-motor drive system is provided next. The concept is verified by at first examining steady state operating conditions of a five-phase two-motor drive and a

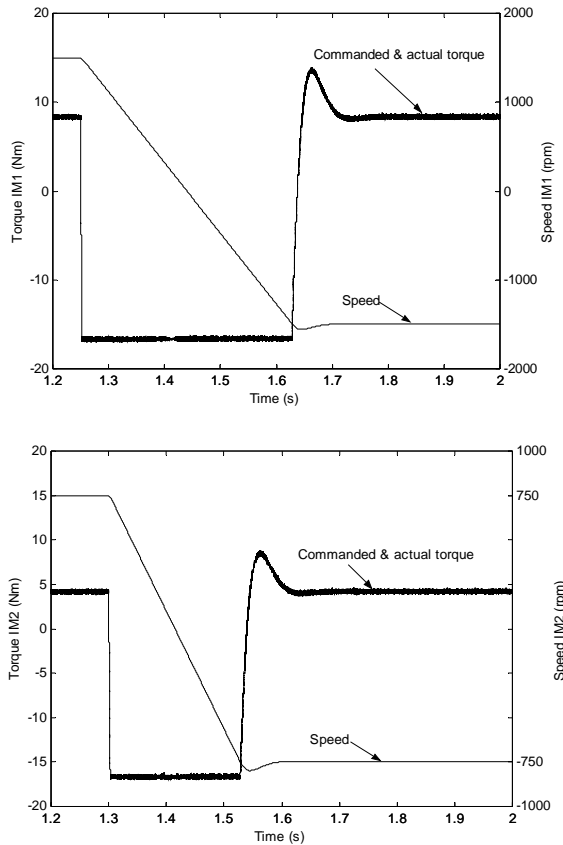


Fig. 12. Torque and speed responses of the two machines for reversing transients.

seven-phase three-motor drive. A detailed simulation of a five-phase two-motor drive system with indirect rotor flux oriented control is then undertaken and existence of the fully decoupled dynamic control of the two machines is confirmed.

The main advantage of the concept is the saving in the required number of inverter legs. Its main shortcoming is an increase in the stator winding losses due to the flow of non-flux/torque producing currents through the stator windings. This shortcoming is pronounced most when all the machines of the multi-motor system have the same number of phases.

11. REFERENCES

- [1] G.K.Singh, "Multi-phase induction machine drive research – a survey", Electric Power Systems Research, Vol. 61, No. 2, 2002, pp. 139-147.
- [2] M.Jones, E.Levi, "A literature survey of state-of-the-art in multiphase AC drives", Int. Universities Power Engineering Conference UPEC, Stafford, UK, 2002, pp. 505-510.
- [3] S.Gataric, "A polyphase Cartesian vector approach to control of polyphase AC machines", IEEE Ind. Appl. Soc. Annual Meeting IAS, Rome, Italy, 2000, CD-ROM Paper no. 38-02.
- [4] D.C.White, H.H.Woodson, "Electromechanical Energy Conversion", John Wiley and Sons, New York, NY, 1959.
- [5] V.Vuckovic, "Opsta teorija elektricnih masina", Nauka, Beograd, 1992 (in Serbian).
- [6] E.Levi, M.Jones, S.N.Vukosavic, "An even-phase multi-motor vector controlled drive with single inverter supply and series connection of stator windings", IEE Proceedings – Electric Power Applications, vol. 150, no. 5, 2003.
- [7] E.Levi, M.Jones, S.N.Vukosavic, H.A.Toliat, "Independent vector control of a seven-phase three-motor drive system supplied from a single voltage source inverter", IEEE Power Elec. Spec. Conf. PESC, Acapulco, Mexico, 2003, pp. 1865-1870.
- [8] E.Levi, M.Jones, S.N.Vukosavic, H.A.Toliat, "A five-phase two-machine vector controlled induction motor drive supplied from a single inverter", European Power Electronics and Applications Conference EPE, Toulouse, France, Sept. 2003.

12. ACKNOWLEDGEMENT

The authors gratefully acknowledge support provided for the work on this project by the EPSRC (standard research grant GR/R64452/01), and by Semikron Ltd. Mr. M. Jones acknowledges an additional financial support provided for his PhD studies by the IEE, through the IEE Robinson Research Scholarship.

13. APPENDIX: PER-PHASE MOTOR DATA

Per-phase equivalent circuit parameters:

$$R_s = 10 \Omega \quad R_r = 6.3 \Omega$$

$$L_{ls} = L_{lr} = 0.04 \text{ H} \quad L_m = 0.42 \text{ H}$$

Per-Phase Induction Motor Data	Value
Rated torque (Nm)	1.66 7
Rated current (A)	2.1
Rated voltage (V)	220
Rated frequency (Hz)	50
Inertia (kgm ²)	0.03
Rated RMS rotor flux (Wb)	0.56 8
Pole pair number	2

LOSS FUNCTION ON-LINE IDENTIFICATION FOR THE INDUCTION MOTOR DRIVES

Slobodan Vukosavić, Emil Levi, V. Vasić***

*Faculty of Electrical Engineering, Beograd, Serbia & Montenegro, boban@iee.org, *: Liverpool John Moores University, School of Engineering, Liverpool, UK, **University of Novi Sad, Faculty of Technical Sciences, Novi Sad, Serbia & Montenegro*

Abstract: *In this paper, a DSP-based loss function identification for the induction motor drive is proposed and tested. The minimum loss operating point is decided from a functional approximation of the motor and the power converter losses, in the form of a suitably defined loss function. The loss function parameters are obtained on-line from input power measurement and a dedicated identification routine acting in conjunction with the common drive control functions. Proposed on-line identification of the loss function parameters relies upon the signals and states readily available within the drive controller memory and does not involve the user entry nor the initialisation procedure. Proposed controller is suitable for the use with conventional, low cost 16 bit DSP and it has been verified on an experimental setup with a TI DSP. and a standard induction motor.*

Key Words: *Power conversion, induction motor drives, minimum energy control, digital signal processors*

1. INTRODUCTION

Since the onset of the IMD frequency control, efforts were made to improve the IMD efficiency by varying the flux amplitude for a better balance between core and copper losses. The IMDs with the greatest potential for energy saving are the low dynamics drives operating in the constant torque mode with frequent light load intervals [1]. Majority of simpler IM drives, such as the pumps, compressors and the heating, ventilation and air conditioning drives are eligible, as well as are numerous more specific applications such as the elevator drives [2], running mostly with less than a half of the rated torque, and the electrical/hybrid vehicles, where the energy saving increases the zero/low emission range [3]. The IMD power loss reduction is most easily achieved by implementing a loss minimisation controller. The benefit of this approach is its applicability to standard, off-the-shelf induction motors (in contrast to the second possible approach, which is design and manufacturing of a non-standard 'high-efficiency' motor). Worthy results have been achieved over the last two decades, as summarised in a number of excellent surveys [4-7]. In [6], an extensive overview with over one hundred references identifies three distinct approaches to optimum efficiency (minimum loss) control. The use of the the displacement power factor or the rotor slip frequency for the power loss reduction is addressed in [8-10]. The search controllers (SC) [11-17] minimise the drive input power by iterative adjustments of the flux command. Input power is a parabolic function of the flux, that has strictly positive second derivative with the regime-dependent minimum that can be found by various search procedures [11-13,17], including fuzzy and neuro-fuzzy methods [14-16].

The search control solutions have unprecedented parameter independence and the precision is compromised only when the input power dependence on flux is too smooth and flat around the minimum. However, even with a constant output power, a SC never reaches the steady state and produces continuous flux and torque pulsations around the optimum operating point. With search times of well over a second duration and even exceeding 7 seconds [1], the SC is of no practical value in drives with fast changing loads. Abrahamsen [1] finds that the SC in the pump drive load cycle offers only a half of the LMC-obtained power loss reduction. Reduction of the search time to below 2 seconds has recently been achieved using 'golden section' search technique [17]. Nevertheless, the problem of slow convergence remains to be the major drawback of SCs. In addition, the load torque pulsations and the input power measurement errors interfere with the search procedure and may lead to a large drift and instability.

LMC response is smooth and fast, for they use a functional model of the system losses to determine the optimum flux for the given load and speed. This is the main advantage of the LMC approach over the SC method and is an obvious solution for all the contemporary drives, both sensed and sensorless, which have d-q reference frame based control system and therefore anyway require some knowledge regarding the controlled motor. Regardless of whether a loss model controller is applied in the form of the single-phase equivalent circuit [18] or in the d-q frame [19], accurate values of motor parameters are required for the correct operation. Precise modelling of both the fundamental and harmonic losses makes the IM equivalent circuit parameters insufficient and requires the PWM frequency phenomena to be considered as well. Harmonic and stray losses are frequency, temperature and saturation dependent and only indirectly controllable. Loss function gets further complicated if the drive converter losses are taken into account. Successful LMC applications [1,2,5,19-24] therefore deal with a simplified function considering the main flux-dependent power losses, while neglecting the secondary loss components. Commissioning of the loss function parameters at the drive power-up does not secure precise modelling of the loss function components having the temperature, frequency and saturation dependence [23]. LMC approach is therefore heavily dependent on parameter variation effects and simplifying assumptions made in the formulation of the loss function. These LMC drawbacks lead to a sub-optimal flux setting. The problem can be solved by implementation of an on-line identification routine for the loss function parameters, as discussed next.

This paper proposes a novel loss minimization algorithm is proposed. The intention is to preserve the LMC benefits while insuring precise drive loss modelling by means

of an on-line identification routine. The loss function concept is adopted to gain the robustness against the drive and the load originated noise, while keeping the flux convergence fast at all the relevant speeds and loads. The implementation requiring no *a priori* knowledge of the loss function parameters is assumed as the principal design goal. On-line loss function identification is developed and implemented to secure precision of the optimum, acquire the robustness against the thermal and frequency drift in parameters, and waive the need for the motor parameter entry, leading to a user-free drive commissioning. On-line identification of the loss function parameters is made possible by measuring the input power of the drive. The proposed algorithm can therefore be viewed as combining good features of both the search controllers and loss model controllers, while simultaneously eliminating the major shortcomings of these two methods. In particular, the need for precise knowledge of the motor loss function parameters, which is the major drawback of the LMC (while lack of it is the main advantage of the SC) is eliminated by the on-line identification routine. On the other hand, the problem of slow convergence towards optimum efficiency point, which is the main drawback of the SC (while fast convergence is the major advantage of the LMC) does not occur since the algorithm operates in a similar way to ordinary LMCs.

Efficiency controller derived in this paper is conceived to be simple, requiring no additional hardware and having no adverse effect on the drive cost and complexity. The loss function identification is implemented in 32-bit fixed-point arithmetic that can easily be handled by DSP-core micro-controllers [25,26] used in most industrial IMDs. The structure of the loss function and the implementation details related to the on-line identification are elaborated in Section II. Proposed minimum loss controller is outlined in Section III. The experimental results are given in Section IV, where the resulting energy savings are compared to those obtained with the SC approach. Finally, Section V summarises the conclusions.

2. IDENTIFICATION OF LOSS FUNCTION

Energy conversion within the converter and motor leads to the power losses in the motor windings and magnetic circuit, as well as the conduction and commutation losses [27] in the inverter. The motor losses are dominant in low power drives [5,24] and become comparable to the inverter losses for medium and high power drives. In addition to flux-dependent motor and inverter losses, there exist flux-invariant losses, which cannot be reduced by the flux variation, so that only the flux sensitive losses have to be modelled and identified. Precise loss modelling is essential for the loss minimisation. The presence of skin effect, saturation phenomena, thermal and frequency drift of the winding resistances and an increase in the iron losses in the presence of the PWM ripple [28] make the fixed-coefficient functional approximation of the drive power losses extremely difficult. As the winding resistances are two or more times higher at the PWM frequency [29], while the operating temperature, saturation and stray flux have significant impact on the fundamental loss component [6], both harmonic and fundamental losses call for a variable coefficient, on-line updated functional representation. Such a loss function

including all the secondary effects can hardly be identified on-line, due to a multitude of coefficients, noisy environment and a limited word-length of the fixed-point drive controllers [25,26]. The loss function of a reasonable complexity is therefore defined next.

Power losses can be expressed in terms of the drive variables readily available within the digital controller internal RAM. These are the flux estimate or command (Ψ_d), the magnetising (i_d) and the torque generating (i_q) component of the stator current, the stator angular frequency (ω_s) and the rotor speed estimate or feedback (ω_r). Depending on the power rating, the inverter losses are 3-5% and their main constituents are the rectifier, inverter conductive and the inverter commutation losses. With nearly constant voltage drop across the rectifier diodes and the DC-link current being basically proportional to the IMD output power and hence the load, the rectifier losses are considered flux-invariant. Conductive losses of a MOSFET inverter are proportional to $i_s^2 = i_d^2 + i_q^2$, while the IGBT bridge has the conductive loss component depending on the stator current average value, and the one proportional to i_s^2 . The gate drive levels influence the conductive loss of both MOSFET and IGBT inverters. With the switching times having a gradual increase with the current amplitude, the commutation losses are proportional to i^α , where the exponent α is greater than one. Therefore, the error made by modelling the overall flux-dependent inverter losses as $P_{INV} = R_{INV} i_s^2 = R_{INV} (i_d^2 + i_q^2)$ is considered reasonably small, in particular when medium and low power IMDs are under consideration, where the motor losses prevail anyway [5].

Losses in the motor consist of hysteresis and eddy current losses in the magnetic circuit (core losses) and the losses in the stator and the rotor conductors (copper losses). The rotor core losses, being dependent on the slip frequency, are substantially smaller than the stator ones. At nominal operating point, the core losses are typically 2-3 times smaller than the copper losses [5], but they represent the main loss component of a lightly loaded IMD. The main flux power losses are modelled by $P_{FE} = c\Psi_d^2 \omega_s^p$ with $p \in (1.5...2)$ [27]. The exact value of the exponent p depends on the relative ratio of hysteresis to eddy current losses. The stray flux losses depend on the form of the rotor and stator slots and are frequency and load dependent [27]. In view of the EU requirements for 1.1...90kW motors classified into EFF1..EFF3 groups according to their efficiency curves, the total secondary loss (stray flux, skin effect and the shaft stray losses) must not exceed 5% of the overall losses. Considering also that the stray losses are of importance at high load and overload conditions, while the efficiency optimiser is effective at light load, the stray loss is not considered as a separate loss component in the loss function that is to be formulated shortly. The fractional exponent p in the core loss representation is to be avoided in order to facilitate the implementation on low-cost 16-bit fixed-point DSP devices [25,26] used in most contemporary drives. The entire frequency dependent losses are therefore represented as $P_{FE} = c\Psi_d^2 \omega_s^p$ with $p=2$. It should be noted however that formal omission of the stray loss representation in the loss

function and simplified modelling of the stator frequency dependent losses have no impact on the accuracy of the algorithm for on-line identification. These approximations will be simply reflected in variation of one of the loss function coefficients (defined below), associated with stator frequency, as function of the operating conditions. Hence the optimal flux adjustment remains unaffected by the modelling imperfections. Based on the previous considerations, the input power to the drive is given by the following equation:

$$P_{IN}(t) = a i_d^2 + b i_q^2 + c \Psi_d^2 \omega_s^2 + d \Psi_d i_q \omega_r, \quad (1)$$

$$\text{with } a = R_s + R_{INV} \text{ and } b = R_s + R_r + R_{INV}.$$

For the power loss modelling, parameters a , b and c must be accurately known. The fourth factor in (1) is the power delivered to the load (P_{OUT}). When the input power (P_{IN}) measurement is available, exact P_{OUT} is needed in order to acquire correct power loss value and avoid the coupling between the load pulsations and the efficiency optimiser. At the first glimpse, there is no need to identify the parameter d , since its value can be readily calculated. However, the rotor speed and the flux estimates may be in error due to the parameter drift, causing eventually an offset in the $i_q \Psi_d \omega_r$ term. Driven by the $P_{IN}(i_d, i_q, \Psi_d, \omega_r, \omega_s)$ best fit search, the on-line adjustments of the d -parameter can rectify this problem and is therefore included in the on-line identification routine.

Efficiency optimisation proposed in this paper decides the flux level from the analytical minimum of the loss function contained in (1), in which the optimal flux depends upon the drive speed, torque and the parameters a , b , and c . The uncertainty of the initial value and the eventual parameter drift require an on-line identification procedure. The concept adopted hereafter consists in tracking the drive input power P_{IN} and the internal variables ($i_d, i_q, \Psi_d, \omega_r, \omega_s$). The acquired data are further correlated and the parameters (a, b, c, d), that provide the P_{IN} best fit according to (1), are derived. The P_{IN} derivation from the stator voltages and currents is susceptible to PWM-related errors, and it does not account for the inverter losses. Therefore, the input power is derived from the DC-link current and voltage, with a lower PWM noise contents. The additional benefit of this approach is that the $i_{DC}(t)$ and $v_{DC}(t)$ samples are already available within the drive controller: i_{DC} for protection and control purposes, and v_{DC} for dynamic braking, soft-start circuit operation and the PWM compensation. Notice in (1) that four P_{IN} samples, corresponding to four distinct sets of $i_d^2, i_q^2, \Psi_d^2 \omega_s^2$ and $\Psi_d \omega_r i_q$ signals, produce a system of four equations with the a, b, c , and d as unknowns. The solution is readily available, provided the system matrix is not singular.

Noise and measurement errors, approximations made in deriving (1), along with a potentially insufficient excitation brought in by the input signals are all in favour of using additional input information. This means acquiring $M > 4$ sets of input signals and P_{IN} samples, leading in turn to a redundant set of M equations. Moore-Penrose [30,31] based pseudo-inverse of rectangular $P_{M \times 4}$ matrix (PINV block in Fig. 1) gives $W_g = [a_g, b_g, c_g, d_g]^T$ as an approximate solution of the equation $PW=Y$, such that the value of $\|PW-Y\|$ is minimum (i.e. the modulus of the error vector in multidimensional space is the closest possible to the origin in

quadratic sense). Thus the abovementioned problem for higher values of M can be resolved. However, limited word-length (16-32), fixed-point core and 32-bit [25] to 36-bit [26] accumulators of applicable drive controllers impair the precision for large P -matrix dimensions, making the choice of M a design compromise.

Proposed identification procedure is illustrated in Fig. 1. The inputs to the algorithm are the samples of $i_d^2, i_q^2, \Psi_d^2 \omega_s^2, \Psi_d \omega_r i_q$ and $P_{IN} = v_{DC} i_{DC}^F$. They are acquired every $\tau = 200 \mu s$ (the i_{DC}^F signal is obtained from lightly RC filtered DC-link current, over-sampled at a $12.5 \mu s$ rate by 10-bit DSP-integrated ADC unit [25]). As the high frequency components do not contribute to the $W = [a, b, c, d]^T$ identification, the input signals and the input power P_{IN} are averaged within $Q\tau$ intervals, outputting Y_N, A_N, B_N, C_N and D_N each $T=Q\tau$ time units. The averaging is implemented as the sum of Q consecutive τ -spaced samples of each signal (Fig. 1):

$$\begin{aligned} \int_{nT}^{(n+1)T} P_{IN}(t) dt &= a \int_{nT}^{(n+1)T} i_d^2(t) dt + b \int_{nT}^{(n+1)T} i_q^2(t) dt + \\ &+ c \int_{nT}^{(n+1)T} [\Psi_d^2(t) \omega_s^2(t)] dt + \\ &+ d \int_{nT}^{(n+1)T} [\Psi_d(t) i_q(t) \omega_r(t)] dt \\ \Rightarrow Y_N &= a A_N + b B_N + c C_N + d D_N \quad (2) \end{aligned}$$

Correct operation of the identifier requires the proper choice of Q . Notice in Fig. 1 that a sequence of M changeless values of $Y_N \dots D_N$ makes the matrix $P^T P$ singular and the desired W_g values inaccessible. Hence, the averaging interval $T=Q\tau$ should allow most of the input disturbance energy, related to the speed error fluctuations, the load torque and the flux dynamics to pass into matrix P , providing in such a way sufficient excitation for the W_g identification. For the ease of $1/Q$ division (Fig. 1) $Q=2^{10}=1024$ is selected, resulting in $T=204.8ms$. Notice in Fig. 1 the column-vectors $P(:,1) \dots P(:,4)$ created from M successive values of $A_N \dots D_N$, and the M -sized vector Y made out of Y_N averaged power samples. The credibility of $W_g = [a_g, b_g, c_g, d_g]^T$, obtained from the PINV block, relies on the excitation energy contained in the input signals. Hence, in the absence of any input disturbance the matrix P becomes deficient and the W_g values obtained from P should be discarded. The indication of matrix P getting near to being singular or rank-deficient is its smallest singular value (e.g. the smallest nonnegative square root of the $Q_{4 \times 4} = P^T P$ eigenvalues [30,31]). Laborious evaluation of 4×4 matrix eigenvalues $\sigma_1, \sigma_2, \sigma_3$, and σ_4 on a 16-bit DSP is avoided by considering $\det(P^T P) = \sigma_1 \sigma_2 \sigma_3 \sigma_4$, already available as an intermediate result of the matrix $P^T P$ inversion in the block PINV in Fig. 1. Finally, the P -matrix spectral norm and the confidence in W_g are measured by $W_w = \det(P^T P)^{0.25}$ (upper right in Fig. 1).

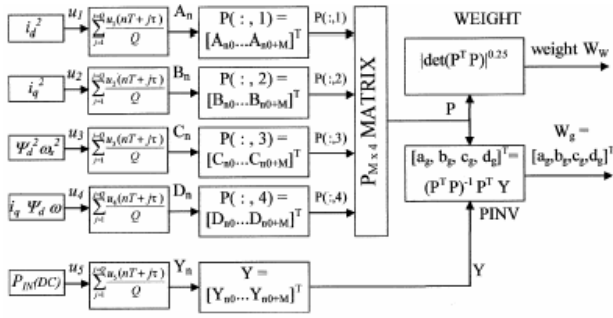


Fig. 1. Derivation of the parameters a , b , c and d from input signals.

Eventual possibility of long-term operation with all the drive variables at constant value prevents the parameters in W_g from being directly used by the loss function in (1). The identification mechanism given in Fig. 2 therefore tracks the difference ΔW between the stored W_e integrator output and the acquired W_g . Whenever the 'weight' signal W_w exceeds W_{MIN} , indicating a satisfactory amount of energy in P matrix and a sufficient reliability of W_g parameters, the 'GAIN' signal assumes a non-zero value, enabling in such a way the convergence of the W_e output towards the W_g input. The value of $G_{MAX} = 0.5 \text{ s}^{-1}$ limits the maximum rate of W_e change. The W_{MIN} choice depends on the noise, specific A/D resolution and the DSP word-length and is therefore defined in Section IV on the basis of several experimental runs.

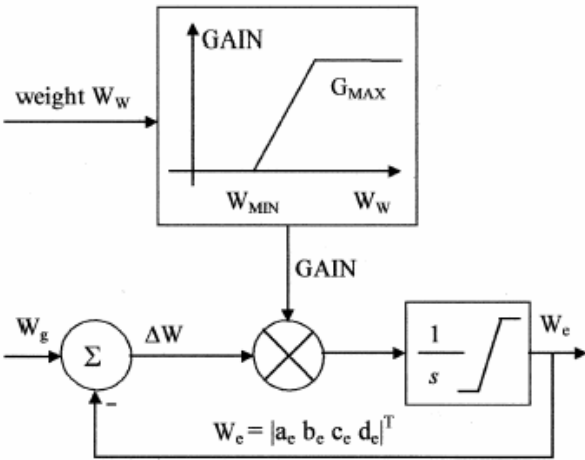


Fig. 2. Identification of the loss function parameters a , b , c and output power parameter d .

3. FLUX CONTROLLER

Assuming linearity of the magnetic circuit, $\Psi_{md} = L_m i_{md}$ and considering equation (1) would reduce to

$$P_N(t) = P_N(i_d, i_q, \omega_r, \omega_s) = a i_d^2 + b i_q^2 + c L_m^2 i_d^2 \omega_s^2 + d L_m i_d i_q \omega_r \quad (3)$$

since for d-axis variables in any steady state the rotor d-axis current equals zero and therefore $i_{md} = i_d$. With the desired torque T_{em} , the power loss P_γ is resolved in terms related to i_d , T_{em} and the supply frequency ω_s , as follows:

$$P_\gamma(i_d, T_{em}, \omega_s) = (a + c L_m^2 \omega_s^2) i_d^2 + \frac{b T_{em}^2}{(d L_m i_d)^2} \quad (4)$$

In the absence of saturation and specifying the rotor time constant T_r and the slip frequency $\omega_{slip} = \omega_s - \omega_r \approx R_R i_q / \Psi_{md}$, the power losses are expressed in terms of the operating conditions (ω_r and T_{em}) and the magnetising current:

$$P_\gamma(i_d, T_{em}, \omega_r) = (a + c L_m^2 \omega_s^2) i_d^2 + \frac{2c R_R \omega_r T_{em}}{d} + \frac{T_{em}^2}{d^2} (b + c R_R^2) \frac{1}{L_m^2 i_d^2} \quad (5)$$

Now, the steady-state optimum is readily found, based upon the loss function parameters (a , b , c and d) and the rotor time constant:

$$i_d^{opt} = \left(\frac{\gamma}{\alpha} \right)^{0.25}$$

$$\text{where } \alpha = (a + c L_m^2 \omega_s^2) \text{ and } \gamma = \frac{T_{em}^2}{d^2 L_m^2} (b + c R_R^2) = \gamma_1 + \gamma_2 \quad (6)$$

Parameter $\gamma_2(T_r)$ in (6) comes as a consequence of the iron losses P_{FE} depending on the supply frequency ω_s and not the rotor speed ω_r . Notice in (6) that $\gamma_2(R_R) \ll \gamma_1$, as the ratio (γ_2/γ_1) may be proved to be inferior to relative iron losses ($P_{FE}/P_{nom} \ll 1$). Therefore, the rotor resistance uncertainty has an insignificant impact on the i_d^{opt} value derived from (6). Moreover, even $\pm 25\%$ drift of γ_2 in conjunction with $P_{FE} = 0.05 P_{nom}$ results in an i_d^{opt} offset less than 0.1%. However, analytical optimum derived from (6) does not have any practical value. As shown in [12,18], the non-linearity of the magnetising curve $\Psi_{md} = f(i_{md})$ has to be taken into account for the proper operation of the efficiency controller.

For induction motors, the following magnetising curve functional approximation has been proposed [32]:

$$\left(\frac{i_{md}}{i_{md}^{nom}} \right) = \beta \left(\frac{\Psi_{md}}{\Psi_{nom}} \right) + (1 - \beta) \left(\frac{\Psi_{md}}{\Psi_{nom}} \right)^S, \quad (7)$$

where the i_{md}^{nom} and Ψ_{nom} are the rated magnetising current and flux values, respectively. For standard induction motors, parameters $\beta=0.7$ and $S=9$ provide precise estimation of the i_{md} up to flux levels of 1.1 [p.u.] [33]. In the case of high efficiency motors [32], the saturation is less emphasized due to a lower flux density, and the best fit for the parameter β in (7) shifts towards $\beta=0.9$. The function (7) fails as the flux level drops below 0.1 [p.u.], where the magnetizing curve bends and inflects as it comes closer to the origin. However, for the flux range of practical interest, extending from 20% to 100%, the approximation (7) with $\beta=0.7$ and $S=9$ is sufficiently accurate for efficiency control calculations of standard induction motors. In such a way, parameter setting is limited to the definition of the rated values (i_{md}^{nom}, Ψ_{nom}) on the $\Psi_{md} = f(i_{md})$ magnetising curve.

Considering saturation phenomenon, the loss function assumes the following form:

$$P_\gamma(\Psi_{md}, T_{em}, \omega_r) = a i_d^2(\Psi_{md}) + (b + c R_R^2) \frac{T_{em}^2}{d^2 \Psi_{md}^2} + c \omega_r^2 \Psi_{md}^2 + \frac{2c \omega_r R_R T_{em}}{d} \quad (8)$$

In the light of (7), the i_d^2 in (8) involves factors Ψ_{md}^9 and Ψ_{md}^{18} and makes unfeasible the analytical expression for the optimum flux value. On the other hand, the linear case analytical solution in (6) involves as well a relatively complex $y(x) = x^{0.25}$ calculation. Division, fractional power and trigonometric calculations on fixed-point 16-bit DSP controllers [25,26] involve multi-cycle, lengthy routines incompatible with the real time requirements. Programming method frequently used to resolve such problems corresponds to the operation of SAR [34] – successive approximation register A/D devices. The abovementioned example $y(x) = x^{0.25}$ is solved by searching the y value resulting in $y^4 = x$. For an n -bit precision of y , the search procedure executes n -times the loop, wherein a new modified value of y , y_a is attempted, the test $y_a^4 > x$ is performed, and the y_a value is further driven according to the test result. The looping starts by setting the MSB of the $y_a = 0$ word and clearing it back to zero when $(y_a^4 > x) = \text{TRUE}$. It proceeds by testing all the n -bits in decreasing order, ending with the LSB and obtaining in such a way the n -bit binary word representing $y(x) = x^{0.25}$.

Identical approach is used in calculating Ψ_{md} leading to a minimum $P_\gamma(\Psi_{md})$ of (8). Strictly positive $\partial^2 P_\gamma / \partial \Psi_{md}^2$ reduces the problem to finding the $\Psi_{md} = \Psi_{opt}$ value where the first derivative $g(\Psi_{md}) = \partial P_\gamma / \partial \Psi_{md}$ (Eq. (9)) changes the sign; i.e. $g(\Psi_{opt}) = 0$. For most frequently encountered P_γ slopes in $\Psi_{md} = \Psi_{opt}$ region [1,4,11], an error of $1/1024 \approx 0.1\%$ in Ψ_{opt} leads to an insignificant increase in P_{IN} (0.0003%, sensitivity results in Table I). Therefore, a 10-loops successive approximation procedure is written, searching for the 10-bit Ψ_{md} argument that results in $g(\Psi_{md}) = 0$. In each step (see (9) below), the values of Ψ_{md}^{-3} , Ψ_{md}^9 and Ψ_{md}^{17} are calculated, multiplied by $P_1..P_4$ parameters and summed into $g(\Psi_{md})$. Implemented in 24x device [25], procedure of finding the optimum requires approximately 4000 instruction cycles and an execution time of 0.2 ms. Notice at this point that the parameter values $P_1..P_4$ are derived from on-line retrieved $W_e = [a_e \ b_e \ c_e \ d_e]^T$ loss function coefficients (Figs. 1 and 2).

$$g(\Psi_{md}) = \frac{\partial P_\gamma}{\partial \Psi_{md}} = P_1 \Psi_{md}^{-3} + P_2 \Psi_{md}^9 + P_3 \Psi_{md}^{17} + P_4 \Psi_{md}^9 \quad (9)$$

The SAR method applied to (9) returns the $\Psi_{md} = \Psi_{opt}$, the flux value reducing the power losses to the minimum for the given load conditions (T_{em} , ω_r). The magnetizing current $i_{md}^* = f(\Psi_{opt})$, corresponding to the optimum flux is readily obtained from (7). Applied to the drive ($i_d^* = i_{md}^*$), the d-axis current reference cannot force the flux to $\Psi_{md} = \Psi_{opt}$ optimum instantaneously. The flux dynamics (Fig. 3) and the rate of change depend on the d-axis current command and the rotor time constant T_r . The flux optimum $\Psi_{opt} = f(T_{em}, \omega_r)$ is reached with a T_r delay, when the load speed and torque may already change. Seeming inconsistency is common to all the SSC, LMC and SC solutions. For an unpredictable character

of the load torque, the efficiency controller is to drive the system towards the steady state optimum [1,2,4-6,9,11], calculated from the current values of the T_{em} and ω_r . Finding the optimum flux trajectory in transient states requires *a priori* knowledge of the load torque and the load cycle, unknown in most cases.

In the cases of rapid flux transition, the i_d^* reference should exceed temporarily the i_{md}^* optimum, accelerating the flux convergence towards the optimum. However, large flux transients and forced $i_d^* \gg i_{md}^*$ magnetisation produce the d-axis rotor current reaction and a notable increase in both rotor and stator losses [12]. Therefore, proposed efficiency controller involves a smooth d-axis current reference generation. The i_d^* signal is calculated each $T_{eff} = 10$ ms by solving $g(\Psi_{md}) = 0$, deriving $i_{md}^* = f(\Psi_{opt})$ from (7) and limiting the slope di_d^*/dt to 0.1 [p.u./ms]. A consequence of a limited slope is that the flux drift changes the net torque for the given i_q^* , introducing in that way an undesired coupling between the speed/torque and the efficiency controller [2,11]. Decoupling of these loops requires the i_q^* reference adjustment: the q-axis current is calculated from the actual torque reference T_{em}^* and the present value of Ψ_{md} , obtained from the non-linear flux estimator (Fig. 3).

Derived in the previous sections, the proposed solution overcomes the drawbacks of the existing optimum efficiency controllers. It eliminates the need for initial settings and improves the precision through the on-line loss-model identification, while enabling fast convergence, obtainable with LMCs. Potential sources of errors are at the first sight the omission of the secondary loss components (see discussion prior to (1) in Section II), and the issue was thoroughly investigated through the experimental runs.

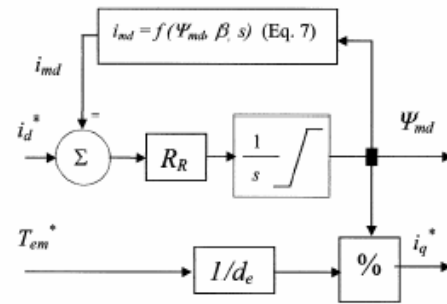


Fig. 3. Flux estimator.

4. EXPERIMENTAL VERIFICATION

Proposed solution is directly applicable in any type of vector controlled induction motor drive, in both sensed and sensorless mode. It is for this reason that the on-line identification algorithm was described in terms of the general flux Ψ_d , without specifying whether the flux is stator, air-gap or rotor. The inputs of the on-line loss function parameter identifier of Figs. 1-2 (i_d^2 , i_q^2 , $\Psi_d^2 \omega_s^2$, $\Psi_d \omega_r i_q$), as well as the electromagnetic torque required for solving the optimum flux equation (9), could be obtained in various ways, depending on the actual structure of the vector control system. In principle, either reference or estimated (if available) values could be used. However, having in mind that the optimum flux setting is to be determined for the subsequent time interval rather than for the previous time

interval (to which the estimated values would apply), the natural choice is to use the reference values within the control system. This consideration applies to the stator current components, electromagnetic torque and flux values. Angular frequency ω_s is always available within a vector control system and rotor speed of rotation can be a measured value, an estimated value or a value calculated from known frequency ω_s and the reference angular slip frequency value. The last of the three possibilities is used here. As far as the motor data are concerned, the algorithm requires the knowledge of only the rated magnetising flux and rated magnetising current, the data that are anyway required in any vector controlled induction motor drive. Finally, rotor resistance needs to be known and this is again a standard requirement for vector controlled drives. It should however be noted that sensitivity of the algorithm to rotor resistance variation is extremely small, as illustrated in Section III.

Developed structure is verified experimentally through the series of test runs with a standard 4-pole, 50 Hz, 2.2 kW induction motor coupled to a separately excited DC generator, used as controllable load. The loss model identification and the efficiency optimiser are coded in assembler language on a TMS320F243 device running at 20MHz [25], hosting at the same time all the other drive control function of a MOOG manufactured DBS 8/22 standalone single-axis vector controlled drive unit. The overall control system structure is illustrated in Fig. 4, where inter-linking and signal flows between controller constituent parts (Figs. 1-3) are shown. As can be seen in Fig. 4, all the inputs for the on-line loss function parameter identification, as well as the motor torque, are obtained using the reference signals of the indirect rotor flux oriented controller. It should be noted that the magnitude of the rotor flux and the d-axis magnetising flux are considered to be the same in this implementation. This condition holds true in any steady state, while the difference between the two is negligibly small under transient conditions with rotor flux oriented control, so that this approximation has no impact on the accuracy of the algorithm. The identification procedure (Fig. 1) is implemented with $T_{spi}=12.5\mu s$ over-sampling of the RC-filtered DC-link current, $\tau=200\mu s$ sampling of the drive internal variables required in (1), $Q=1024$ and hence $T=Q\tau=204.8ms$ averaging interval and $M=50$ Y-vector length, leading to a 50×4 P-matrix and a $T_g = MQ\tau = 10.24s$ refresh time of the $W_g = [a_g, b_g, c_g, d_g]^T$ loss function parameters.

The signals in Fig. 1 are represented as 32-bit fixed-point numbers except the input signals (i_d, i_q, \dots), that are Q14, 16-bit words. The P-matrix compilation, consisting of the data collection and averaging, is interrupt-driven and

involves approximately $2.5e6$ instruction cycles (or 128ms) within each $T_g = 10.24s$ interval. The W_g and W_w calculation (on the right in Fig. 1) is done only once each 10 seconds, and is therefore executed in the background ('main loop'). It involves less than $1.5e6$ instruction cycles, corresponding to the execution time of 75ms. In addition, each $T_{eff} = 10ms$ the value of $\Psi_{md} = \Psi_{opt}$ is derived from (9) by SAR method, requiring 4000 cycles and $200\mu s$. Hence, proposed efficiency controller uses less than 5% of the available processing power, leaving enough execution time for the other drive control functions.

The purpose of the first set of test runs is to verify the adequacy of the P_{IN} approximation in (1) and loss model formulation of (4). The excitation to the W_g identifier is insured by injecting 0.1 p.u. saw-tooth signal in both d- and q-axis current references (it should be noted however, that the algorithm is in essence test-signal-free; the signal injection is used here for the testing purposes only and the issue will be clarified later on, after some additional tests have been performed). Under perfectly ideal operating and modelling conditions, the loss function parameters a, b and c would have been constant regardless of the motor speed of rotation and load torque values. The relative changes of loss function parameters a_g, b_g and c_g ($a_r = (a_g - a_0)/a_0, b_r = (b_g - b_0)/b_0, c_r = (c_g - c_0)/c_0$) are plotted for the worst-case T_{em} found and the operating frequency sweeping from zero to the rated value in Fig. 5. The copper-losses related a_g and b_g parameters stay within the $\pm 0.5\%$ range, while the relative change of the core loss coefficient c_g exceeds 1% for the shaft speeds lower than 10%, due to the adoption of the simplified $P_{FE} = c\Psi_d^2\omega_s^2$ core loss model. In simple terms, inaccuracies introduced in modelling of the core losses and omission of the explicit stray loss representation are automatically corrected by the on-line identification of the coefficient c , so that the term $c\Psi_d^2\omega_s^2$ corresponds at any given frequency to the actual sum of the core and stray losses (i.e. stator frequency dependent losses). A similar consideration applies to the thermal drifts in resistance values, that are reflected in values of the coefficients a and b and therefore automatically compensated by the on-line identification algorithm.

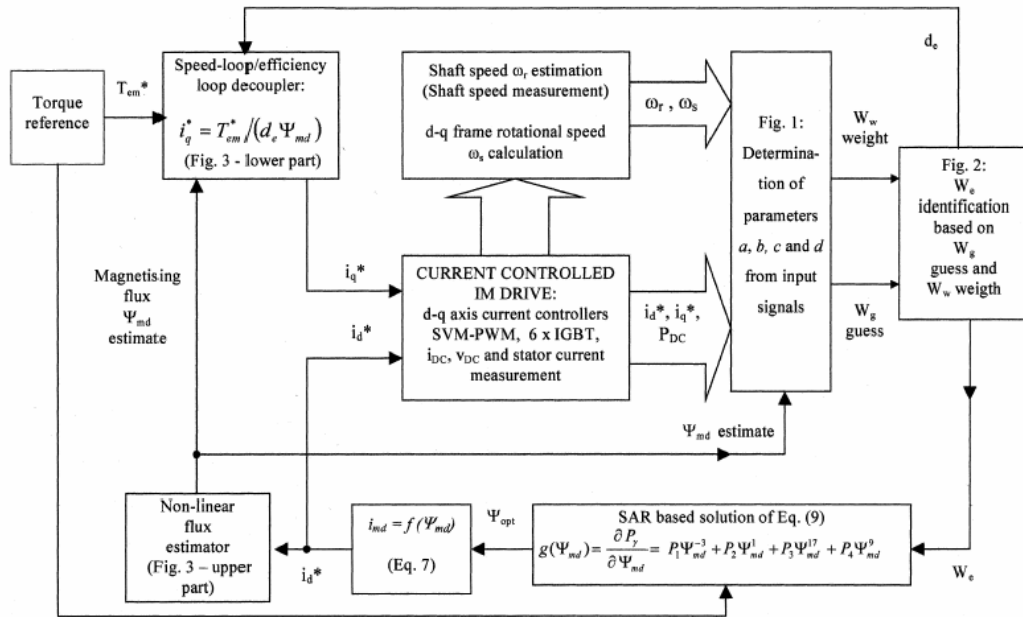


Fig. 4. The complete control structure of the indirect rotor flux oriented induction motor drive with implemented optimum efficiency controller.

As shown in Fig. 6, the load dependence of the W_g parameters is tested at the rated speed and with the load torque sweeping from 0 to 1.5 p.u. (i.e. 22.5 Nm). For the load ranging from zero to 120%, all the parameters stay within the $\pm 1\%$ range. Parameter c_g exceeds the 1% error band for loads in excess of 120%, at which point the stray losses increase due to high stator and rotor currents.

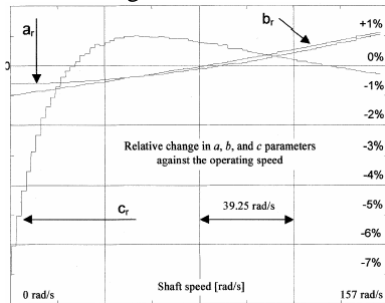


Fig. 5. Speed dependence of the loss function parameters. $T_{em} = 10 \text{ Nm}$ (2/3 p.u.), ω_r sweeps from 0 to ω_{nom} . $a_r = (a_g - a_0)/a_0$, $b_r = (b_g - b_0)/b_0$, $c_r = (c_g - c_0)/c_0$, where $a_0 = 0.1411$, $b_0 = 0.21$ and $c_0 = 0.0617$.

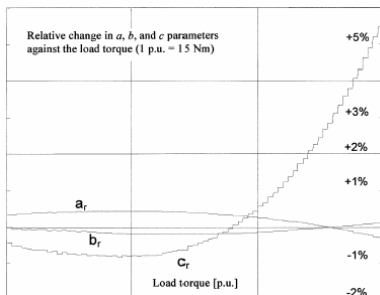


Fig. 6. Load dependence of the loss function parameters. T_{em} sweeps from 0 to 22.5 Nm (1.5 p.u.), $\omega_r = \omega_{nom}$. The a_r , b_r and c_r are explained in Fig. 5.

It has to be noted that the system proposed in Figs. 1-3 may reach the required precision even at $\omega_r < 10\%$, provided the drive operates in this regime for several W_g identification cycles, required for the W_e vector (Fig. 2) to reach the steady state value $[a_e, b_e, c_e, d_e]^T$. On the basis of Fig. 5, this new $W_e(\omega_r < 10\%)$ value may have the c_e parameter differing from nominal c_0 by up to 7%. Notice as well that the algorithm for on-line identification of the loss function parameters could, on the basis of these considerations, be executed only once and the values of the coefficients a , b and c would still suffice for all the load torque values below 120% and all the speed values above 10%. The algorithm is nevertheless kept running continuously in the implementation, so that the best possible efficiency is ensured at all speeds and for all load torque values. In the second set of experimental runs (Fig. 7-9), the goal is to recognise the minimum disturbance required for a reliable identification of the loss function parameters and to enact the criterion function threshold (W_{MIN} in Fig. 2). The drive is running at the rated speed $\omega_r = 147 \text{ rad/s}$, loaded with $T_{em} = 10 \text{ Nm}$ (0.67 p.u.) and having the rated magnetising current. In Figs. 7-9, the experimental traces of relative variations a_r , b_r and c_r are shown, along with the corresponding W_w criterion function, included for the reference. The a_r , b_r , c_r and W_w values are passed from the DBS drive to a PC over the RS485 link. In Fig. 7, the torque reference (q-axis) is undisturbed, while the magnetizing current (d-axis) comprises on top a slow swinging (10 s) triangular form disturbance $\Delta i_d(t)$ with an adjustable amplitude. The traces indicate that a $0.05 i_{md}^{nom}$ disturbance ($0.035 I_{nom}$) is required to keep the relative errors below the 1% threshold. Corresponding value of W_w is 0.006. In Fig. 8, a similar test is performed with disturbance applied to the torque reference (q-axis), keeping at the same time the d-axis unperturbed. Required torque disturbance for the

estimate errors better than 1% is 0.05 p.u, and the coinciding W_w value is 0.005.

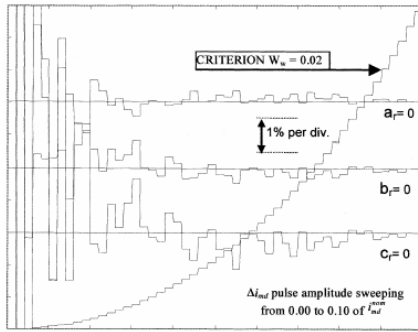


Fig. 7. Relative change in a , b and c estimates and the W_w criterion function versus Δi_{md} ranging from 0 to $0.1 i_{md}^{nom}$ ($0.07 i_{nom}$). Ramp shaped $\Delta i_d(t)$ disturbance with a $T_{id} = 10s$ period and a Δi_{md} amplitude is superimposed on the i_d^* ($M=50$).

It can be seen that with a P-matrix 50×4 ($M=50$), the appropriate value for the W_{MIN} threshold is 0.005-0.006. The data processing in Fig. 1 and in particular the $Q\tau$ averaging require disturbance energy be spread in the frequency range below 5 Hz. Supposed case of a complete steady state without any disturbances in either of d- or q-axis would lead to a $W_w(=0) < W_{MIN}$, discarding the W_g estimates (Fig. 2) and keeping W_e unaltered. To activate the identifier having $M=50$ vector lengths, either d- or q-axis (flux or torque current) should have a superimposed disturbance with an amplitude of at least 0.05 p.u. (according to Figs. 7 and 8). The disturbance does not need to be a rapidly varying quantity. The required disturbance is of such a small value that it is likely to be always present in the drive, eliminating therefore the need for its external generation. In the case of a long term steady state operation, and assuming that a perfectly smooth running of the drive is achieved (without any existing fluctuation in d- and q-axis currents), a self-imposed $\Delta i_d^* = 0.035 i_{nom}$ slowly varying ramp (i.e a ramp generated by the DSP programme; this approach was used for the tests described in conjunction with Figs. 5-8) would suffice (Fig. 7) to refresh the parameters, having at the same time the torque generation undisturbed owing to decoupling mechanism given in Fig. 3.

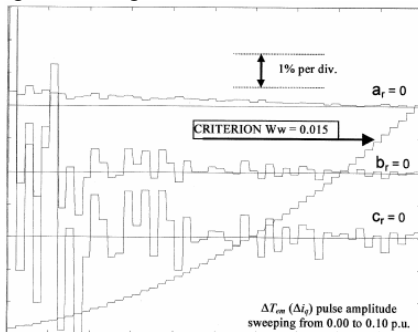


Fig. 8. Relative change in a , b and c estimates and the W_w criterion versus ΔT_{em} ranging from 0 to $0.1 T_{nom}$. Ramp shaped load torque disturbance with a $T_q = 5s$ period and the ΔT_{em} amplitude is produced by the excitation control of the DC machine ($M=50$).

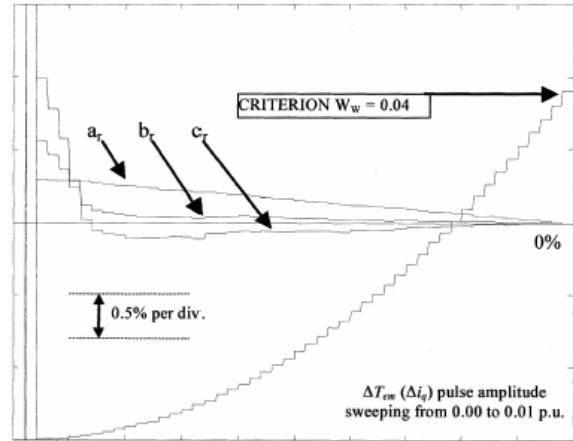


Fig. 9. Relative change in a , b and c estimates and the W_w criterion function versus ΔT_{em} defined as in Fig. 8. The P matrix columns and the Y vector length are increased from $M=50$ to $M=250$, and the W_g refresh time $T_g = MQ\tau$ from 10.24s to 51.2s.

It is of interest to investigate the influence of the vector length M and the amount of the input disturbance required for the identification. The experiment charted in Fig. 8 is repeated with $M=250$, resulting in a 250×4 P-matrix and $T_g = 51.2s$ refresh cycle. A longer acquisition time extends the disturbance energy collection, increases the $\det(P^T P)$ value and reduces the necessary d- and q-axis disturbance. As from experimental traces in Fig. 9, the W_w threshold can be reduced to 0.002, while the minimum disturbance level required for the proper identification reduces to 1%. The eventual choice of M value clearly depends on the expected rate of change in the loss function parameters (i.e. the thermal time constants) and the amount of the RAM memory available within the digital drive controller. The next set of experimental runs verifies the sensitivity of the proposed scheme to the measurement noise. Since it is desirable to have a test-signal-free solution, a higher resolution than 8-bit should be used. Based on the results in Figs. 7-9 and the noise sensitivity, the 10-bit A/D resolution is sufficient for the application, since it ensures that the naturally existing disturbance in the drive is sufficient for the excitation of the on-line identification function (i.e. a test-signal-free solution is obtained). A further resolution increase may contribute to a further performance improvement. Incorporation of 12-bit A/D unit within compact single-chip DSP controllers is already available [26]. The last set of experiments compares the effectiveness of the proposed efficiency controller to the one obtained with a conventional search controller. The experimental traces of the flux and the drive power are grouped in Fig. 10 for the pulsating torque operation at 1450 rpm. Flux traces are the output of the non-linear flux estimator of Fig. 3. The steady state high-torque and low-torque flux and P_{IN} values obtained with the proposed efficiency controller and the SC are equal down to the resolution limits, proving that the proposed solution reaches the true optimum. The SC waveforms are slow on the load transients. For the load cycle in Fig. 10, proposed controller reduces the overall energy consumption by 13.32%, compared to the SC.

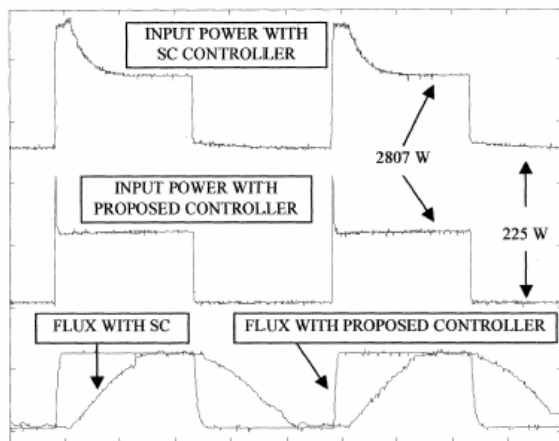


Fig. 10. The flux and the input power experimental traces for the proposed efficiency controller and the search controller running both with $T_{eff} = 10\text{ms}$ sampling time at 1450 rpm. The torque steps from approximately 1 Nm to 15 Nm and back each 10 seconds. The drive is running in the speed control mode, and the load pulsing is performed by switching the resistive load in the armature circuit of the DC machine.

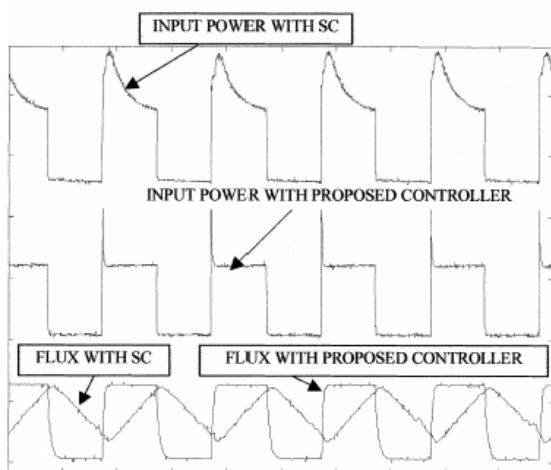


Fig. 11. A comparison of the flux and the input power experimental traces for the proposed efficiency controller and the search controller for the case of rapidly varying load torque. All the data as in Fig. 10, except that the load torque steps from low to high value and back each 4 seconds.

It should be noted that only the existing disturbance within the drive is used for activation of the on-line identification algorithm in this test. The experiment illustrated in Fig. 10 applies to a relatively slowly changing load torque (10 s period of the load torque change). Another experiment is therefore performed, in essence identical to the one shown in Fig. 10, but this time for a rapidly varying load torque. The load torque now changes every 2 s from low to high value and vice versa (4 s period). The results are shown in Fig. 11. As can be seen in Fig. 11, the SC controller does not manage to establish the operation with the optimum flux adjustment, due to its slow convergence and rapid nature of the load torque change. In contrast to that, the proposed controller is characterised with extremely rapid convergence, so that the optimum flux level is reached during the drive operation for each torque value setting without any difficulty.

In this case the proposed controller reduces the power consumption by 26.5 %, compared to the SC controller.

5. DISCUSSION AND CONCLUSIONS

In this paper, a novel method for minimum loss control of induction motor drives is proposed. The developed optimum efficiency controller can be viewed as an original combination of the SC and LMC, since input power is measured, while the optimum flux value is calculated. The proposed controller is therefore of novel and unique structure, compared to all the optimum efficiency controllers proposed in the past. The idea of the proposed method is to retain good features of both the SC and LMC approaches, while eliminating their major drawbacks. The input power measurement is used in order to identify on-line the loss function parameters. This eliminates the problems encountered in LMC implementations and related to the parameter variation effects during the drive operation and the requirement for *a priori* knowledge of the motor parameters. Using the on-line identified loss function parameters, the optimum flux value is calculated, so that the major drawback of the SC method, slow convergence, is eliminated as well. A very accurate and very fast optimum efficiency control is achieved in this way, which does not require any knowledge regarding the controlled motor, except for the values that have anyway to be known beforehand for any induction motor drive (rated magnetising current and flux, and rotor resistance). The complete algorithm, consisting of the on-line identification routine, the optimum flux value calculation and the non-linear flux estimator, is described in detail and is further implemented in a DSP. Detailed coverage of all the relevant issues related to the actual DSP-based implementation is provided, ensuring therefore repeatability of the proposed solution. The first part of the experimental investigation examined the behaviour of the on-line identified loss function coefficients against the drive load torque and against the operating speed. It is shown that for all the speeds higher than 10% of the rated and for all the load torque values below 120% it would suffice to identify only once the loss function parameters and to use these values for all the other operating conditions within these limits. Nevertheless, to ensure the best possible operation over the entire speed and load torque regions, the on-line identification routine is kept running at all times. It is also shown that the modelling inaccuracies, present in the formulation of the loss function, are automatically compensated by the on-line identification routine. Next, the minimum level of disturbance required for the excitation of the on-line identification routine was investigated in detail. It is concluded that the required level of disturbance is so small that it is likely to exist anyway in any drive in which the controller is implemented. Should the need arise, the required disturbance can be generated by the DSP in such a manner that operation of the flux, torque and speed loops is not affected. Finally, operation of the complete efficiency optimisation algorithm is tested for a slowly varying load torque and a rapidly varying load torque, and is compared to the operation of a classic SC. The results demonstrate the superiority of the proposed solution, since significantly higher energy saving is achieved, especially for the case of

rapidly changing load torque. The fact that the solution does find the optimum flux value, corresponding to the minimum input power, is confirmed by the comparison with the SC operation as well. It is believed that the proposed minimum loss control algorithm has a rather general validity. Apart from being directly applicable to a variety of sensed and sensorless vector control schemes for induction motor drives, it can be easily extended to other types of AC motor drives, such as for example a synchronous reluctance motor drive. As a matter of fact, the optimum efficiency control method developed here is applicable to any electric motor drive that has one degree of freedom, required for the optimisation.

6. REFERENCES

- [1] F.Abrahamsen, F.Blaabjerg, J.K.Pedersen, P.Z.Grabowski, P.Thogersen, "On the energy optimized control of standard and high-efficiency induction motor in CT and HVAC applications," *IEEE Trans. on Industry Applications*, Vol. 34, No. 4, 1998, pp. 822-831.
- [2] N.Mutoh, N.Ohnuma, A.Omiya, M.Konya, "A motor driving controller suitable for elevators," *IEEE Trans. on Power Electronics*, Vol. 13, No. 6, 1998, pp. 1123-1134.
- [3] A.Consoli, W.Cardaci, G.Scarcella, A.Testa, "Efficiency optimization techniques in induction motor drives for electric vehicle applications," *Proc. 15th Electric Vehicle Symposium EVS-15*, Brussels, Belgium, 1998, CD-ROM Paper No. 196.
- [4] D.S.Kirschen, D.W.Novotny, T.A.Lipo, "Optimal efficiency control of an induction motor drive," *IEEE Trans. on Energy Conversion*, Vol. EC-2, No. 1, March 1987, pp. 70-76.
- [5] F.Abrahamsen, F.Blaabjerg, J.K.Pedersen, P.B.Thogersen, "Efficiency optimized control of medium-size induction motor drives," *Conf. Rec. IEEE IAS Annual Meeting*, Rome, Italy, 2000, pp. 1489-1496.
- [6] F.Abrahamsen, J.K.Pedersen, F.Blaabjerg, "State-of-art of optimal efficiency control of low cost induction motor drives," *Proc. Power Electronics and Motion Control Conf. PEMC'96*, vol. 2, Budapest, Hungary, 1996, pp. 163-170, 1996.
- [7] J.M.Moreno-Eguilaz, J.Peracaula, "Efficiency optimization for induction motor drives: past, present and future," *Proc. Electrimacs'99*, Lisbon, Portugal, 1999, pp. I.187-I.191.
- [8] H.R.Andersen, J.K.Pedersen, "Low cost energy optimized control strategy for a variable speed three-phase induction motor," *Proc. IEEE Power Elec. Spec. Conf. PESC '96*, Baveno, Italy, 1996, pp. 920-924.
- [9] S.K.Sul, M.H.Park, "A novel technique for optimal efficiency control of a current source inverter fed induction motor," *IEEE Trans. on Power Electronics*, Vol. 3, No. 2, 1988, pp. 192-199.
- [10] P.Famouri, J.L.Cathey, "Loss minimization control of an induction motor drive", *IEEE Trans. on Industry Applications*, Vol. 27, No. 1, 1991, pp. 32-37.
- [11] D. S.Kirschen, D.W.Novotny, T.A.Lipo, "On line efficiency optimization of a variable frequency induction-motor drive," *IEEE Trans. on Industry Applications*, Vol. IA-21, No. 4, 1985, pp. 610-616.
- [12] I.Kioskeridis, N.Margaris, "Loss minimization in scalar-controlled induction motor drives with search controllers", *IEEE Trans. on Power Electronics*, Vol. 11, No. 2, 1996, pp. 213-220.
- [13] .M.Moreno-Eguilaz, M.Cipolla, J.Peracaula, P.J. da Costa Branco, "Induction motor optimum flux search algorithms with transient state loss minimization using a fuzzy logic based supervisor," *Proc. IEEE Power Elec. Spec. Conf. PESC'97*, St. Louis, Missouri, 1997, pp. 1302-1308.
- [14] G.C.D.Sousa, B.K.Bose, J.G.Cleland, "Fuzzy logic based on-line efficiency optimization control of an indirect vector-controlled induction motor drive", *IEEE Trans. on Industrial Electronics*, Vol. 42, No. 2, 1995, pp. 192-198.
- [15] M.G.Simoes, B.K.Bose, R.J.Spiegel, "Fuzzy logic based intelligent control of a variable speed cage machine wind generation system", *IEEE Trans. on Power Electronics*, Vol. 12, No. 1, 1997, pp. 87-95.
- [16] B.K.Bose, N.R.Patel, K.Rajashékara, "A neuro-fuzzy-based on-line efficiency optimization control of a stator flux-oriented direct vector-controlled induction motor drive," *IEEE Trans. on Industrial Electronics*, Vol. 44, No. 2, 1997, pp. 270-273.
- [17] M.Ta-Cao, Y.Hori, "Convergence improvement of efficiency-optimization control of induction motor drives," *Proc. IEEE IAS Annual Meeting IAS'2000*, Rome, Italy, 2000, CD-ROM Paper No. 38_04.
- [18] D.S.Kirschen, D.W.Novotny, W.Suwanwisoot, "Minimizing induction motor losses by excitation control in variable frequency drives," *IEEE Trans. on Industry Applications*, Vol. IA-20, No. 5, 1984, pp. 1244 - 1250.
- [19] G.O.Garcia, J.C.Mendes Luis, R.M.Stephan, E.H.Watanabe, "An efficient controller for an adjustable speed induction motor drive," *IEEE Trans. on Industrial Electronics*, Vol. 41, No. 5, 1994, pp. 533-539.
- [20] R.D.Lorenz, S.M.Yang, "Efficiency optimized flux trajectories for closed-cycle operation of field-orientation induction machine drives", *IEEE Trans. on Industry Applications*, Vol. 28, No. 3, 1992, pp. 574-580.
- [21] F.F.Bernal, A.G.Cerrada, R.Faure, "Model-based loss minimization for DC and AC vector-controlled motors including core saturation", *IEEE Trans. on Industry Applications*, Vol. 36, No. 3, 2000, pp. 755-763.
- [22] J.H.Chang, B.K.Kim, "Minimum-time minimum-loss speed control of induction motors under field-oriented control," *IEEE Trans. on Industrial Electronics*, Vol. 44, No. 6, 1997, pp. 809-815.
- [23] I.Kioskeridis, N.Margaris, "Loss minimization in induction motor adjustable-speed drives," *IEEE Trans. on Industrial Electronics*, Vol. 43, No. 1, 1996, pp. 226-231.
- [24] K.Matsuse, T.Yoshizumi, S.Katsuta, S.Taniguchi, "High-response flux control of direct-field-oriented induction motor with high efficiency taking core loss

- into account,*" IEEE Trans. on Industry Applications, Vol. 35, No. 1, 1999, pp. 62-69.
- [25] *TMS320F243 users manual*, Texas Instruments, SPRU276.
- [26] *DS56805 users manual*, Motorola Semiconductors, DSP56F805/D Rev. 1.
- [27] G.C.D.Sousa, B.K.Bose, J.Cleland, R.J.Spiegel, P.J.Chappell, "*Loss modeling of converter induction machine system for variable speed drive,*" Proc. IEEE Int. Conf. on Industrial Electronics, Control, Instrumentation and Automation IECON '92, San Diego, CA, 1992, pp. 114-120.
- [28] A.Boglietti, P.Ferraris, M.Lazzari, M.Pastorelli, "*Influence of the inverter characteristics on the iron losses in PWM inverter-fed induction motors,*" IEEE Trans. on Industry Applications, Vol. 32, No. 5, 1996, pp. 1190-1194.
- [29] S.C.Peak, J.L.Oldenkamp, "*A study of system losses in a transistorized inverter-induction motor drive system,*" IEEE Trans. on Industry Applications, Vol. IA-21, No. 1, 1985, pp. 248-258.
- [30] E.H.Moore, "*General analysis,*" Memoirs American Philosophical Society, 1935, Chapter III, Section 29, pp. 197-209.
- [31] R.Penrose, "*A generalized inverse for matrices,*" Proc. Cambridge Philosophical Society, Vol. 51, 1955, pp. 406-413.
- [32] F.M.H.Khater, R.D.Lorenz, D.W.Novotny, K.Tang, "*Selection of flux level in field-oriented induction machine controllers with consideration of magnetic saturation effects,*" IEEE Trans. on Industry Applications, Vol. IA-23, No. 2, 1987, pp. 276-282.
- [33] E.Levi, M.Sokola, S.N.Vukosavic, "*A method for magnetizing curve identification in rotor flux oriented induction machines,*" IEEE Trans. on Energy Conversion, Vol. 15, No. 2, 2000, pp. 157-162.
- [34] R.J. van de Plassche, *Integrated analog to digital and digital to analog converters*, Boston: Kluwer Academic Publishers, 1994.

POWER QUALITY: STATE OF THE ART AND FUTURE TRENDS

J. V. Milanović, Department of Electrical Engineering and Electronics, UMIST, Manchester, UK

Abstract: *The paper introduces the terminology and basic definitions related to power quality (PQ). It describes and justifies the need for the research in this important area and discusses some of the latest developments in this field of research. The paper then indicates some of the future trends of research and areas in which further research and development are needed having in mind de-regulation of electrical power industry and perceived increase in penetration of renewable energy sources in electrical power networks.*

Key Words: power quality, definitions, sags, harmonics

1. INTRODUCTION

Power Quality is a phrase used to broadly encompass the entire scope of interaction among electrical suppliers, the environment, the systems and products energized, and the users of those systems and products. It is more than the delivery of "clean" electric power that complies with industry standards. It also involves the maintainability of that power, the design, selection, and the installation of every piece of equipment (and software) in the electrical energy system. Covering the entire electrical system, stretching from the generation plant to the last utility customer, power quality can be perceived as a measure of how the elements affect/interact with a system as a whole.

Though, quality of electricity supply has been a problem ever since the conception of electricity, it only started to receive considerable attention from researchers and industry in 1980's. With increasing integrated circuit densities, faster processor speeds, increasingly sensitive equipment, and growth in application of Programmable Logic controllers (PLC), high efficiency Variable Speed Drives (VSD) and Shunt Capacitors (SC) for Power Factor (PF) correction, the chances of interference occurring rose sharply. Therefore, the need arose for better understanding of the whole phenomenon in order for the adequate preventive actions to be taken to ensure that the production processes continue to operate satisfactorily. A part from the introduction of sophisticated equipment in production processes, there is also an increased awareness of power quality issues by the end-users that put an additional pressure to utilities which are already exposed to an increased competitiveness due to deregulation of electrical power industry.

Because of the aforementioned the need for solutions to potential power quality problems grows rapidly. The ultimate reason for increased awareness of Power Quality issues is an economic value. The major drivers for the increased interest in this topic can be sub-divided as follows: i) Industry is facing revitalization with more automation and modern microprocessor and power electronic controlled highly sensitive equipment (VSD, PLC, etc.) ii) The electricity customers became more aware of their rights and negotiating power and demand low-cost electricity of high reliability and quality that suits their particular needs. iii) Deregulation of Electrical Power Industry brings increased competition among utilities to meet and maintain customer confidence. There is no longer one single utility that supplies electricity

but a number of independent companies that compete to retain existing customers and expand their customer base. iv) Governments' commitments to meet the requirements of Kyoto protocol about the reduction of green-house gases in the atmosphere fostered the shift in electricity generation from large power plants connected to the transmission system towards smaller units connected at lower voltage levels and using renewable energy sources (sun, wind, photovoltaics) for generation of electricity. Most of those are connected to the network through power electronics devices that potentially may introduce further power quality disturbances. v) Manufacturers of electrical power equipment and appliances are facing extremely competitive market that requires thorough understanding of transmission and distribution power system disturbances and problems that may arise from them in order to apply appropriate design and protective measures in their products.

The fact is that modern power utilities are supplying the power of as good or even better quality than in the past however, the electrical environment is too uneven for the sensitive microprocessor and power electronic equipment being installed to improve industry performance control and to enhance everyday life at home. The quality of their product - electrical power starts to count a lot among their customers.

As some of the problems related to power quality are relatively new and in spite of the fact that power quality analysis, monitoring and solutions have been included in the electrical engineering curriculum over last ten years many generations of engineers have not been trained for these topics, while being confronted with them on a daily basis. Many European (and other national) standards still lag in modern installation practice in the United States and the UK. Power quality standards do exist, but in many countries they are not obligatory or are interpreted differently by energy users and suppliers. Therefore there is a need for further education and training in this important and expanding area.

This paper offers some of the definitions of power quality related phenomena and presents an overview of major issues and trends facing electrical power utilities, industry and research community.

2. TERMS AND DEFINITIONS

In order to understand and successfully deal with all the issues associated with power quality it is necessary to set terms of reference to avoid potential confusion and misunderstanding between various parties involved. There is a need for common terminology in order to: i) Avoid confusion from many different terms that have similar meanings. ii) Develop standards for characterizing and categorizing monitoring and measurement results. iii) Permit statistical analysis of data obtained from different sources. iv) Facilitate communication when describing encountered problems.

An ideal, perfect power supply would be one that is always available, always within voltage and frequency limits (tolerances) and has pure disturbance free sine wave. In reality however, this is seldom the case. As the voltage is the

main parameter at the point of interaction between the utility network and the customer and a common denominator for all customers connected to the network, definitions of power quality are often related to voltage quality. It is said that the power quality is good if the voltage: i) Has a constant sine wave shape with fundamental frequency only. ii) Is supplied at constant, rated frequency. iii) Forms a symmetrical three-phase power system. iv) Has a constant root-mean-square (RMS) value, unchanged over time. v) Is unaffected by load changes. vi) Is reliable, i.e., the energy is available when required. Complementary term to voltage quality is current quality. It is required that the current drawn by the customer's equipment is a single-frequency sine wave of constant amplitude and frequency and that the current sine wave is in phase with the supply voltage sine wave. The power quality therefore, would be the combination of voltage and current quality. In broader terms, the power quality problem is defined [1] as any occurrence manifested in voltage, current, or frequency deviations which results in failure or misoperation of end-use equipment. The term power quality itself is the reflection and expression of remarkable evolving, growing and improving of various technical aspects of both delivering and using of electrical energy. International Organization for Standardization (ISO) defines [2] quality as the ability of a product or service to satisfy user's needs, and quality of service as the collective effect of service performance which determines the degree of satisfaction of a user of the service. The keywords used (user's satisfaction) are the main reason for most of ambiguities related to the PQ, as various users, i.e. customers, have different expectation about the PQ. Those customers who are either likely to incur financial losses, or suffer a potentially hazardous situation are most interested in clear definition of the PQ and adequate PQ maintenance. Today, mainly industrial customers with continuous processes are those who are willing to invest in order to obtain improved quality of supply [3-6]. Although this sector on average comprises less than 5-10% of all customers, total losses and damages caused by the various PQ disturbances there are expressed in millions (or even billions) of funds per year [7,8].

In related standards, current definitions of power quality have different formulations, and according to that, different interpretations. The most encountered and used definitions of the PQ are: i) Concept of powering and grounding sensitive electronic equipment in a manner that is suitable to the operation of that equipment (and compatible with the premise wiring system and other connected equipment) [9,10]. ii) Set of (technical) parameters defining the properties of the power supply as delivered to the user (in normal operating conditions) in terms of continuity of supply and characteristics of voltage (symmetry, frequency, magnitude, waveform, etc.) [11]. iii) Characteristics of the electricity at a given point on an electrical system, evaluated against a set of reference technical parameters [9] (part 61000-4-30). iv) Ability of a device, equipment or system to function satisfactorily in its electromagnetic environment without introducing intolerable electromagnetic disturbances to anything in that environment [9]. v) Estimate of the deviation with respect to specified explicit or implicit values of electrical energy supply, or of the

aggregate supply criteria ensured by an electrical system, [2] (part 161-01-7).

As it can be seen from the above definitions even the basic term used as a common denominator – power quality – has different formulations: voltage quality, current quality, quality of power supply, service quality, electrical energy quality, electromagnetic compatibility, quality of consumption, etc.

Power quality disturbances/variations can be broadly subdivided in two categories: 1. Disturbances (Transients

Voltage Sags (Dips) and Swells, Interruptions of supply)

2. Steady State Variations (Voltage Regulation, Harmonic Distortion, Voltage Flicker)

Some of the definitions (though they also vary dependent on the source) of the most frequently used power quality terms (broadly based on IEEE 1159 standard) are given below for the completeness of discussion:

Overvoltage: An increase in the RMS value of voltage above 110% for more than 1 min. (Different value from 110% can be used if the normal operating voltage is outside the 90%-110% range.)

Interruption: A decrease in the RMS voltage to less than 0.1 p.u. for a duration not exceeding 1 min (short interruption / in excess of 1 min (long interruption). (The total loss of supply followed by automatic restoration of supply.) *Voltage Sag (Dip):* A short duration (less than 1 min) reduction (between 0.1 p.u. and 0.9 p.u.) in RMS voltage.

Voltage sag magnitude: The remaining RMS voltage in percent or per-unit (p.u.) of the pre-fault voltage during the "event". (In the case of the non-rectangular sag, the sag magnitude is a function of time.)

Voltage drop: The difference between the pre-"event" RMS voltage and the RMS voltage during the "event".

Voltage sag duration: The duration of the RMS reduction of the voltage sag. (The persistent time that the voltage of the phase with the lowest magnitude is lower than 0.9 p.u. of the nominal voltage.)

Point-on-wave of sag initiation: The phase angle of the voltage at the moment the voltage waveform shows a significant drop compared to its normal waveform. (The phase angle is measured with respect to the last upward zero-crossing of the voltage waveform.)

Phase-angle jump (shift): The difference in voltage phase-angle between the pre-"event" voltage and the voltage during the sag. (A positive phase-angle shift indicates that the phase-angle of the during-"event" voltage waveform leads the pre-"event" waveform.)

Voltage unbalance (imbalance): A condition in which the three phase voltages differ in magnitude, are displaced from their normal 120° phase relationship, or both.

Voltage notch: A switching or other disturbance of the normal voltage waveform, lasting less than 0.5 cycle and initially of the opposite polarity to that of the waveform.

Transient: A sudden, non-power frequency change in the steady state condition of the waveform of voltage, current or both that is unidirectional in polarity (primarily either positive or negative) – impulsive transient / that includes both positive and negative polarity values – oscillatory transient. *Voltage Flicker:* The modulation in the RMS value of the fundamental frequency voltage component.

(Impression of unsteadiness of visual sensation induced by a light stimulus whose luminance or spectral distribution fluctuates with time.)

Harmonics: Sinusoidal component of a periodic waveform having a frequency that is an integer multiple of a fundamental frequency (50Hz or 60Hz).

3. MAJOR ISSUES

It has to be pointed out that the power quality, or rather inadequate power quality becomes an issue only if customers suffer some (appreciable) financial loss. Based on the losses to production incurred to customers due to inadequate power supply over recent years two power quality events emerged as the most significant ones namely, voltage sags and harmonics. These two particular phenomena will be addressed in more detail in the sequel.

3.1 Voltage sags (dips)

The faults in the power system are the major cause of voltage sags (dips) on the electric delivery system. Three phase (symmetrical) faults lead to severe sags at a large number of buses over wide geographical region (depending on the network topology). These faults fortunately, are very rare in the power system. Single line-to-ground fault and other asymmetrical faults typically cause sags with higher magnitudes however, they are much more common in the power system. The adverse weather conditions (lightning strikes), contamination of insulators, animal contact and accidents involving construction or transportation activities are typical causes of the faults in the power system. Lightning is the most common cause of faults on overhead lines in transmission and distribution networks and it is very dependent on weather conditions and geographical region [12]. For faults caused by lightning strikes, there is a strong correlation between sag incident rate and flash density (the number of lightning flashes per square kilometre per year) [13]. Normally customers do not experience an interruption following a transmission system fault. However, the entire power system, including the distribution system (or parts of it), will experience voltage sags [14]. This is due to the fact that transmission networks are of a highly meshed topology, which facilitates voltage sag propagation. For the faults in distribution networks (typically having a radial topology) a single line (feeder) may trip following the fault, or customers connected to that feeder (and eventually adjacent feeder) may experience voltage sags with low magnitudes while the rest of the network remains largely unaffected. Voltage sags affect each phase of a three-phase system differently depending on the nature of disturbance (symmetrical or asymmetrical), transformer and equipment connections. As the large number of the equipment in customers' plant is single-phase, it is important to assess voltage sag performance of the bus for each phase separately. Using only the lowest of the three phase voltages or the average voltage of the three phases to characterise the sag may result in erroneous results for both single-phase and three-phase equipment [15-17].

Major consequences of voltage sags include unwanted tripping of sensitive controls, dropping out of relay contacts, motor contactors and electromechanical relays, high-intensity discharge lighting, Adjustable Speed Drives (ASD), Programmable Logic Controllers (PLC), computers,

numerically controlled machines and other devices connected to the supply through ac/dc rectifiers (due to drop in dc voltage and large inrush current after voltage recovery). As most of these devices can be found in modern industrial plant or commercial facility no wonder that losses to customers due to voltage sags have been estimated in various recent surveys to hundreds even billions of dollars per annum.

Undoubtedly the monitoring of voltages at power system buses is the best way to assess voltage sag performance of the bus. This approach however has several disadvantages: The monitoring period can be very long (several years) if accurate results are required [18]; The extraction of the relevant information about sag characteristics may be very difficult and extremely time consuming; The consequences of system changes (network topology, generation pattern, loading conditions, etc.) are difficult to assess; The extrapolation of the results of monitoring to sites not monitored could give unreliable assessment of voltage sag performance [18]. The other possibility to assess voltage sag performance is by means of computer simulations. The main advantages of simulation based stochastic prediction of voltage sags are: It doesn't take many years of monitoring to achieve the required accuracy. (Providing that the appropriate mathematical models are used.) It is possible to assess voltage sag performance of a system that does not yet exist; Voltage sag performance for various network topologies, generation patterns, loading conditions, etc. can be assessed.

3.2 Harmonics

Higher harmonics in power system appear due to periodic distortion of the voltage or current waveform. The distortion comes from nonlinear devices, principally loads though nonlinear elements in the network also contribute to waveform distortion. Some load equipment does not draw a sinusoidal current from a perfectly sinusoidal voltage source, i.e., the relationship between voltage and current at every instant of time is not constant. Harmonic currents flowing through the system impedance result in harmonic voltages at the load. So the voltage distortion is the result of the interaction between harmonic currents drawn by the nonlinear load and the impedance of the power system itself. It can be easily calculated as the product of corresponding harmonic current and system impedance at that frequency. Because of low equivalent impedance, the power system can normally absorb a significant amount of harmonic current without serious voltage distortion. (High short-circuit capacity systems will be able to absorb more harmonic current than weak, low-capacity systems.) [19-22]

Harmonic sources can be broadly divided in three groups: a) Saturable devices (due to: physical characteristics of the iron core): transformers, rotating machines, nonlinear reactors. b) Arcing devices (due to: physical characteristics of the electric arc): furnaces, welders and fluorescent lighting (about 50% of a modern building's load). c) Power electronics (due to semiconductor device switching which occurs within a single cycle of the power system fundamental frequency) including ASDs, DC motor drives, electronic power supplies, etc.

The areas particularly vulnerable to harmonic distortion are commercial city centres [23,24]. The electrical load in

these areas mainly consists of (mostly) single-phase electronic loads (switch mode power supplies), fluorescent lighting and ASD (for high voltage air conditioning systems in particular). DC voltages for powering electronic and microprocessor based equipment are commonly derived from the output of single-phase full-wave diode bridge rectifiers or switch mode dc/dc power converters. High 3rd order harmonic current is typical for switch-mode power supplies. The 3rd order harmonic current components do not cancel in the neutral of a three-phase system which creates a concern of overloading of neutral conductors and overheating of transformers. In addition to present composition of loads in commercial areas switch-mode power supplies are beginning to find application in electronic ballasts for fluorescent lighting (which represent 40% - 60% of a commercial building load). So, the percentage of load which contains electronic power supplies is increasing and therefore possibility of even more acute harmonic problems.

The increased voltage harmonic distortion results in [19,25,26]: i) Thermal stress (overheating of transformers, motors and cables) - through increasing copper, iron and dielectric losses; ii) Insulation stress - through the increase of peak voltage, i.e., voltage crest factor; and iii) Load disruption. It is generally characterised by: i) High crest factor, i.e., the ratio of peak current and RMS current. (In a pure sine wave crest factor is 1.41 while on a nonlinear load crest factors of 5 have been recorded. Such high crest factor can cause operation of breakers with low tolerance to transient currents): ii) Voltage flat topping (electronic equipment is sensitive to this as it relies on the peak voltage to charge its power capacitor).

There is along list [20,22,25,26] of consequences of harmonic distortion in power system. Some of the most frequent are listed below: interference with communication circuits (telephone interference - 800Hz), capacitor or transformer failure, capacitor fuse blowing, transformer overheating at less than full load and decreased efficiency which requires de-rating of transformers (K-factor transformers), motor overheating (usually for voltage distortion levels above 8%), high neutral currents (this is major concern in commercial buildings as neutral to earth voltages create common mode noise problems, circulating currents flowing in transformers, high voltage drop at loads and eventually failure of neutral conductor), unstable operation of zero-crossing firing circuits (semiconductors are switched at zero-crossing to reduce electromagnetic interference) dielectric breakdown of insulated cables, breaker (higher di/dt at zero-crossing) and fuse (both, due to higher harmonics (skin effect) and spikes) nuisance tripping, digital clocks, real time clocks, video cassette recorders, microwave timers etc. gaining time, horizontal lines of display interference on video display units and TV receivers, shimmering displays, pixel jitter and colour variations on high resolution monitors, PC's and PLC's "hanging" requiring soft boot or power off to reset, hard disc data corruption, interference with power meters (induction disk W-meters where the error can be as high as 35%), flickering incandescent lighting, audible noise due to resonant problems caused by harmonics in discharge lighting, etc. (Most of these problems (but not all) are usually triggered by either series or parallel resonance between incorrectly rated power factor correction capacitors (sometimes even by high capacitance

cables) and system impedance (mainly transformer impedance) which leads to amplification of harmonic currents and voltages generated by the nonlinear load.)

Harmonic analysis method [21,26-31] can be generally divided in four stages: i) Preliminary assessment (hand calculations to determine system resonant frequencies). ii) Harmonic measurements (to characterise the behaviour of harmonic sources. iii) Computer simulations (to investigate different conditions and system configurations). iv) Solution development (i.e., changing capacitor sizes and/or locations and installing harmonic filters). As far as computer simulations are concerned as the only appropriate method for multi scenario analysis and initial solution development there are the following options available: i) Time domain simulations [32] where the system is modelled in detail and a time-domain simulation is performed until steady-state is reached, identification of steady-state and computation time are limiting factors though actual waveforms can be obtained and subsequently analysed using Fourier analysis. ii) Harmonic load flow studies where [33-35] calculation of harmonic currents from voltages is performed with inclusion of power flow constraints (actual system conditions can be considered). iii) Linear admittance matrix solution (frequency domain studies) where a separate system model is developed for each frequency component included in the study. The frequency scan gives a visual picture of impedance levels and potential voltage distortion. The major difficulty in applying this method is in the choice of the impedance values for different components, particularly for higher frequencies [28]. The other potential drawback is the assumption that the current waveform of the nonlinear load is not significantly affected by the voltage waveform [36] iv) Hybrid approach where time domain simulations and frequency scan analysis are combined.

4. FUTURE RESEARCH DIRECTIONS

Voltage sags and harmonics have been already identified as two major power quality issues facing modern utilities and their customers. Therefore, future research directions in these two areas will be discussed in the sequel in more detail.

As far as voltage sags are concerned the questions that remained unanswered so far include: i) *Voltage sag characterisation and indices*. Majority of existing standards and monitoring / benchmarking projects define voltage sags as two-dimensional events with voltage sag magnitude and duration being main characteristics. Other sag characteristics namely, point on wave of sag initiation, phase angle jump and in particular sag asymmetry (in case of three phase voltage sags) remain largely excluded from sag description and characterisation though it has been already demonstrated that the equipment is sensitive to those other parameters as well. Fundamental research is needed therefore on characterisation (description) of voltage sags with respect to more than two parameters and development of both equipment sensitivity indices and system performance indices for system benchmarking. Ideally this research should lead to development of a single index (or set of indices) that can be used for both purposes. Of particular importance here is characterisation and description of three-phase equipment sensitivity to three phase events. ii) *Extraction of voltage sag characteristics* from actual recordings of system sag performance. A large number of monitoring projects in

various networks around the world have been already completed (or are under way) with the aim to assess system voltage sag performance based on monitoring system voltages at selected buses. It is therefore, required to develop suitable technique for extraction of relevant information about sag characteristics from huge data bases containing monitoring results. Data mining techniques in combination with signal analysis techniques could be used for this purpose. iii) Further *development of stochastic/probabilistic methods* for the assessment of system sag performance and validation of these techniques against monitoring results. The limitations of stochastic/probabilistic methods for prediction of system sag performance should be established as well as the extent to which power system model needs to be developed in order to obtain results of simulations that match monitoring data. iv) Having in mind perceived increased penetration of renewable distributed generation into power system the *influence of voltage sags on converter connected generators* in particular should be investigated. v) Along the similar line, *the influence of large penetration of renewable generation on network sag performance* should be investigated having in mind different possible generation patterns and different generation mix (i.e., conventional, wind, converter connected). vi) Further research is also needed in the area of *design of mitigation equipment* (though not exclusively related to voltage sags) and *improvement of ride through capabilities to voltage disturbances of end user equipment*. vii) It is generally accepted view that the voltage sags are important as much as they cause disruption of production and financial losses to customers. It is of fundamental importance to *develop methodology for the assessment of potential financial losses to different classes of customers due to voltage sag*. Risk analysis in combination with probabilistic methods could be used in this purpose. The methodology could be used to justify (or not) investment in mitigating equipment, which is still very often of prohibitive costs to a lot of customers.

The major issues that require further investigation in the area of harmonic studies include: i) *Validation of network and individual load models* to be used in harmonic studies. In particular validation of simulation results through comparison with harmonic measurements. ii) *Development of probabilistic harmonic models for aggregate loads* (e.g., large commercial buildings or industrial plants) to be used in large system simulations. iii) *Development of analytical techniques for the assessment of system harmonic performance* and optimal filter placement without having to perform time domain simulations or frequency scan. Inherent structure theory [37] after suitable modifications could be used for this purpose. iv) *Investigation into allowable harmonic distortion levels* that different equipment can withstand without major malfunction or disruption. v) *Development of control algorithms for large pulse-width – modulated (PWM) converters* that will allow harmonic mitigation. This is particularly important when large PWM converters are used as the interface between renewable distributed generators and the network or when they are part of large motor drives. vi) Further *development of active filters* in order to increase their ratings and broaden the are of application.

5. CONCLUSIONS

The paper presented short introduction to power quality, identified the importance of the area and major drivers behind recent increased interest in this line of research. It further presented an overview of existing (sometimes conflicting and ambiguous) definitions of power quality and definitions of different (most widely investigated) power quality phenomena. As the power quality is very broad subject covering many different phenomena and processes the paper focussed in the second part on discussing in detail two phenomena namely, voltage sags and harmonics, that are generally viewed as being the most important power quality phenomena facing modern utilities and industry. Finally the paper identified possible future research directions in both of these areas.

6. REFERENCES

- [1] R.C.Dugan, M.F.McGranaghan and H. Wayne Beaty, "Electrical Power Systems Quality". McGraw Hill, 1996.
- [2] IEC 60050, "International Electrotechnical Vocabulary (IEV)", International Electrotechnical Commission.
- [3] S.T.Chang, K.Y.Chua, C.C.Siew and T.L.Tan, "Power quality initiatives in Singapore", CIRED 2001, Conference Publication No. 482, IEE, June 2001.
- [4] C.Greiveldinger, N.Baumier, C.Derquenne, P.Fauquembergue and C.Degand, "Measured and perceived quality: Conclusion of the experiment named QUALIMAT", CIRED '97, Conference Publication No. 438, IEE, June 1997.
- [5] M.Marchand, "The seven services which EDF provides to small and medium-sized companies", CIRED '97, Conference Publication No. 438, IEE, June 1997.
- [6] IEEE Standard 493, "Design of reliable industrial and commercial power systems", (Gold book), IEEE, New York, 1997.
- [7] D.L.Sikes, "Comparison between power quality monitoring results and predicted stochastic assessment of voltage sags – "real" reliability for the customer", IEEE Trans. on Industry Applications, Vol. 36, No. 2, 2000.
- [8] O.Souto, J.Oliveira and L.Neto, "Induction motors thermal behaviour and life expectancy under non-ideal supply conditions", 9th International IEEE Conference on Harmonics and Quality of Power, Orlando, Florida, October, 2000.
- [9] M.H.J.Bollen and E.Styvaktakis, "Characterization of three-phase unbalanced dips - as easy as one-two-three", IEEE Power Engineering Society, Summer Meeting, July 2000, Seattle, USA.
- [10] M.H.J.Bollen, "Characterisation of voltage sags experienced by three-phase adjustable speed drives", IEEE Trans. On Power Delivery, Vol. 12, No. 4, 1997.
- [11] P.K.Ghosh and L.G.Durante, "Measurement performance testing for nonsinusoidal environments", IEEE Trans. On Power Systems, Vol. 14, No. 4, 1999.
- [12] J.D.Glover, M.Sarma, *Power System Analysis and Design*, Third edition, Brooks/Cole, Thomson Learning Inc, 2001.
- [13] E.W.Gunther, H.Mehta. "A Survey of Distribution System Power Quality-Preliminary Results". IEEE Transactions on Power Delivery, Vol. 10, No. 1, 1995, pp. 322-329.
- [14] J.Lamoree, D.Mueller, M.J.Samotyj. "Voltage Sag Analysis Case Studies". IEEE Transactions on Industry Applications. Vol. 30, No. 4, 1994, pp.1083-1088.

- [15] P.B.Steciuk and J.R. Redmon. "Voltage Sag Analysis Peaks Customer Service". IEEE Computer Applications in Power. October 1996, pp. 48-51.
- [16] L.E Conrad, M.H.J.Bollen. "Voltage Sag Coordination for Reliable Plant Operation". IEEE Transactions on Industry Applications, Vol. 33, No. 6, 1997, pp. 1459-1463.
- [17] M.H.J.Bollen and L.D.Zhang. "A Method for Characterisation of Three-Phase Unbalanced Sags from Recorded Voltage Wave shapes". Department of Electric Power Engineering, Chalmers University of Technology, Gothenburg, Sweden.
- [18] M.R.A.Qader. "Stochastic Assessments of Voltage Sags due to Short Circuits in Electrical Networks". PhD thesis, Department of Electrical Power Engineering, UMIST, 1997.
- [19] CIGRE WG 36-05, "Harmonics, Characteristic parameters, methods of study, estimates of existing values in the network" Electra, No. 77, 1981, pp. 5-54.
- [20] J.Arillaga, D.A.Bradley, P.S.Bodger, *Power system harmonics*, Wiley, 1985.
- [21] J.Arillaga, B.C.Smith, N.R.Watson, A.R.Wood, *Power system harmonics analysis*, Wiley, Chichester, UK, 1997.
- [22] G.J.Wakileh, *Power Systems Harmonics - Fundamentals, Analysis and Filter Design*, Springer, 2001.
- [23] Mansoor, A., et. al, "Predicting the Net Harmonic Currents Produced by Large Numbers of Distributed Single Phase Loads", IEEE Transactions on Power Delivery, Vol. 10, No. 4, 1995.
- [24] Grady, W.M., et. al, "Estimating the Net Harmonic Currents Produced by Selected Distributed Single Phase Loads", Power Engineering Society Winter Meeting 2002, Vol. 2, pp. 1090-1094.
- [25] IEEE Task Force Report, "Effects of Harmonics on Equipment", IEEE Trans. on Power Delivery, Vol. 8, No. 2, 1993, pp. 672-680.
- [26] "Tutorial on Harmonics Modelling and Simulation", IEEE Power Engineering Society, TP-125-0, 1998.
- [27] E.W.Palmer, and G.F.Ledwich, "Three-phase modelling of power system loads", IEE Proc.-C, Vol. 140, No. 3, 1993, pp. 206-212.
- [28] A.S.Morched and P.Kundur, "Identification and modelling of load characteristic at high frequencies, IEEE Trans. On Power Systems, Vol. 2, No. 1, 1987, pp. 153-160.
- [29] M.Fauri, "Harmonic Modelling of Nonlinear Load by means of Crossed Frequency Admittance Matrix", IEEE Trans. on Power Systems, Vol. 12, No. 4, 1997
- [30] E.W.Palmer and G.F.Ledwich, "Three-phase harmonic modelling of power system loads", IEE Proc.-C, Vol. 140, No. 3, 1993, pp. 206-212.
- [31] E.B.Makram and S.Varadan, "A Generalised load modelling Technique Using Actual Recorded Data and its Use in a Harmonic Load Flow Program.", Electric Power System Research, Vol. 27, 1993, pp. 203-208.
- [32] S.A.Soliman, A.M. Al-Kandari and M.E.El-Hawary, "Time domain Estimation Techniques For Harmonic Load Models", *Electrical Machines and Power Systems*, No. 25, 1997, pp. 885-896.
- [33] D.Xia, G.T.Heydt, "Harmonic power flow studies, part I – formulation and solution", IEEE Trans. on Power Apparatus and Systems, Vol. 101, No. 6, 1982, pp. 1257-1265.
- [34] D.Xia, G.T.Heydt, "Harmonic power flow studies, part I – formulation and solution", IEEE Trans. on Power Apparatus and Systems, Vol. 101, No. 6, 1982, pp. 1266-1270
- [35] W.Xu, J.R.Marti and H.W.Dommel, "A multi-phase harmonic load flow solution technique", IEEE Trans. on Power Systems, Vol. 6, No. 1, 1991, pp. 174-182.
- [36] S.Varadan, E.B.Makram, "Harmonic load identification and determination of load composition using a least squares method", Electrical Power System Research, Vol. 37, 1996, pp. 203-208.
- [37] G.Carpinelli, et.al, "Inherent Structure Theory of Networks and Power System Harmonics", IEE Proceeding Generation Transmission Distribution, Vol. 145, No.2, 1998.

AN OVERVIEW OF CURRENT TRENDS IN AUTOMOTIVE POWER ELECTRONICS

Dušan Graovac, Friedrich Schwamm, ATENA GmbH, Liebigstr. 5a, 85757 Karlsfeld, Deutschland

Abstract: The aim of this paper is to present power electronics/energy trends in automotive industry. After examining the car energy economy, an overview of semiconductor components trends is given, followed by general survey of novel energy sources like hydrogen energy (internal combustion and fuel cells) and photovoltaic. In the end an important subject of safety in automotive electrical development is presented.

Key Words: Automotive Power Electronics, Fuel Cells, Solar Energy, Hydrogen Energy, Safety Applications

1. INTRODUCTION

The automobile electrical system is nowadays undergoing a real revolution. Increased functionality, energy saving, environmental issues, reliability/safety demands and performance/cost optimization are strong driving forces for the almost only industry branch unaffected by current economic situation. Industry established semiconductor component manufacturers are orientating more and more of their facilities towards automotive applications. The automotive OEMs are seriously appreciating the electrical system influence on the car performance and price and are more ready to further invest in this area, which can clearly be seen both through the R&D investments and through the serious increase in number of automotive subcontractor companies. In order to minimize green-house effects as well as the use of the world's fossil fuel reserves, the efforts in "clean energy" cars development are intensified, leading to new use of alternative energy sources and electrical energy storage components.

The purpose of this paper is to present power electronics and energy trends in automotive applications. After a semiconductor components overview, a survey of novel energy sources (hydrogen and photovoltaic) is given. In the end an important subject of safety in automotive electrical development is presented.

2. SEMICONDUCTOR COMPONENTS

Semiconductor area in automotive power electronics has two strong motivators for further development: high cost of the car generated electricity and the move towards 42V board net, dictated by market demanded increase in functionality (X-By-Wire systems, electric actuators, EMC, etc.). In addition, increase in the system complexity together with required safety level implies the use of self-diagnostic capable actuators and sensors as well as the fail-safe or fail-silent actuators.

The cost of automotive electricity can be calculated as follows [1]: Petrol has a heat energy content of 43.5 MJ/kg and a density of 0.73 kg/L, which gives volumetric energy content of about 32 MJ/L, or round 8.8 kWh/L. If the first approximation of car engine efficiency is <40% and the combined efficiency of alternator/belt is around 45%, a liter of petrol gives approximately 1.6 kWh to a car's electrical system. Lead-free petrol in Germany costs about 1.08€, leading to the cost of car generated electricity of about

0.675€/kWh. For the comparison, the price of 1kWh in residential area in Germany is around 0.0116€, almost sixty times less expensive.

Also, increased functionality leads to extended power demand. The required average power consumption is given in fig. 1. According to the German OEMs group "Forum Bordnetz" initiated originally by Daimler-Chrysler AG, the peak power demand in year 2005 will be around 22kW, some 10 times greater than average.

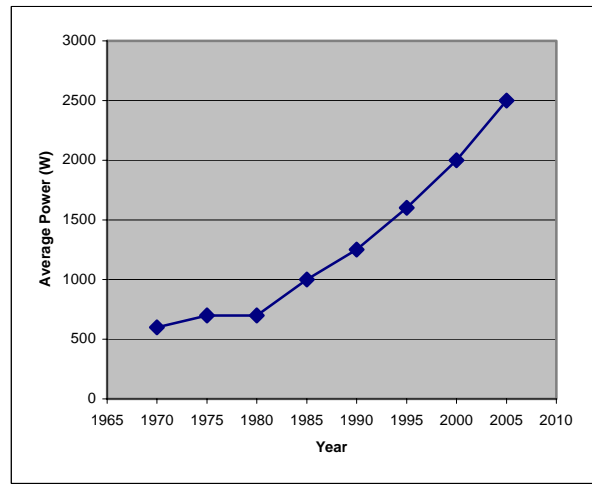


Fig. 1. Average electric power consumption.

Power electronics, compared to its well established industrial applications, is relatively new for automotive. There are three important challenges: reliability, electromagnetic compatibility (EMC) and cost. **Reliability:** The ambient temperature range can vary from -40°C to 125°C leading to great thermal stress on power modules and electrolytic capacitors; Severe vibration require specific mechanical design of the connectors and fasteners; Salt and water spray require sealed packaging for converters. **EMC:** Both conducted and radiated noise can cause malfunction of other electronic equipment. **Cost,** especially with the high production volumes in auto-industry, is the main factor – in order to make the power electronics more present in car production the goal is to reduce current price to its fourth.

2.1. 12V Board net

A typical 12V board net [1], [2] is presented in fig. 2. Basic trends are to: Replace electromechanical relays, fuses, end switches in dashboard control with semiconductor switches; Minimize the power losses of the switches used; Move to the electromechanical actuators from hydraulic ones (active suspension, electromagnetic valves); Have intelligent self-protected actuators with integrated bus communication system for both the actuator control and the status feedback.

isolator film layers. Such a system requires pressure, hydrogen concentration, filling and temperature control and is equipped with different power electronics converters controlling electromechanical valves, motors and resistive loads.

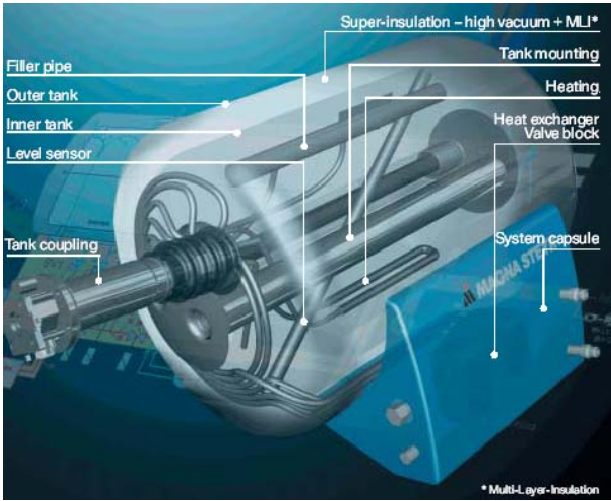


Fig. 5. BMW liquid hydrogen tank.

3.2. Hydrogen energy – fuel cells

Originally applied in aerospace area, the fuel cells have been neglected for a long time as a “commercially non-viable product”, but after a recent technology break-through they are considered as the most likely successor to the ICE [7]. There is a number of commercially available fuel cells; however, the most of them operate on high temperatures (even up to 1200°C). Best suited for automotive (and the most used one) is the Proton-Exchange Membrane (PEM) fuel cell. Such FC operates on 80°C and has a thin plastic sheet as an electrolyte. Fig. 6. presents a block diagram of such a system.

Fuel cell has a small DC output voltage [8] (between 1V and 2V) and high current capability and is accordingly packed into stacks. To power-condition the FC output a non-isolated DC/DC converter is used. The type of the converter (buck or boost) is determined by the FC stack output voltage. The role of the converter is not limited to energy conversion - it also has to protect the system from slow output fluctuations, reverse currents and abrupt load changes.

If a fuel cell is directly hydrogen supplied, the FC system consists of a stack and a converter. Some manufacturers try to avoid problems of hydrogen on-board storage by using some (easy to store and to tank) hydrogen-rich fuel such as Methanol (CH₃OH) or “clean-gasoline” (CHF). Through the reforming process methanol is converted into hydrogen. Addition of a reformer deteriorates system efficiency and leads to a limited CO₂ emission.

In addition, the FC systems can be divided in two groups according to application: APU (Auxiliary Power Unit) FC systems, where the FC is used to supply electronic devices on the board net and Propulsion FC Systems, where the FC system supplies a traction motor and inverter. In this area OEMs are not unified in the motor choice: while the European manufacturers seem to prefer permanent magnet synchronous motor, in USA is the induction motor mainly used, the Japanese use both technologies.

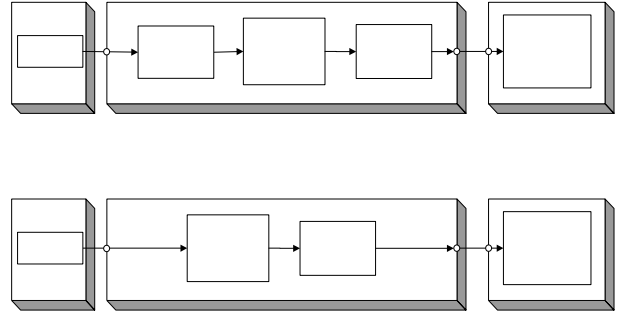


Fig. 6. Fuel cell system.

Table 1 gives an overview of the FC powered vehicles characteristic with the major OEMs.

Table 1. FC powered vehicles

Manufact./Model	kW	fuel	application
BMW/745h	5	H ₂	APU
Daimler/NECAR4	70	H ₂	Tract./APU
Daimler/NECAR3	50	CH ₃ OH	Tract./APU
Fiat	7	H ₂	Tract./APU
GM/Chevy S-10	25	CHF	Tract./APU
OPEL/Zafira Gen3	94	H ₂	Tract./APU
Ford/Focus FCV	85	H ₂	Tract./APU
Renault/FCHV	90	H ₂	Tract./APU
PSA/Hydro-Gen	55	H ₂	Tract./APU
VW/EU Capri	15	CH ₃ OH	Tract./APU
Toyota/FCHV-5	90	CHF	Tract./APU
Honda/FCX	85	H ₂	Tract./APU
Mazda/Premacy	85	CH ₃ OH	Tract./APU
Mitsubishi/Space-liner	40	CH ₃ OH	Tract./APU
Nissan	10	CH ₃ OH	Tract./APU

3.3. Photovoltaic

There are two basic applications of solar energy in automotive industry: on-board - where the solar cell is integrated in the car roof and indirect applications, where huge stationary photovoltaic systems are used to produce hydrogen. Such solar/hydrogen systems exist for instance in Neunburg – Wald/Bavaria (Germany) and in Mojave Desert (USA). However, due to technology limitations, current efficiency of this method is limited to 15%.

Typical on-board application (Daimler, Audi, VW) is shown in fig. 7, where a solar cell (typical power 30W-150W) is used to supply loads such as fan-motors or to charge the battery. Such system is often required to be self-supplied and to operate when the car is switched-off.

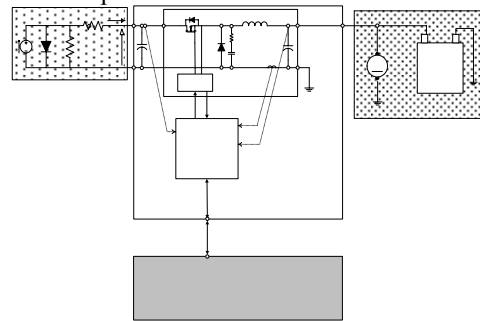


Fig. 7. Typical on-board photovoltaic application.

Solar array characteristic [9] is presented in fig. 8. In order to improve intrinsic low efficiency, a buck dc/dc converter is normally used and controlled to achieve maximum power point of the array. Since the solar cell operation is strongly dependent on the insolation and the temperature, a maximum power point tracking (MPPT) algorithm must be used. The basic goal is to adjust complex load (converter + load) impedance to the output impedance of the photovoltaic cell. Though different MPPT methods, such as: constant voltage reference, constant current reference, incremental conductance method, peak power tracking etc, have been reported, a constant voltage reference method is mostly used in automotive because of its low cost, although the system performance with this method is the lowest one.

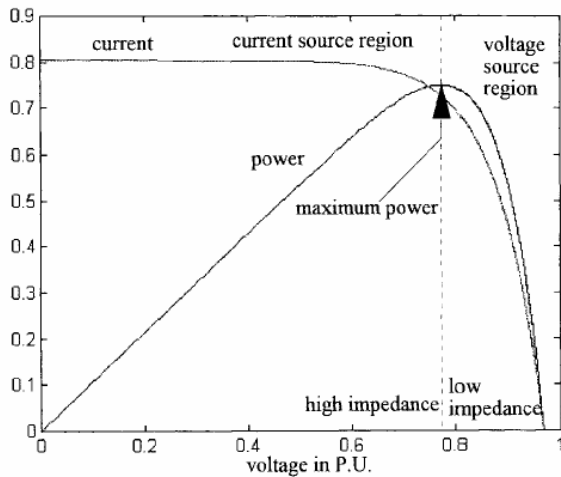


Fig. 8. Solar array characteristic.

4. SAFETY CRITICAL AUTOMOTIVE DEVELOPMENT

For safety critical automotive systems an optimum needs to be found between safety and the system costs. Therefore a design guide line needs to be established which gives a correlation between hazard potential and tolerable rates. Since there are established methods in Aero industries on how to design and certify safety critical fly by wire systems the standard (JAR) [10] shall be compared against the relevant standard for automotive systems (IEC) [11]. As Fig. 9 shows, both standards relate criticality to the potential of loss of human lives. From the detailed criticality definitions it can be concluded that the four criticality groups are slightly different scaled on the criticality axis. Taking these aspects into account it strikes that in the range of high hazard potentials the requirements for airworthy systems are much stricter than for automotive systems while there is a good matching in the range of low hazard potentials between both standards. For the definition of the actually required safety there are two aspects of relevance. First the tolerable frequency of severe accidents caused by system malfunctions within the system fleet on the roads is deemed to be less than 1 / year. Second the size of the system fleet to be considered. This depends on the annual production and system life time. With these two aspects the safety requirement for SIL-3 (Safety Integrity Level) automotive systems will end up to event rates between 10^{-10} [1/h] and 10^{-9} [1/h]. From these figures it can be concluded that there is quite a good

matching between the safety requirements for aero engine systems and automotive systems.

Safety comparison IEC (Auto) <-> JAR (Avio)

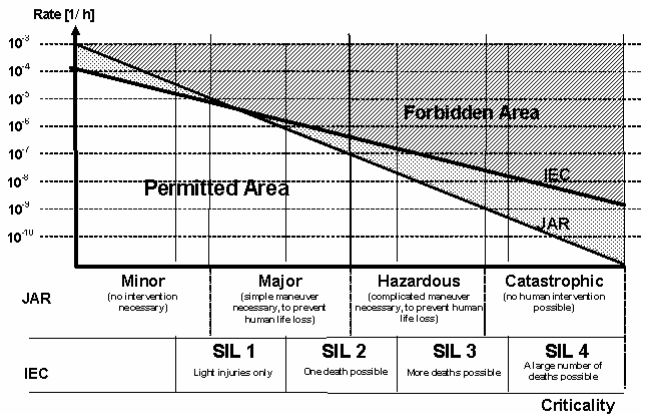


Fig. 9. Safety comparison JAR - IEC.

Fig. 10 shows a process of a system architecture development at ATENA. Starting from an initial customer specification – here also named as ‘diffuse specification’ – the so called Top Events (undesired system malfunctions) are defined qualitatively. From the hazard potentials of these Top Events and from the probability of the hazard relevant system operating points the maximal rates of these Top Events are derived. Next, basic system concepts will be defined which should meet the performance and safety requirements. With this information, each system concept is subjected to an iteration loop of FTA (Fault Tree Analysis) and FMEA (Failure Mode and Effect Analysis) with each Top Event to achieve finally effort optimised system architectures and redundancy concepts for every basic system concept. These architectures will be assessed against feasibility and hardware effort. For visibility reasons the assessment results are listed in a matrix to derive the best suited system architecture out of the analysed system concepts. From this basis a verifiable system design specification and an Interface Control Document (ICD) are produced, which forms a base line for the further system development. From this process a system failure catalogue can easily be produced which is in particular very useful for the later software development.

Entwicklung der System-Architektur

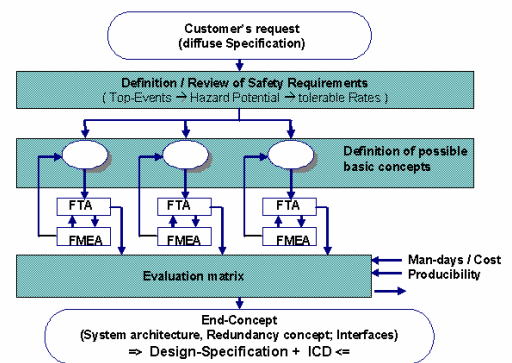


Fig. 10. System architecture development.

Fig. 11 gives a rough overview of the ATENA Software development process. Here the software development for a dual redundant control unit is presented. First block shows the development of Design Specification, ICD and system Failure catalogue. At the next step an Offline Simulation of the System is performed in which the control unit is modelled as a two channel box. In this phase the system and software requirements are validated and it also covers a first verification of the software design. Here the previously mentioned failure catalogue is used to test system behaviour on failure events in the different operating points. After the simulation shows satisfying results the control unit software will be automatically generated and down loaded into target hardware. The models of the control unit environment will be converted and downloaded in a dSpace processor system for real time simulation. The real time test phase starts with simulated system components and ends with a virtual system where many real system components are implemented. Finally the Control unit is tested in the real environment, which

should be a demonstration that all aspects of the customer's intent and the Design Specification are fulfilled. With an aero engine control unit this is a very important matter in the case of a first flight.

5. CONCLUSION

Power electronics found a wide application field in automotive electronics area. New functionality, energy saving, environmental issues, and performance/cost optimization are strongly influencing further development both in semiconductor manufacturing and in power electronics systems development. In addition, new challenges arise from "clean energy" cars development using the power electronics for alternative energy sources output conditioning.

In order to make new cars safe and reliable, experiences from aerospace are used both in new standards and recommendations as well as in the system development.

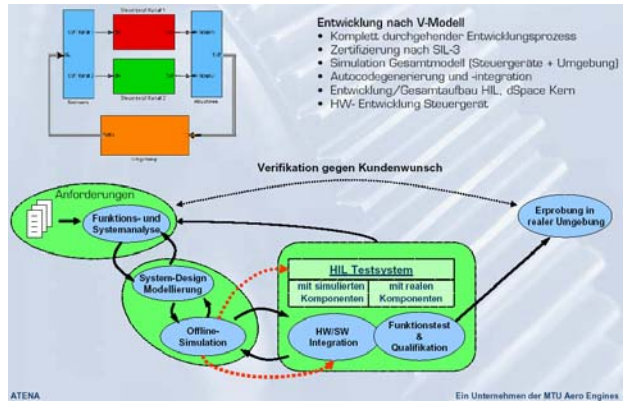


Fig. 11. SW and system development for a safety critical two channel system.

5. REFERENCES

- [1] J. Kassakian, H. Wolf, J. Miller, C. Hurton, "Automotive Electrical Systems circa 2005", IEEE Spectrum, August 1996, pp. 22-27
- [2] C.Chan, K.Chau, "An Overview of Power Electronics in Electric Vehicles", IEEE Trans. on Industrial Electronics, Vol.44, No.1, Feb.1997, pp.3-13.
- [3] A. Graf, "Semiconductor Technologies and Switches for new Automotive Electrical Systems", European Automotive Congress - EAEC, Barcelona (E), July.1999
- [4] E. Bretz, "By-Wire Cars Turn the Corner", IEEE Spectrum, April 2001, pp. 68-73
- [5] Bayern-Innovativ, Kooperationsforum: "Mechatronik für den Automobilbau", Nürnberg (D), Mai 2003
- [6] BMW CleanEnergy, "Hydrogen Future"
- [7] T. Gilchrist, "Fuel Cells to the Fore", IEEE Spectrum, Nov. 1998, pp. 35-40
- [8] M. Lukas, K. Lee, H. Ghezal-Ayagh, "An Explicit Dynamic Model for Direct Reforming Carbonate Fuel Cell Stack", IEEE Trans. on Energy Conversion, Vol.16, No.3, Sep.2001, pp.3-13.
- [9] E. Koutroulis, K. Kalaitzakis, N. Voulgaris, "Development of a Microcontroller-Based, Photovoltaic Maximum Power Point Tracking Control System", IEEE Trans. on Power Electronics, Vol.16, No.1, Jan.2001, pp.46-54.
- [10] Joint Aviation Requirements, JAR 25/AMJ 25.103
- [11] IEC61508, Functional Safety of Electrical/Electronic/Programmable Electronic Safety-Related Systems

THREE PHASE ZCS FREQUENCY CONVERTER

Vladislav Damec, Jan Dudek, Petr Chlebiš, VŠB - Technical University, Faculty of Electrical Engineering and Computer Science, Department of Power Electronics and Electrical Drives, Ostrava, Czech Republic

Abstract: The article is focused on the advanced power semiconductor converter area. The contribution deals with the principle analysis, construction and measured properties of the ZCS frequency converter. The examined converter is the series resonant current-type DC-link frequency converter. The converter is a kind of PWM controlled current-type frequency converter. The main advantage of this conception is almost sinusoidal output voltage and a small level of electromagnetic emissivity. It's possible to reach higher efficiency by using the series resonant DC-link compared to the hard-switched inverter with a sine wave filter. The laboratory device with power about 3kW was built. This physical model based on IGBT with serial diode is controlled by DSP. The results of measurement are shown in the paper.

Key Words: Converter Circuits, Converter Control, Resonant converters, Soft switching, ZCS converters

1. INTRODUCTION

The series resonant current-type inverters are intended for DC-link current-type frequency converters. The main idea of the paper is to enrich the current-type DC-link with a series resonant DC-link to reach the soft-switching of the converter. It's possible to reach higher efficiency by using the series resonant DC-link compared to the hard-switched inverter.

2. THE POWER TOPOLOGY

The power topology is derived from the converter shown in [1]. The main parts of the power circuit are the input rectifier, output inverter and DC-link. The DC-link is a new conception, it uses the series resonant circuit to reach a zero current switching of the power switches. The converter has to be complemented by two capacitor batteries, which accumulate the energy of off-turned phases. The basic power topology is shown in the Fig. 1. The transistors $T_{10} - T_{15}$ together with diodes $D_{10} - D_{15}$ build the current-type rectifier. The transistors $T_{20} - T_{25}$ together with diodes $D_{20} - D_{25}$ build the current-type inverter. It's necessary to use diodes in series with IGBT transistors to eliminate the antiparallel diodes, which are included in almost all IGBT transistors. The capacitor batteries are set up of the capacitors $C_{11}-C_{13}$ and $C_{21}-C_{23}$. The DC link is build from inductors L_{DC} , L_R and L_{sat} and from capacitor C_R .

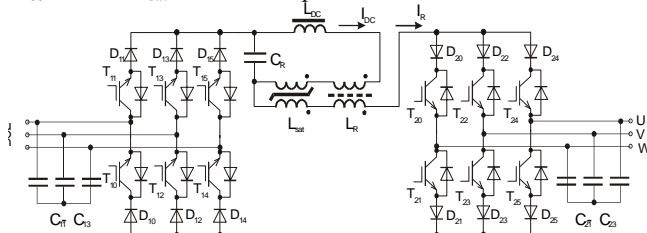


Fig. 1. Basic power topology of the series resonant converter

2.1 Work cycle of the DC-link

A basic form of the DC-link is shown in Fig. 2.

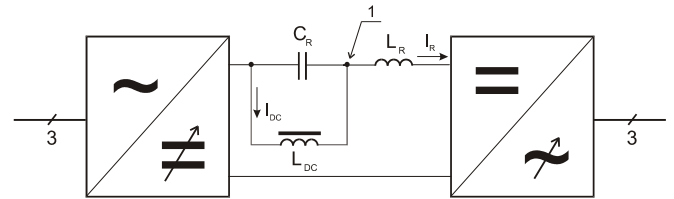


Fig. 2. Basic form of the DC-link

The DC-link works as follows. The inductor L_{DC} accumulates energy during the working cycle and the I_{DC} current is constant. An inductance of L_{DC} is large, approx. 1000x larger than L_R . The capacitor C_R and inductor L_R build the series resonant circuit and the resonant current superimposes at node 1 to the I_{DC} current. The ideal I_R current waveform is shown in the Fig. 3.

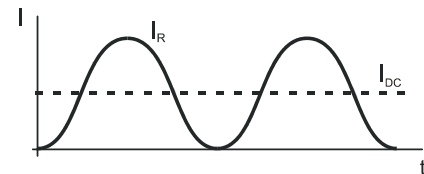


Fig. 3. Ideal DC-link current I_R

It is a description of an ideal resonant circuit. The U_{CR} magnitude is directly proportional to the I_{DC} current. But the real circuit isn't without losses and the resonant cycles would be suppressed. So it's necessary to add some energy to the resonant circuit during the work cycle.

It's necessary to have some energy reserve to reach the stable run of the converter. The energy reserve supply the power losses in the resonant circuit and some energy is supplied into the output capacitors $C_{21}-C_{23}$. The principle how to get the energy to the resonant circuit is shown below.

The DC-link is open-circuited at the zero point of I_R . There is allowed the change of switching combination of both switching bridges at the zero point of I_R current. The DC-link is kept opened, the current I_{DC} flows in L_{DC} charges C_R and feeds the energy into resonant circuit. The amount of energy in resonant circuit can be derived as follows:

$$E_1 = \frac{1}{2} C_R \cdot U_{LR1}^2 \quad (1)$$

where

C_R is a capacity of resonant capacitor in F and U_{LR1} voltage given on inductor L_R at the beginning of the resonant cycle.

The energy in inductor L_R in point of maximal value of I_R current can be derived similarly because all of the energy is accumulated in L_R :

$$E_2 = \frac{1}{2} L_R \cdot I_{Rp}^2 \quad (2)$$

where L_R is resonant inductance, I_{Rp} peak current in resonant inductor, for unclamped converter reaches: $I_{Rp} = (2.2 - 2.5) I_{DC}$

We can derive from (1) and (2) and from energy consistence law:

$$U_{LRI} = \sqrt{\frac{L_R}{C_R}} \cdot I_{RP} = (2.2 \div 2.5) \cdot \sqrt{\frac{L_R}{C_R}} \cdot I_{DC} \quad (3)$$

where

I_{DC} current flown in L_{DC}

3. CONTROL OF THE CONVERTER

3.1 Output voltage control

The converter employs a delta modulation technique to control the output voltage. The delta modulation technique is derived from binary hysteresis regulators. The hysteresis isn't obtained by regulator insensitivity but it's obtained by discrete time sampling. The delta modulation technique is a discrete control method of the converter, which works as follows.

Inverter control algorithm computes the difference between the reference and the real output voltage values and determines the switching pattern for the next period to minimize the difference between the reference and real the voltages. The switching combination is shown in the Tab.1, where U^* means required value of voltage.

Rectifier control algorithm computes the difference between the reference and the real input current values and determines the switching pattern for the next period to minimize the difference between reference and real current. The switching combination is shown in the Tab.2, where I^* means required value of current and the lowes difference means negative value of difference.

Tab. 1. Switching combination of output three-phase inverter	
$dif_{uv} = (U_u - U_v) - U_{uv}^*$, $dif_{vw} = (U_v - U_w) - U_{vw}^*$, $dif_{wu} = (U_w - U_u) - U_{wu}^*$	
highest absolute difference and its polarity	Switching combinations
$dif_{uv} > 0$	T_{22}, T_{21}
$dif_{uv} < 0$	T_{20}, T_{23}
$dif_{vw} > 0$	T_{24}, T_{23}
$dif_{vw} < 0$	T_{22}, T_{25}
$dif_{wu} > 0$	T_{20}, T_{25}
$dif_{wu} < 0$	T_{24}, T_{21}

Tab. 2. Switching combination of input three-phase converter	
$dif_1 = I_1 - I_1^*$, $dif_2 = I_2 - I_2^*$, $dif_3 = I_3 - I_3^*$	
conditions	Switching combinations
$dif_1 < dif_2 < dif_3$	T_{11}, T_{14}
$dif_3 < dif_2 < dif_1$	T_{10}, T_{15}
$dif_1 < dif_3 < dif_2$	T_{11}, T_{12}
$dif_2 < dif_3 < dif_1$	T_{13}, T_{10}
$dif_2 < dif_1 < dif_3$	T_{13}, T_{14}
$dif_3 < dif_1 < dif_2$	T_{15}, T_{14}

3.2 The DC-link control

The DC-link is controlled by simply compare method. This method needs a powerful controller, but it allows some inaccuracies in voltage measurements.

The disadvantage of this method is it's low working speed and it can be used in systems, which have powerful control system. For example, this task has to be done in $10\mu s - 50\mu s$ by resonant frequency 7 kHz.

The advantage of this method is more stable run of the converter, because the critical U_{CR} measurements are done repeatedly.

4. THE LABORATORY MODEL OF SERIES RESONANT CONVERTER

The laboratory device of the converter with the series resonant circuit is shown in Fig.4.



Fig. 4. The laboratory device

The IGBT-type BSM50GB120DN2 transistors are used in the laboratory device. It's necessary to use HFA30PB120 diodes in series with each transistor to eliminate the influence of anti-parallel diode build in the common IGBT transistors. The resonant circuit consists of the resonant capacitor C_R (polypropylene pulse capacitor) and resonant inductance L_R . The circuit in basic form isn't control system failure proof, it needs an auxiliary circuit to protect against control system failure. The power semiconductors can be damaged by overvoltage rising from inductances, which occurs by opening inductance with nonzero current. The basic circuit topology (Fig.1) has to be also enriched by the overvoltage protection of the DC-link. The suitable concept of overvoltage protection is in using a fast thyristor and auxiliary circuits. The capacitors in input/output filters work with a hard current pulses and have to endure it.

The DSP control kit eZdsp 2812 is used for control the laboratory model. It employs the DSP TMX 320F2812, which is able to reach the computing power up to 150MIPS and which has all the necessary peripherals on the chip. The C-programming language is used for implementing of the control algorithm into DSP.

5. EXPERIMENTAL RESULTS

The typical waveforms in the DC link are shown in Fig. 5. The converter supplies the induction motor 1kW, 220/127V, 50Hz, 1450min^{-1} . The waveforms of output voltage and current for output frequency of 50 Hz and 16,66 Hz are shown in the Fig. 6. and Fig.7. The measured output voltage harmonics and the THD coefficient is shown in the Fig. 8.

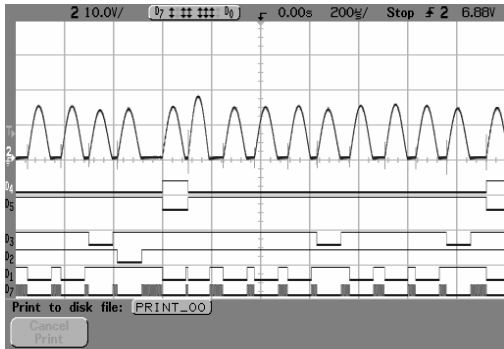
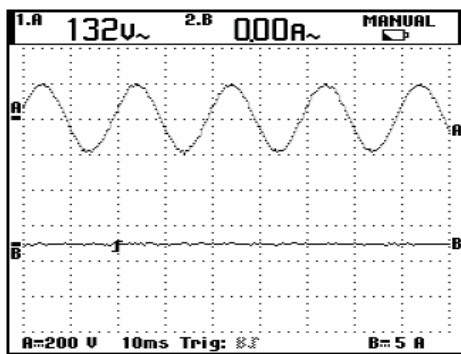
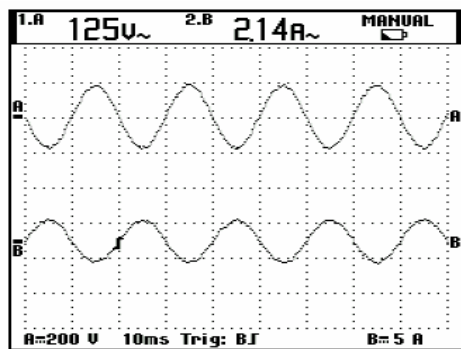


Fig.5. Typical DC-link waveforms

The channels for the next figures are: 1-output phase voltage, 2- output phase current



a)



b)

Fig. 6. Output current and voltage of the laboratory device. Output frequency 50Hz

a) by zero of output load
by output current 2A

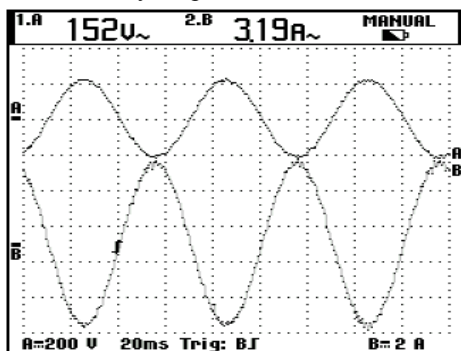


Fig. 7. Output current and voltage of the laboratory device. by output current 3A and output frequency 16 2/3Hz

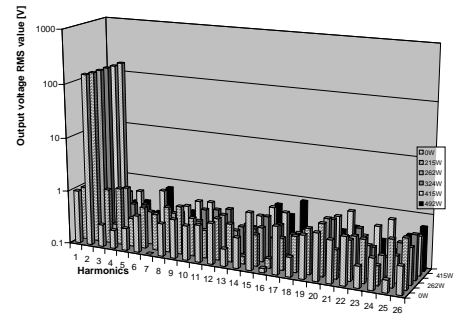
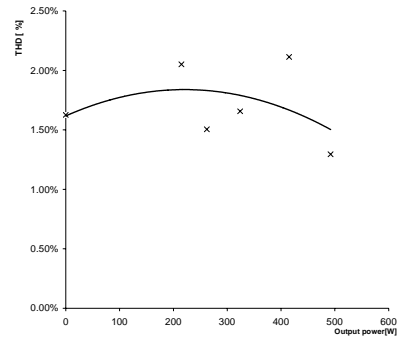


Fig. 8. Results of output voltage harmonic and THD analysis

REFERENCES

- [1] Klos A., *Stromrichter-Netzrückwirkungen in Theorie und Praxis*
- [2] Steimer P., Grünling J., Wernier P. & col.: ABB Industrie, 3BHT 490 183R0003
- [3] Weber A., Dalibor T., Kern B. & col: Reverse Blocking IGCTs
- [4] S.G.Abeyratne, J.Horikawa, Y.Murai, T.A.Lipo, *Current-Clamped, Modified Series Resonant DC-link Power Converter for a General Purpose Induction Motor Drive*, in IEEE trans. of Power Electronics 1997, p. 201-212
- [5] Holtz J., *Gate Assisted Reverse and Forward Recovery of High-Power GTO's in Series Resonant DC-Link Inverters*, in IEEE Transactions on Power Electronics 1999, p. 227-232
- [6] Elasser A., Parthasarathy V., Torrey D., *A study of the Internal Device Dynamics of Punch-Through and Nonpunch-Through IGBT'S Under Zero-Current Switching*, IEEE Transactions on Power Electronics 1997, p. 21-35
- [7] Chlebiš P., Damec V., *Design and control of ZCS Frequency Converter*, Applied Electronics, ZCU Plzeň 2002
- [8] Chlebiš P., Damec V., *ZCS Frequency Converter with a Series Resonant DC-link*, in EDPE 2001, Košice SR, p. 256-260
- [9] Texas Instruments: TMS320F28x documentation, <http://www-s.ti.com/sc/psheets/spru509c/>

G SERIES CONVERTER STABILIZED WIND TURBINE WITH PERMANENT MAGNET SYNCHRONOUS GENERATOR

Stevan Grabic, Nikola Celanovic*, Vladimir Katic, University of Novi Sad, Faculty of Technical Sciences, Novi Sad, Serbia & Montenegro, *ABB Corporate Research, Baden-Dättwil, Switzerland

Abstract: This paper investigates the use of a series connected converter to solve the instability of the grid connected wind turbine with permanent magnet synchronous generator. Using simplified models and mechanical analogies it first introduces the solution of the control problem and then discusses some of its limitations.

Key Words: PMSG, wind turbine, instability, active damping, series converter

1. INTRODUCTION

Unlike synchronous generators in the power plants, which usually have both regulated power input on the mechanical side and damper windings on the electrical side, wind-driven permanent magnet synchronous generators (PMSG) have neither. It is the main goal of this paper to show how a series connected converter from Fig. 1, can stabilize such a system.

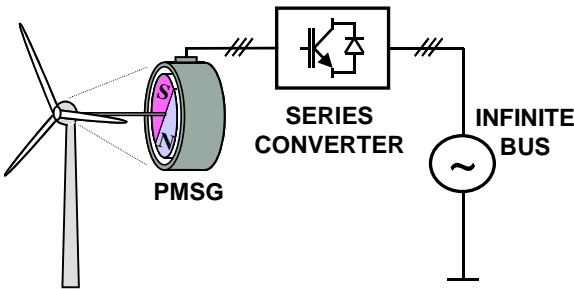


Fig. 1. Wind turbine driven PMSG connected to the infinite bus through series converter.

The study will focus on the simplified model from Fig. 2 where the synchronous generator is modelled by a three-phase voltage source u_{EMF} and the synchronous inductance x_S . The amplitude of the voltage source u_{EMF} equals the generator speed n . The series converter and the grid are modelled as two additional three-phase voltage sources¹.

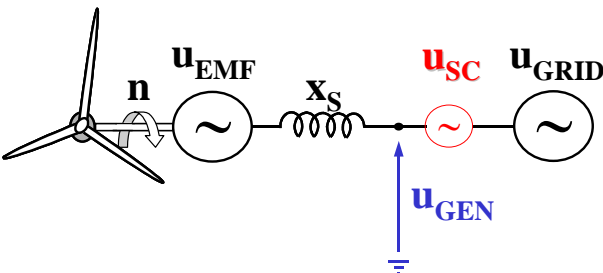


Fig. 2. Simplified representation of the system.

For the practical application of this approach the voltage rating (i.e. power rating) of the series converter should not exceed 20% of the generator rating. This limits the control authority of the series converter to provide only the dynamic phase shift θ_{SC} between the generator and the grid voltage.

Equations (1), (2) and Table 1 illustrate the relationship between the voltage rating of the series converter and its capability to change the phase of the grid voltage.

$$u_{SC} = u_{GEN} - u_{GRID} = \sin(\omega t + \theta_{SC}) - \sin(\omega t) = 2 \cos\left(\frac{\theta_{SC}}{2}\right) \cos\left(\omega t + \frac{\theta_{SC}}{2}\right) \quad (1)$$

$$|\theta_{SC}| = 2 \cdot a \cos\left(\frac{|u_{SC}|}{2}\right) \quad (2)$$

Table 1. Series converter voltage and the corresponding maximum phase shift.

$ u_{SC} $ (p.u.)	$ \theta_{SC} $ (deg)
0.05	2.9
0.10	5.7
0.15	8.6
0.20	11.5

Finally, Fig. 3 illustrates the phase shift in the generator that results from the use of the series converter. How to control the series converter voltage, respectively the phase shift in the grid voltage in order to achieve the desired stabilizing effect is the topic of the following sections.

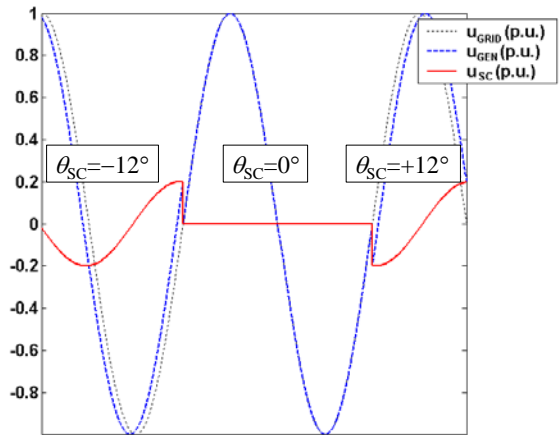


Fig. 3. Phase shift in the generator voltage that can be achieved with 20% series converter.

2. LOW FREQUENCY MODEL OF THE SYSTEM

Equation 3 shows the normalized steady state power angle characteristic of the system from Fig. 2. Because wind power plant mechanical time constant τ_{mech} is orders of magnitude larger than the electrical time constant τ_{el} , the steady-state power-angle characteristic (3) can be used to construct the dynamic model valid for the low frequency range.

$$p_{el} = \frac{|u_{EMF}| \cdot |u_{GEN}|}{x_S} \sin(\theta + \theta_{SC}) \quad (3)$$

¹ All the models in this paper are normalized

In this system the speed of the generator changes very little and the series converter does not influence the generator voltage, therefore it is valid to assume $|u_{EMF}| = |u_{GRID}| = 1$ in order to write the moment equation (4). Equations (5)-(7) represent the mechanical equations of the system, and

Fig. 5 contains the simulation diagram of the whole model (4)-(7).

$$m_{el} = \frac{p_{el}}{n} = \frac{\sin(\theta + \theta_{SC})}{x_S} \quad (4)$$

$$m_{mech} = \frac{v_{wind}^3}{n} \quad (5)$$

$$\tau_m \frac{dn}{dt} = m_{mech} - m_{el} \quad (6)$$

$$\frac{1}{\omega_{GRID}} \frac{d\theta}{dt} = n - 1 \quad (7)$$

Fig. 4 compares the simulation results of the simplified and detailed model of the system described in the Appendix.

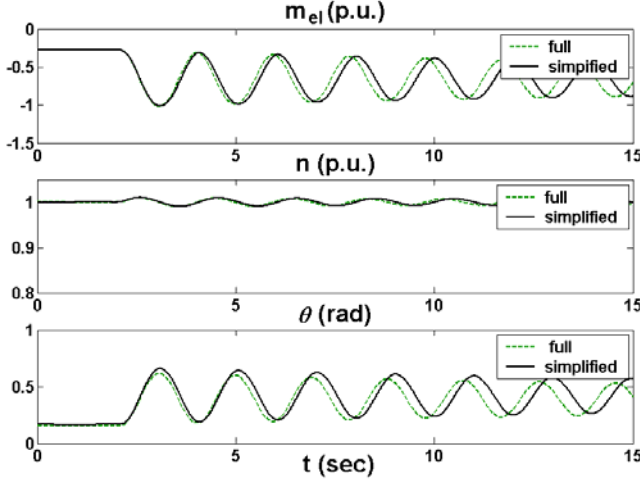


Fig. 4. Response of the grid connected PMSG to the step change in the wind speed.

The system response to the step change in wind speed is oscillatory with very little damping. The differences in the simulation results from the two models are due to the approximations used. Nevertheless, the simplified model contains the insight necessary to develop the stabilizing controller.

3. SOLUTION OF THE DAMPING PROBLEM

Fig. 6a shows polyphasor form of the simplified model from Fig. 2. The mechanical equivalent of the system from

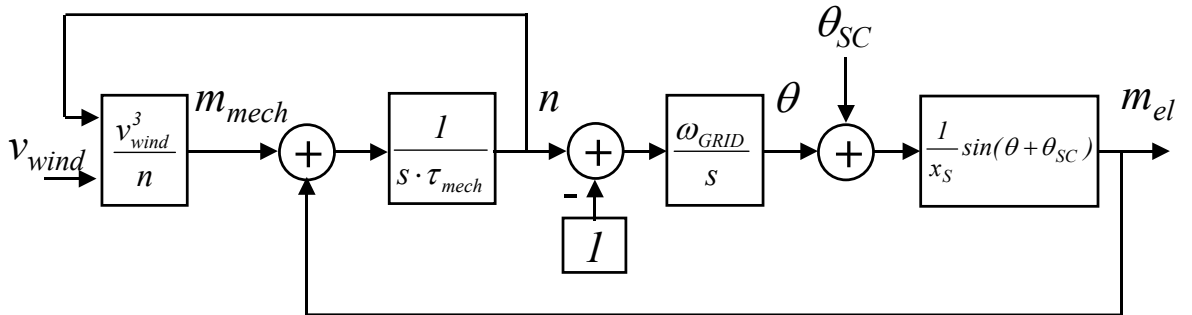


Fig. 5. Simulation diagram of the simplified model.

Fig. 6b. consists of the linear spring $f_{spring} \approx x$ connected between the infinite support (IS) and inertia J. In the steady state $\omega = \omega_{IS}$ and $m_{mech} = m_{spring}$. A step change in the mechanical torque causes this system to oscillate at its natural frequency, quite similar to the original electromechanical model. The form of the torque of the spring (8) is the same as (4).

$$m_{spring} \approx \sin(\theta). \quad (8)$$

Fig. 7a, introduces linear damper $f_{DMP} \approx -\frac{dx}{dt}$. The torque component of the linear damper m_{DMP} is proportional to the time change of the distance between the damper terminals

$$\begin{aligned} m_{DMP} &= -k_{DMP} \cdot \frac{d}{dt} \left(2 \cdot \sin \frac{\theta}{2} \right) = \\ &= -k_{DMP} \cdot \cos \left(\frac{\theta}{2} \right) \cdot \frac{d\theta}{dt} \end{aligned} \quad (9)$$

In order to introduce the damping torque into the original system the torque component in (4) resulting from series converter should equal the mechanical torque component m_{DMP} from (9).

The torque component of the series converter, m_{SC} can be derived by linearizing (4),

$$m_{el} = \frac{1}{x_S} \sin(\theta + \theta_{SC}) = \frac{1}{x_S} \sin(\theta) + \theta_{SC} \cdot \frac{1}{x_S} \cos(\theta), \quad (10)$$

$$m_{SC} = \theta_{SC} \cdot \frac{1}{x_S} \cos(\theta). \quad (11)$$

Equalizing (9) and (11) results in the expression for the phase shift angle needed to achieve the damping effect equivalent to the damping of the linear damper.

$$\theta_{SC} = -x_S k_{DMP} \cdot \frac{\cos(\frac{\theta}{2})}{\cos(\theta)} \cdot \frac{d\theta}{dt}. \quad (12)$$

For the PMSG in question from no load to full load condition $\cos(\frac{\theta}{2}) / \cos(\theta) \approx 1$ which allows further simplification of (12).

Finally, substituting (7) results in the very simple expression for phase shift angle needed from the series converter

$$\theta_{SC} = -k_{DMP} \frac{d\theta}{dt} = -k_{DMP} \cdot \omega_{GRID} \cdot (n-1). \quad (13)$$

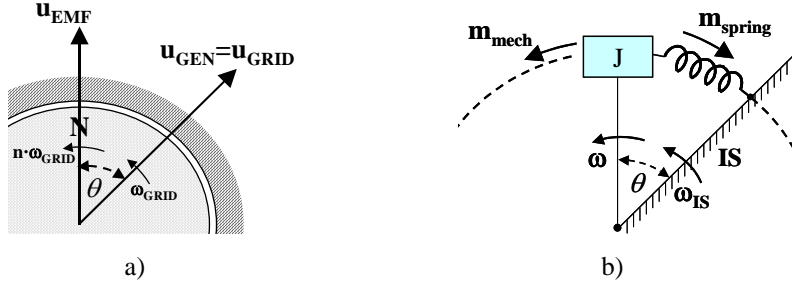


Fig. 6. Grid connected PMSG. a) Polyphasor representation. b) Analogous mechanical representation

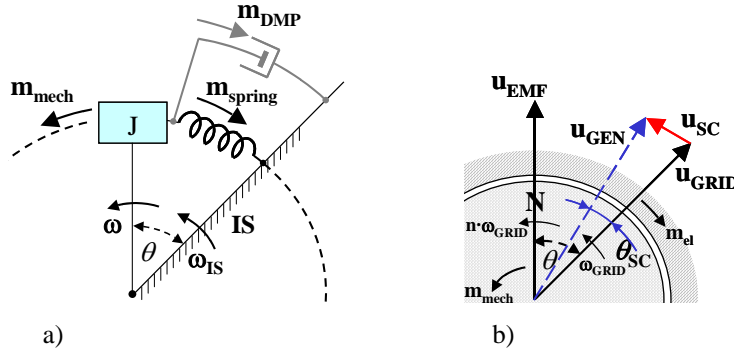


Fig. 7. Effect of the damping. a) Mechanical system. b) Polyphasor representation of the PMSG connected to the grid through series converter.

The simplified model neglects the system electrical dynamics in order to highlight dynamic properties at the frequencies where the slow mechanical time constant is dominant. Now, Fig. 8 shows location of the poles of the linearized close loop system model from the Appendix when the damping factor, k_{DMP} is increased from 0 to 0.9.

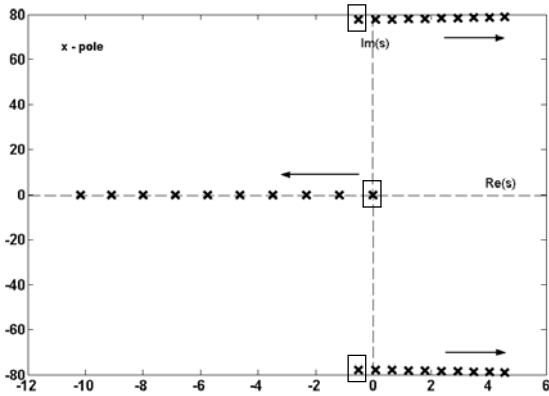


Fig. 8. Location of the poles of the linearized model for different damping factors.

The one real and a pair of complex poles within squares are the poles of the open loop system, $k_{DMP} = 0$. Imaginary part of the complex poles equals ω_{GRID} . The fact that even for low values of the damping factor the poles shift to right half plane indicate the possible stability issues with the proposed controller.

5. SIMULATION RESULTS

The simplified model has provided insight how to control the phase shift introduced by the series converter, but due to

many simplifying assumptions the more complete model from the Appendix can better verify the performance of the controller. Simulations in dq reference frame require implementation of the grid voltage phase shift (A.7), which can be written in the form of linear transformation of rotation

$$\begin{bmatrix} u_{GENd} \\ u_{GENq} \end{bmatrix} = \begin{bmatrix} \cos(\theta_{SC}) & -\sin(\theta_{SC}) \\ \sin(\theta_{SC}) & \cos(\theta_{SC}) \end{bmatrix} \begin{bmatrix} u_{GRID} \\ u_{GRID} \end{bmatrix}. \quad (14)$$

From there the voltage of the series converter can be expressed (15). Finally, Fig. 9 shows the full model of the system. As expected (from the analysis in the previous section) the system was unstable even for very small values of damping coefficient, k_{DMP} . Fortunately the low pass filter (LPF) in the feedback path is enough to prevent the excitation of the system at the grid frequency.

$$\begin{bmatrix} u_{SCd} \\ u_{SCq} \end{bmatrix} = \begin{bmatrix} u_{GENd} \\ u_{GENq} \end{bmatrix} - \begin{bmatrix} u_{GRIDd} \\ u_{GRIDq} \end{bmatrix} = \begin{bmatrix} \cos(\theta_{SC}) - 1 & -\sin(\theta_{SC}) \\ \sin(\theta_{SC}) & \cos(\theta_{SC}) - 1 \end{bmatrix} \begin{bmatrix} u_{GRIDd} \\ u_{GRIDq} \end{bmatrix}. \quad (15)$$

The final results from Fig. 10 show the stable system with several different values of the damping coefficient, k_{DMP} . Clearly, higher damping factors require higher voltage from the series converter, and there is a trade-off between the desired level of damping and the power rating of the series converter. Nevertheless, 20% or even lower rated series converter promises quite good performance.

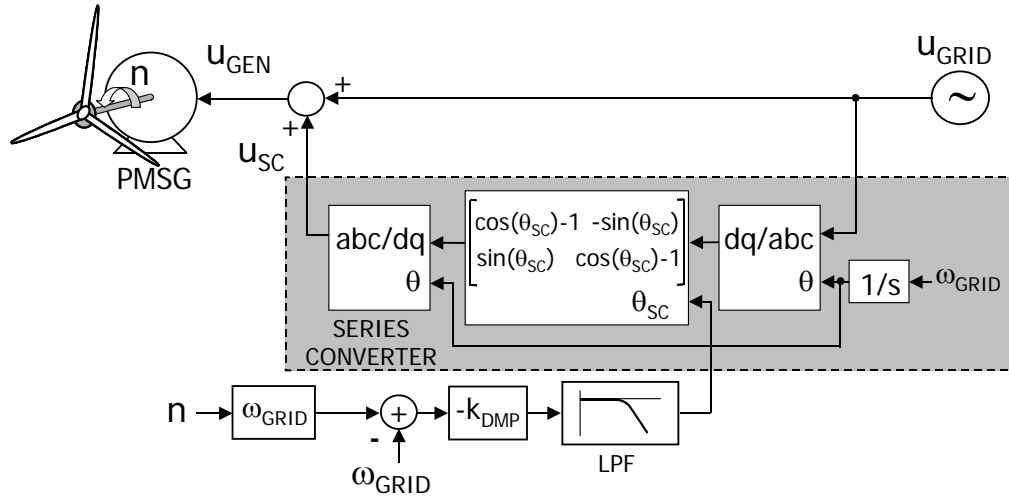


Fig. 9. Control diagram of the series converter stabilized wind turbine with PMSG.

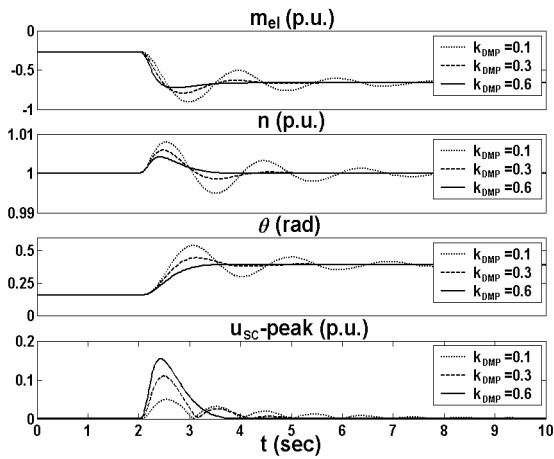


Fig. 10. Response of the actively damped PMSG to the step change in the wind speed.

6. CONCLUSION

This paper has shown that the series converter with less than 20% of the system rating can provide an effective way to damp the grid connected wind turbine with PMSG. The modelling approach from this paper can be used as a starting point in further investigation of this complex nonlinear system.

7. ACKNOWLEDGMENT

Many thanks to ABB Switzerland for supporting this work through summer internship program and in other ways.

8. REFERENCES

- [1] Hau E., *Wind-turbines*, Springer-Verlag, New York, 2000.
- [2] Dubois M. R., *Review of Electromechanical Conversion in Wind Turbines*, Final Literature Review, April 2000, TU Delft, Nederland.
- [3] Grauers A., *Design of Direct-driven Permanent-Magnet Generators for Wind turbines*, Ph.D. Thesis, 1996, Chalmers University, Goteborg, Sweden.
- [4] Grauers A., Lindskog A., "PM Generator with Series Compensated Diode Rectifier", Nordic Workshop on

Power and Industrial Electronics (NORpie'2000), Aalborg, Denmark, 13-16 June 2000, Proceedings pp. 59-63.

- [5] Fitzgerald A E., Kingsley Jr. C., Umans S., *Electric Machinery*, McGraw-Hill Book Co, 1985.
- [6] Bühler H., *Einführung in Die Theorie Geregelter Drehstromantriebe*, Birkhäuser Verlag Basel und Stuttgart, 1977.
- [7] William W. S., *Theory And Problems of Mechanical Vibrations*, Schaum's Outline Series, 1964.

Appendix

Normalized model of the PMSG:

$$\tau_{el} \frac{di_d}{dt} = -r_s i_d + x_s i_q n + u_d \quad (\text{A.1})$$

$$\tau_{el} \frac{di_q}{dt} = -r_s i_q - x_s i_d n - \psi_{pm} n + u_q \quad (\text{A.2})$$

$$\tau_m \frac{dn}{dt} = \psi_{pm} i_q + m_{mech} \quad (\text{A.3})$$

$$\frac{1}{\omega_s} \frac{d\theta}{dt} = n - 1 \quad (\text{A.4})$$

$$m_{mech} = \frac{v_{wind}^3}{n} \quad (\text{A.5})$$

Controller model:

$$\theta_{SC} = -k_{DMP} \cdot \omega_s \cdot (n - 1) \quad (\text{A.6})$$

$$u_d + j \cdot u_q = (u_{GRIDd} + j \cdot u_{GRIDq}) \cdot e^{j(\theta + \theta_{SC})} \quad (\text{A.7})$$

Model parameters:

$$\omega_{GRID} = 77.6 \text{ rad/s}$$

$$r_s = 3.8e^{-3} \text{ p.u.}$$

$$x_s = 0.61 \text{ p.u.}$$

$$\psi_{pm} = 1.06 \text{ p.u.}$$

$$\tau_{mech} = 11.5 \text{ s}$$

$$\tau_{el} = 7.8 \text{ ms}$$

A NOVEL POWER INVERTER FOR SWITCHED RELUCTANCE MOTOR

Željko Grbo, Slobodan Vukosavić*, University of Novi Sad, Faculty of Technical Sciences, Novi Sad, * Faculty of Electrical Engineering, Beograd, Serbia & Montenegro

Abstract: In numerous drive applications, the switched reluctance motors (SRM) outperform conventional AC and DC drives. Although apparently simpler, the SRM drives are nowadays more complex and expensive than their conventional AC drives counterparts. That is the reason SRM have not found wider acceptance. This paper presents a new simple inverter topology for SRM. One of its most significant advantages is that both magnetizing and demagnetizing voltage may reach the DC-bus voltage level while being contemporarily applied during the conduction overlap in the SRM adjacent phases. At the same time, the voltage stress across the power switches equals the DC-bus voltage. This paper is supported with experimental results obtained with a 6/4 - switched reluctance motor

Key Words: switched reluctance motor, inverter.

1. INTRODUCTION

Switched reluctance motor consists of salient poles stator with concentrated windings on each pole and salient poles rotor with no windings or magnets at all. Energizing the stator poles in an appropriate way allows a continuous and controllable rotor movement, [1]. In Fig.1 the operation of a 6/4 motor is presented. The principle of switched reluctance motor is known since 19. century, but only the advent of the power semiconductor switches started strenuous research activity on this type of motor drives. The main advantages of switched reluctance motor are their rugged construction and a low cost. Disadvantages include a high acoustic noise, a large torque ripple and the use of an uncommon power converter topology.

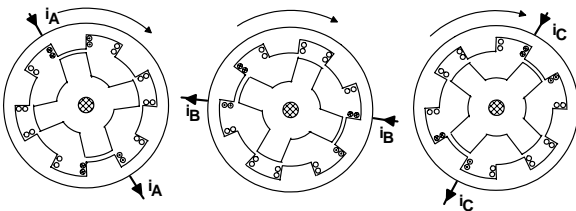


Fig. 1. Movement of a 6/4 SRM.

The torque ripple and noise can be reduced by means of advanced control strategies for the phase current profiling, [2], [3], [4] and by a particular mechanical design. Switched reluctance motors have not yet found broad acceptance. Significant reason is uncommon power converter. There are numerous power converters for switched reluctance motor but there is not yet a simple, rugged, low cost and high performance inverter circuit. Based on the motor requirements, this paper presents a new topology for the switched reluctance motor. In Section 2, functional requirements for SRM inverter are defined and some typical power topologies are described. In Section 3, the new inverter circuit is proposed. Experimental verification of the proposed circuit are presented in Section 4. Conclusions are given in Section 5.

2. SRM INVERTER REQUIREMENTS

In light of the torque production, it is possible to formulate basic requirements for the SRM drive power circuit.

a) For the purpose of the phase current control, it is necessary to modulate the phase voltage. This is especially important at low speed, when the motor back-emf is low.

b) The voltage gain of the inverter should be maximum possible in order to extend the constant power operation mode and increase the top speed.

c) Large fall time of phase current result in negative torque and this time can be reduced if demagnetizing voltage is sufficiently high.

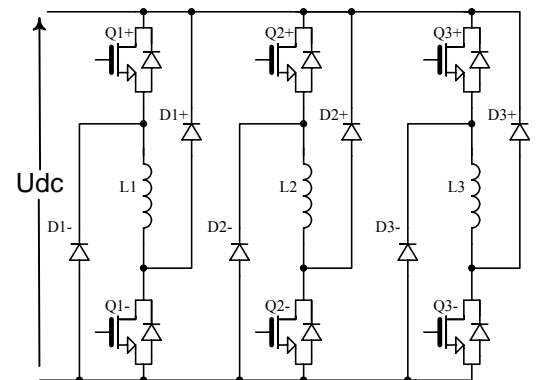
d) It is necessary, at the same time, to control current in one phase and force demagnetizing of some other phase of motor. This is crucial for reduction of torque ripple.

e) Inverter has to be single rail in order to reduce the voltage stress across the semiconductor switches.

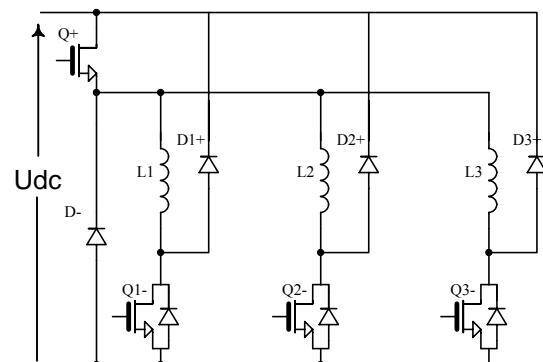
f) The power converter must not impose bifilar windings or rely upon the motor construction.

g) A low number of semiconductor switches is required.

In literature [5], [6] a comparative evaluation of existing SRM inverter topologies is performed. According to the analysis, the two most promising inverter circuits are asymmetrical half bridge inverter and the Miller inverter. These circuits are presented in Fig.2.



(a)



(b)

Fig. 2. Typical inverters for SRM. (a) Asymmetrical half bridge inverter. (b) Miller inverter

Phase current in asymmetrical half bridge inverter is controlled selecting from three possible states:

i) Both switches in a phase lag are on, and phase is energized from power supply (magnetizing).

ii) Both switches in a phase lag are off. Phase current commutates to the diodes and decay rapidly (demagnetizing).

iii) Only one of the switches is off. The voltage across winding is near zero and phase current decays slowly (freewheeling).

Each phase is controlled independently and by proper selection of phase states it is possible to satisfy all the functional requirements, but the number of semiconductor switches is large and cost of this inverter is high.

In order to reduce number of switches, Miller inverter is derived.

In each phase the three switching states are available:

i) Both the Q+ switch and switch in phase lag are on (magnetizing).

ii) Switch Q+ is off and switch in phase lag is off. Phase current flows through diode D- and diode in appropriate phase lag and phase current decays rapidly (demagnetizing).

iii) Switch Q+ is off. The voltage across phase winding is near zero and decays slowly (freewheeling).

The main disadvantage of Miller inverter is that motor phases can not be controlled independently. When the switch Q+ is on, the forced demagnetization of any of the phases is not feasible. It is shown, [5], that demagnetizing voltage in Miller inverter reduces to one half of power supply voltage.

Other topologies proposed up to now suffered similar control insufficiencies, [5], [6], or required an unacceptable rating of semiconductor switches.

3. PROPOSED CIRCUIT

The novel inverter topology is presented in Fig.3. As in the case of asymmetrical half bridge and Miller inverter, an inverter for a 6/4 switched reluctance motor is presented.

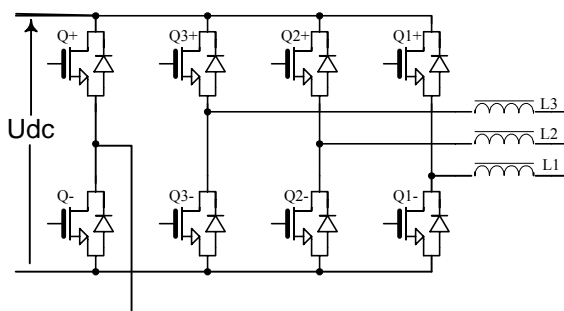


Fig.3. The new inverter.

Notice, though, that conclusions drawn hereafter may be extended to motors with the other number of stator and rotor poles.

The inverter consists of four typical half bridge lags. In the case of N phase motor inverter consist of N+1 half bridge lag. One inverter lag (Q+,Q-) is common for all phases. The switching states related to the L1 winding are:

A) Magnetizing phase.

A1) Q1- and Q+ are on, Fig.4(a) (positive L1 flux).

A2) Q1+ and Q- are on, Fig.4(b) (negative L1 flux).

Notice at this point the two possible directions of the phase current. In both A1 and A2 switching states, full bus voltage is available across the winding.

B) Demagnetizing phase. Q- is on (A1 magnetizing) or Q+ is on (A2 magnetizing). The switches in off-going phase lag are off. Phase current commutates to body diodes and decay rapidly. In Fig.4(c) is presented demagnetization of phase 1 in the case of magnetization with A1 method. During demagnetization stored energy in the off-going phase is returned to the power supply and on-going phase.

C) Freewheeling. The winding can be short-circuited either turning off switches (Q+,Q-) or (Q1+,Q1-). Phase current decay slowly. This state is presented in Fig.4(d), in the case of magnetization using A1 method and turning off lag (Q1+,Q1-).

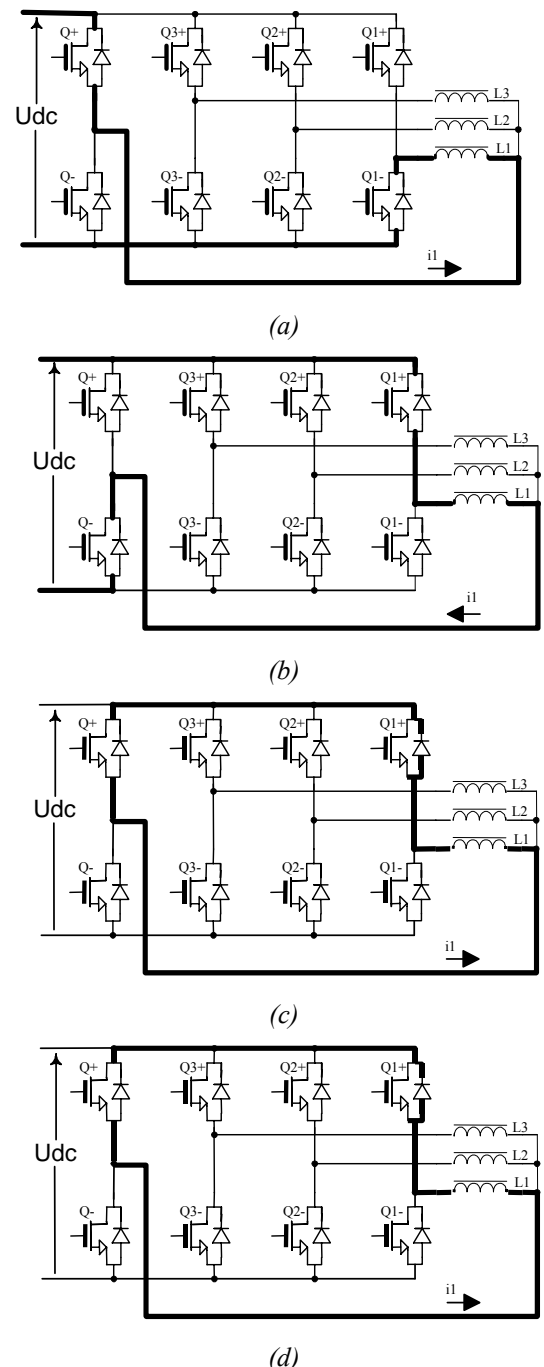


Fig.4. Switching states of phase 1. (a) Magnetization (A1 method). (b) Magnetization (A2 method) (c) Demagnetization. (d) Freewheeling.

During low speed operation phase current has to be limited or controlled in order to reduce torque ripple. This can be done alternating between states A and B or between

states A and C. It is preferable to use states A and C because this results in lower switching frequency for the same current ripple.

It is important to show that at the same time is possible to control current in on-going phase and make forced demagnetization in off-going phase. This is illustrated in Fig.5.

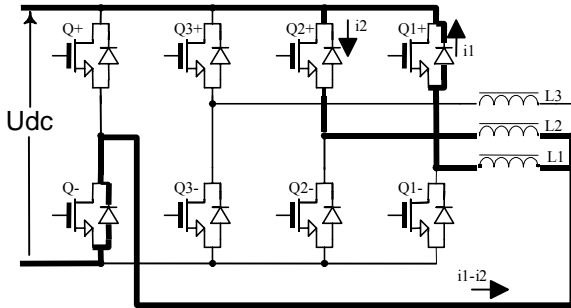


Fig.5. Simultaneous conduction of adjacent phases.

In Fig.5 it is assumed that phase 1 is off-going and phase 2 is on-going. It can be observed that currents of two adjacent phases have to have opposite direction. In the case of three phases switched reluctance motor this results in bipolar phase current. In Fig.6 phase voltages and currents for all three phases, during one complete rotor revolution, are presented. High speed operation is assumed.

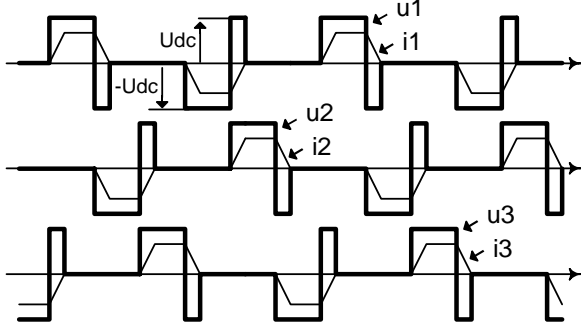


Fig.6. Phase voltages and currents (one complete revolution).

4. EXPERIMENTAL RESULTS

Proposed inverter circuit is investigated experimentally. In experiments a 6/4 motor is used. Motor has following characteristics:

- Number of phases 3
- Stator pole width 36°
- Rotor pole width 36°
- Airgap 0.3mm
- Rotor length 50.2mm
- Resistance per phase 4Ω

Stator winding inductance profile versus rotor position is observed experimentally at low stator current and presented in Fig.7.

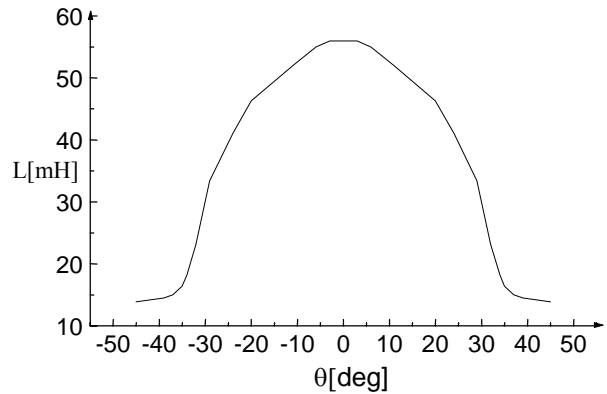
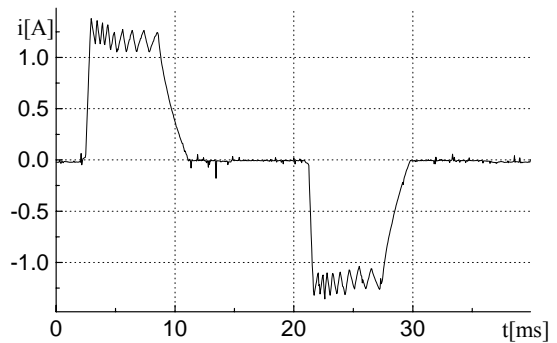


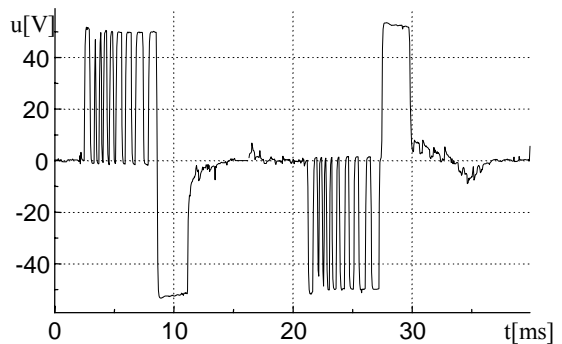
Fig.7. Unsaturated stator phase inductance versus rotor position

In Fig.8 the measured waveforms of phase current and phase voltage are shown. During experiments input voltage was 50V and hysteresis current regulator is used.

It is easy to note bipolar character of phase current. Also, from phase voltage diagrams is clear that regulation is done alternating between states A and C.



(a)



(b)

Fig.8. Current control. (a) Phase current. (b) Phase voltage

5. CONCLUSION

The switched reluctance motor drives went through significant development since the advent of the semiconductor devices. Simple motor construction did not yet result in a simple, cost effective power converter, and the SRM therefore did not find wider application field. In order to overcome that problem this paper proposes a novel,

advanced power inverter topology. The main characteristics of new inverter are:

All of the available bus voltage used in both the magnetizing and demagnetizing, even during the overlap of the adjacent phases conduction.

$2(N+1)$ semiconductor switches (N is the number of the stator phases).

Simple gates drive (IC driver with bootstrap supply).

Voltage rating of all switches does not exceed the bus voltage. Current rating of all switches is equal to maximum phase current.

Simple wiring.

In the case of three phases SRM bipolar phase current.

In comparison to asymmetrical half bridge converter this converter is superior because of $2(N-1)$ smaller number of semiconductor switches, simpler wiring and simpler driver circuit.

In comparison to Miller inverter this circuit is superior because for the same number of semiconductor switches there is not limitation in demagnetizing voltage.

In comparison to voltage source inverter for induction motor the new inverter has two more switches, but total cost of motor and power converter can be comparable. It is believed that new inverter will open new fields for applications of switched reluctance motor drives.

6. REFERENCES

- [1] P. J. Lawrenson et al., "Variable-speed switched reluctance motors", IEE Proc., vol.127, pt.B, no.4, pp.253-265, July 1980.
- [2] R. S. Wallace, D. G. Taylor, "A balanced commutator for switched reluctance motors to reduce torque ripple", IEEE Trans. Power Electronics, vol.7, no.4, pp.617-626, October 1992.
- [3] I. Husain, M. Ehsani, "Torque ripple minimization in switched reluctance motor drives by PWM current control", IEEE Trans. Power Electronics, vol.11, no.1, pp.83-88, January 1996.
- [4] K. Russa, I. Husain, M. E. Elbuluk, "Torque-ripple minimization in switched reluctance machines over a wide speed range", IEEE Trans. Ind. Appl., vol.34, no.5, pp.1105-1112, Sept./Oct. 1998.
- [5] S. Vukosavic, V. Stefanovic, "SRM inverter topologies: a comparative evaluation", IEEE Trans. Ind. Appl., vol.27, no.6, pp.1034-1047, Nov./Dec. 1991.
- [6] M. Barnes, C. Pollock, "Power electronic converters for switched reluctance drives", IEEE Trans. Power Electronics, vol.13, no.6, pp.1100-1111, Nov. 1998.

DESIGN AND SIMULATION OF WORKING IN PARALLEL TRANSISTOR INVERTERS

Georgi Kunov, Elissaveta Gadjeva* Technical University of Sofia, Department of Power Electronics, Sofia, Bulgaria, *Technical University of Sofia, Department of Electronics, Sofia, Bulgaria

Abstract: The development in the manufacturing technologies for power semiconductor devices (MOSFET and IGBT) provides the possibility of producing a variety of power transistor inverters, working at higher frequencies. Several applications require inverters, significantly exceeding in power the possibilities of a single inverter. In the present work, a full-bridge inverter circuit is investigated and a design methodology is developed for parameter calculation of the active and the passive components. The validity of the design methodology is confirmed using PSpice simulation. The parallel operation of four inverters is modeled and simulated. The obtained results prove that uniform loading is achieved, which allows to reach a load power equal to the power of a single inverter multiplied by the inverter number.

Key Words: Power Electronics, Transistor Inverters, Induction Heating

1. INTRODUCTION

The theory of inverters for induction electro-technologies was developed and it acquired its complete form with the introduction of the thyristor semiconductor devices. A number of investigations and monographs are devoted to this topic [1,2,3]. Various electrotechnologies need power supplies at high frequencies. Transistor inverters are widely used in these cases.

The basic principles of the electrical energy conversion are borrowed from the thyristor ones. Two types of inverters are most widely applied: the current-source inverter and the resonant inverter. The current-source inverter has a parallel resonance circuit. It is characterized by a lower ratio of the maximal transistor current to the DC supply current. However, the specific features of the electromagnetic processes require the connection of an additional diode in parallel with the transistor [4]. This leads to worsening the circuit efficiency. The resonant inverters [5] usually work with connected in series compensation of the inductive character of the load. The sinusoidal transistor current allows decreasing the switching losses. However, this mode of operation is characterized by a higher ratio of the maximal transistor current to the DC supply current.

The investigated in the present paper full-bridge parallel resonant inverter is characterized by a relatively good ratio of the maximal transistor current to the DC supply current and decreased switching losses in the turn-on interval (ZVS).

2. ONE BRIDGE INVERTER: DESIGN METHODOLOGY AND SIMULATION

The inverter circuit is shown in Fig. 1a. The induction electro-technological device is usually represented by an equivalent circuit, consisting of inductance L_r and a resistor R_r , connected in series. The power factor of this load is lower ($\cos(\varphi) \approx 0.1$). The capacitor C_r is of value that allows compensating entirely the reactive energy of the L_r inductance. In this way the parallel resonant circuit works at

its resonant frequency. The inductance L_s is connected in series with the parallel resonant circuit. In this case it is separated into two equal parts (L_{s1} and L_{s2}).

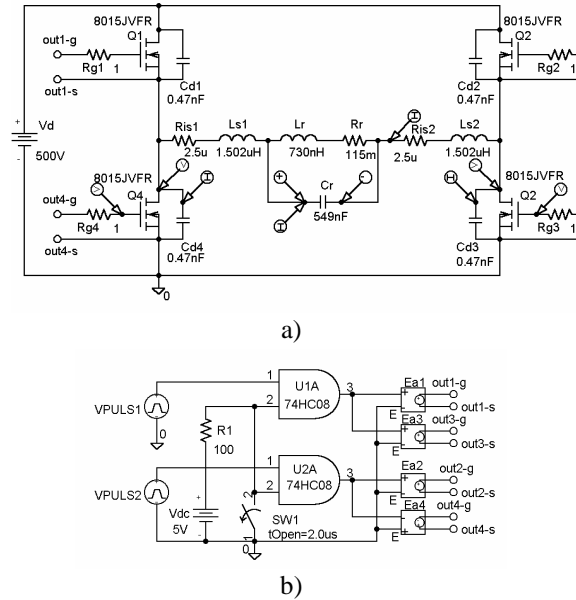


Fig. 1. The inverter circuit

At sufficiently high frequencies, the wires connecting the parallel compensated load and the inverter can play the role of these inductances.

The resistors R_{s1} and R_{s2} which are connected in series are introduced due to the specialties in the work of the simulation program, which does not allow the direct connection of an inductance element with a voltage source.

Since the current I_{Ls} in the inverter diagonal and the voltage V_{Cr} on the resonant load are of the same phase, the parallel resonant circuit can be considered as a voltage inverter of an active-inductive load type in the diagonal (a connection of L_s and R_{eo} in series).

2.1. Design methodology

The dependencies between the circuit currents, voltages and the passive element values are obtained by the first harmonic method.

In the case of a power supply voltage $V_d = 500V$, the two-polar rectangular voltage on the bridge diagonal is replaced by sinusoidal one. The effective value of this voltage $V_{d(1)}$ is determined according to the spectral Fourier analysis theory.

$$V_{d(1)} = \frac{4V_d}{\pi\sqrt{2}} = 450.16V$$

The dependencies between the values as well as between the phases of the basic inverter currents and voltages are illustrated by the vector diagram shown in Fig. 2.

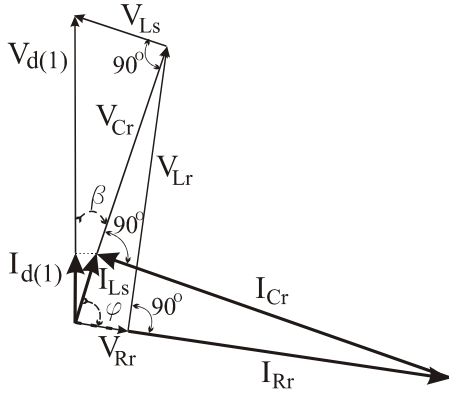


Fig. 2. The vector diagram

On the basis of this vector diagram, an inverter design methodology is developed as shown in Table 1. Calculations are performed for two powers: $P=15\text{kW}$ and $P=60\text{kW}$. The following data have been preliminary assumed:

- operation frequency: $f=250\text{ kHz}$;
- load factor: $\cos(\varphi) = 0.1$;
- supply voltage: $V_d=500\text{V}$.

Table 1. The inverter design methodology

No	formulae	15kW	60kW
1	$I_{d(1)} = \frac{P}{V_{d(1)}}$	33.32A	133.28A
2	$I_{s(1)} = \frac{I_{d(1)}}{\cos(\beta)}$	36.06A	144.26A
3	$V_{Ls(1)} = V_{d(1)} \sin(\beta)$	172.27V	172.27V
4	$L_s = \frac{V_{Ls(1)}}{\omega I_{s(1)}}$	3.041 μH	0.760 μH
5	$I_{Cr} = I_{s(1)} \text{tg}(\varphi)$	358.8A	1435.16A
6	$V_{Cr} = V_{d(1)} \cos(\beta)$	415.8V	415.8V
7	$C_r = \frac{I_{Cr}}{\omega V_{Cr}}$	549nF	2.197 μF
8	$I_{Lr} = I_{Rr} = \frac{I_{s(1)}}{\cos(\varphi)}$	360.6A	1442.6A
9	$V_{Lr} = V_{Cr} \sin(\varphi)$	413.72V	413.72V
10	$L_r = \frac{V_{Lr}}{\omega I_{Lr}}$	730nH	183nH
11	$V_{Rr} = V_{Cr} \cos(\varphi)$	41.58V	41.58V
12	$R_r = \frac{V_{Rr}}{I_{Rr}}$	115m Ω	28.82m Ω
13	$R_{eo} = \frac{L_r}{R_r C_r}$	11.56 Ω	2.89 Ω
Checking the calculation accuracy			
14	$\beta = \arctg\left(\frac{\omega L_r}{R_{eo}}\right)$	22.45°	22.44°
15	$f = \frac{1}{2\pi} \sqrt{\frac{1}{L_r C_r} - \left(\frac{R_r}{L_r}\right)^2}$	250.15kHz	249.97kHz

The angle β defines the inductance type of the current in the inverter diagonal. Its value has to be sufficient for realizing ZVS by turn-on of the transistors. The determination of β is accomplished by its time-domain equivalent t_β :

$$t_\beta \geq (4 \div 5)(t_r + t_f) ,$$

where t_r is the rise time and t_f is the fall time of the transistors.

The value $t_\beta=250\text{ns}$ has been accepted in the calculations. Hence $\beta = t_\beta \cdot f \cdot 360^\circ = 22.5^\circ$

An appropriate transistor type for the case in particular is APT8015JVFR (producer Advanced Power Technology). Based on its *Spice* model [6] shown in Fig. 3, a simulation of the inverter is performed using the calculated values of L_s , C_r , L_r and R_r for the power 15kW.

2.2. Circuit Simulation Using OrCAD PSpice

The control pulses of the transistors Q1 ÷ Q4 are formed by the circuit shown in Fig. 1b. The following simulation settings are defined:

- Menu Analysis/Setup/Transient:*
- Print Step:* 20ns; *Step Ceiling* 20ns
- Menu Analysis/Setup/Options:*
- ABSTOL=1mA; CHGTOL=1 μC ; PIVREL=1m
- RELTOL=0.025; VNTOL=100mV
- Dependent sources Ea1 ÷ Ea4: GAIN=3.

The parameter values of the control sources are given in Table 2.

```

*SRC=8015JVFR;8015JVFR;MOSFETs N;
*Power>100V; APT 800V 44A 0.15ohm ISOTOP
*SYM=POWMOSN
.SUBCKT 8015JVFR 10 20 30
* TERMINALS: D G S
M1 1 2 3 3 DMOS L=1U W=1U
RD 10 1 70.2M
RS 40 3 4.75M
RG 20 2 3.41
CGS 2 3 13.9N
EGD 12 0 2 1 1
VFB 14 0 0
FFB 2 1 VFB 1
CGD 13 14 10.2N
R1 13 0 1
D1 12 13 DLIM
DDG 15 14 DCGD
R2 12 15 1
D2 15 0 DLIM
DSD 3 10 DSUB
LS 30 40 7.5N
.MODEL DMOS NMOS (LEVEL=1
LAMBDA=341U VTO=3.1 KP=79.5)
.MODEL DCGD D (CJO=10.2N VJ=0.6
M=0.68)
.MODEL DSUB D (IS=183N N=1.5 RS=12.5M
BV=800 CJO=3.16N VJ=0.8 M=0.42 TT=280N)
.MODEL DLIM D (IS=100U)
.ENDS
    
```

Fig. 3. Spice model of the APT8015JVFR

transistor

Table 2. The parameter values of the control sources

	V1	V2	TD	TR	TF	PW	PER
VPULSE1	0V	5V	0s	50ns	50ns	1.55µs	4µs
VPULSE2	0V	5V	2µs	50ns	50ns	1.55µs	4µs

The simulation results for the commutation period of the MOSFET transistors are shown in Fig. 4.

Using these results, the adequateness of the implemented model of the transistor APT8015JVFR can be assessed.

The obtained time-delay $t_{d(off)}^{sim} = 150\text{ns}$ is in accordance with the transistor datasheet: $t_{d(off)} = (97 \div 145)\text{ ns}$.

The calculated values of the time intervals t_r and t_f due to the ZVS existance, are defined by the relationships:

$$t_r = t_f = \frac{\pi}{2} \sqrt{2(C_{oss} + C_d)} = 171\text{ns},$$

where $C_{oss} = (1470 \div 2000)\text{ nF}$ is the output transistor capacitance according to the datasheet.

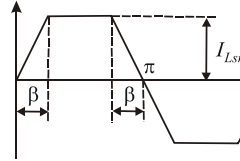
$C_d = 470\text{ pF}$ is the externally connected capacitor between the drain and the source.

A displacement between the turn-on pulses (dead time) is necessary for the normal processing of ZVS:

$$T_{dt} > t_{d(off)} + t_{r/f}$$

This condition is fulfilled by defining the duration of the turn-on pulse in Table 2 ($PW = 1.55\text{ }\mu\text{s}$).

The waveforms of the simulated currents I_{Ls} , I_{Cr} and the voltage V_{Cr} shown in Fig. 5 are in a very good agreement with the calculated values (Table 1). It is seen from the waveform in Fig. 5a that the current I_{Ls} and the voltage V_{Cr} are of the same phase. The current I_{Ls} has a shape near to trapezoidal. It can be approximated as follows:



$$\beta = 22.5^\circ = 0.3927\text{ rad}$$

$$I_{Ls} = \frac{4I_{Lsm}}{\beta\pi\sqrt{2}} \sin(\beta) = \dots$$

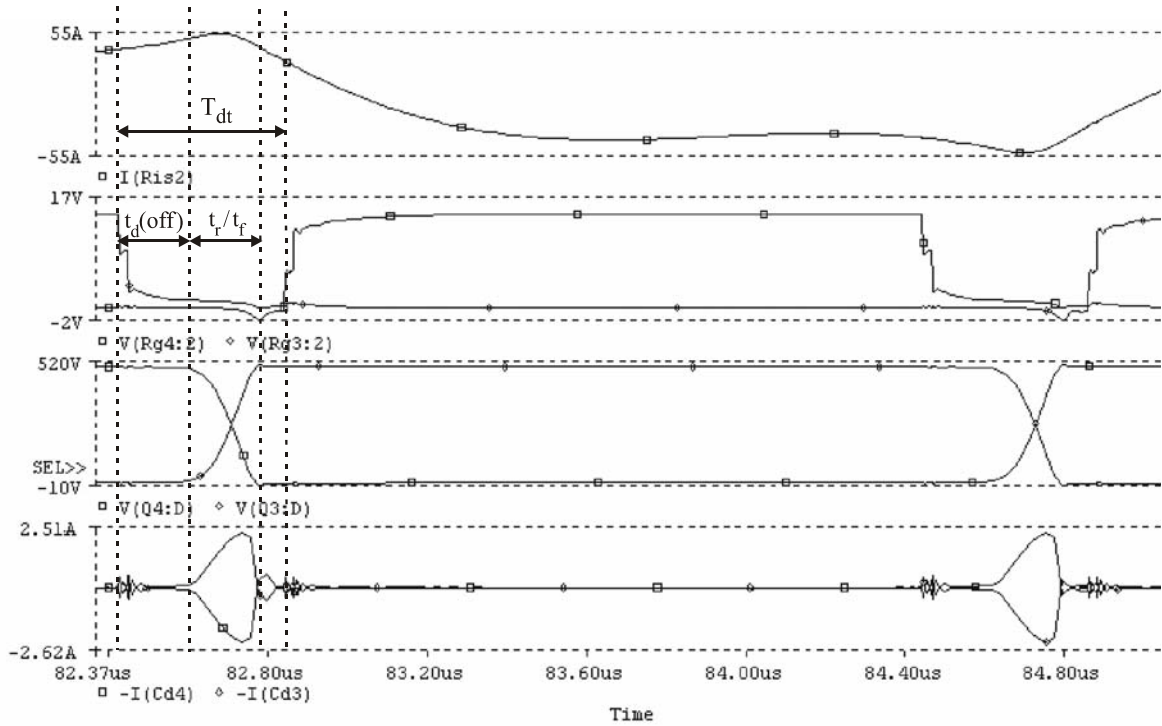


Fig. 4. The simulation results for the commutation period of the MOSFET transistors

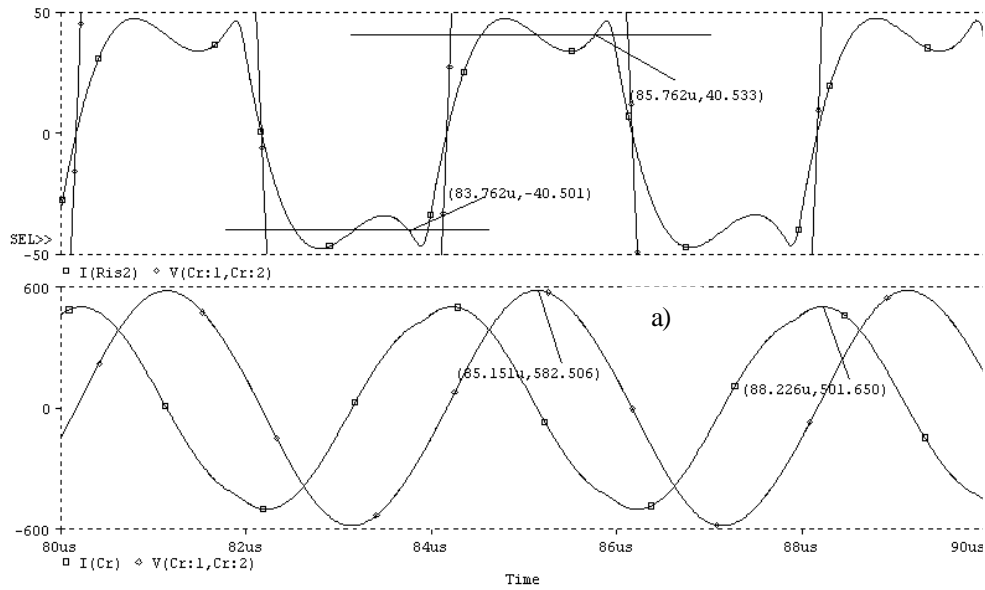


Fig. 5. The waveforms values for the currents I_{Ls} , I_{Cr} , and the voltage V_{Cr}

The maximal values of the current I_{Cr} and the voltage V_{Cr} are marked in Fig. 5b. The corresponding effective value does not differ significantly from the calculated ones (the relative error is of the order of about 1%).

3. WORKING IN PARALLEL INVERTERS

The circuit, consisting of four inverters, working in parallel on a common load (R_r , L_r , C_r), is shown in Fig. 6. The load is calculated for the output power of 60 kW (Table 1). Each of the inverters ensures one a quarter of this power. This condition is realized by the parallel connection according to the load through the inductance L_s connected in series. Its value is four times greater than the calculated value for the power of 60 kW.

The waveforms shown in Fig. 7 illustrate the uniform loading of each inverter. The values of currents $I_{S1} \div I_{S4}$ correspond to the power of 15 kW. The V_{Cr} does not change, as the β angle does not vary. The I_{Cr} current increases four times.

4. CONCLUSIONS

A design methodology is developed for the parameter determination of the full-bridge inverter circuit. A very good agreement between the calculated and simulated results has been achieved. Hence the proposed methodology can be used for an engineering design. The possibility for obtaining higher output power by using of working in parallel full-bridge inverters and for achieving an equal loading of each inverter, is confirmed.

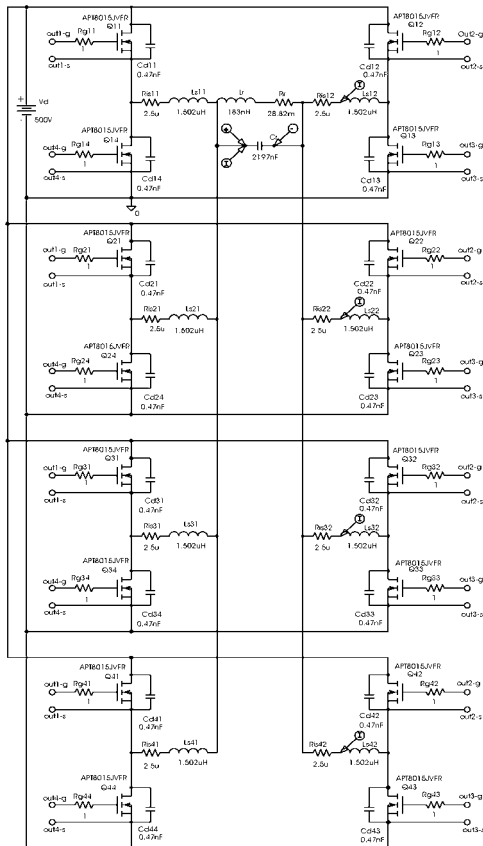


Fig. 6. The circuit of four inverters working in parallel

The obtained in this way effective value of the I_{Ls} current does not differ significantly from the calculated one, presented in Table 1.

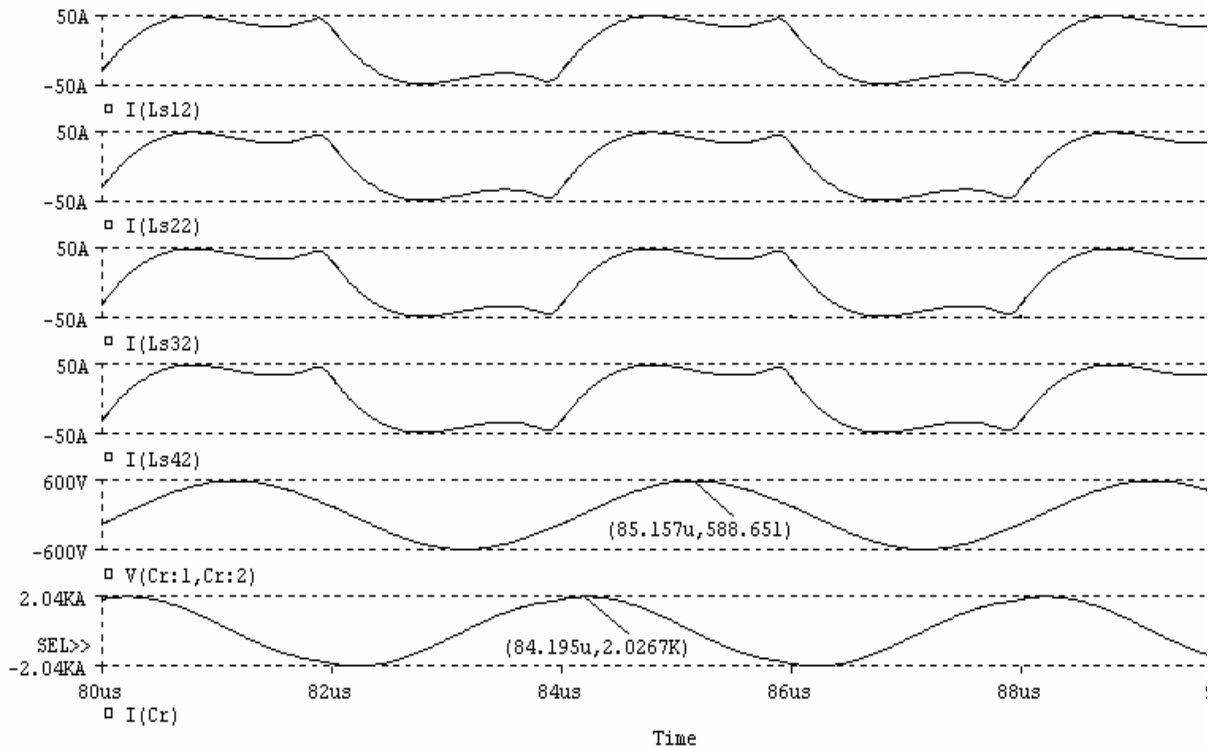


Fig. 7. The waveforms illustrating the uniform loading of each inverter

5. REFERENCES

- [1] E. Berkovich, J. Ivenskii, A. Yoffe, A. Matchak, B. Morgun, "Thyristor converters for higher frequency intended for electrotechnological equipment", Energoatomizdat, St. Peterburg, 1983 (in Russian)
- [2] F. Labrique, G. Segulier, R. Bausiere, "Les Convertisseurs de L'Electronique de Puissance", Vol. 4, "La Conversion Continu-alternatif, Technique and Documentation", Lavoisier, Paris, 1995.
- [3] N. Mohan, T. Underland, W. Robin, Power Electronics, 1989, Wiley & Sons Inc.
- [4] F. Dede, V. Estev, J. Jordan, J. Gonzalez, F. Maset, "On the Design and Control Strategy of High Power, High Frequency Converters for Tube Welding Applications", The Pce Yokohama Conference'93, Yokohama, Japan, April 1993.
- [5] D. Loveless, R. Cook, V. Rudnev, "Considering Nature and Parameters of Power Supplies for Efficient Induction Heat Treating", Industrial Heating, June 1995.
- [6] <http://www.advancedpower.com>

STEADY-STATE ANALYSIS OF POWER CONVERSION SYSTEMS

Armando Bellini, Stefano Bifaretti, Stefano Costantini, University of Rome "Tor Vergata", Electronic Engineering Department, Rome, Italy

Abstract: *The paper presents an interactive program useful to analyse the steady-state behaviour of power systems including static converters. In particular, beginning by a netlist-like description of the system structure and the values of its parameters, the program allows at first the determination of the steady-state values of the system state variables at a prefixed initial instant and, successively, the computation of several features characterizing the steady-state behaviour.*

Key Words: *Simulation of Power Systems, Conversion Systems, Piecewise linearization.*

1. INTRODUCTION

The behaviour of electrical or electromechanical systems including static converters can be analysed using several simulation programs or computation environments. Their utilization is certainly useful when either the dynamic behaviour of the whole system or a phenomenon of short duration must be analysed. On the contrary, when the simulation is performed to characterize the steady-state behaviour of the system, to avoid the analysis of a prolonged transient, a different approach can be used. When only forced commutated converters are present, generally all the commutating instants can be simply determined; so the most convenient approaches make use of a frequency analysis. On the other hand, when some commutations are of natural type (turn-on of diodes, turn-off of diodes or thyristors) the determination of their commutating instants in a frequency analysis framework is quite complex; thus an approach in the time domain becomes convenient.

Various approaches for directly analysing in the time domain the steady-state behaviour of this kind of systems have been already presented in literature since many years [1-10]. Initially the main objective of these approaches was the determination, in a direct way without computing the transient, of both the steady-state values of the state variables, at a prefixed initial instant, and the natural commutation instants of the power semiconductors. Further developments regarded the direct computation of the static characteristics and the direct analysis of the stability.

One of the most formalized and complete approaches was initially presented by Bellini, De Carli and La Cava in 1978 [1] and afterwards developed by De Carli [3] and by Bellini et al. [4-6]. The approach has been used to analyse different conversion systems and has allowed the solution of various problems, for instance: the choice of the most convenient control strategy and modulation technique for induction motor drives, the comparison among different converter structures, the determination and the reduction of the harmonic distortion caused by the conversion system, etc.

The first applications of the analysis method required, for every single problem, the implementation of a dedicated computation program; to avoid this inconvenience, the authors presented a first formulation of a general program [4] useful for different conversion systems. However, the modest availability of memory in DOS environment restricted the

use of the general program to the simulation of systems characterized by a limited number of state variables. Besides, also the graphic interface was not particularly accurate.

The situation deeply modified in the last few years with the coming of 32-bit Windows operating systems and the availability of graphic packages for the development of the computation programs; therefore, the interest in a general interactive program took new vigour. For that reason the authors realized a new version of the general program developed with Delphi. With respect to the previous version, the proposed one presents a new procedure for the calculation of exponential matrices, an enhanced interactivity and a better graphic appearance.

A detailed description of the new program is presented in [10]; the present paper is dedicated to illustrate the procedures used to calculate the mean values and the harmonic coefficients of the most significant circuit variables.

The program was, then, particularized for the study of the voltage and current distortions at the distribution network bus-bars due to the presence of a high power AC/DC converter [11].

2. BASICS OF THE PROPOSED APPROACH

The main peculiarities of the approach concern:

- the piecewise linearization of the system dynamics during a period;
- the mathematical representation of the system behaviour in each time interval;
- the automatic generation of the matrices of the dynamic models;
- the procedures adopted to calculate the transition matrices;
- the determination of the steady-state initial conditions and the timings;
- the determination of mean values and harmonic coefficients.
- the stability analysis.

The paper at first illustrates the methodologies used for the mathematical representation of the system behaviour and to find out the steady-state initial conditions and the timings. A greater attention is subsequently dedicated to illustrate the procedures used for determining the mean values and the harmonic coefficients.

2.1. Mathematical representation of the system behaviour

Power systems including static converters consist of a set of power semiconductors (transistors, diodes, thyristors, GTO's) and other components (capacitors, inductors, transformers, electrical machines) connected according to different configurations. Due to the on-off operation of power semiconductors, the behaviour of the whole conversion system is non-linear; however, it is possible to effect a piecewise linearization by considering the converters as variable topology circuits and by determining, for each conducting state of power semiconductors, an appropriate mathematical model of the whole system; this latter operation

can require suitable simplifying hypothesis. In order to implement simple and efficient computation procedures and to allow an easy interactive employment of the program, it is convenient to choose the same state variables for all the models.

The set of the possible conducting states of the converter is limited; moreover the symmetries of the circuit and the periodicity of its steady-state operation makes possible to limit the analysis to the topologies which occur during an observation interval (t_0, t_0+T_0) , whose duration T_0 is equal to the period (or a sub multiple of the period) of the supply (or output) voltage.

The commutations of power semiconductors subdivide the observation interval in s subintervals, during which the conducting state does not vary; therefore, under generally acceptable hypothesis, in each subinterval the behaviour of the system can be described by a linear time-invariant dynamic model, whose input is characterized by constant or sinusoidal waveforms.

The commutation instants can be subdivided in:

- forced commutation instants, imposed by the control device of the converter and therefore known a priori;
- natural commutation instants depending on the operating conditions of the system and so unknown a priori.

As example, commutation instants due to the turn-on or turn-off of a transistor are forced; on the contrary, commutation instants due to the conduction state change of a diode are natural.

The forced commutation instants subdivide the observation interval in f intervals of predetermined duration; the generic h^{th} interval can include some natural commutation instants and then it can be subdivided in n_h subintervals, of which n_h-1 have unknown duration. So the number of the natural commutation instants, i.e. of the subintervals of unknown duration, is $(s-f)$.

During a generic k^{th} subinterval (t_{k-1}, t_k) , the system is described by the following linear time-invariant model:

$$\dot{\mathbf{x}}(t) = \mathbf{A}_k \mathbf{x}(t) + \mathbf{B}_k \mathbf{u}_k(t) \quad (1)$$

where k is the index identifying the subinterval ($k = 1..s$), \mathbf{A}_k and \mathbf{B}_k are the dynamic and input matrices, $\mathbf{x}(t)$ is the state vector of dimension m (as previously mentioned each model uses the same state variables) and $\mathbf{u}_k(t)$ is the input vector of dimension r_k .

The integration of state equation (1) in subinterval (t_{k-1}, t_k) gives:

$$\mathbf{x}(t_k) = \exp[\mathbf{A}_k (t_k - t_{k-1})] \mathbf{x}(t_{k-1}) + \int_{t_{k-1}}^{t_k} \exp[\mathbf{A}_k (t_k - t)] \mathbf{B}_k \mathbf{u}_k(t) dt$$

To avoid the computation of the convolution integral, it is convenient to modify the structure of the system model taking into account that input vector $\mathbf{u}_k(t)$ is generally composed by segments of constant functions and/or sinusoidal functions of assigned angular frequency ω .

Therefore, by introducing a vector $\boldsymbol{\mu}(t)$, defined as:

$$\boldsymbol{\mu}(t) = \begin{bmatrix} 1 \\ \sin[\omega(t-t_0)] \\ \cos[\omega(t-t_0)] \end{bmatrix}$$

input vector $\mathbf{u}_k(t)$ can be expressed as:

$$\mathbf{u}_k(t) = \boldsymbol{\Gamma}_k \boldsymbol{\mu}(t) \quad (2)$$

where $\boldsymbol{\Gamma}_k$ is a $(r_k \times 3)$ constant coefficient matrix.

In its turn, vector $\boldsymbol{\mu}(t)$ can be considered as the state vector of the following auxiliary system, moving in free evolution:

$$\dot{\boldsymbol{\mu}}(t) = \boldsymbol{\Omega} \boldsymbol{\mu}(t) \quad (3)$$

being

$$\boldsymbol{\Omega} = \begin{bmatrix} 0 & 0 & 0 \\ 0 & 0 & \omega \\ 0 & -\omega & 0 \end{bmatrix} \quad \boldsymbol{\mu}(t_0) = \begin{bmatrix} 1 \\ 0 \\ 1 \end{bmatrix}$$

Aggregating eqs. (1), (2) and (3), the following augmented state model moving in free evolution is obtained:

$$\dot{\boldsymbol{\xi}}(t) = \mathbf{S}_k \boldsymbol{\xi}(t) \quad (4)$$

being

$$\boldsymbol{\xi}(t) = \begin{bmatrix} \mathbf{x}(t) \\ \boldsymbol{\mu}(t) \end{bmatrix} \quad \mathbf{S}_k = \begin{bmatrix} \mathbf{A}_k & \mathbf{B}_k \boldsymbol{\Gamma}_k \\ \mathbf{0} & \boldsymbol{\Omega} \end{bmatrix}.$$

Therefore the value of state vector $\boldsymbol{\xi}(t)$ at the end of subinterval (t_{k-1}, t_k) becomes

$$\boldsymbol{\xi}(t_k) = \boldsymbol{\Phi}_k \boldsymbol{\xi}(t_{k-1}) \quad (5)$$

where

$$\boldsymbol{\Phi}_k = \exp(\mathbf{S}_k \tau_k)$$

and

$$\tau_k = t_k - t_{k-1}$$

denotes the duration of the subinterval.

2.2. Determination of the steady-state initial conditions and the timings

Supposing that all the subintervals durations are known, applying eq. (5) to all the subintervals, we have:

$$\boldsymbol{\xi}(t_0 + T_0) = \boldsymbol{\Phi} \boldsymbol{\xi}(t_0) \quad (6)$$

being

$$\boldsymbol{\Phi} = \boldsymbol{\Phi}_s \boldsymbol{\Phi}_{s-1} \dots \boldsymbol{\Phi}_1$$

Partitioning matrix $\boldsymbol{\Phi}$, eq. (6) can be rewritten as:

$$\begin{bmatrix} \mathbf{x}(t_0 + T_0) \\ \boldsymbol{\mu}(t_0 + T_0) \end{bmatrix} = \begin{bmatrix} \boldsymbol{\phi} & \boldsymbol{\varphi} \\ \mathbf{0} & \boldsymbol{\chi} \end{bmatrix} \begin{bmatrix} \mathbf{x}(t_0) \\ \boldsymbol{\mu}(t_0) \end{bmatrix} \quad (7)$$

that leads to:

$$\mathbf{x}(t_0 + T_0) = \boldsymbol{\phi} \mathbf{x}(t_0) + \boldsymbol{\varphi} \boldsymbol{\mu}(t_0) \quad (8)$$

where matrices $\boldsymbol{\phi}$ and $\boldsymbol{\varphi}$ depend on the elements of dynamic matrices \mathbf{S}_k and the durations of the s subintervals.

In steady-state operation, it is always possible to find a periodicity condition between final value $\mathbf{x}(t_0 + T_0)$ of the state vector and initial one $\mathbf{x}(t_0)$, given by:

$$\mathbf{x}(t_0) = \mathbf{R} \mathbf{x}(t_0 + T_0) \quad (9)$$

Substituting (8) in (9) the following relationship is obtained:

$$\mathbf{x}(t_0) = (\mathbf{I} - \mathbf{R} \boldsymbol{\phi})^{-1} \mathbf{R} \boldsymbol{\varphi} \boldsymbol{\mu}(t_0) \quad (10)$$

Owing to the presence of natural commutations, the durations of $s-f$ subintervals are unknown a priori; therefore, to calculate the steady-state initial conditions, it is necessary to employ an iterative procedure, starting by suitable initial values for the unknown durations and successively testing if the conditions determining the natural commutations

(generally turn-off of diodes and thyristors and turn-on of diodes) are verified.

In order to computerize the verification of the conditions determining the natural commutations, it is convenient to associate to each of them a constraint equation that can be written as:

$$c_h^T \xi(t_h) = 0 \quad (11)$$

where c_h^T is a constant row-vector and t_h is the natural commutation instant taken into account.

Once determined initial state vector $x(t_0)$ and all the timings, the state vector at the end of each subinterval can be computed by applying eq. (5) to all the subintervals. The iterative procedure will be illustrated in an apposite paper.

3. DETERMINATION OF MEAN VALUES AND HARMONIC COEFFICIENTS

3.1. Mean values

The determination of the mean values of the most significant quantities of the power system is achieved by employing a new augmented state system and calculating the transition matrices of the new dynamic matrices. During the k^{th} subinterval, (t_{k-1}, t_k) , a generic variable $y(t)$ (being y a state variable or, more in general, a linear combination of state variables) can be expressed as:

$$y(t) = \gamma_k^T \xi(t) \quad (12)$$

when vector γ_k depends on the selected linear combination and can also assume different values according to the interval taken into consideration.

All the variables, whose mean value is different from zero, have a period equal to T_0 ; therefore mean value \bar{y} can be computed by the following equation:

$$\bar{y} = \frac{1}{T_0} \sum_{k=1}^s \gamma_k^T \int_{t_{k-1}}^{t_k} \Phi_k(\tau) \xi(t_{k-1}) d\tau \quad (13)$$

which uses only the values of augmented state ξ at the commutation instants.

The integrals that appear in (13) can be computed by means of a new augmented state system, which, in each subinterval, is defined by the following model:

$$\dot{\eta}(t) = \mathcal{Q}_k \eta(t) \quad (14)$$

being

$$\eta(t) = \begin{bmatrix} \xi(t) \\ \nu(t) \end{bmatrix} \quad \mathcal{Q}_k = \begin{bmatrix} S_k & \mathbf{0} \\ \frac{1}{T_0} \gamma_k^T & 0 \end{bmatrix}.$$

In fact, assuming $\nu(0) = 0$, the value of auxiliary variable ν at the final instant of the observation interval is equal to the mean value of variable $y(t)$.

3.2 Determination of the Harmonic Coefficients

The procedure described above can be employed, with slight modifications, also for the computation of harmonic coefficients. The formulation is different according to whether variable $y(t)$ has a period equal to observation interval T_0 or to a multiple of T_0 .

When variable $y(t)$ has a period equal to T_0 , assuming

equal to 0 the initial instant, coefficients a_m and b_m of the m^{th} harmonic are defined as:

$$a_m = \frac{2}{T_0} \int_0^{T_0} y(t) \cos(m\omega t) dt$$

$$b_m = \frac{2}{T_0} \int_0^{T_0} y(t) \sin(m\omega t) dt$$

being $\omega = 2\pi/T_0$.

The dynamic matrices of the augmented state system to be used to determine the values of coefficients a_m and b_m become:

$$\mathcal{Q}_k = \begin{bmatrix} S_k & \mathbf{0} \\ Y_k & \Omega_m \end{bmatrix},$$

in which:

$$Y_k = \frac{2}{T_0} \begin{bmatrix} \gamma_k^T \\ 0 \end{bmatrix} \quad \text{and} \quad \Omega_m = \begin{bmatrix} 0 & m\omega \\ -m\omega & 0 \end{bmatrix}.$$

In this way, at the final instant of the observation interval vector ν (which now has two components) becomes equal to:

$$\begin{aligned} \nu(T_0) &= \int_0^{T_0} \exp[\Omega_m(T_0-t)] \begin{bmatrix} \frac{2}{T_0} y(t) \\ 0 \end{bmatrix} dt = \\ &= \exp[\Omega_m T_0] \int_0^{T_0} \exp[-\Omega_m t] \begin{bmatrix} \frac{2}{T_0} y(t) \\ 0 \end{bmatrix} dt. \end{aligned} \quad (12)$$

Exponential matrix $\exp[\Omega_m t]$ is equal to:

$$\exp[\Omega_m t] = \begin{bmatrix} \cos(m\omega t) & \sin(m\omega t) \\ -\sin(m\omega t) & \cos(m\omega t) \end{bmatrix}.$$

So:

$$\exp[\Omega_m T_0] = \begin{bmatrix} 1 & 0 \\ 0 & 1 \end{bmatrix},$$

therefore:

$$a_m = \nu_1(T_0) \quad \text{and} \quad b_m = \nu_2(T_0).$$

If the period of $y(t)$ is equal to lT_0 , coefficients a_m and b_m of the m^{th} harmonic are defined as:

$$a_m = \frac{2}{lT_0} \int_0^{lT_0} y(t) \cos(m\omega t) dt$$

$$b_m = \frac{2}{lT_0} \int_0^{lT_0} y(t) \sin(m\omega t) dt$$

being $\omega = 2\pi/lT_0$.

As previously pointed out, the system behaviour during the entire supply period can be evaluated by the evolution of the state variables during the observation interval. Therefore, also coefficients a_m and b_m can be computed taking into account only the evolution during the observation interval.

The extension is obvious when l is equal to 2, i.e. when variable $y(t)$ is associated to a mono-phase symmetric circuit. In this situation, in fact, coefficients a_m and b_m (different from zero only when m is odd) can be calculated, taking into consideration only the observation interval, using the same expressions as the previous case, with the only difference that:

$$a_m = -v_1(T_0) \quad \text{and} \quad b_m = -v_2(T_0).$$

In fact, when T_0 is equal to a half of a period, matrix $\exp[\Omega_m T_0]$ becomes:

$$\exp[\Omega_m T_0] = \begin{bmatrix} -1 & 0 \\ 0 & -1 \end{bmatrix}.$$

More complex is the extension to the cases $l = 3$ and $l = 6$, i.e. when variable $y(t)$ is associated to a three-phase circuit. The description will be made taking into account only the case of a symmetric circuit, which involves $l = 6$.

Applying the integration only to a half period, coefficients a_m e b_m (different from zero only when m is odd and not multiple of 3) can be obtained as:

$$a_m = \frac{2}{3T_0} \int_0^{3T_0} y(t) \cos(m\omega t) dt$$

$$b_m = \frac{2}{3T_0} \int_0^{3T_0} y(t) \sin(m\omega t) dt$$

being $\omega = \pi/3T_0$.

Also in this case, the integration can be limited to an observation interval, but it is necessary to take into consideration the shapes of two variables. To simplify the computations, it is convenient to select the projections of the three-phase representative vector of variable $y(t)$ on an orthogonal reference frame (α , β), properly chosen. For instance, if the direction of axis α is chosen so that in the observation interval variable $y(t)$ and its projection $y_\alpha(t)$ on axis α are related by the following relation:

$$y(t) = \frac{2}{3} y_\alpha(t),$$

and the direction of axis β is perpendicular and delayed with respect to axis α , follows:

$$y(t+T_0) = \frac{1}{3} y_\alpha(t) - \frac{\sqrt{3}}{3} y_\beta(t)$$

$$y(t+2T_0) = -\frac{1}{3} y_\alpha(t) - \frac{\sqrt{3}}{3} y_\beta(t).$$

Therefore:

$$\begin{aligned} \int_0^{3T_0} y(t) \cos(m\omega t) dt &= \int_0^{T_0} \frac{2}{3} y_\alpha(t) \cos(m\omega t) dt + \\ &+ \int_0^{T_0} \left[\frac{1}{3} y_\alpha(t) - \frac{\sqrt{3}}{3} y_\beta(t) \right] \cos[m\omega(t+T_0)] dt + \\ &+ \int_0^{T_0} \left[-\frac{1}{3} y_\alpha(t) - \frac{\sqrt{3}}{3} y_\beta(t) \right] \cos[m\omega(t+2T_0)] dt = \\ &= \int_0^{T_0} y_\alpha(t) \cos(x) dt + \varepsilon(m) \int_0^{T_0} y_\beta(t) \sin(x) dt, \end{aligned}$$

being:

$$x = m\omega t \quad \text{and} \quad \varepsilon(m) = \text{sign} \left[\sin \left(\frac{m\pi}{3} \right) \right].$$

In a similar way, the following equality can be obtained:

$$\int_0^{3T_0} y(t) \sin(x) dt = \int_0^{T_0} y_\alpha(t) \sin(x) dt - \varepsilon(m) \int_0^{T_0} y_\beta(t) \cos(x) dt.$$

During the k^{th} subinterval, (t_{k-1}, t_k) , variables $y_\alpha(t)$ and $y_\beta(t)$ can be expressed as:

$$y_\alpha(t) = \gamma_{\alpha k}^T \xi(t)$$

$$y_\beta(t) = \gamma_{\beta k}^T \xi(t).$$

Choosing matrices Y_k as:

$$Y_k = \frac{2}{3T_0} \begin{bmatrix} \gamma_{\alpha k}^T \\ -\varepsilon(m) \gamma_{\beta k}^T \end{bmatrix},$$

at the final instant of the observation interval vector v become equal to:

$$v(T_0) = \frac{2}{3T_0} \exp[\Omega_m T_0] \int_0^{T_0} \exp[-\Omega_m t] \begin{bmatrix} y_\alpha(t) \\ -\varepsilon(m) y_\beta(t) \end{bmatrix} dt. \text{ Mul}$$

tiplying vector $v(T_0)$ by the following matrix:

$$\begin{aligned} Z = \exp[-\Omega_m T_0] &= \begin{bmatrix} \cos\left(\frac{m\pi}{3}\right) & -\sin\left(\frac{m\pi}{3}\right) \\ \sin\left(\frac{m\pi}{3}\right) & \cos\left(\frac{m\pi}{3}\right) \end{bmatrix} = \\ &= \begin{bmatrix} \frac{1}{2} & -\frac{\sqrt{3}}{2} \varepsilon(m) \\ \frac{\sqrt{3}}{2} \varepsilon(m) & \frac{1}{2} \end{bmatrix}, \end{aligned}$$

the following vector:

$$\mu = Z v(T_0) = \frac{2}{3T_0} \int_0^{T_0} \exp[-\Omega_m t] \begin{bmatrix} y_\alpha(t) \\ -\varepsilon(m) y_\beta(t) \end{bmatrix} dt \text{ is}$$

obtained, whose components:

$$\mu_1 = \frac{2}{3T_0} \int_0^{T_0} y_\alpha(t) \cos(x) dt + \frac{2}{3T_0} \varepsilon(m) \int_0^{T_0} y_\beta(t) \sin(x) dt$$

$$\mu_2 = \frac{2}{3T_0} \int_0^{T_0} y_\alpha(t) \sin(x) dt - \frac{2}{3T_0} \varepsilon(m) \int_0^{T_0} y_\beta(t) \cos(x) dt$$

assume the values of harmonic coefficients a_m and b_m .

4. CONCLUSIONS

The paper illustrates some peculiarities of a general program useful for analysing the steady-state behaviour of power systems including static converters. In particular, the program allows the computation of the initial values of the state variables, the instants in which the natural commutations take place, the mean values and the harmonic coefficients of the system state variables and of their linear combinations. Moreover, it makes a direct analysis of the system stability and allows the shapes drawing of the most significant system quantities.

In this paper, particular care has been devoted to the approach used to determine the mean values and the harmonic coefficients.

The employed methodologies were already elaborated since many years. The current version of the program presents several improvements, an enhanced interactivity and a better graphic appearance.

5. REFERENCES

- [1] A. Bellini, A. De Carli, M. La Cava, "System theory approach to the analysis of converter fed systems", *International Conference on Electrical Machine. ICEM '78*, Brussels, 1978.
- [2] K. Al-Badwaih, El-Bidweiby, "Steady-state analysis of static power converters", *IEEE Trans. on Industry Applications*. IA-18, 1982.
- [3] A. De Carli, "Steady-state behaviour of converter fed systems", *3rd IFAC Control In Power Electronics and Electrical Drives*. Lausanne, 1983.
- [4] A. Bellini, C. Picardi, "A generalized program to analyse electrical or electromechanical systems including static converters", *IASTED Journal of Modelling & and Simulation*. Vol.6, No. 1, 1986.
- [5] A. Bellini, D. Grimaldi, C. Picardi, "Steady-state and stability analysis of static power conversion systems", *IAS Annual Meeting*., Denver, 1986.
- [6] A. Bellini, D. Grimaldi, C. Picardi, "Steady-state analysis of current source inverter induction motor drives", *International Conference on Electrical Machine. ICEM '86*, Munchen, 1986.
- [7] D. Maksimovic, "Automated steady-state analysis of switching power converters using a general-purpose simulation tool", *Power Electronics Specialists Conference, PESC '97*, St. Louis (Missouri, USA), 1997.
- [8] T. Kato, W. Tachibana, "Periodic steady-state analysis of an autonomous power electronic system by a modified shooting method", *IEEE Trans. Power Electronics*, vol. 13, May 1998.
- [9] F. Del Águila López, P. Palà Schönwälder, J. Bonet Dalmau, R. Giralt Mas, "A Discrete-Time Technique for the Steady State Analysis of Non-linear Switched Circuits with Inconsistent Initial Conditions", *IEEE International Symposium on Circuits and Systems*, Sydney (Australia), 2001.
- [10] A. Bellini, S. Bifaretti, S. Costantini, "A General Program to Analyse the Steady-State Behaviour of Power Systems Including Static Converters", *The Third IASTED International Conference on Power and Energy Systems, EuroPES 2003*, Marbella, Spain, September 3 - 5, 2003.
- [11] A. Bellini, S. Bifaretti, S. Costantini, "An Interactive Program to Determine the Harmonics Produced by an AC-DC Converter", *IEEE-PES, Power Tech'03 International Conference*, Bologna June 23-26, 2003.

COMPARATIVE ANALYSIS ON TWO MODELS OF RELUCTANCE MOTOR

Alecsandru Simion, Leonard Livadaru, Sergiu Călugăreanu, Emanuel Romila, "Gh. Asachi" Technical University of Iași, Faculty of Electrical Engineering, Iași, Romania

Abstract: This paper presents a study of a reluctance motor both on a test bench and in computer-aided FEM analysis. The obtained results are subsequently compared with a new model that changes the rotor structure in order to obtain superior performance.

Key Words: Laminated rotor, FEM analysis

1. STEPS IN DESIGN OF RELUCTANCE MOTORS

Usually, for the design of the three-phase reluctance motors certain steps must be accomplished. The start-point is the determination of the polar pitch. It is necessary for this purpose to impose some of the parameters and the others have to be calculated. We talk about: M_{emax} - electromagnetic torque that the motor have to develop; C_d - factor that takes into account the ratio between leakage reactances and direct-axis synchronous reactance; k_{w1} - winding factor; α_2 - length versus polar pitch ratio; k_{rx} - factor that depends on the resistance R_1 , direct-axis synchronous reactance X_d and quadrature-axis synchronous reactance X_q , that is the difference between the two reactances corresponding to the two axis; A_0 - linear current density corresponding to no-load operation; A - linear current density corresponding to under-load operation; B_δ - air-gap flux density; C_1 - phase voltage versus induced voltage ratio; p - polar pairs. These factors and some of the quantities are chosen from diagrams or equations of the magnetic field theory.

The value of the polar pitch which for the moment represent only a preliminary quantity could be obtained for example with the expression given in [1]. The final value results after the estimation of the operation characteristics that represents the variation with output power, P_2 , of different quantities. The calculus process consists of successive iterations that ends when the final values are similar to those imposed by the designer [2], [3]. The calculus of a three-phase reluctance motors include the following steps:

- establish of main geometrical quantities;
- air-gap calculus;
- calculus of stator slots and stator winding;
- design of the rotor provided with a special "squirrel cage" winding for start operation;
- calculus of the magnetic circuit;
- estimation of the operation characteristics for synchronous operation;

As an example one designed a reluctance motor with the following rated parameters: $P_N = 1000W$, $U_{1N} = 220V$, $n_N = 1500$ rot /min, $\cos\phi_N = 0.42$, $I_{1N} = 5.3A$.

The calculus was made by using the MathCad software. By analytical determination the current diagram was obtained and finally the *developed mechanical power line* with an acceptable precision was established.

The mathematical design was verified by using a FEM magnetostatic and transient magnetodynamic analysis (the latter for the study of the start-up but which not represent the aim of this paper). As follows one presents some of the results:

- Figure 1: The geometry of the motor resulted from the calculus: outer diameter of the stator 134 mm; inner diameter of the stator 80 mm; length 103 mm; $W_{1c} = 42$ turns per slot; single-layer winding with $2p=4$ and $q = 3$; air-gap $\delta = 0,4$ mm and the flux lines distribution.

- Figure 2: Flux density color map.

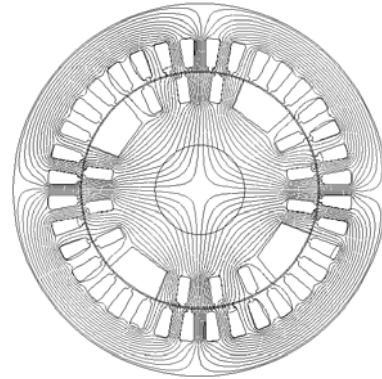


Fig. 1. Geometry and flux lines distribution



Fig. 2. Flux density color map

The following figures (fig. 3,4,5 and 6) presents some of the results obtained on the test bench by direct acquisition with a DAQ card. It is shown the variation of the input power, P_1 , stator phase current, I_1 , output torque, M_2 and power factor, $\cos\phi_1$.

It has to be pointed out that in comparison with the no-load current, the under-load current has a decrease area followed by an increase area simultaneously with the output power (this variation is similar to a V shape and its explanation can be made starting from circle diagram or from the expression of the current [4]).

As regards the power factor, the value corresponding to rated power value is of 0.4, which is pretty close to the value obtained from calculus, 0.42. The power factor increases up to 0.5 when the power reaches the value of $P_2 = 2000W$, that is $2 \cdot P_{2N}$.

This model has been analyzed both with a FEM analysis in a magnetostatic solver [5]. The curve torque versus internal angle is presented in figure 7.

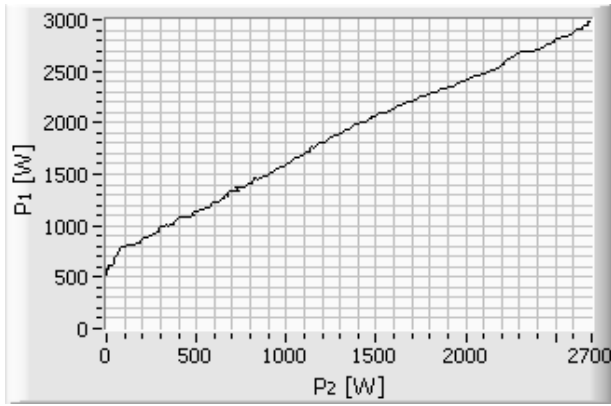


Fig. 3. Input power versus output power

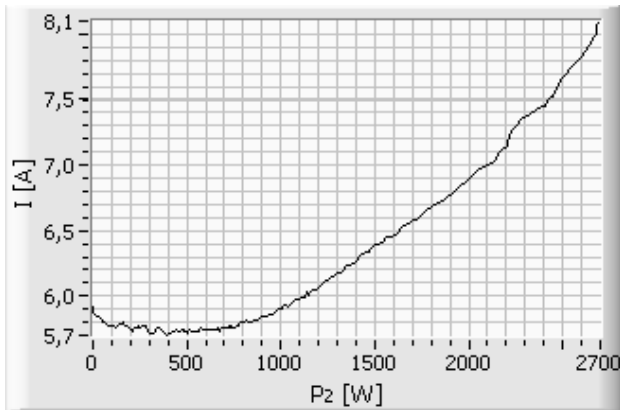


Fig. 4. Current versus output power

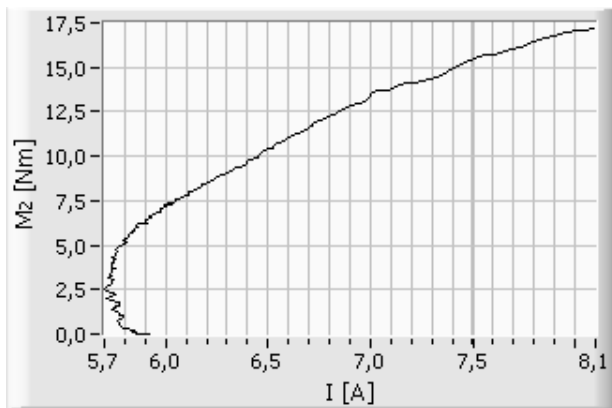


Fig. 5. Output torque versus output power

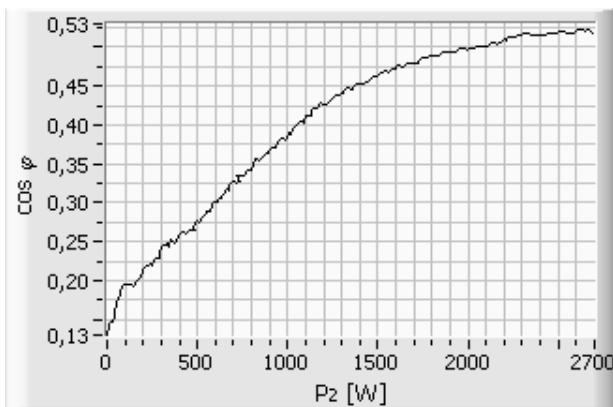


Fig. 6. Power factor versus output power

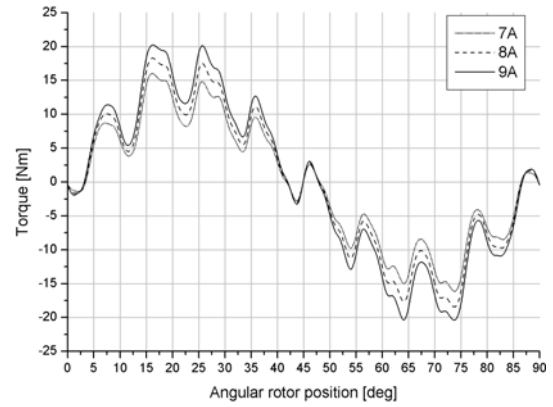


Fig. 7. Torque versus internal angle

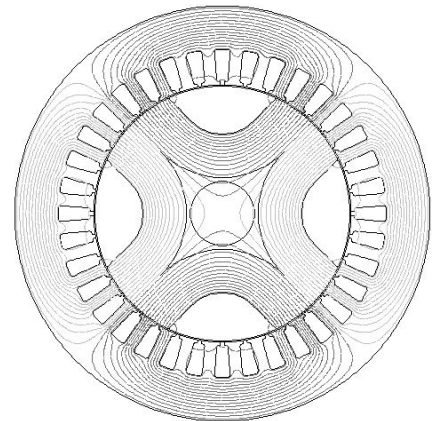


Fig. 8. Geometry and flux lines distribution

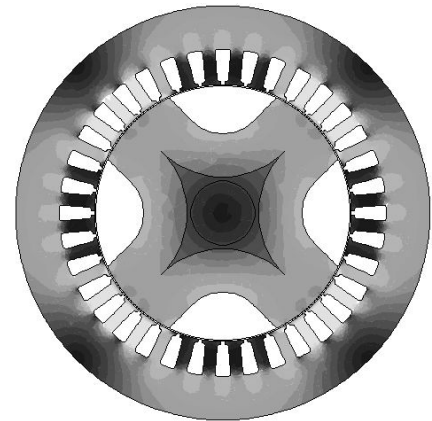


Fig. 9. Flux density color map

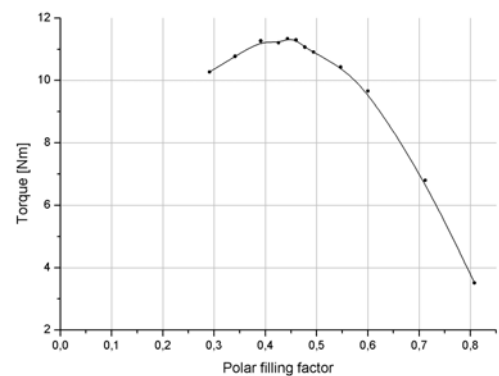


Fig. 10. Pull-out torque versus pole filling

The three curves correspond to three different current values: 7A, 8A and 9A. Of great importance are the values of the pull-out torque which correspond to the amplitude of the fundamental. These values vary between 12 and 16 Nm. The value that corresponds to 7A is of 12 Nm and it is very close to the experimental value, 12.7 Nm.

2. STUDY OF THE RELUCTANCE MOTOR WITH LAMINATED ROTOR (RMLR)

The second part of the paper contains an analysis of a motor with a special rotor obtained as a radial assemblage of laminations made of cold-rolled steel with orientated grains of iron. The design takes into consideration the pathways of the flux lines and the necessity of creating a high difference between the direct-axis and quadrature-axis reactances.

The figures 8 and 9 presents the geometrical structure and flux lines distribution (fig. 8) and the flux density color map (fig. 9) corresponding to a certain polar filling factor of $\alpha_p = 0.45$.

The most important element that has to be pointed out for this structure refers to the polar filling factor, the quantity that put in view the ratio between the rotor pole width and the stator polar pitch. For our study we have used different values in the limits $0.28 \div 0.8$.

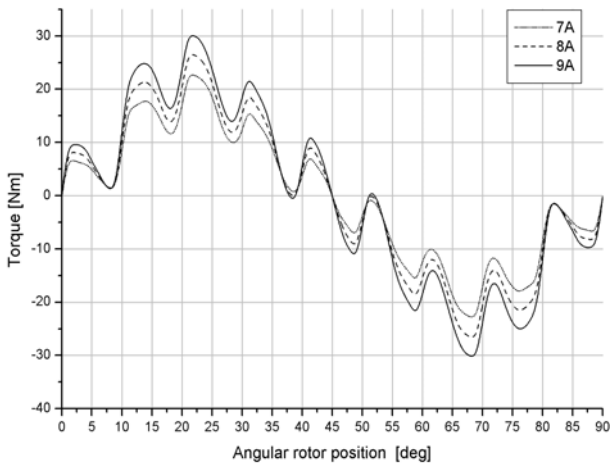


Fig. 11. Torque versus internal angle characteristic

Figure 10 shows the variation of the pull-out torque of the model for different values of α_p when the primary current remains constant at its rated value which is 5.3A.

The maximum developed torque corresponds to a polar filling factor of $\alpha_p = 0.45$. It is interesting to notice that this value of the torque is close to the value of the real model but obtained for a higher current (6.6A, fig. 4). So we can conclude that the new model, RMLR, is a more convenient solution. For the same stator geometry, the presence of the new rotor determines an increase of the torque with approximately 25%.

For a better comparison of the two models the figure 11 presents the angular characteristic of the RMLR.

The amplitude of the fundamental of these torques corresponding to 7, 8 and 9A is of 16.5, 19.5 and 22.4 Nm respectively.

Another way to compare the performance of the two models is given in figure 12, which presents the dependence of the torque with the value of the current.

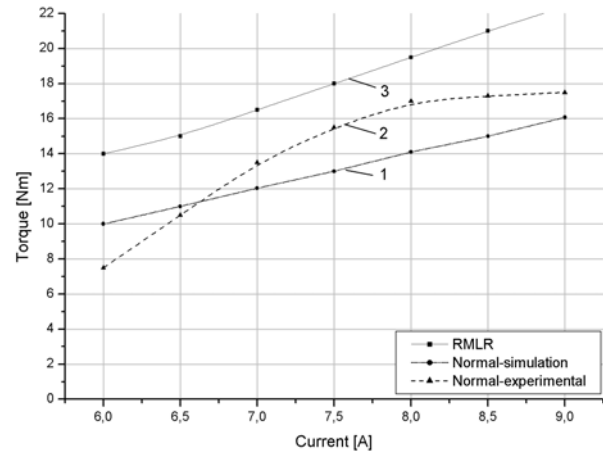


Fig. 12. Output torque versus current

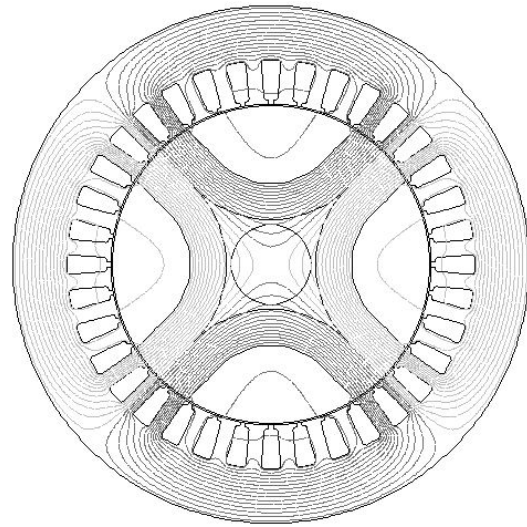


Fig. 13. Flux lines distribution - $\alpha_p = 0.28$



Fig. 14. Flux density color map - $\alpha_p = 0.28$

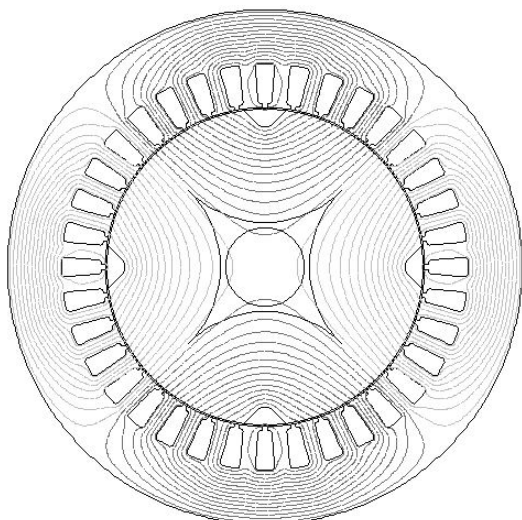


Fig. 15. Flux lines distribution - $\alpha_p = 0.81$

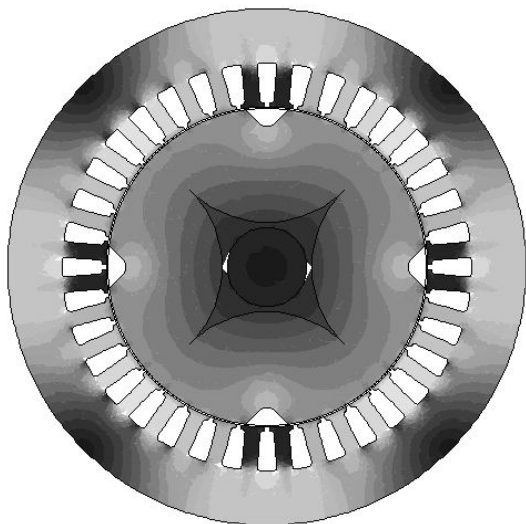


Fig. 16. Flux density color map - $\alpha_p = 0.81$

It is easy noticeable that the curve3, which is situated above the other two curves, develop a higher torque with approximately 25% for a pole filling factor of 0.45.

As concerns the influence of the pole filling factor upon the electromagnetic parameters of the model, it is interesting to compare the flux lines distribution and the flux density color map for two values very different from the optimum value. Thus, the figures 13 and 14 refers to a value of $\alpha_p = 0.28$ and the figures 15 and 16 to $\alpha_p = 0.81$. For the both situations we have taken into account the same rotor position (internal angle).

3. CONCLUSIONS

1. The paper brings some contributions concerning the design of the three-phase reluctance motor and the analyse of the magnetic field based on finite element software packages;

2. The use of the PC and FEM analysis allows the estimation of under-load operation and angular characteristics corresponding to steady-state operation even when the software is dedicated to the study of machines with isotropic rotor (it is well-known that the reluctance motors have anisotropic rotors). It was analysed the influence of the pole filling factor on the value of the pull-out torque;

3. The experimental results obtained on the physical model validate both the new design formulations for the estimation of geometrical quantities and shows an increasing of the performance of the model with radial assembled laminations on the rotor since a much higher value of the ratio X_d/X_q is obtained.

4. REFERENCES

- [1] Al. Simion, I. Vartolomei, L. Livadaru, S. Călugareanu, "On the CAD of the three-phase reluctance motor", The 11th International Symposium on Power Electronics - Ee 2001, Novi Sad (YU), nov. 2001, p.(269-273).
- [2] Al. Simion, G. Mardarasevici, L. Livadaru, "Reluctance motor - design", Iasi, 1993 (in romanian).
- [3] M.I. Postnikov, V.V. Ralle, "Sinchronie reaktivnie dvigateli", Izd. Tehnika, Kiev, 1970.
- [4] Al. Simion, "Special electrical machines", Chişinău, 1995 (in romanian).
- [5] *** - FLUX-2D - Finite element software for Electromagnetic Applications; Version 7.61, CEDRAT, France.

RESULTS RECURRENCE ON GENETIC ALGORITHM ESTIMATION OF THE INDUCTION MOTOR EQUIVALENT SCHEME PARAMETERS

Zdravko Andonov¹, Borislav Jeftenić², Slobodan Mircevski¹, ¹Faculty of Electrical Engineering Skopje, Macedonia, ²Faculty of Electrical Engineering, Beograd, Serbia & Montenegro

Abstract: Induction motors are used in electrical drives where simple reliable and robust machine is the first requirement. For the induction motor drive model stator, rotor and mutual resistances and inductances must be known. In the used method based on genetic algorithms the main goal is to estimate equivalent circuit parameters with the minimal estimation error between the calculated motor characteristics and catalogue one. The idea is using induction motor steady-state equivalent circuit to estimate motor parameters so that calculated values would be very close to known catalogue data. The used catalogue data could have influence on the recurrence of results, so in this paper this is analyzed.

Key Words: Induction motor, parameter estimation, genetic algorithms

1. INTRODUCTION

Induction motors are used in electrical drives where simple reliable and robust machine is the first requirement. Therefore nowadays induction motors participate in over 85% of all installed AC drives, in power ranging from few watts to over 10 MW. As result of power electronics development and control systems improvement, in last years induction motor replace DC motor more frequently in adjustable speed drives (ASD).

In induction motor adjustable speed drives the accurate dynamic model of machine is necessary. For the induction motor drive model stator, rotor and mutual resistances and inductances must be known. They could be determined experimentally or estimated with a help of some motor model based on catalogue data.

The genetic algorithm is method, which may be used to solve a system of nonlinear equations. The genetic algorithm uses objective functions based on some performance criterion to calculate an error. However, the genetic algorithm is based on natural selection using random numbers and does not require a good initial estimate. That is, solutions to complex problems could evolve from poor initial estimates. Genetic algorithms manipulate strings of numbers and measure each string's strength with a fitness value. The stronger strings advance and mate with other strong strings to produce offspring. One of the most important advantages of the genetic algorithm over the other techniques is that it is able to find the global minimum, instead of a local minimum, and that the initial estimate need not be close to the actual values.

In the used method based on genetic algorithms the main goal is to estimate equivalent circuit parameters with the minimal estimation error between the calculated motor characteristics and catalogue one. The idea is using induction motor steady-state equivalent circuit to estimate motor parameters so that calculated values would be very close to known catalogue data.

Induction motor equivalent circuit must correspondents to reality, but for the adjustable speed drive purposes the effects of saturation, hysteresis, eddy current, deep rotor bars and etc haven't influence on the working conditions.

Using the equivalent circuit the equations for the current, power, torque, power factor and efficiency can be implemented.

The equivalent circuit parameters estimation is multi-variable optimization problem. There are more input values (catalogue data) and the five equivalent circuit parameters have to estimated. The estimation of the motor parameters and their recurrence depend on the number of catalogue data used in calculation. Because the result recurrence is very important for this kind of estimation, we made analysis of input data influence on the obtained equivalent circuit data. The analysis shows great influence on the results.

2. GENETIC ALGORITHMS

Genetic algorithms have been used to solve difficult problems with objective functions that do not possess properties such as continuity, differentiability, etc. These algorithms maintain and manipulate a family, or population of solutions and implement a "survival of the fittest" strategy in their search for better solutions. This provides an implicit as well as explicit parallelism that allows for the exploitation of several promising areas of the solution space at the same time. Genetic algorithms search the solution space of a function through the use of simulated evolution- the survival of the fittest strategy. In general the fittest individuals of any population tend to reproduce and survive to the next generation.

The algorithm process populations of strings called chromosome. There are three operators involved in search process: reproduction, crossover and mutation. With these operators the algorithm give chance to string to survive and produce better string. The value of objective function is called fitness.

The basic steps of the genetic algorithm are: initialization, generation of initial population, calculation of fitness, fitness scaling, applying of reproduction, crossover and mutation. Except the initial steps, the process continues in the close loop, so the search process can continue indefinitely. Therefore the stopping rule is necessary to tell algorithm to stop.

2.1. Reproduction

Working on the entire population reproduction operator creates a new generation from old one. The creation of new generation is based on individual an average fitness. Reproduction operator determines the number of copies that particular individual will have in the next generation.

2.2. Crossover

The crossover operator takes two individuals and creates new, mating and swapping part of the string. The result of the crossover is two new strings that move to the next generation. For the binary strings can be used simple

crossover. For the real valued representation can be used simple, arithmetic and heuristic crossover, developed by Michalewicz.

2.3. Mutation

Mutation involves the random number change in some individuals producing single new solution. In this way is introducing variation into population. Binary mutation flips a random bit with predefined probability. In the real valued representation are used: uniform, non-uniform, multi-non-uniform and boundary mutation.

2.4. Termination and evaluation functions

The genetic algorithm moves from one to another generation selecting and reproducing parent until a termination criterion is met. The most used termination criteria are the maximum number of generations. The next strategy is population convergence criteria. This means that when the sum of the deviations among individuals becomes smaller than predefined values algorithm stops. The algorithm, also, can be terminated when lack of improvements in the best solution in the predefined number of generations. Also, other criteria can be used depend on implementation of algorithm. Different criteria can be used in the same algorithm, and the process stops when one (or more) criteria is met.

3. INDUCTION MOTOR MODEL

Stator, rotor and mutual resistances and reactances could be obtained with model using only catalogue data

Usually, the following catalogue data is known: Nominal power; Nominal phase voltage; Nominal current; Nominal speed; Nominal slip; Nominal power factor; Nominal efficiency; Breakdown torque; Locked rotor torque; Locked rotor current; Number of pole pairs.

Depending of the parameter purposes various methods different catalogue data are used for obtaining motor's resistances and reactances.

The idea of the proposed model is using induction motor steady-state equivalent circuit to estimate motor parameters so that with calculated values of resistances and reactances, to be very close to known catalogue data. The usage of steady state equivalent circuit for the parameter estimation produces nonlinear multi variable functions.

Induction motor equivalent circuit must correspondents to reality, but for the adjustable speed drive purposes the effects of saturation, hysteresis, eddy current, deep rotor bars and etc haven't influence on the working conditions. Equivalent circuit of induction motor for each phase is shown in **Fig. 1**.

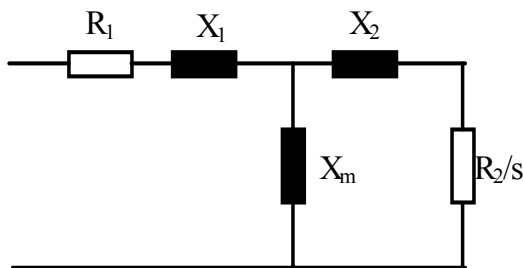


Fig. 1. Equivalent circuit of induction motor for parameter estimation based on catalogue data

In **Fig. 1** are presented following elements: X_m is magnetic field reactance connected in magnetic branch. It is

obviously that a resistance, which represents power losses in magnetic core, is missing. Magnetic core losses are too low and this simplification produces neglect estimation error; R_1 is stator resistance; $X_{1\sigma}$ is a stator reactance; $X_{2\sigma}$ is a rotor reactance; R_2 is rotor resistance and s is rotor slip.

The equivalent circuit shown in **Fig. 1** and the basic induction motor relations allow to be set the needed equations.

Parameter estimation will be should be done in two steps:

1. Using catalogue data and equitation based on the experience, the initial values for the reactances and resistances can be estimated;
2. Involving genetic algorithms the final values are calculated. The objective function, which has to be minimized, is an error between catalogue data and estimated values.

One of the possible problems in the catalogue data estimation of the induction motor parameters is the fact that electrical machines are manufactured and supplied according to the stipulation, contained in the parts of IEC Publication 34 and in the accordance with the term of the agreement. The tolerances related to the induction motors according IEC Publication 34-1 are given in the

4. RESULTS

4.1. Induction motors data

For the recurrence analysis, the five induction motors with the known equivalent circuit parameters are used. These motors are for the different purposes and different voltage and speed. The basic information for the each motor is given in the **Table 1**.

Table 1. The basic data for the used motors

Type	Power [kW]	Voltage [V]	Speed [RPM]	Purpose
WRI M	736	4000	1773	General
SCIM	400	400	742	CSI
SCIM	250	400	989	VSI
SCIM	18.5	380	1465	General
SCIM	2.2	220	700	General

WRIM-Wound rotor induction motor; SCIM - squirrel cage induction motor; CSI - current source inverter; VSI- voltage source inverter

4.2. Description of the problem

For the induction motor equivalent circuit parameters estimation based on catalogue data using genetic algorithms the program in the MATLAB environment was developed.

For analysis of the induction motor parameters estimation and results recurrence depend on used catalogue data the program was run for the different set of the input data:

1. All catalogue data for the nominal speed
2. All catalogue data for the nominal speed without efficiency
3. All catalogue data for the nominal speed and breakdown torque
4. All catalogue data for the nominal speed and breakdown torque without efficiency

For the each set of the input data the estimation of the motor parameters is done with and without knowledge of the stator resistance R_1 , so the total number of analyzed cases is eight. For the electrical drives the presume of known stator resistance is not problem because this resistance can be easy measured, or in the inverter drives calculated. The same procedure was done for the five different induction motors.

The problem about accuracy of catalogue data and influence on the estimated results mentioned in the previous heading is analyzed and present in the [1].

Program was run twenty times for the each data set for testing purposes and the elimination of possible errors in the algorithm. The goal function is minimal difference between catalogue data and calculated with the induction motor parameters. Termination criteria are difference lower than 1 %, or 1000 generations.

4.3. Result analysis

The general conclusion was that the recurrence of the results doesn't depend on the motor type. The influence of the used catalogue data is dominant. Because of that in the paper only results for the 250 kW SCIM are presented.

Catalogue data for the nominal speed

The estimation error of the resistances for the both cases (without and with knowledge of stator resistances are shown in Fig. 2 and Fig. 3

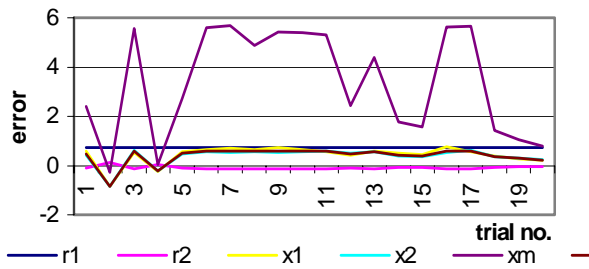


Fig. 2. Parameters error for the different trials

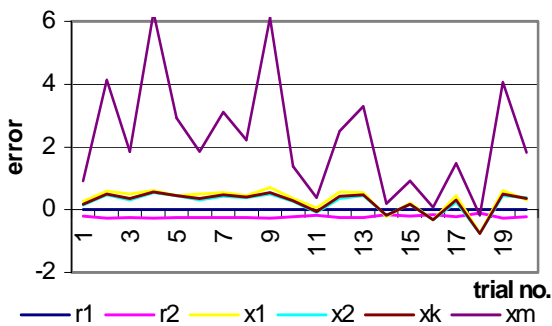


Fig. 3. Parameters error for the different trials and R_1

It is obvious that recurrence of the estimated parameters in both cases for the mutual inductance is bad, but for the other parameters the situation is better.

Catalogue data for the nominal speed without efficiency

Parameters estimation errors are shown in Fig. 4 and Fig. 5. The recurrence of the estimated data and their errors has the same trend line. This case can be treated as better solution because there are one data less for calculation (method goes faster).

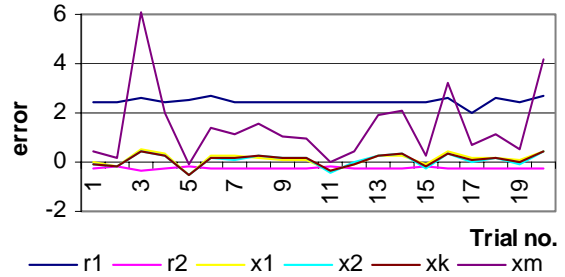


Fig. 4. Parameters error for the different trials

Catalogue data for the nominal speed and breakdown torque

When the breakdown torque is involved in the algorithm all estimated values became with the lower error and the trend line of the recurrence of the calculated motor parameters became near to constant. That means that this case is better than the previous. The errors for the estimated motor parameters are shown in the Fig. 6 and Fig. 7.

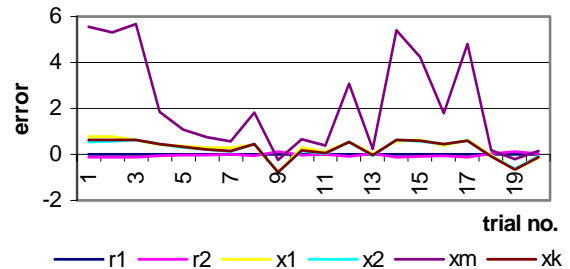


Fig. 5. Parameters error for the different trials and R_1

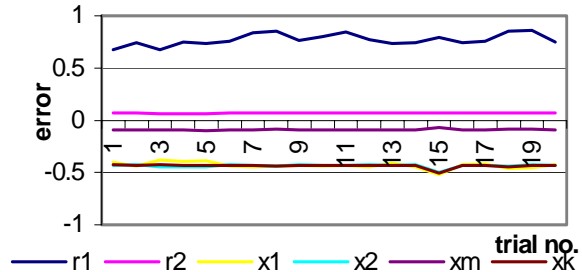


Fig. 6. Parameters error for the different trials and R_1

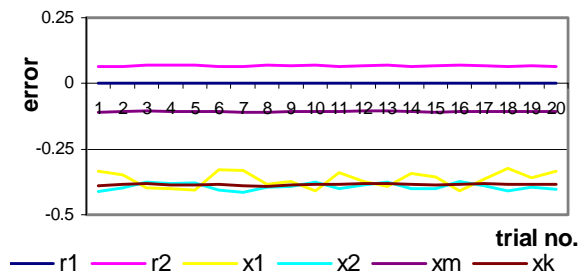


Fig. 7. Parameters error for the different trials and R_1

Catalogue data for the nominal speed and breakdown torque without efficiency

The errors for the estimated motor parameters do not show any significant changes in the recurrence trend line. The main goal in this case is reduction of the calculation needs. Error lines are shown in the Fig. 8 and Fig. 9

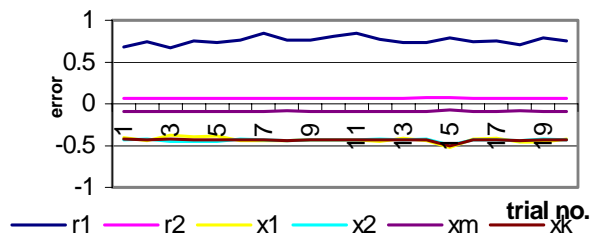


Fig. 8. Parameters error for the different trials and R_1

5. CONCLUSION

Genetic algorithms can be used to solve difficult problems with objective functions. With usage of genetic algorithms can be avoided complicated calculation of partial differentials, complicated equations etc.

In this paper is shown one of possible application of genetic algorithm for estimation of induction motor steady state equivalent circuit parameters. The purposed algorithm with the used goal function can estimated needed parameters.

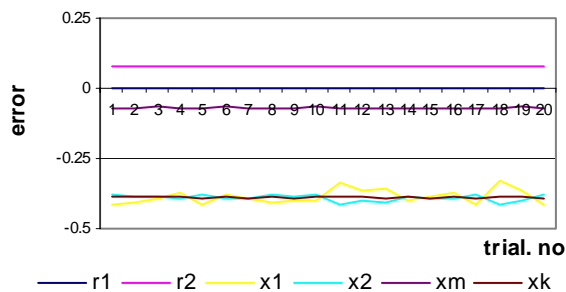


Fig. 9. Parameters error for the different trials and R_1

The results obviously show that the type, size and speed of the induction motor there is no influence on recurrence of the results. All analyzed motors have the same recurrence trend line.

The great influence on the estimated motor parameter have the selection of the catalogue data which are include in the objective function for the parameter estimation.

Also, it is shown that catalogue data for the efficiency there is no influence on the recurrence of the results.

6. REFERENCES

- [1] Z. Andonov, B. Jeftenic, S. Mircevski, *The catalogue data accuracy influence on genetic algorithm estimation of the induction motor equivalent scheme parameters*, ETAI 2003, Ohrid, 2003.
- [2] Z. Andonov, S. Mircevski, *Estimation of large induction motor drive's parameters with catalogue data*, ICEM'98, Istanbul, Turkey, 1998.
- [3] Z. Andonov, S. Mircevski, *Catalogue data parameter estimation of induction motor electrical drive*, PCIM'96, Nuremberg, Germany, 1996.
- [4] P. Pillay, R. Nolan, T. Haque, *Application of genetic algorithms to motor parameter determination for the transient torque calculation*, IEEE Trans. on IA, vol. 33, no.5, pp.1273-1282.
- [5] G. Cvetkovski, L. Petkovska, M. Cundev, S. Gair, *Genetic algorithms as utility for design optimization of electrical machines*, ISTET'97, Palermo, Italy, 1997.
- [6] Ansuji S., Shokoooh F., Schinzinger R., *Parameter Estimation for Induction Machines Based on Sensitivity Analysis*, IEEE trans. on Industry Application, vol.25, no.6, 1989, pp. 1035-1040.
- [7] P. Vas, *Artificial intelligence based electrical machines and drives*, Oxford press, 1999.
- [8] C. R. Houck, J. A. Joines, M. G. Kay, *A genetic algorithm for function optimization*, A Matlab implementation. 1996.
- [9] MATLAB v6 documentation, Mathworks, 2000.

SENSORLESS VECTOR CONTROL OF INDUCTION MOTOR WITH NEURAL NETWORK

Martin Kuchar, Pavel Brandstetter, Martin Kaduch

VSB Technical University of Ostrava, Faculty of Electrical Engineering and Computer Science, Department of Power Electronics and Electrical Drives, Ostrava, Czech Republic

Abstract: Rotor position and speed sensors are required for vector control of induction motor. Because there are some applications in industry, where these sensors cannot be used, sensorless control technique should be used. In this paper rotor speed estimator are considered, which is based on feedforward artificial neural network. It is demonstrated that such estimator, in contrast to conventional model-based approaches, does not depend on a knowledge of machine parameters. It is further shown that accurate estimates can be obtained in situation of varying load without the need for explicit load monitoring.

Key Words: Sensorless control, neural networks, induction motor, vector control, DSP

1. INTRODUCTION

In modern control techniques for induction motor with high dynamic requirements the speed transducer such as tachogenerator, resolver or mainly digital shaft position encoder are used to obtain speed information. These sensors are sources of trouble. The main reasons for the development of sensorless drives are:

- reduction of hardware complexity and cost
- increased mechanical robustness
- working in hostile environments
- higher reliability
- decreased maintenance requirements
- unaffected moment of inertia

Many types of speed estimator have been presented for electrical drives but in general these can be classified into 'conventional' or AI-based.

It is main advantage of AI-based techniques over classical model-based techniques, that it does not require model representation of the motor and the drive development time can be rapidly reduced.

Conventional types of estimators can be classified into open loop estimators, MRAS and observers (Kalman, Luenberger).

In general open-loop flux and speed estimators use monitored stator voltages and stator currents. These estimators have accuracy problems, mainly at low speeds and are dependent on knowledge of motor parameters.

The main difficulties of Kalman filter are specifying of right covariance matrices because for many cases the required statistical information is not available.

2. SPEED ESTIMATOR USING FEEDFORWARD NEURAL NETWORK

First it is necessary to design right structure of ANN and it is also important to determine such inputs to ANN, which are available in structure of vector control and from which is able to estimate a rotor speed of IM. It does not exist a recommended method for determination of ANN structure, so the final ANN was designed by means of trial and error. The main goal was to find the simplest neural network with good accuracy of speed estimation. This is the key for industry use of ANNs.

It has been designed three layer feedforward 8-22-1 ANN with following inputs: $u_{s\alpha}^*(k)$, $u_{s\alpha}^*(k-1)$, $u_{s\beta}^*(k)$, $u_{s\beta}^*(k-1)$, $i_{s\alpha}(k)$, $i_{s\alpha}(k-1)$, $i_{s\beta}(k)$, $i_{s\beta}(k-1)$. The activation functions in hidden layer are tansigmooids and output neuron has linear activation function. The network has been implemented in vector control of induction motor and entire drive was simulated in program Matlab and then it has been implemented in real drive controlled by DSP powered by Texas Instruments. Training stage is performed in Matlab using Levenberg-Marquardt algorithm.

For implementation of neural speed estimator onto real electrical drive it is necessary to obtain such training data, which determine the desired behavior of artificial neural network. The training data set was obtained from real vector controlled induction motor drive. For this purpose 90 000 samples were measured for each of the input and output signals. During training stage it was used 30 000 samples only and it was achieved an error 5×10^{-3} . Another data was used for testing phase.

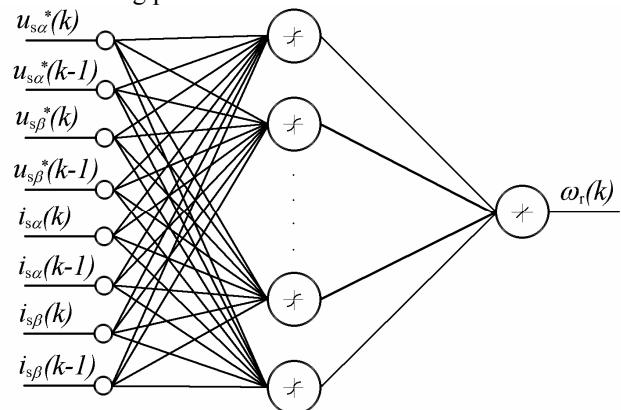


Fig. 1. Designed neural network for speed estimation (8-22-1)

Entire structure of vector controlled drive is shown in fig. 2. Voltage signals of measured stator currents are transformed from stationary reference frame $[\alpha, \beta]$ into reference frame oriented on the rotor flux linkage space vector $[x, y]$, that is done in Block of Vector Shift 2 (BVN2). Output of this block are real stator currents i_{1x} , i_{1y} , which are feedback signals to the current controllers R_{i1x} , R_{i1y} . The decoupling rotation voltage components u_{xe} , u_{ye} , which are evaluated in Block of Decoupling Circuit (BZV), are added to the outputs of mentioned controllers. The inverse shift (from reference frame oriented on the rotor flux linkage space vector to stationary reference frame) is done in Block of Vector Shift 1 (BVN1). The signals from this block are inputs to the Block of ANN-based Vector Pulse-Width Modulator (ANN-PWM – it is described in [8]). Last mentioned block ensures right switching of six IGBT in Transistor Frequency Converter (TMF). Controller R_u processes a control error between computed and reference value of stator voltage space vector modulus. The real value of this modulus is computed from values u_{1x}^* , u_{1y}^* in block of Vector Analyzer (VA).

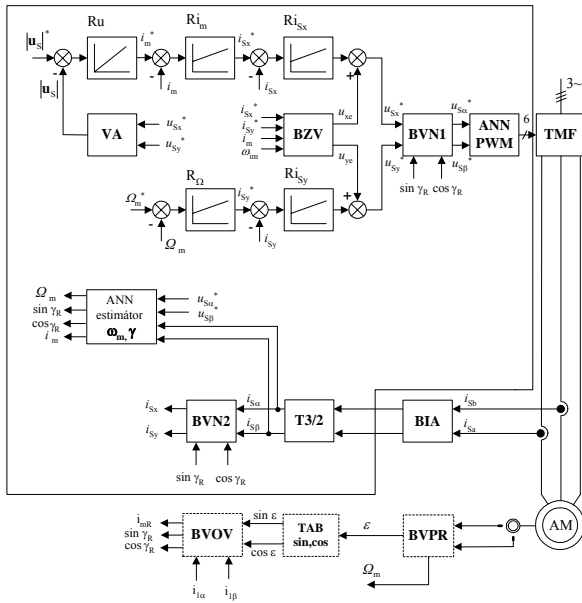


Fig.

2. Structure of sensorless vector controlled induction motor drive

It is necessary to determine the oriented angle γ , which is used in $BVN1$, $BVN2$. The angle is evaluated in the Block of Evaluation of Oriented Quantities ($BVOV$). During training stage needful rotor position (angle ε) is obtained by means of speed sensor. Then the position is determined by integration of estimated rotor speed. $BVOV$ is based on so-called current model. Controller R_{ω} processes a control error between estimated Ω_m and reference value Ω_m^* of mechanical speed.

3. DSP IMPLEMENTATION

The sensorless vector controlled induction motor drive structure including neural speed estimator has been implemented onto digital signal processor TMS320C40, which provides high computing power for presented control. The processor works with 32-bit data in floating-point arithmetic. It allows summation, subtraction, multiplication and division in one machine cycle. Instruction cycle interval is 50 ns, while most instructions are performed in one machine cycle.

For testing of the method it was used wound-rotor induction machine 2,7 kW. Entire control system is shown in fig. 3., and it has been realized at Technical University of Ostrava (Czech Republic).

The core of the system is mentioned DSP, which utilizes additional information from other peripherals – Analog to Digital and Digital to analog converter (A/D, D/A), Block of Switching Pulses (BSP), Block of Evaluation of Rotor Position (BEPR), which processes the signals from incremental encoder (1024 pulses per rotation with two shifted outputs => overall 4096 pulses/rotation). BSP is needful for right communication with modern IGBT frequency converter (TFC). Block of Isolated Amplifiers (BIA) is important to get signals of stator currents, which are sensed by means of LEM current sensors. Block of A/D converter includes four-channel, 12-bit A/D converter (total conversion time of all channel is 800ns). Significant part of the control system is a board of D/A converter for representation of interesting quantities. Communication between DSP and PC is ensured by serial interface.

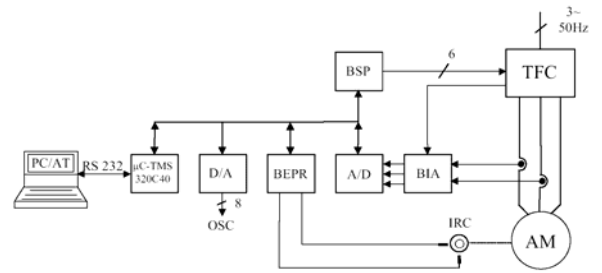


Fig. 3. DSP control system

4. EXPERIMENTAL RESULTS

In the chapter it will be presented important quantities of the drive. First it is used estimated rotor speed only as input to the speed controller. It is tested speed estimation accuracy. Such configuration is convenient for scalar controlled induction motor drive, direct vector control of induction motor and similar structures, which do not require rotor position information. Experimental results are shown in fig. 5, 6.

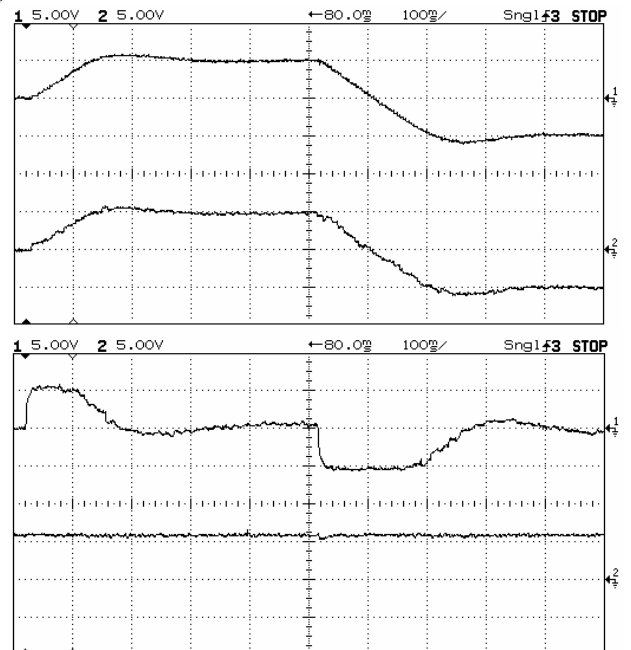
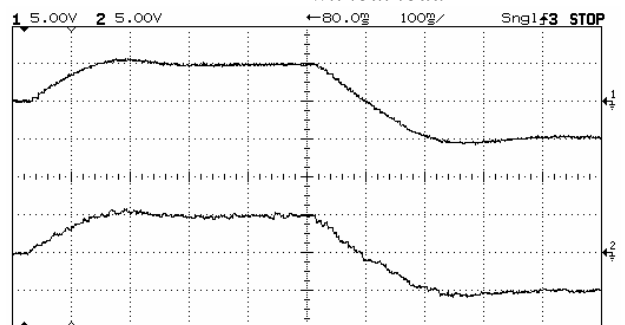


Fig. 5. Real and estimated mechanical speed, torque-producing and flux-producing stator current, ch1: $n=f(t)$, ch2: $n_{est}=f(t)$, $m_n = 60rpm/V$, ch1: $i_{sy}=f(t)$, ch2: $i_{sx}=f(t)$, $m_i=1A/V$, first run-up to 300 rpm and reversion to -300 rpm without load



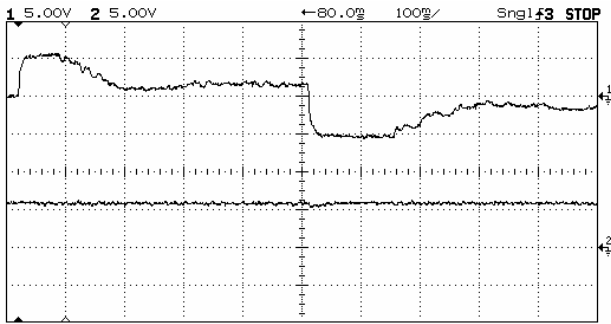


Fig. 6. Real and estimated mechanical speed, torque-producing and flux-producing stator current,
 $ch1: n=f(t)$, $ch2: n_{est}=f(t)$, $m_n = 60rpm/V$,
 $ch1: i_{sy}=f(t)$, $ch2: i_{sx}=f(t)$, $m_i=1A/V$
 first run-up to 300 rpm and reversion to -300 rpm with load

In the second stage it is used estimated rotor speed and position too. Presented structure of vector control uses the reference frame oriented on rotor flux. So rotor position information is needful. This drive is speed sensorless. Experimental results are shown in fig. 7, 8.

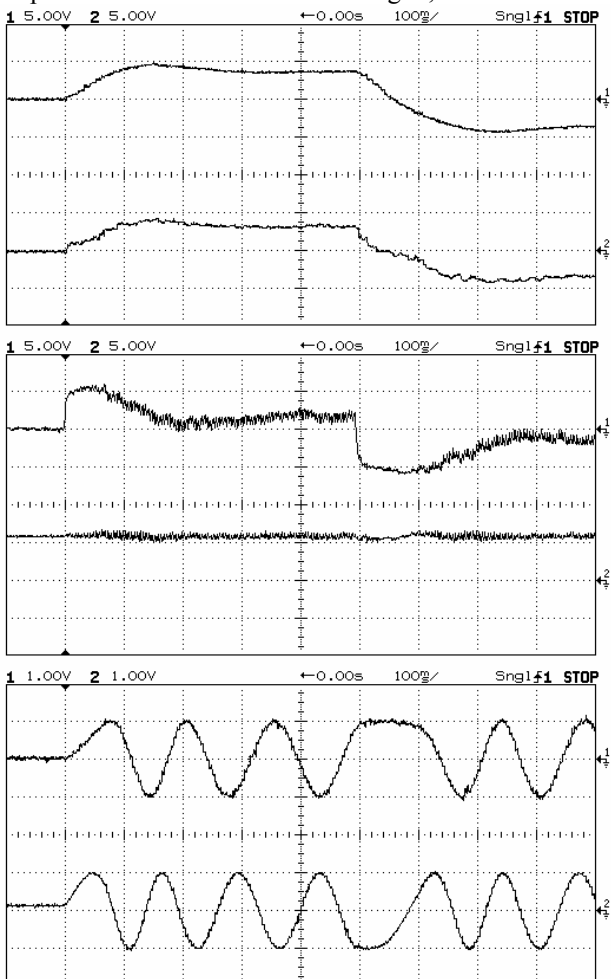


Fig. 7. Real and estimated mechanical speed, torque-producing and flux-producing stator current, Real sine value of rotor position and oriented angle,
 $ch1: n=f(t)$, $ch2: n_{est}=f(t)$, $m_n = 60rpm/V$,
 $ch1: i_{sy}=f(t)$, $ch2: i_{sx}=f(t)$, $m_i=1A/V$
 $ch1: \sin \varepsilon=f(t)$, $ch2: \sin \gamma=f(t)$

first run-up to 200 rpm and reversion to -200 rpm without load

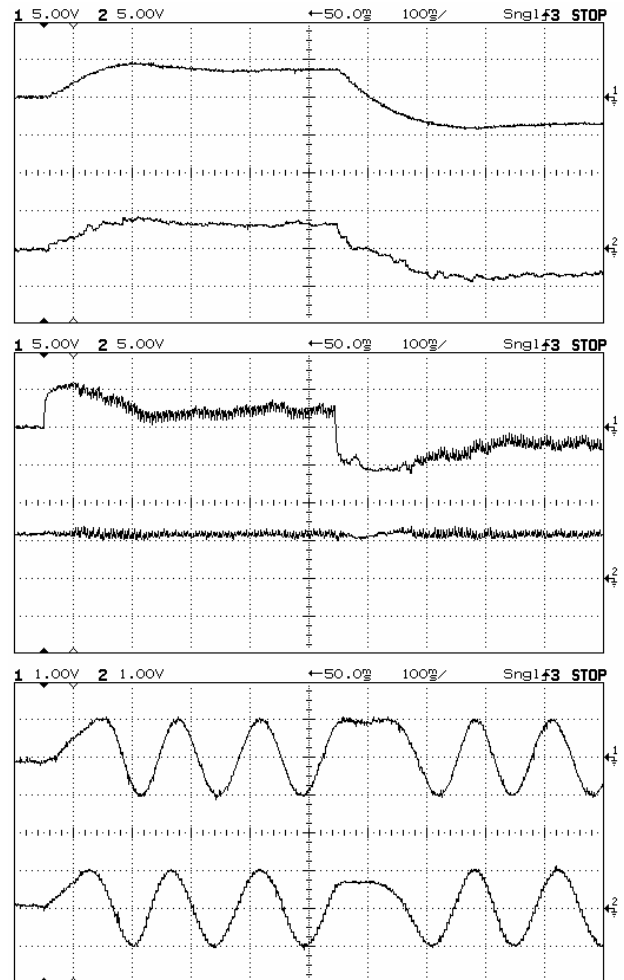


Fig. 8. Real and estimated mechanical speed, torque-producing and flux-producing stator current, sine value of real and estimated rotor position,
 $ch1: n=f(t)$, $ch2: n_{est}=f(t)$, $m_n = 60rpm/V$,
 $ch1: i_{sy}=f(t)$, $ch2: i_{sx}=f(t)$, $m_i=1A/V$
 $ch1: \sin \varepsilon=f(t)$, $ch2: \sin \gamma=f(t)$
 first run-up to 200 rpm and reversion to -200 rpm with load

5. CONCLUSION

In the paper it is presented sensorless induction motor drive with vector control. The speed estimator is based on feedforward neural network. During training stage the neural network does not have any training patterns, which represent a behavior of the drive with load, but ANN speed estimator works correctly even in such situations. It is clear that the network shows its basic ability – generalization. The range of estimated rotor speed is not anyway limited and it depends on application requirements and corresponding training data. When it is used estimated speed only, the results are excellent and the difference between real and estimated rotor speed is minimal. In the second stage it is used estimated speed and position too. Accuracy of estimated rotor speed is good but ripple of torque-producing stator current is a bit higher. It can be improved by more frequented estimation (every 500 μ s instead of 5 ms. Sampling frequency of speed regulation is 5 ms, but sampling frequency of current regulation is 500 μ s,

so it is needful to know an information about rotor position every 500 μs , but used measuring hardware can not collect the training data so fast). The lowest boundary of fine speed estimation is about 30 rpm. Department of Power Electronics and Electrical drives in Ostrava deals with sensorless drives, so last year it was realized an observer based on extended Kalman filter. In the end it is possible to compare computing demands of each types of speed estimators. It is shown in table 1.

Table 1. *Execution times of each algorithm*

Algorithm	Execution time TMS320C 40 [μs]
Vector control of induction motor	60
Extended Kalman filter	370
ANN speed estimator and rotor position evaluation	205

5. REFERENCES

- [1] Vas, P.: Artificial-Intelligence-Based Electrical Machines and Drives, Oxford science publication, 1999, ISBN 0 19 859397 X
- [2] Brandštetter, P.: AC regulation drives – Modern control methods, VŠB-TU Ostrava 1999, ISBN 80-85723-27-1
- [3] Neborák I.: Modelling and simulation of electrical regulation drives, VŠB-TU Ostrava 2002, ISBN 80-248-0083-7
- [4] Texas Instruments: TMS 320C40 Users Guide, Digital Signal Processing Product, 1995
- [5] Brandštetter, P. - Kuchař, M. - Palacký, P. – Vinklárek, D.: Sensorless Induction Motor Drive with Vector Control, EPE-PEMC 2002, Dubrovnik 2002
- [6] Demuth, H., Beale, M.: Neural Network Toolbox, for use with Matlab, ver. 4.
- [7] Vas, P., Stronach, A.F., Rashed, M., Neuroth, M.: DSP Implementation of Speed-Sensorless Induction Motor Drives Using Artificial Intelligence, Conference Proceedings PCIM 99, Nurnberg, Germany
- [8] Brandštetter, P. - Kuchař, M. - Palacký, P.: Vector Control of Induction Motor Drive using ANN-based VPWM, EPE 2003, Toulouse 2003, France
- [9] Fedor, P., Perdukova, D., Timko, J.: Study of Controlled Structure Properties with Reference Model. Acta Technica, ISSN 0001-7043, CSAV 46, 2001

PHASE ANGLE STANDARD

Zoran Mitrović, University of Novi Sad, Faculty of Technical Sciences, Novi Sad, Serbia and Montenegro

Abstract: A phase angle standard with very low measuring uncertainty of $3 \mu\text{rad}$ is developed. The standard is based on a two channel high-stability arbitrary waveform AC source for voltage of up to 120 V and current of up to 6 A with high phase angle resolution which is realized as a development device with full computer control. Proprietary auto-calibration method is implemented for achieving ultimate performances in phase angle accuracy. High performances of the phase angle standard is thoroughly evaluated and presented briefly.

Key Words: *phase angle measurement, power factor measurement, calibrator, standard, automated measurement*

1. INTRODUCTION

Phase angle measuring instruments differ according to application, principles of operation, complexity, specifications etc. Common to all of them is that from time to time their characteristics must be evaluated. Phase-angle standards serve this purpose.

In power applications, frequencies of interest are from several tens of hertz to several kilohertz. In past decades digital function generators with precision D/A converters became state-of-the-art in voltage, current and power calibrators. As easy it is to generate two voltage signals with controllable phase angle at 10 V level, problems arise when these signals are amplified to high voltage and current levels 0.

This work presents a phase angle standard that fulfills all metrological conditions for a national phase angle standard 0.

Basically, the standard consists of:

- Two-channel AC voltage and current source that generates sinusoidal voltage and current with controllable amplitudes, common frequency and phase angle, and
- An auto-calibration method that provides required phase angle accuracy.

2. VOLTAGE AND CURRENT SOURCE

The two-channel voltage and current source is designed to fulfill following requirements:

- Frequency range 10 Hz to 10 kHz
- Voltage range 0 V to 120 V
- Current range 0 A to 6 A
- Output power: voltage 25 W, current 100 W
- Short-term stability: better than 10 ppm with respect to range
- Phase angle: 0° to 360°
- Phase angle resolution: equivalent to time delay of 5 ns
- Manual and automatic operation

The source block diagram shown in Fig. 1 explains its internal structure.

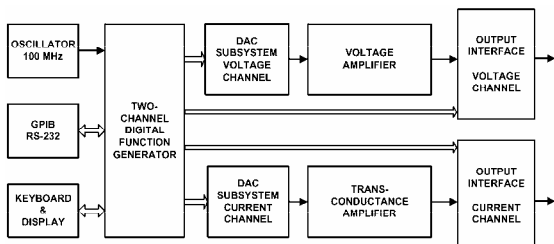


Fig. 1. *Two-channel source block diagram*

The main oscillator provides automatic data reading and sending to DAC subsystem for the two channels. Keyboard and display are intended for user interface when operating as stand-alone device. Two interfaces (GPIB and RS-232) with standard SCPI instructions provide remote operation.

2.1. Two-Channel Digital Function Generator

The two-channel digital function generator presents central part of the voltage and current source. The embedded CPU provides man-machine interface for autonomous operation and computer-device interface for remote operation via GPIB or RS-232 interface.

This generator provides galvanically isolated interface to two DAC subsystems. Samples of two signals are calculated and held in EEPROM memories. Operating at 100 MHz (based on TCXO with mark/space ratio of 1:1) memory read interface is able to provide 5 ns phase difference increment between two output signals. Output signals are generated with 64 to 8192 equidistant samples with 8 to 16 bit programmable resolution. Phase angle can be changed by:

- recalculating samples for two signals,
- delaying one of two signals with respect to the other with 5 ns resolution, and
- by combination of the above.

Recalculation of samples permit very high phase resolution, under $0.01 \mu\text{rad}$, with expense of longer time required (in range of seconds). Digital delay is performed almost instantly.

2.2. DAC Subsystem

The two identical DAC subsystems with 7.07 V maximum RMS output generate input signals for output amplifiers.

DAC subsystem schematic (Fig. 2) shows two DACs, one of multiplying deglitched type for sample generation, and the other which provides voltage reference and output signal amplitude. The DAC interface is serial in order to minimize the number of signals that cross the galvanical barrier.

Stable power is essential for this subsystem, because all power line influences due to non-ideal PSRR will be amplified and present at output. Thanks to high number of samples the first-order output filter provides enough anti-aliasing with almost zero signal phase deviation.

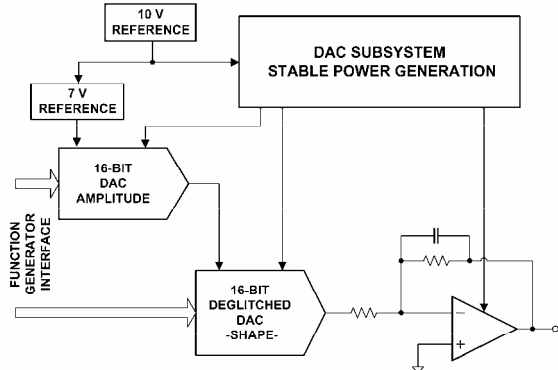


Fig. 2. *DAC subsystem diagram*

From outputs of two DAC subsystem two low level signals with the same frequency, variable amplitude and phase angle are lead to the voltage and transconductance amplifier to provide high level voltage and current outputs.

2.3. Voltage Amplifier

As seen at Fig. 3, the DAC output drives an error amplifier in the voltage amplifier section. Inverting configuration provides that amplifier input signal mean value is zero, which significantly reduces nonlinearities in this stage.

Because of the poor offset characteristics of power amplifiers the offset compensation circuitry shifts the input OP AMP operating point in such a manner that the amplifier's output offset is zero. This circuit compensates the overall offset and can be shut off programmably whenever the user decides that this feature is not needed.

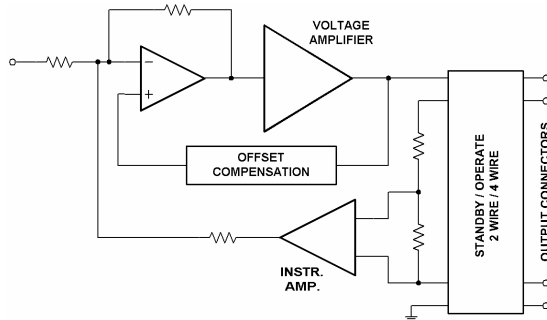


Fig. 3. Voltage amplifier

Output interface contains guard signals generation, two wire / four wire feedback voltage divider connection to output device and standby / operate function.

2.4. Transconductance Amplifier

Similar to voltage amplifier, the transconductance amplifier generates output current which is proportional to input voltage. Current sense shunt is floating so the output is ground referenced, which has great impact on stability and noise suppression.

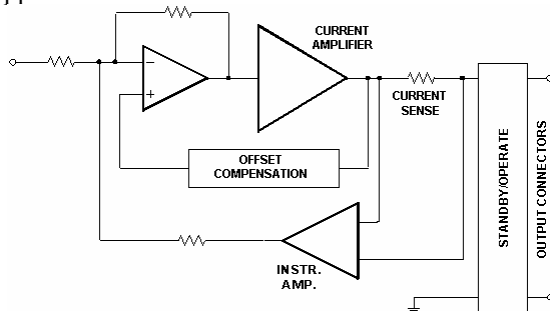


Fig. 4. Transconductance amplifier

Output interface circuit generates necessary guard signals and provides standby / operate function.

Transformerless amplifier configuration in both amplifiers is essential for the better stability, higher frequency range and better phase angle controllability.

2.5. Auto-calibration Procedure

Phase angle specifications are not given for the two channel source. Due to characteristics of power amplifiers, phase angle depends on voltage and current level and on signal frequency. High stability of the voltage, current and phase angle generated nevertheless allow that auto-calibration procedure can be performed only when either of the voltage, current or frequency is changed.

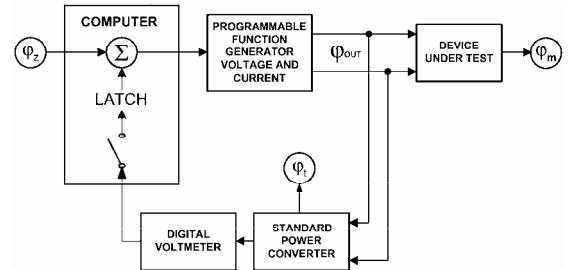


Fig. 5. Auto-calibration procedure

As seen in Fig. 5, output signals are presented to the device under test and to the standard power converter 0 which provides DC voltage proportional to the AC apparent power on its inputs. When needed, i.e. when frequency, voltage and/or current is changed, the phase angle calibration is performed. The "switch" in the computer is set, standard power converter output is measured, phase angle correction is calculated and stored into the LATCH. After that, the "switch" is turned off and until the next calibration the value held in the LATCH is used to provide the phase angle correction.

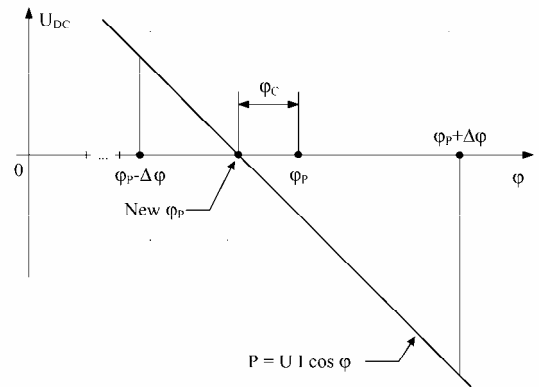


Fig. 6. Determining the phase angle correction

As an assumed phase angle of 90° (φ_P) the previously calculated correction value is added to the initial (hardware-defined) phase angle of 90° between voltage and current. The value $\Delta\varphi$ which will be added and subtracted to (from) the current 90° value (φ_P) is determined knowing the standard power converter's constant as the value of angle at which the output voltage of the standard power converter will be near the upper level of the 100 mV voltmeter's range in order to minimize the DC voltage induced error. Measurements are taken at both phase angle values: ($\varphi_P - \Delta\varphi$) and ($\varphi_P + \Delta\varphi$) several times and the average value is calculated.

The new supposed value of 90° phase angle (φ_P) is calculated by linear interpolating a zero-crossing of a straight line through two measured points at ($\varphi_P - \Delta\varphi$) and ($\varphi_P + \Delta\varphi$). The new phase angle correction value is obtained by subtracting this value from the initial 90° value.

3. MEASURING UNCERTAINTY ESTIMATION

Measuring uncertainty of the realized phase-angle standard is the key metrological characteristic, and all decisions during the concept, development and realization phase were restricted by the extreme requirements - to achieve the measuring uncertainty that is:

- far less than measuring uncertainty of the existing national standard in Serbia and Montenegro;

and

$$s_U = 24 \mu\text{V} . \quad (11)$$

Based on (7) the measuring uncertainty of the AC power measurement is less than:

$$s_P = 1.5 \cdot 10^{-3} \text{ W} . \quad (12)$$

Finally, for near-nominal AC voltage and current values (120 V and 5 A), based on (5), the measuring uncertainty of the phase angle correction is less than 3 μrad .

4. EXPERIMENTAL RESULTS

Thorough tests were taken in several past months in order to establish the phase angle standard's measuring uncertainty and other important characteristics.

The short-term stability of the voltage, current and power is given in Fig. 8. In the time interval of two minutes which is in most cases enough for establishing measurement data in computer-controlled measuring system, output signals present extremely high stability of several parts per million, which is high-end in many national laboratories' AC calibrators.

A half-hour phase angle deviation from its 90° value is presented in Fig. 9. The standard power converters' output is measured and recorded at the power factor set to zero (phase angle of 90°).

Measuring uncertainty of 3 μrad is clearly seen. The major part of this uncertainty is due to poor filtering at the standard power converter's output at low power factors.

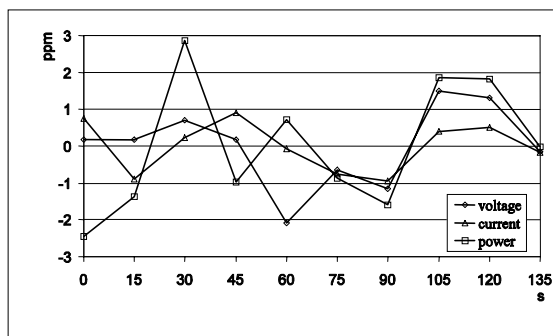


Fig. 8. Short-term stability $U, I, P; f=53 \text{ Hz}; \text{ ppm/s}$

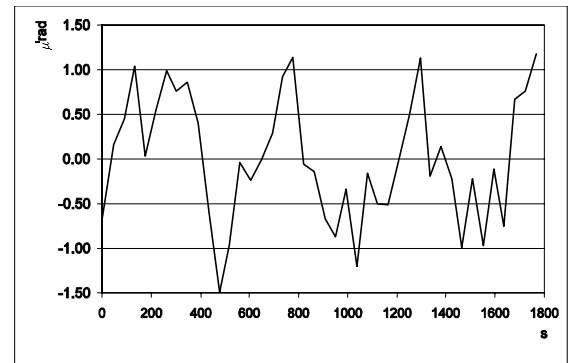


Fig. 9. Phase-angle stability $\mu\text{rad/s}$

The mean value of the initially set phase angle remains almost unchanged in 30 minutes, despite the fact that auto-calibration was not performed during that period, which highlights the high stability of the two-channel source.

5. CONCLUSION

The phase angle standard presented in this paper is developed to fulfill all the requirements to become the new national standard of Serbia and Montenegro.

As an experimental device with more functionality than is needed for the national phase angle standard, the two channel voltage and current source can be used as a basic AC source for development of many different precision instruments and devices, such as voltage, current, power and energy calibrators, AC bridges etc.

6. REFERENCES

- [1] Z. Mitrović, "Contribution to Phase-Angle Standard Development" (in Serbian), PhD Thesis, Faculty of Technical Sciences, Novi Sad, 2003.
- [2] P. Miljanić, Z. Mitrović, I. Župunski, V. Vujičić, "Toward New Standard of AC Voltage, Current, Power, Energy and Phase Angle – Experimental Results" (in Serbian), 4th Congress of Metrologists of Serbia and Montenegro, Belgrade, 2003.
- [3] P. Miljanić, "Etalon naizmjeničnog napona, struje i snage", 3rd Congress of Metrologists of Yugoslavia, Novi Sad, 2000.
- [4] P. Miljanic, B. Stojanovic and P. Bosnjakovic, "The Development of a High Precision Power Meter", IEEE Conf. Precision Electromagnetic Measur. Dig., Delft, The Netherlands, 1984, pp. 67-68.
- [5] Guide to the Expression of Uncertainty in Measurement, ISO, 1993

CONTROL STRATEGY FOR OPTIMISED COMPOUND SET OF SUPERCAPS AND ELECTROCHEMICAL BATTERIES FOR ROAD VEHICLES

Salvatore D'Arco, Diego Iannuzzi, Enrico Pagano, University of Naples "Federico II", Department of Electrical Engineering, Naples, Italy

Abstract: The paper deals with use of supercaps as auxiliary devices of on board energy sources. It shows that they can successfully support current peaks, temporarily requested by electrical road vehicles. The co-action is useful to improve energetic efficiency of the whole driving system and to take longer battery life. These advantages can be really reached in practice only by implementing proper control techniques. The paper suggests one of these techniques and by means of a digital simulation and some experimental test gives evidence to many practical problems and to some possible solutions of them. A sample numerical example is finally given for better explaining the suggested control technique.

Key Words: Control, supercaps, vehicles

1. INTRODUCTION

Duty cycles of road vehicles are characterised by repetitive high power demands, spaced by time intervals with low mechanical loads and short times braking operations. When electric road vehicles are dealt with, duty cycles are squeezed, because they are mainly used on the inside of towns and, hence, due to urban traffic, starting and braking operations are quickly occurring in series. Designs of on board electrical energy sources have to deal with these peculiarities of duty cycles and must provide to realise supplying systems that obtain the highest possible fuel distance and the longest possible operating life.

Supercaps can be successfully used in electric road vehicles for supporting electrochemical batteries, according to the block diagram of fig.1. It is known that one of the factors affecting the life of electrochemical batteries is their transient overloading, also if it is limited to short time intervals. Therefore, proper design of battery rating must not only take into account their capacity in terms of Ampere x hours, but also the maximum current needed by power train for starting and for supporting accelerations. Nowadays supercaps represent an auxiliary device, useful to contribute to short-time load current peaks. To this end they must be co-opted in the on board energy source, they must be discharged until they are capable to supply the requested auxiliary current. Afterwards, they must be re-charged to be on the ready for the further supporting action. These operating conditions are made possible by the use of a power electronics device, which provides either to increase or to decrease intermediate voltage to obtain that supercaps are respectively either discharged or charged. In both cases intermediate voltage have always to be controlled and arranged either for squeezing current according to a given amplitude versus time law or for carrying on the restoring electrical charge without overloading electrochemical battery. Some authors have already suggested the use of supercaps as auxiliary devices on board of road electric vehicles (see for example [1],[2]).

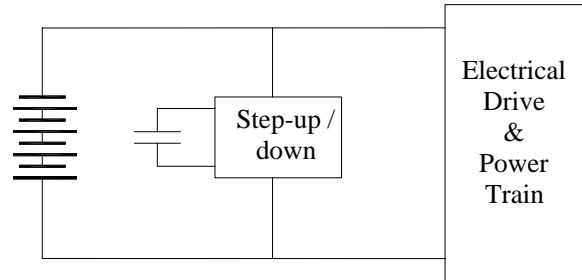


Fig. 1. Block diagram of the electrical power section of an electric road vehicle

We have, however, found only a few experimental results about the behaviour of supercaps operating in parallel with electrochemical batteries supported by suitable control algorithms in order to investigate about the optimisation of power flows between the electrochemical batteries and supercaps-set.

Current absolute values and related to source weights are preliminarily given. The paper suggests a suitable control algorithm of step up electronic devices and gives some numerical results referred to different duty-cycles of the power train.

2. ELECTRICAL POWER SECTION OF AN ELECTRIC ROAD VEHICLE

Electrical power sections of electric road vehicles (EV) consist of many subsystems and each of one interacts with all others. The basic configuration of a sample electrical drive for EV is shown in fig. 1. DC power section of the drive is traditionally constituted by an electrochemical battery, capable to cover the main power demand of power train in the time interval between two consecutive home repairs. Nowadays it is possible to improve this section by adding a supercap set and an additional DC/DC electronic power converter, which provides to a bi-directional flow of electrical energy and controls voltage output during load power variations. Supercap sets improve power supplying sections, because they cover current peaks during braking and starting and, hence, obtain increases of batteries life and of efficiency.

Both results are, however, obtained at the best only if the supporting action of supercaps to electrochemical batteries is properly controlled. The evaluation of the more useful control strategies can be obtained by analyzing the behaviour of the both power sources for solving problems related to their integration and to their fully compatibility. Theoretical analyses of such system operating conditions can be successfully performed on the basis of their mathematical models and on the digital simulation of practical applications. In the following, each component of the system is shortly analysed and analytically represented. Where previous technical literature does not give enough experimental results to validate theoretical model (i.e. for the step-up and the electrochemical capacitor-based device) results of bench tests of subsystems are given.

2.1 Electrochemical batteries

The behaviour of electrochemical batteries is not only dependent on the currents they carry out, but, also, on their state of charge. These behaviour can be, however, still be represented by an equivalent electrical network consisting of a source of constant voltage, E_b a variable inner resistance whose values are function of two variables, i_b and Q_b , i.e. $R_b(i_b, Q_b)$. Results of our previous theoretical and experimental researches [3] have shown that for lead-acid batteries a polynomial approximation of R_b may be obtained. For this reason we can set:

$$R_b(i_b, Q_b) = \sum_{v=0}^N \alpha_v(Q_b) \cdot i_b^v.$$

2.2 Electrochemical capacitor-based device

Electrochemical capacitor modules can be successfully used to store electrical energy [4] in the on board power supply systems of electrical vehicles because they have high value of p.u. capacity (i.e. very high values of ratios capacity/weight and capacity/volume see for example tab.1) so that it is possible to assemble small modules with high energy and power densities.

Different equivalent circuits of supercaps are given by technical literature [5]. For DC applications they can be represented by an RC series as shown in fig.2. The series resistance, R_s , has a very small value, while the capacitance C_s is very high (see tab.1).

Table1. Characteristic parameters of some supercaps.

Type	v	C_s	R_s	C/Weight	C/Vol	Power density	Energy density
	[V]	[F]	[mΩ]	[F/kg]	[mF/m ³]	[W/kg]	[Wh/kg]
Epcos 67F/42V	42	67	18	6.7	7.0	2450	1.6
Epcos 150F/42V	42	150	12	9.4	10.0	2297	2.3
Epcos 100F/56V	56	100	18	3.6	2.8	1600	1.6
Maxwell BMOD0115	42	145	10	9.0	6.6	2900	2.2
Maxwell BMOD0117	14	435	4	66.9	58.0	1900	1.8

These capacitors are, hence, capable to change electrical energy rapidly and with high efficiency [6]. Supercapacitor's mathematical model (see fig.2) for use in power applications has been validated by means of experimental tests on the EPCOS module ($R=30$ mΩ, $C=67$ F, $V=42$ V).



Fig. 2. Electrochemical capacitor equivalent circuit

Supercaps have p.u. power density (i.e. electrical power/weight) greater than this of electrochemical batteries. For this reason they are useful in practice to cover transient charging and discharging operations. Capacitor sets are chosen in agreement with rated battery capacitance and according to vehicle duty cycles, because the maximum energy amount, which they have to store is related to the load power requirements.

When a electrochemical capacitor-based device is used, the control of the capacitor voltage respect to the bus-bar voltage is made by a bi-directional DC/DC converter: during discharge operations, the converter acts as step-up, supplying

load in spite of capacitor energy. During charge operations, the converter acts as step-down, feeding the capacitor either from electrochemical battery system or from the load during energy recovering time intervals.

2.3 Step-up Converter

Supercaps can be used in practice only if they are equipped by step-up and step-down converters. Their performance analysis should be, hence, carried out by referring to dynamic operations of such converters, whose non-linear behaviour has to be taken into account. It is known that non-linearities of step-up converters can not be easily approached by analytical functions. Practical results can be, however, easily obtained by means of digital simulations, implementing and solving non-linear systems of differential equations. The supercap electric power supplying section can be, generally, represented by an equivalent electrical network of the type of fig.3, where supercaps are still simulated by means of a RC series. Well-known text books [7] suggest the transfer function of ideal DC/DC converters by means of the following equations:

$$d = \frac{t_{on}}{T_s}, \quad (1)$$

$$\frac{v_u}{v_{in}} = \frac{1}{1-d},$$

where d , is the switch duty ratio, T_s is the switch time period and t_{on} the switch on duration.

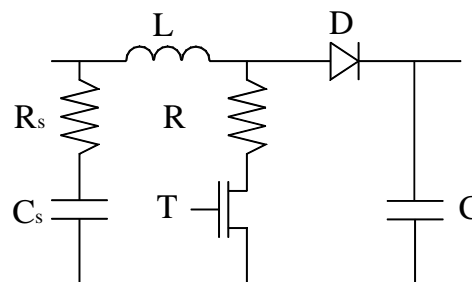


Fig.3 Equivalent electrical supply network of supercap acting on step-up converter

Eq.s (1) represent the mathematical model of an ideal step-up, because they don't take into account the effect of parasitic element, due to losses associated with the inductor, the capacitor, the switch and diode. This model cannot be successfully used in practice in the whole range of duty cycle (i.e. for $0 \leq d \leq 1$) because it obtains accuracies that exceed limits required by many practical applications. As an example fig. 4 shows a family of characteristics of a step-up converter for output currents ranging between 2-60 A. The main parameter values of the step-up considered are given in the same figure. It shows that voltage amplification vs duty cycle laws differ from ideal one mainly for higher value of duty ratio. For each output current it exists a breakdown value of duty cycle, which represents the upper operating value. Besides, fig.4 gives evidence that the maximum value of voltage amplification depends on the load current and that it decreases as load current increases. Numerical values evidenced by fig. 4 show that digital simulations of electrical drives must use mathematical models of step-up capable to take into account losses of real components.

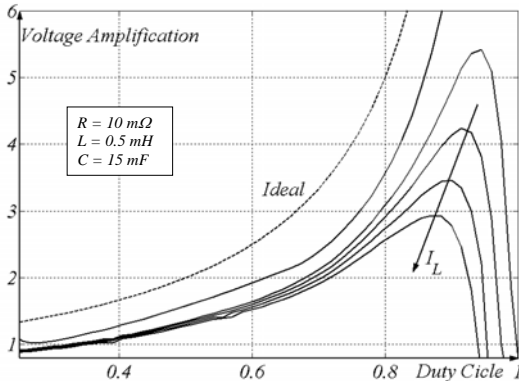


Fig.4. Voltage Amplification Characteristics of a step up chopper for different output current value

3. CONTROL STRATEGY

To really improve battery life and to optimise sizes and weights, power supply sections of EV using compound sets involving supercaps and electrochemical batteries, require a preliminary evaluation of control strategies and, then, the design and the accomplishment of proper control techniques. Strategies provide to state how to manage energy flows from, to and between electrochemical batteries and supercaps. Therefore, their goal is to give rise to control algorithms of power flows that obtain the highest possible values of charge and discharge efficiencies and that provide to smooth battery current peaks. During acceleration times or load variations these last ones have to be supported by supercaps. Currents carried out by batteries are strictly connected with the dc link voltage. Therefore, PFS implies the control of chopper output voltage by varying its duty cycle. With reference to a sample case, where only discharge time are dealt with, we have pointed out a control technique which combines a feedback control on the battery current with a “threshold” control as shown by fig.5. The control technique enables the chopper to operate only when the load current exceeds a given threshold value.

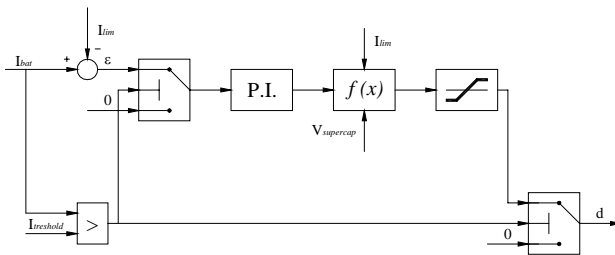


Fig.5. Digital control system scheme of the electrical drive.

Therefore, in a preliminary phase, the control system has to compare actual current, flowing from battery set, with the given threshold value. The comparison is made by a block, whose logical output enables two switch blocks in cascade (fig.5). Really, to avoid interferences with other elements of the control scheme (as PI regulator), the current threshold has to be set to a value slightly lower than the limit one (i.e. $0.9 \cdot i_{lim}$). Furthermore, if the current threshold is assumed too close to the limit value, the current oscillation, intrinsically generated by chopper operations, can give rise to repeated threshold overcoming during feedback operations. As a consequence, we can have an unstable behaviour of the system and a remarkable increase of current amplitude oscillations.

If battery current is lower than the limit value, chopper duty cycle has to be set to nil, so that the controlled semiconductor device in the chopper remains in an interdiction state. In such a way, the chopper diode is reversed biased, thus always disconnecting the supercap from the power train. Otherwise, if the load current exceeds the battery limit value, chopper has to be active and has to impose an output voltage equal to:

$$v = e - R_b \cdot i_{lim}$$

where R is the resistance of the battery set and e is the no-load voltage. As a first approach to the evaluation of the duty cycle, it can be used the following relationship which correlates the duty cycle of a step up chopper with the input and the output voltages:

$$d = 1 - \frac{v_{in}}{v_{out}}$$

Therefore, during supercap discharge, the control system has to set a progressively increasing duty cycle theoretically equal to

$$d = 1 - \frac{e - R_b \cdot i_{lim}}{v_{supercap}} \tag{2}$$

where $v_{supercap}$ is the actual voltage on the supercap set. Eq.(2) implies inaccuracies due to the approximation of the models and to errors made in the evaluation of supercap voltage. Above all, the battery set resistance can not be assumed constant, since it varies with the current and with the state of charge (SOC). Moreover, the control algorithm is very sensitive to a variation of the battery set resistance. With the aim of increasing the stability and robustness of the system, a control feedback of the batteries current can be added. Then, the current error, deriving from the comparison between the actual batteries current value and the given limit one, is evaluated by a PI standard regulator. The evaluation of the duty cycle is adjusted by adding at the limit current the PI output signal Δi , i.e.:

$$d = 1 - \frac{e - (R_b \cdot i_{lim} + \Delta i)}{v_{supercap}} \tag{3}$$

Referring to the control scheme of fig.5, eq.(3) is evaluated by the “f(x)” block. The approximation made for the chopper transfer function can give rise to an unstable behaviour when supercap voltage decreases and reaches a given low value. This phenomenon is due to control system, that requires voltage higher than the maximum value, which a real chopper can reach in practice before the output voltage rapidly decreases. For this reason, the addition of a saturation block for the duty cycle signal is suitable. In particular, saturation block has to limit duty-cycle when it exceeds a value corresponding to the maximum output voltage of the chopper for each load current; in our case the limit value has been set to 0.8.

Besides, another switch needs to be put in the control scheme for preventing error accumulations in the PI regulator, when the current is lower than the threshold and the chopper is disabled. This variation of the PI state, especially if the chopper is disabled for a long time interval, may produce a slower dynamic performance and current

overshooting when the chopper is again reactivated. A simple solution is to set the current error to nil during this phase.

Finally fig.6 shows the scheme of the electrical drive emphasizing the connection of the control system and the presence of the transducers.

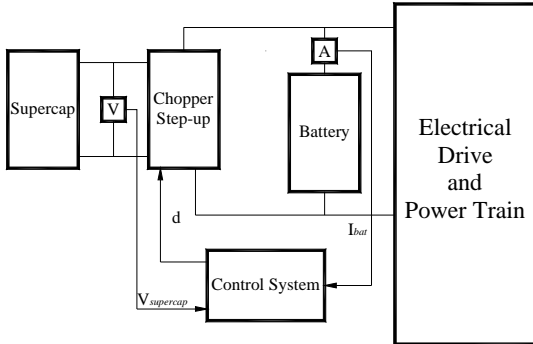


Fig.6. Block diagram of the whole system needed to drive electrical vehicles

4. DIGITAL SIMULATION OF A SAMPLE APPLICATION

A sample numerical application can be useful to better explain working operations of an electrical drive for EV. The drive has been simulated in Simulink Environment. Specifically, different block models reproducing the physical dynamic of the drive components have been realized and they have been connected as shown in fig.7. Attention has been mainly focused on two different aspects:

- to verify the energetic efficiency and the possible integration of a battery-set, a supercap device and a finally step-up chopper;
- the dynamic performances of suggested control technique.

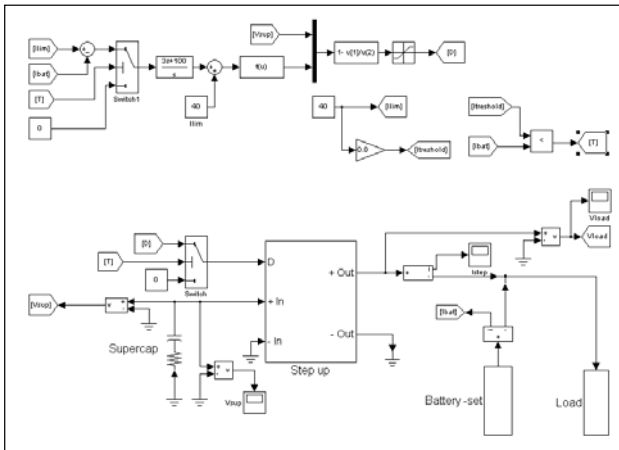


Fig.7. View of practical set-up of digital simulation

With reference to the first point it is possible to quantify the energetic efficiency of the whole system by means of the deep of discharge of supercap-set. This means to evaluate the contribution in terms of discharge energy of the two storage devices when a load peak occurs. For this reason it has been simulated a system of 18 batteries by 12.75 Volt with a capacity of 60 Ah, coupled with a step-up with two series supercaps by 67 F, initially charged at 42Volt. The step up chopper has a switching frequency of 10 kHz and an inner capacitance of 15 mF. In the simulation it has been considered a transient load step variation from 5kW to 16kW.

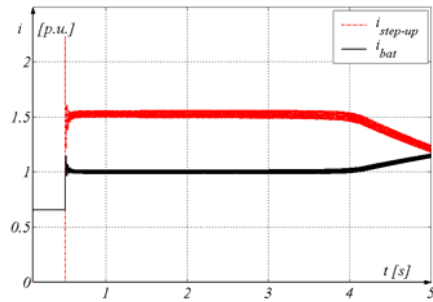


Fig. 8. Batteries and step-up currents carried out by a transient load variation

Fig. 8 shows the currents carried out by supercaps and batteries in p.u. of the limit current; during initial 0.5s time interval load current is lower than the limit current, set to 40A. Therefore, the contribution of supercap is nil. When the load switches, the supercap acts limiting the battery current approximately to the reference value. As it can be easily seen in the fig.9, voltage across the supercap progressively decays from an initial value of 1 p.u. until to 0.52 p.u.. The energy supplied by supercap set is almost equal to 3/4 of the previous by stored energy. In order to hold a constant output voltage, as the input voltage decreases, control system obviously has to increase step-up duty cycle. When duty cycle reaches the saturation value equal to 0.8, the supercap device contributes only partially to load feeding.

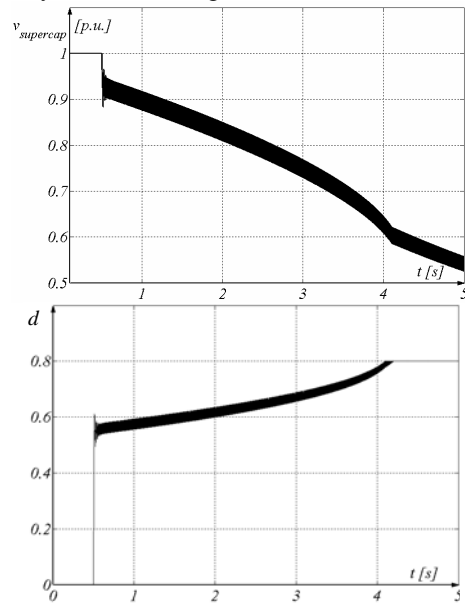


Fig. 9. Supercap voltage and switch duty ratio

When the phenomena appears the dc-bus voltage decreases and the limit batteries is overcame. Furthermore, the simulation (see fig.9) shows that supercap stored energy is not sufficient, in this case, to satisfy the power demand of the load.

With reference to second point, the dynamic response is satisfactory because the batteries current reaches the reference value with an oscillation bandwidth about 3% in a time interval of 0.1 second.

5. CONCLUSIONS

In the last few years many papers have been published dealing with the use of supercaps in compound supplying systems together with traditional electrochemical batteries.

They have generally underlined the usefulness of supercaps as auxiliary devices for supporting load current peaks. Always it is also written that proper control laws have to be pointed out for dc/dc converters needed for charging and discharging supercaps. The paper has dealt with a practical application of these compound systems for supplying electrical road vehicles and has presented a practical example of control law. A digital simulation of the whole driving system on board and of the power train effort gave evidence to some of practical problems arising when such compound techniques are used. The paper has also suggested some possible solutions to these problems. As a conclusion it has shown that proper designed supercap sets can be very useful to reach the expected results to improve system efficiency and to take longer battery life.

6. REFERENCES

- [1] Burke, A.F.; Hardin, J.E.; Dowgiallo, E.J.; Application of ultracapacitors in electric vehicle propulsion systems; Power Sources Symposium, 1990., Proceedings of the 34th International , 25-28 Jun 1990 Page(s): 328 –333;
- [2] Dowgiallo, E.J.; Hardin, J.E.; Perspective on ultracapacitors for electric vehicles; Battery Conference on Applications and Advances, 1995., Proceedings of the Tenth Annual , 10-13 Jan 1995 Page(s): 153 –157;

- [3] Piegari L., Tortora C., Veneri O.: A mathematical model of charge and discharge for lead batteries in electric road vehicles, EVS 18, October 20-24 2001, Berlin (Germany);
- [4] B.E. Conway: Electrochemical Supercapacitors: Scientific Fundamentals and Technological Application, Kluwer Academic/Plenum Publishers, New York, 1999
- [5] Zubieta, L.; Bonert, R.; Characterization of double-layer capacitors (DLCs) for power electronics applications Industry Applications Conference, 1998. Thirty-Third IAS Annual Meeting. The 1998 IEEE, Volume:2, 12-15Oct. 1998 Page(s): 1149 -1154 vol.2;
- [6] E. Pagano, L. Piegari, P. Tricoli: Ultracap – Based new Electrical Drives for off-road vehicles and rover- to be published on VDI 2003 – Antriebs systeme fur Off-Road-Ein satze;
- [7] N. Mohan, T. M. Undeland, W. P. Robbins: Power Electronics - Converter, Applications, and Design, John Wiley & Sons, Inc., 2002.

7. SHORT LIST OF THE SYMBOLS USED

R_b	<i>battery resistance</i>
R_s	<i>supercap resistance</i>
C_s	<i>supercap capacitance</i>
e	<i>battery no-load voltage</i>
$v_{supercap}$	<i>supercap voltage</i>
d	<i>chopper switch duty ratio</i>
i_{lim}	<i>limit current for the battery set</i>
i_{bat}	<i>battery current</i>
Q_b	<i>battery state of charge</i>

DIGITAL SLIDING MODE CONTROL OF X-RAY APPARATUS ELECTRICAL DRIVES

Čedomir Milosavljević, Darko Mitić, Boban Veselić, Milić Pejović, University of Niš, Faculty of Electronic Engineering, Niš, Serbia and Montenegro

Abstract: This paper presents system for coordinated control of three motors drive of X-ray system for thomography. The goal of the control system is to achieve taking of quality layer photographs. These photographs can be obtained if during the motion of X-ray source, X-rays are always crossing same two points. Operator, just above the scanning layer, determines the first point and the other point is on the photographic film. The operator also specifies the velocity of scanning. Presented problem has been solved by implementation of digital variable structure system with sliding mode algorithm. Simulation and experimental results are also presented.

Key Words: Variable structure control systems, sliding modes, tracking control.

1. INTRODUCTION

It is unquestionable fact that X-ray diagnostics in a great deal relies on the quality of X-ray photographs. One of the most quality techniques is so called thomography scanning. This technique achieves scanning of one specific layer of the patient. The whole procedure is performed in the following way: During scanning, the X-ray source and the casket with film, which are placed at the opposite sides of the patient, are simultaneously moving with the same velocities, but in the opposite directions. During this movement, the X-ray source is also rotating around the joint, in order to provide X-rays to cross-predefined points: above the scanning layer and on the film. The layer is defined by the doctor, and implemented by the X-ray technician. The manufacturer of X-ray apparatus, in our country is Ei-Jugorendgen Corporation. Their apparatus, called "Tomorastix" is technological obsolete solution based on Siemens license. The realization of above-mentioned motion is achieved with rigid joint (lever) between X-ray source and casket with film, which support must be manually adjusted every time when new scanning parameters are required. This fact increases preparation time. The basic idea is to make this apparatuses more flexible and productive by allowing the operator to set parameters over keyboard and monitor, while the apparatus with control system could automatically perform scanning according to input parameters. It is not very hard to conclude that solving of this problem requires implementation of three servomotors. For the realization of the control elements for every servo system, and for their coordinated control, a following request has been set: Obligation to use modern technological solutions based on information technologies with implementation of digital signal processor (DSP).

After predefined basic project demands, technical demands has been studied in detail, kinematics of system motion is defined, and on it's basics referent trajectories have been determined, what will be the subject of second section. The third section contains analyses of different control algorithms abilities for realization of presented task. On the ground of that analyses it is concluded that the variable structure digital control (DVSC) algorithm is the most

common for realization of the presented problem. Short description and servo system projection on the bases of DVSC algorithm is given in section four. The fifth section is dedicated to simulation and experimental verification of projected system using laboratory model. The conclusion and the references are given at the end of the paper.

2. DEFINITION OF DESIRED TRACKING TRAJECTORIES

The basic configuration of the above-mentioned apparatus, beside the table for patient, contains the post, which moves along the table. The post drive is achieved by servomotor, over gear head and gear wheel with chain. The post carries X-ray source. The X-ray source rotates around the joint drove by its servomotor with appropriate gear head. The casket with film, which is placed under the table, during the scanning moves simultaneously with the post, but in the opposite direction. As a drive for the casket with film it is anticipated separate servo drive with gear head and gear wheel with chain. The system for post drive is then the leading system, while the other two systems, drives for rotation of X-ray source and casket, are the tracking systems. In order to define motion trajectories, we should first define the trajectory of the leading system. The scanning is always performed with the constant velocity, so the post drive is the velocity servo system. It should achieve predefined velocity profile. Because the constant velocity is required, we picked the trapezoidal shape of referent velocity. So, the drive must reach the desired position with linearly increasing velocity, during scanning the drive must have constant velocity, and after that the velocity must linearly decrease until it reaches zero. After the end of scanning, and before the start of a new one, this drive must be set initial (zero) position. Considering the fact that the X-rays, in the plane parallel to the post motion direction, must always cross the same point, other two drives – X-ray and casket – must be positioning servo systems which will perform synchronous motion, in common functional dependence with the post position. On the basis of above mentioned, the referent post velocity is

$$\omega_s = \begin{cases} \frac{A}{t_1}t & \text{for } 0 < t \leq t_1 \\ \mathbf{A} & \text{for } t_1 < t \leq t_2 \\ -\frac{A}{t_1}t & \text{for } 0 < t \leq t_1 \end{cases} \quad (1)$$

Integration of (1) gives current position of the post

$$\theta_s = \begin{cases} \frac{A}{2t_1}t^2 & \text{for } 0 < t \leq t_1, \\ \mathbf{A}t - \frac{At_1}{2} & \text{for } t_1 < t \leq t_2, \\ -\frac{A}{2t_1}\{t - (t_1 + t_2)\}^2 - 2t_1t_2 & \text{for } 0 < t \leq t_1. \end{cases} \quad (2)$$

On the basis of X-ray apparatus kinematics, the following functional dependences for the X-ray source and casket are given:

Referent position of motor for casket drive is

$$\theta_k = \frac{1}{N_2} \left(-\frac{Hx_c - hx}{H-h} \right). \quad (3)$$

The time derivative of the equation (3) gives the casket drive motor velocity profile

$$\omega_k = -\frac{1}{N_2} \frac{h}{H-h} \dot{x}, \quad (4)$$

where: H - stands for X-ray distance from the table, h - stand for the distance between virtual point and the table, x - stands for post position according to the initial (zero) position, N_2 - stands for reduction of gear head for casket drive. Minus sign in equations (3) and (4) is due to the opposite motion directions of casket and post.

Referent position of X-ray source is

$$\theta_z = \arctg\left(\frac{x_c - x}{H-h}\right), \quad (5)$$

while the referent velocity is

$$\omega_z = \frac{1}{1 + \left(\frac{x-x_c}{H-h}\right)^2} \frac{\dot{x}}{H-h}. \quad (6)$$

Geometrical shapes of referent velocity for post drive and reference position for casket drive are shown on figs. 1 and 3, respectively

Initial positions of X-ray motor drive and casket motor drive are respectively

$$\theta_{z0} = \arctg\left(\frac{-x_c}{H-h}\right), \quad (7)$$

$$\theta_k = \frac{1}{N_2} \frac{H}{H-h} x_c. \quad (8)$$

After establishing the motion laws, maximal velocities, mechanism parameters the appropriate motors, gear heads, encoders and servo amplifiers has been chosen for the drives of the post, casket with film and X-ray source. The DC motors with permanent magnets are chosen as well as planetary gear heads and opto-electronic encoders with 1000 counts per turn resolution with signals for direction detection, which gives total resolution of 4000 counts per turn. As servo amplifiers, four quadrant amplifiers with pulse wave modulation are chosen. All mentioned elements can be found on the market, and for this problem we picked elements manufactured by Maxon Corporation because of their quality and unification. For implementation of digital control algorithm it is anticipated DSP manufactured by the Texas Corporation, type TMS320LF2407, which is specially designed for motion control.

3. SELECTION OF CONTROL ALGORITHMS

After establishing the desired motion trajectories and elements necessary for system physical realization we approach to determination of control algorithms for above mentioned servo systems.

The post drive is velocity servo system with constant velocity in the operating area and slope velocity in the area before and after the operating area. According to the fact that the motor as a plant, in this system, is of type zero, in order to achieve referent velocity without error in operation area, it is necessary to introduce integral action in the system. It

means that is necessary to import PI controller. This will cause the error while tracking the slope velocity to be constant and as smaller as the gain of control loop is bigger. But, this could lead to the stability problem and it could increase controller complexity. The increase system type order could result in bigger dynamic errors. From the other hand, because the drives of casket and X-ray source are position servo systems, which follow the post position in accordance to functional dependences, the dynamic trajectory deviations of the post from the referent trajectories will necessarily cause deviations of motion trajectories of a casket and X-ray source. This deviation would lead to the degradations in the quality of scanning which is unacceptable. For this reasons the post velocity control must be achieved with the high quality. In the last ten years of the 20. century many studies have been performed, which showed that the variable structure with sliding mode control algorithms can provide high quality of servo systems even with digital signal processing. For that reason, in this research it is initially accepted to realize motion control for above mentioned apparatus with algorithms based on sliding mode (SM). Digital implementation of these algorithms at some point degrades the properties of SM, which in that case became quasi sliding. Control system, in that case, loses invariance to the parameter and external disturbances, but it remains extremely robust. Different approaches are recommended in the literature in order to realize digital SM. In this research it is implemented algorithm developed on the Department of Automatic Control of Electronic faculty in Niš, published in the paper [1]. In order to complete this paper in the next section some basic elements of mentioned algorithm will be presented.

4. DIGITAL CONTROL SM ALGORITHM

We will start from the dynamic system that describes the plant (in this case above-mentioned drives) with the discrete time model

$$\mathbf{x}((k+1)T) = \mathbf{A}_d \mathbf{x}(k) + \mathbf{b}_d u(kT) + \mathbf{d}(kT) \quad (9)$$

where $\mathbf{x} \in \mathfrak{R}^n$ - system state vector, $u \in \mathfrak{R}$ - scalar control, $\mathbf{d} \in \mathfrak{R}^l$ - disturbance vector, T - sampling period, \mathbf{A}_d and \mathbf{b}_d are respectively $n \times n$ state matrix and n - dimensional input vector. It is assumed that the pair $(\mathbf{A}_d, \mathbf{b}_d)$ is fully controllable. Considering the fact that the nature of controlled processes is continual, parameters of presented model are obtained according to the equation

$$\mathbf{A}_d = e^{\mathbf{A}T}, \quad \mathbf{b}_d = \left(\int_0^T e^{\mathbf{A}\tau} d\tau \right) \mathbf{b}, \quad \mathbf{d} = \left(\int_0^T e^{\mathbf{A}\tau} d\tau \right) \mathbf{f}, \quad (10)$$

where \mathbf{A} , \mathbf{b} , \mathbf{f} are appropriate parameters of the continuous time model. It is further assumed that the so-called matching conditions [2] are satisfied, i.e. all disturbances, external and internal are acting through the control channel.

The goal is to determine such a control $u(k)$ which will on the hyper plane S ,

$$S = \left\{ \mathbf{x} \mid s(\mathbf{x}) = \mathbf{c}^T \mathbf{x}(k) = 0, k = 0, 1, 2, \dots; \right. \quad (11)$$

$$\left. \mathbf{c}^T \in \mathfrak{R}^{1 \times n}, c_i = const; \mathbf{c}^T \mathbf{b}_d \neq 0, \right.$$

which defines desired motion, provide stable quasi-sliding mode (QSM).

As it is well known, system motion with QSM consists from three modes [3]: reaching mode (RM), quasi-sliding mode (QSM), and steady state mode (SS). Starting from the

Lyapunov function $V(\mathbf{x}) = |s(k)|$ or $V(\mathbf{x}) = s^2(\mathbf{x})$ for discrete system necessary conditions for formation and existence of QSM can be stated in several ways

$$\begin{aligned} 1) & |s(k+1)| \leq |s(k)|; \\ 2) & \Delta s(k) \operatorname{sgn} s(k) < 0 \cup [s(k+1) + s(k)] \operatorname{sgn} s(k); \\ 3) & |s(k+1)s(k)| < s^2(k) \end{aligned} \quad (12)$$

$$4) 2s(k)\Delta s(k) < \Delta s^2(k), \quad \Delta s(k) = s(k+1) - s(k)$$

what depend from the definition of QSM itself. Continuous-time sliding mode can be formed only by switching control, while in discrete-time system, in ideal conditions, can achieve discrete sliding mode (DSM) with digital control without switching (except in the sampling moments). The condition for formation of such sliding mode is given by equation [4]

$$s(k+1) = s(k) = 0, \quad \forall k > k^* \quad (13)$$

which can be stated as follows: if for some $k=k^*$ $s(k^*)=0$, then $s(k>k^*)=0$. Practically equation (13) is deduced to the condition $s(k+1)=0$. From this condition, and after substituting (9) in (11) u becomes

$$u = -(\mathbf{c}^T \mathbf{b}_d)^{-1} \mathbf{c}^T \mathbf{A}_d - (\mathbf{c}^T \mathbf{b}_d)^{-1} \mathbf{d} \quad (14)$$

Substituting (14) in (9) gives motion equation in the sliding mode.

If we first assume nominal system without disturbances (external and internal), control (14) become

$$u = u_{eq} = -(\mathbf{c}^T \mathbf{b}_d)^{-1} \mathbf{c}^T \mathbf{A}_d \quad (15)$$

If the desired dynamics in the reaching mode is expressed by the equation [3]

$$s(k+1) - s(k) = u_{eq} - f(s(k), x(k)) \quad (16)$$

where $f(s(k), x(k))$ is nonlinear function of system state and sliding plane, it provides system robustness even in the disturbance action case.

Golo [1] suggested that instead of model (9) one should use model

$$\begin{aligned} \delta \mathbf{x}(k) &= \frac{\mathbf{x}(k+1) - \mathbf{x}(k)}{T} = \mathbf{A}_\delta \mathbf{x}(k) + \mathbf{b}_\delta u(kT), \\ \mathbf{A}_\delta &= \frac{\mathbf{A}_d - \mathbf{I}}{T}; \mathbf{b}_\delta = \frac{\mathbf{b}_d}{T}, \end{aligned} \quad (17)$$

and reaching law

$$\begin{aligned} \delta s(k) &= \frac{s(k+1) - s(k)}{T} = -\mathbf{c}_\delta^T \mathbf{A}_\delta \mathbf{x}(k) - \Phi(s(k), \mathbf{x}(k)), \\ \mathbf{c}_\delta^T \mathbf{b}_\delta &= 1, \Phi(s(k), \mathbf{x}(k)) = \min \left\{ \frac{|s(k)|}{T}, \sigma + q|s(k)| \right\} \operatorname{sgn}(s(k)), \end{aligned} \quad (18)$$

$q, \sigma > 0.$

Such control law provides reaching of the sliding mode in a finite time, with soft descent, what provides ideal sliding in the nominal system, i.e. extreme robustness and quasi-sliding mode in the case of parameter and external disturbances. Robustness can be further improved by implementing additional disturbance estimator in the form of [5]

$$\mathbf{d}(k) \approx \mathbf{d}(k-1) = \delta \mathbf{x}(k) - \mathbf{b}_\delta u(k-1) - \mathbf{A}_\delta \mathbf{x}(k-1) \quad (19)$$

with assumption that the disturbance and its derivate are bounded.

The determination of controller parameters is performed in the following way: the characteristic polynomial roots in the sliding mode, which provide asymptotic stability of the discrete system are given as

$$\delta_i = \frac{e^{-\alpha T} - 1}{T}, \quad \alpha_i > 0, \alpha_i \neq \alpha_j, i, j = 1, 2, \dots, n-1. \quad (20)$$

and then the coefficients which define sliding hyper plane \mathbf{c} are calculated according to

$$c_i = \frac{1}{(i-1)!} \frac{d^{i-1} \prod_{j=1}^{n-1} (\delta - \delta_j)}{d \delta^{i-1}} \Big|_{\delta=0}. \quad (21)$$

what finally gives for the implemented system model

$$\mathbf{c}_\delta^T = [c_1, c_2, \dots, c_{n-1}, 1] \mathbf{P}^{-1} \quad (22)$$

where \mathbf{P} is transformation matrix:

$$\mathbf{P} = \mathbf{M}_c \begin{bmatrix} a_2 & \dots & a_n & 1 \\ \vdots & & & 1 \\ a_n & & 1 & \\ 1 & & & \mathbf{0} \end{bmatrix} \quad (23)$$

\mathbf{M}_c is the controllability matrix of the system $(\mathbf{A}_\delta, \mathbf{b}_\delta)$, while $a_i, i=2, \dots, n$ are coefficients of characteristic polynomial

$$\det[\delta \mathbf{I} - \mathbf{A}_\delta] = \delta^n + a_n \delta^{n-1} + \dots + a_2 \delta + a_1 \quad (24)$$

Remark: In the case of tracking systems, state variables in the model (9) represent the deviation of system output from the system input and its derivatives up to $n-1$ order. Considering the fact that the system for presented case can be approximated by the second order, so beside error signals it is necessary to have knowledge of its first derivative too. Because the desired motion trajectory of the leading system is known and preciously controlled, its first derivative is known too. In the other case appropriate estimation of the motion trajectory derivative is required.

Laboratory model which was used to verify the effects caused by implementation of digital control algorithm consists of two small motors with similar parameters, two channel and four quadrant transistor power amplifiers with pulse wave modulation and two opto- electronic encoders. The control signal was generated from the PC with acquisition card ED2001, which has two A/D and two D/A converters, counting section and connection panels. Control algorithm is realized in C programming language.

Motors with amplifiers as plants was identified with nominal continuous model [1]:

$$\dot{\mathbf{x}}(t) = \begin{bmatrix} \dot{x}_1 \\ \dot{x}_2 \end{bmatrix} = \begin{bmatrix} 0 & 1 \\ 0 & -16 \end{bmatrix} \begin{bmatrix} x_1 \\ x_2 \end{bmatrix} + \begin{bmatrix} 0 \\ 680 \end{bmatrix} u(t) \quad (25)$$

for which electrical time constant, viscous and Columb friction and mechanical load were neglected.

Implementation of the described procedure with the sampling period of $T=0.0004$ s, gives:

$$\mathbf{A}_d = [1, 0.0003987; 0, 0.99362]$$

$$\mathbf{b}_d = [0.99362; 0.27113],$$

$$\mathbf{A}_\delta = [0, 0.99680681575797; 0, -15.94890905212781]$$

$$\mathbf{b}_\delta = [0.135710330286; 677.828634715417]$$

$$\mathbf{c}_\delta^T = [-0.0220632, -0.00147088] \text{ for } \alpha=15; \text{ We chose}$$

$q=10, \sigma=20; \mathbf{c}_\delta^T \mathbf{A}_\delta = [0, -0.00146618];$ so the control is

$$u(k) = -0.00146618x_2(k) - \min\{2500|s(k)|, 20+10|s(k)|\}$$

5. SIMULATION AND EXPERIMENTAL RESULTS

For the verification of the whole control system of abovementioned X-ray apparatus, and considering limited equipment resources, system for the post motion control was

simulated by the computer. Namely, as it was stated before, that system is velocity servo system with trapezoidal velocity profile, and it is not very hard to archive high accuracy of tracking such velocity trajectory. Other two electromotor system are supposed to track trajectories (3) and (5) in a functional dependence of angular position and velocity of leading system.

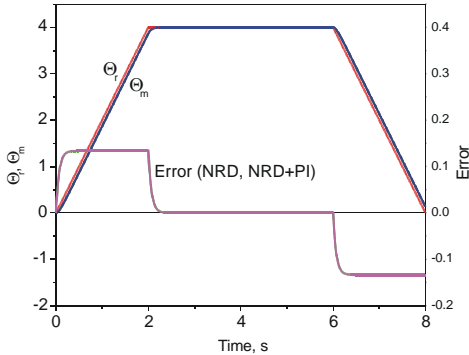


Fig. 1. Tracking error of post control system without information of reference signal derivative.

Simulation results for post drive system and casket drive systems are shown of figs. 1-3. Note that the disturbance rejection capabilities is exhibited. Fig. 4 represents commutation function $s(t)$ for the case when above mentioned digital algorithm (DVSC) was implemented, and when PI compensator was added to the algorithm.

In Fig. 5 and Fig. 6 a results of experimental verification of projected system for casket and X-ray source control system are given.

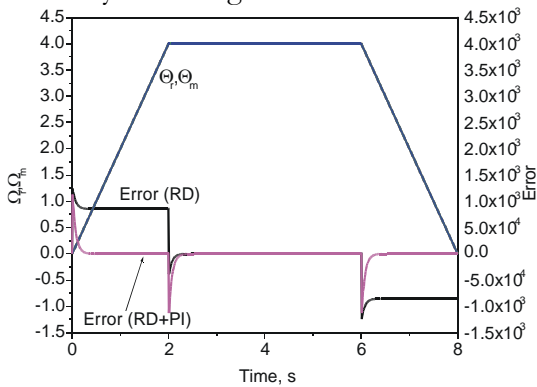


Fig. 2. Tracking error of post control system with information of reference signal derivative, obtained by real differentiator (RD) and with RD and additional proportional-integral compensator (RD+PI).

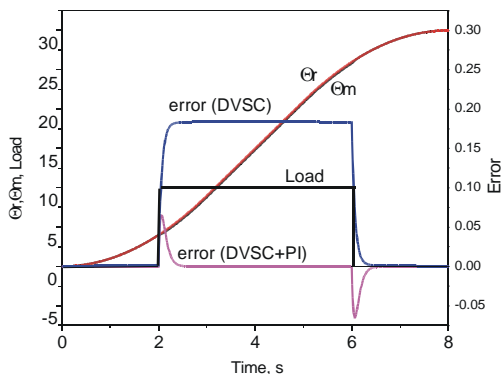


Fig. 3. Tracking error of casket control system with information of reference signal derivative :DVSC-projected

system; DVSC+PI- projected system with additional proportional-integral compensator.

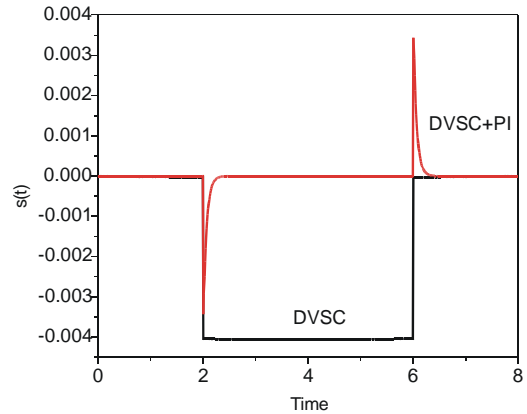


Fig. 4. Switching function dynamics of projected casket control system without or with proportional-integral compensator.

For the final verification of the projected system for coordinated control, additional system for animation of X-ray apparatus motion was realized. That additional system was realized with additional PC with acquisition card ED2001 and appropriate software. The animation results are shown on the figs. 7-9. On the bases of these figures it can be concluded that projected system has real chances for practical implementation in the X-ray system for thomography scanning.

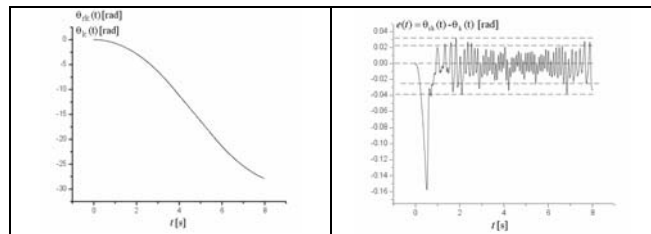


Fig. 5. Experimental results of casket positioning.

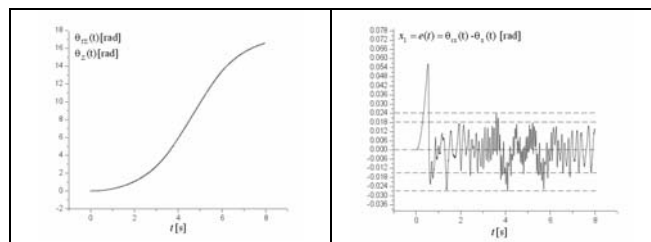


Fig. 6. Experimental results of X-ray source positioning.

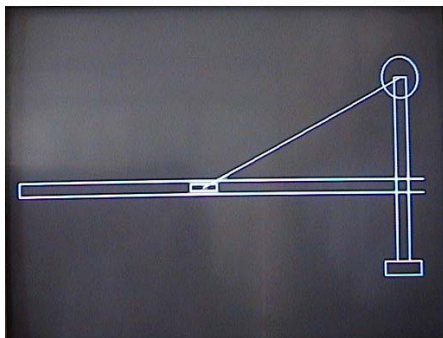


Fig. 7. Starting position.

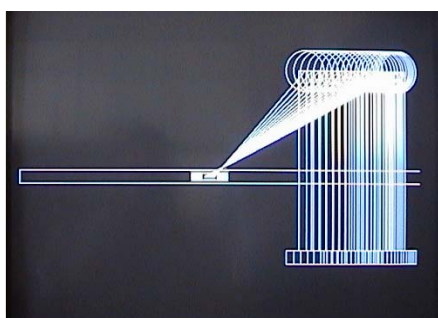


Fig. 8. Inter position.

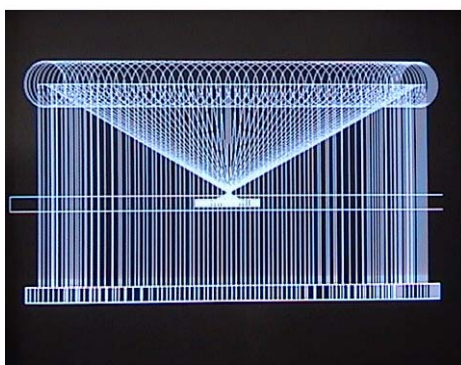


Fig. 9. Final position.

6. CONCLUSION

This paper is dedicated to the design, simulation and experimental verification of the digital control system for the electrical drive for tomography scanning. In the basis, the control problem is reduced to design of the velocity and position tracking servo systems, which are supposed to track the referent velocity or position profiles under mutual coordination. Namely, The leading system is velocity servo system with trapezoidal referent velocity, which position should be tracked by other two servo systems, according to the desired functional dependences. Since those trajectories are of ramp, parabolic or transcendental type, and high tracking accuracy is required, the problem was solved by digital sliding mode implementation. Short description of the implemented algorithm and control law design were given. Results of the digital simulation and laboratory model experimental investigation have proved high quality of the designed control system.

Acknowledgment

This research has been supported by the Ministry of Science, Technologies and Development of the Republic of Serbia, under project IT0125.

REFERENCES

- [1] Golo, G., Milosavljević, Č., (2000) *Robust discrete-time chattering free sliding mode control*, Systems&Control Letters 41, 19-28.
- [2] B. Draženović, "The invariance conditions in variable structure systems", *Automatica*, vol. 5, 1969, pp. 287-295.
- [3] W. Gao, Y. Wang, A. Homaifa, (1995) "Discrete-time variable structure control systems", *IEEE Trans. on Industrial Electronics*, vol. 42, no. 2, , pp.117-122.
- [4] Bučevac, Z. (1985) *Design of Digital Descrete Control Systems with Sliding Mode*, Ph. D. Disertation (in Serbian), Mech. Eng. Faculty University of Belgrade.
- [5] Su, W.-C., Drakunov, S. V., Ozguner, U. (2000) *An $O(T^2)$ boundary layer in sliding mode for sampled-data systems*. *IEEE Trans. AC-45*, No 3, 482-485.

PRINCIPLES OF OPERATION AND CONTROL OF DOUBLY FED RELUCTANCE MACHINES

Milutin G. Jovanović

School of Engineering and Technology, Northumbria University
Ellison Building, Newcastle upon Tyne NE1 8ST, United Kingdom

Abstract: The paper presents the fundamental space vector theory and analysis of one interesting and unusual slip power recovery machine - the Brushless Doubly Fed Reluctance Machine (BDFRM). This machine is a counterpart of the more famous Brushless Doubly Fed Induction Machine (BDFIM), and it is also closely related to a conventional double excited wound rotor induction machine (DEWRIM). The main advantage of the BDFRM over the BDFIM is the absence of copper rotor losses and therefore potentially higher efficiency. Furthermore, the reluctance rotor makes it much easier to control than the BDFIM and more reliable compared to the DEWRIM. The paper will explain the basic principles of the BDFRM operation, develop dynamic and steady state models, and finally examine some of its attractive properties.

Key Words: Brushless Drives/Control/Reluctance Drives

1. INTRODUCTION

A significant development in the early 1970s was the invention of the brushless doubly fed induction machine (BDFIM), also known as the self-cascaded induction machine [1]. This machine is a descendent of the classic cascaded configuration (Fig. 1), originally used in high torque applications with some adjustable speed capability. The speed control in these systems was normally achieved by external resistance variations on the stator side¹ which effectively eliminated the need for slip rings and brushes. The advantage of brushless structure was, however, offset by the very impractical and bulky dual machine construction offering poor drive efficiency (one of the two machines was usually operated at higher slips).

The previous deficiencies of the cascaded arrangement have been largely overcome by collapsing the two machines in a single BDFIM frame. The two stator windings now share the same magnetic circuit², but they do not directly couple because of different both pole numbers and applied frequencies. With a special cage rotor composed of nested coils and the number of nests equal to the *sum of the pole pairs of the stator windings*, it can be shown that there is rotor position dependent mutual coupling between the stator windings required for the machine to produce torque [2].

¹ In a modern implementation (Fig. 1), one would use a variable frequency power electronic supply for this purpose.

² It is possible using parallel paths for the two windings to be accommodated in the same slots.

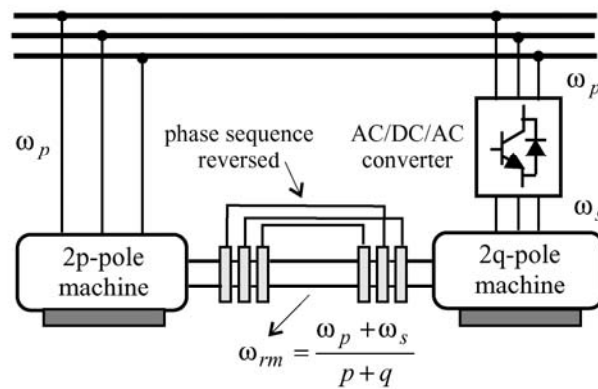


Fig. 1. Modern converter-fed cascaded machine (in reality, there is no slip rings - they are presented here just to show electrical connections of the rotor windings)

In the 1970s work on the BDFIM did not progress much beyond the basic design and the appearance of some prototypes. However, in the 1980s the advent of power electronics and low cost computing resulted in a revival of interest in the machine. Since then it has been used on a trial basis in some applications with modest speed ranges [3].

At the same time as the BDFIM was being developed some preliminary work was also being carried out on its close cousin, the brushless doubly fed reluctance machine (BDFRM) [4]. However, due to the lack of high saliency reluctance rotors available at the time, the machine could not give performance competitive with similar machines. It was consequently largely forgotten until the early 1990s [5, 6] when it has started to receive increasing attention from the research and industrial community.

The motivations for considering the BDFRM are a mixture of academic, practical and economic reasons. The machine is intellectually extremely interesting because of its unusual operating principle. The use of a cageless rotor, that can be similar to that of a synchronous reluctance machine (Synrel), should provide higher efficiency and more robust design than a comparably rated BDFIM [7] while retaining all the BDFIM merits the

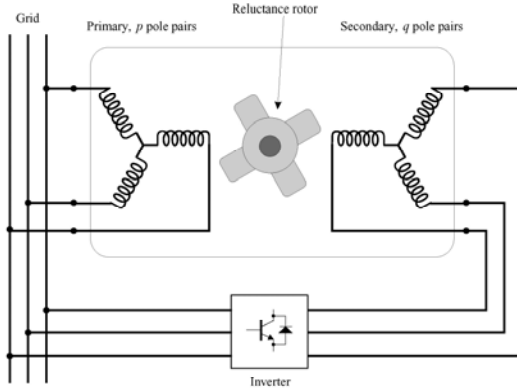


Fig. 2. Conceptual diagram of the BDFRM

most important being the possibility of using a partially rated inverter. Therefore, for larger drives the total system cost may lower considerably in comparison with conventional solutions, and especially in applications with restricted speed variations (such as wind turbines [6, 8] and pumps [3, 8]) where the inverter size can be further reduced. Another preferable feature of the machine is that, with the appropriately rated inverter, it allows user control of its mains power factor [9]. Finally, the absence of slip rings and brushes increases its reliability and lowers maintenance requirements relative to the Double Excited Wound Rotor Induction Machine (DEWRIM) which can be an extremely important advantage in, say, recently very popular off-shore wind power applications.

2. BASIC OPERATION PRINCIPLE

Fig. 2 is a simplified schematic of the BDFRM double winding structure. One can see that the windings are both connected to the mains supply - the primary directly, and the secondary indirectly via an inverter³. The reluctance rotor can be of any standard Syncrel's configurations - from a simple 'dumbbell' shape through to an axially-laminated or multiple barrier design. Unlike a conventional machine, the two stator windings and the rotor all have mutually different pole numbers as mentioned previously. The question we'll attempt to answer in the following is: "How does the machine develop any useful torque under this condition?"

In order to properly understand the essential torque producing mechanism of the BDFRM, we shall make the standard assumptions for ideal machine analysis: a linear magnetic circuit, sinusoidally distributed windings, and sinusoidal excitation currents. In addition, we shall assume that the inverse air-gap of the machine can be modelled as⁴:

$$g^{-1}(\theta, \theta_{rm}) = m + n \cos p_r(\theta - \theta_{rm}) \quad (1)$$

³It is also possible to short the secondary windings and operate the BDFRM as an induction machine. This 'fail-safe' mode may either be used for starting to prevent the inverter overloading, or in case of inverter failure during normal operation.

⁴It has been shown that this approximation adequately captures the basic influence of the rotor on the BDFRM performance [10, 11].

where $m \geq n > 0 \triangleq$ some design parameters, $p_r \triangleq$ number of rotor poles (not pole pairs), $\theta_{rm} \triangleq$ mechanical angular position of the rotor high-permeance axis and $\theta \triangleq$ mechanical angle around the machine.

If the $2p$ -pole primary and $2q$ -pole secondary windings are being fed with three phase sinusoidal currents of frequencies ω_p and ω_s and amplitudes I_{pm} and I_{sm} respectively, then the corresponding resultant mmfs per air-gap are:

$$F_p(\theta) = F_{pm} \cos(\omega_p t - p\theta) = \frac{3}{2} n_p I_{pm} \cos(\omega_p t - p\theta) \quad (2)$$

$$F_s(\theta) = F_{sm} \cos(\omega_s t - q\theta) = \frac{3}{2} n_s I_{sm} \cos(\omega_s t - q\theta) \quad (3)$$

where $n_{p,s} \triangleq$ effective turns/phase/pole of the windings.

The basic operation of the machine follows from the well-known expression for the interaction of the above mmf waveforms with the inverse air-gap function (1) to produce a flux density in the air-gap:

$$B_{p,s}(\theta, \theta_{rm}) = \mu_0 g^{-1}(\theta, \theta_{rm}) F_{p,s}(\theta) \quad (4)$$

Substituting (1) and (2) into (4) one can derive the following relationship:

$$B_p(\theta) = \mu_0 m F_{pm} \left[\cos(\omega_p t - p\theta) + \frac{n}{2m} \cos[(\omega_p - p_r \omega_{rm})t - (p - p_r)\theta] + \frac{n}{2m} \cos[(\omega_p + p_r \omega_{rm})t - (p + p_r)\theta] \right] \quad (5)$$

where $\theta_{rm} = \omega_{rm} t$ (in steady state) and $\omega_{rm} \triangleq$ rotor angular velocity.

A number of remarks can be made about (5). Firstly, it has a similar form to a modulated waveform after mixing in a radio transmitter. However, in this case we have a frequency shift in relation to both the temporal and spatial terms. Secondly, note that the resultant flux density waveform has a component at the same temporal and spatial frequencies⁵ as the winding mmf, as well as two sidebands whose frequencies are dependent on the number of rotor poles (p_r). It is therefore possible to choose a value for p_r so that these are equal to the respective secondary mmf frequencies. In this case, the rotor modulating influence provides magnetic coupling between the two windings which is the necessary pre-requisite for the machine torque production.

Considering the primary sidebands and the secondary mmf waveform the above conjecture is equivalent to:

$$\cos[(\omega_p \pm p_r \omega_{rm})t - (p \pm p_r)\theta] = \cos(\omega_s t - q\theta) \quad (6)$$

Equating the relevant terms it is easy to show that⁶:

$$\omega_{rm} = \frac{\omega_p \pm \omega_s}{p \pm q} \quad (7)$$

$$p_r = |p \pm q| \quad (8)$$

⁵The meaning of 'spatial frequency' is hidden in the θ multiplying terms in (5). It is nothing else but the pole number of a particular flux density component.

⁶The same angular velocity relationship applies to a traditional cascaded machine.

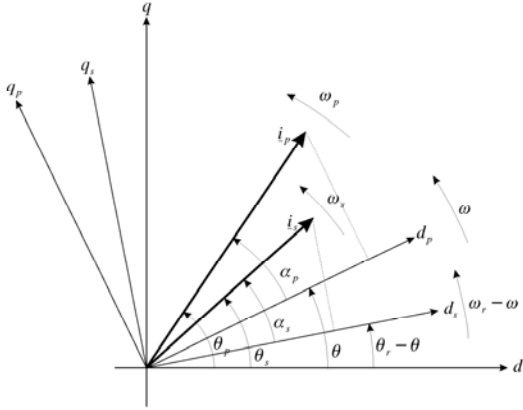


Fig. 3. Reference frames and characteristic angles used in space vector theory of BDFRM

The condition in (7) means that the rotor has to be rotating at this ω_{rm} for its mixing action to change the primary temporal frequency to become that of the secondary. Similarly, if (8) is satisfied then the p pole-pair field of the primary is being transformed to the q pole-pair field of the secondary. Exactly the same relationships as above are found looking at the secondary flux sidebands interactions to the primary field via the rotor.

The only way that the machine can develop torque is if the flux linking both windings is a function of the rotor position. One may suspect that this is the case from (7). This assertion can be formally proved by calculating the BDFRM phase inductances [5, 11]. The obtained expressions indeed show that only the mutual inductances between the primary and secondary windings are rotor position dependent i.e. they contain $dL/d\theta_{rm}$ terms (the self inductances are constant). This results in variations of co-energy in the machine with rotor movement and consequently the torque can be produced.

The fact that only the mutual inductances are responsible for torque production means that the fundamental component of the flux density for each winding (see (5) for the primary example) does not by itself contribute to any torque and is effectively a leakage component. This is clearly in contrast to a conventional machine (where the main flux component is torque producing) and represents one of the principal limitations of the machine.

3. DYNAMIC EQUATIONS

The dynamic equations for the BDFRM are very unusual and interesting but their development is quite complex [5] to be presented in this paper (a detailed derivation can be found in [11]). For a thorough understanding of these equations one should first examine the reference frames they are defined with respect to (Fig. 3). As usual in practice, the subsequent study shall imply that $p_r = p + q$ and $p_r\omega_{rm} = \omega_r = \omega_p + \omega_s$ this corresponding to the '+' case in (7) and (8). This approach is common in the BDFRM literature.

The stationary dq frame equations in standard space

vector notation can be shown to be [11]:

$$\underline{v}_{p_s} = R_p \underline{i}_{p_s} + \left. \frac{d\lambda_{p_s}}{dt} \right|_{\theta_r, \text{const}} + j\omega_r L_{ps} \underline{i}_{s_s}^* e^{j\theta_r} \quad (9)$$

$$\underline{v}_{s_s} = R_s \underline{i}_{s_s} + \left. \frac{d\lambda_{s_s}}{dt} \right|_{\theta_r, \text{const}} + j\omega_r L_{ps} \underline{i}_{p_s}^* e^{j\theta_r} \quad (10)$$

$$\lambda_{p_s} = L_p \underline{i}_{p_s} + L_{ps} \underline{i}_{s_s}^* e^{j\theta_r} \quad (11)$$

$$\lambda_{s_s} = L_s \underline{i}_{s_s} + L_{ps} \underline{i}_{p_s}^* e^{j\theta_r} \quad (12)$$

where $\theta_r = p_r\theta_{rm}$ i.e. $\omega_r = d\theta_r/dt$ and L_{p,s,p_s} are the 3-phase self and mutual inductances of the windings [11].

The $\underline{i}_{s_s}^* e^{j\theta_r}$ term in the primary equations is a stationary frame vector rotating at ω_p as follows from:

$$\begin{aligned} \underline{i}_{s_s}^* e^{j\theta_r} &= i_s e^{-j(\omega_s t + \alpha_s)} e^{j\theta_r} = i_s e^{j(\omega_r t - \omega_s t - \alpha_s)} \\ &= i_s e^{j(\omega_p t - \alpha_s)} \end{aligned} \quad (13)$$

Therefore $L_{ps} \underline{i}_{s_s}^* e^{j\theta_r}$ represents the flux coupling to the primary from the secondary as a result of the flux density sidebands mentioned earlier, and it is also revolving at ω_p . Similarly, $L_{ps} \underline{i}_{p_s}^* e^{j\theta_r}$ in the secondary equations is the flux linking from the primary to the secondary rotating at ω_s .

A convenient transformation can now be applied to these stationary frame equations – we shall refer the primary equations to a $d_p q_p$ frame rotating at ω , and the secondary equations to a $d_s q_s$ frame rotating at $\omega_r - \omega$ (see Fig. 3), to get [11]:

$$\underline{v}_{p_r} = R_p \underline{i}_{p_r} + \frac{d\lambda_{p_r}}{dt} + j\omega \lambda_{p_r} \quad (14)$$

$$\underline{v}_{s_r} = R_s \underline{i}_{s_r} + \frac{d\lambda_{s_r}}{dt} + j(\omega_r - \omega) \lambda_{s_r} \quad (15)$$

$$\lambda_{p_r} = L_p \underline{i}_{p_r} + L_{ps} \underline{i}_{s_r}^* \quad (16)$$

$$\lambda_{s_r} = L_s \underline{i}_{s_r} + L_{ps} \underline{i}_{p_r}^* \quad (17)$$

The $\underline{i}_{s_r}^*$ in (16) is a $d_p q_p$ frame current phasor rotating at $\omega_p - \omega$ as $\underline{i}_{s_s}^* e^{j\theta_r}$, its original vector form, is rotating at ω_p relative to a stationary frame (refer to (13)), and we have simply converted this vector to a ω rotating frame. Similarly, the $\underline{i}_{p_r}^*$ in (17), which is a stationary frame vector $\underline{i}_{p_s}^* e^{j\theta_r}$ rotating at ω_s , rotates at $\omega_s - (\omega_r - \omega) = \omega - \omega_p$ with respect to the $d_s q_s$ frame.

From a control viewpoint, it is very important to emphasise that $\underline{i}_{s_r}^* = i_{sd_p} - j i_{sq_p}$ in (16) is actually a complex conjugate of $\underline{i}_{s_r} = i_{sd_s} + j i_{sq_s}$ in (17) where $i_{sd_p} = i_{sd_s}$ and $i_{sq_p} = i_{sq_s}$. Therefore by controlling the secondary current vector \underline{i}_{s_r} one is able to immediately influence the primary flux through $L_{ps} \underline{i}_{s_r}^*$ variations. This feature forms the basis of field oriented control for this machine [12].

The reference frame normally used for vector control is $\omega = \omega_p$ since the primary equations are then in the ω_p frame, and the secondary equations in the ω_s frame. This is a natural choice of frames given the supply frequencies of the windings and the fact that the controllable secondary current $d_s q_s$ components then become DC quantities which are the easiest to control.

It is interesting that (14)-(17) are almost the same equations as for the DEWRIM (except that they are in two

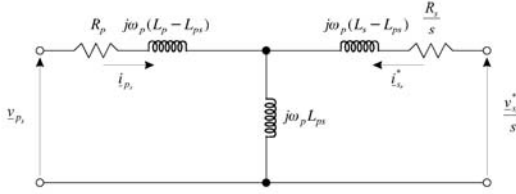


Fig. 4. Steady state model of the BDFRM

different reference frames) despite the fundamentally different physical operation mechanism. The analogies between the two machines can be further highlighted by developing the BDFRM steady state model.

4. STEADY STATE PERFORMANCE

Consider the general reference frame equations of (14)-(17). We can choose $\omega = 0$ so that the primary equations be in a stationary frame and the secondary equations in a frame rotating at the rotor velocity ($\omega_r = p_r \omega_{rm}$). Using this approach, it is possible to derive the following steady state equations for the BDFRM [11]:

$$\underline{v}_{p,s} = R_p \dot{i}_{p,s} + j\omega_p(L_p - L_{ps})\dot{i}_{p,s} + j\omega_p L_{ps}(\dot{i}_{p,s} + \dot{i}_{s,r}^*) \quad (18)$$

$$\frac{\underline{v}_{s,r}^*}{s} = \frac{R_s}{s} \dot{i}_{s,r}^* + j\omega_p(L_s - L_{ps})\dot{i}_{s,r}^* + j\omega_p L_{ps}(\dot{i}_{p,s} + \dot{i}_{s,r}^*) \quad (19)$$

where the 'generic' slip has been defined as $s = -\omega_s/\omega_p$. In the above equations the secondary parameters have not been "referred" to the primary winding in a traditional turns ratio sense (or vice-versa) but a frequency referencing operation has been carried out using the previous slip definition, this allowing us to draw the coupled circuit model of Fig. 4. Despite this fundamental difference in referencing, the model in Fig. 4 is identical in form to that for the DEWRIM.

One of the major differences between the BDFRM and induction machine steady state models are the values of some of the inductances. Due to the fact that a significant fundamental component of the winding fluxes does not couple to the other winding in the BDFRM, the $(L_p - L_{ps})$ terms are much larger than the normal leakage flux of the DEWRIM. The higher leakage inductances have an adverse effect on the rate of change of torque of the BDFRM compromising its transient response compared to the induction machine.

4.1 Torque

Applying the principle of virtual work, one can obtain the following expression for the torque of the machine in terms of primary values⁷ [11]:

$$T_e = j \frac{3}{4} p_r [\Delta_{p,r} \dot{i}_{p,r}^* - \Delta_{p,r}^* \dot{i}_{p,r}] \quad (20)$$

$$= \frac{3}{2} p_r [\lambda_{pd} \dot{i}_{pq} - \lambda_{pq} \dot{i}_{pd}] \quad (21)$$

⁷The same equation applies to a $2p_r$ -pole induction machine.

One can manipulate (20) into a more convenient form expressed in terms of the primary fluxes and the secondary currents:

$$T_e = \frac{3}{2} p_r \frac{L_{ps}}{L_p} [\lambda_{pd} \dot{i}_{sq} + \lambda_{pq} \dot{i}_{sd}] \quad (22)$$

This expression is particularly useful since the secondary currents are the variables one has control over using an inverter, and the primary fluxes are fixed by the grid voltage and frequency.

Equation (22) can be further refined by aligning the primary reference frame d_p -axis with the primary flux vector λ_{p_r} . In this case, the q_p flux component obviously disappears ($\lambda_{pq} = 0$) and (22) can be simplified to:

$$T_e = \frac{3}{2} p_r \frac{L_{ps}}{L_p} \lambda_p \dot{i}_{sq} \quad (23)$$

where $\lambda_p \triangleq$ the magnitude of the primary flux vector.

Expression (23) is a form one would use for torque control. It can be seen that the torque can be controlled independently by \dot{i}_{sq} , whilst $\lambda_p = \lambda_{pd}$ is a constant due to primary winding grid connection. As $\dot{i}_{sq} = \dot{i}_s \sin \alpha_s$ (Fig. 3), the maximum torque per inverter ampere is accomplished at the secondary current angle of $\alpha_s = \pi/2$.

4.2 Power

Using the general expression for complex power in steady state $P_{3\phi} + jQ_{3\phi} = \frac{3}{2}(\underline{v}_{p,s} \dot{i}_{p,s}^* + \underline{v}_{s,r} \dot{i}_{s,r}^*)$ and substituting for (18) and (19), one can develop the relationships for the real and reactive powers into the machine per winding [11]:

$$\begin{aligned} P_{p,s} &= \frac{3}{2} [R_{p,s} \dot{i}_{p,s}^2 + \omega_{p,s} L_{ps} \dot{i}_s \dot{i}_p \sin(\alpha_s + \alpha_p)] \\ Q_{p,s} &= \frac{3}{2} \omega_{p,s} [L_{p,s} \dot{i}_{p,s}^2 + L_{ps} \dot{i}_s \dot{i}_p \cos(\alpha_s + \alpha_p)] \end{aligned} \quad (24)$$

where α_p and α_s are the primary and secondary current angles respectively (Fig. 3).

It should be mentioned that the analysis in this section is based on the steady state model equations which have been derived assuming the primary $d_p q_p$ frame to be stationary (as $\omega = 0$) and the secondary $d_s q_s$ frame to be rotating at ω_r . Keeping this in mind, it can be easily seen from Fig. 3 that $\dot{i}_{s,r} = \dot{i}_s e^{j\alpha_s}$ and $\dot{i}_{p,s} = \dot{i}_p e^{j\alpha_p}$.

With the current phasors defined as above, it can be shown that when (16) is substituted into (20), the latter can be rearranged to give:

$$T_e = \frac{3}{2} p_r L_{ps} \dot{i}_p \dot{i}_s \sin(\alpha_s + \alpha_p) \quad (25)$$

By comparing this expression with (24) we can easily conclude that:

$$P_{p,s} = \frac{3}{2} R_{p,s} \dot{i}_{p,s}^2 + \frac{\omega_{p,s}}{p_r} T_e \quad (26)$$

The total rotational power is simply the sum of the real powers minus the losses:

$$\begin{aligned} P_{rot} &= P_{3\phi} - P_{losses} = \frac{\omega_p}{p_r} T_e + \frac{\omega_s}{p_r} T_e \\ &= \frac{\omega_p + \omega_s}{p_r} T_e = T_e \omega_{rm} \end{aligned} \quad (27)$$

which conforms with the standard definition of output power.

One can see from (26) that the contributions to the machine output power from each winding are:

$$P_{p_{rot}} = \frac{\omega_p}{p_r} T_e \quad (28)$$

$$P_{s_{rot}} = \frac{\omega_s}{p_r} T_e = -s \frac{\omega_p}{p_r} T_e = -s \cdot P_{p_{rot}} \quad (29)$$

$$P_{rot} = P_{p_{rot}} + P_{s_{rot}} = (1 - s) \cdot P_{p_{rot}} \quad (30)$$

Notice that the slip form expression (30) for the BDFRM power is also applicable to an induction machine with $P_{p_{rot}}$ being the electromagnetic power transferred from the stator to the rotor.

The secondary power expression (29) clearly indicates that the BDFRM operates in a manner analogous to the slip power recovery double-fed induction machine as the inverter supplying the secondary winding has to handle only an amount of power dependent on how much the secondary frequency varies from zero i.e. how small is the absolute slip. This ability to control the machine speed over a limited range with a little amount of secondary power (and hence with a partially rated inverter) is one of the main motivations for using this machine.

From (28) and (29) one can also deduce that if $\omega_s = -\omega_p$, the rotational power from the secondary is negative.⁸ This means that the power is flowing out of the secondary winding – i.e. the winding is regenerating, and all the primary power is being returned back to the mains supply via an inverter. Note that, as with an induction machine, the rotor is stationary under this condition (see (7) assuming the ‘+’ case) as $s = 1$ and there is no mechanical power being produced. As a generalisation of this point, one can conclude that for $\omega_s < 0$, a fully regenerative converter is required if there is to be prolonged machine operation in this frequency region. However, if this is only used during the start-up process then it may be sufficient to have resistive dumping as the regeneration mechanism.

If $\omega_s = 0$ then we are feeding DC into the secondary winding. In this situation we can see from (28) and (29) that only the primary contributes to rotational output power but the secondary does not. Therefore the inverter would only have to supply the resistive losses in the secondary winding (refer to (26)), and also there can be no reactive power if DC is flowing ($Q_s = 0$) as can be seen from (24). The BDFRM is operated as a classical $2p_r$ -pole wound rotor synchronous turbo-machine in this case ($s = 0$) with the secondary winding playing the role of a field winding.

If $\omega_s = \omega_p$ then the machine is running in a super-synchronous mode and the power developed is being shared evenly between the two windings. This can be easily confirmed using (29) since $s = -1$. A larger inverter able to carry half the machine output power would be needed for sustained operation under these circumstances.

⁸The ‘negative’ secondary frequency only indicates the opposite phase sequence to the primary winding.

4.3 Power Factor

Another nice feature of the BDFRM is the possibility of power factor i.e. reactive power regulation of its grid connected (primary) winding. Using the same frame alignment conditions as (23) the appropriate expression for the primary reactive power can be derived as [11, 12]:

$$Q_p = \frac{3}{2} \frac{\omega_p \lambda_p}{L_p} (\lambda_p - L_{ps} i_{sd}) \quad (31)$$

This equation shows that one can control Q_p via the secondary d -axis current as λ_p is fixed by the grid voltage. Comparison with (23) leads to the conclusion that the primary reactive power and the torque can be controlled in a decoupled fashion [12]. It follows from (31) that the unity power factor is achieved if $Q_p = 0$ i.e. $i_{sd} = \lambda_p / L_{ps}$.

In a similar manner, one can influence the machine copper losses i.e. its efficiency [9]. In this case, however, the control of torque and primary reactive power is not independent.

5. CONCLUSIONS

This paper has provided a brief introduction to the operation and control properties of the BDFRM. Much research still has to be done on the analysis, design and experimental testing of this machine before the trade-offs in inverter size versus machine size and the subsequent cost issues can be quantified. Only then it will be clear whether the BDFRM has a viable application niche.

REFERENCES

- [1] A. Broadway and L. Burbridge, ‘Self-cascaded machine : A low speed motor or a high frequency brushless alternator,’ *Proc. IEE*, vol. 117, pp. 1277–1290, July 1970.
- [2] S. Williamson, A. Ferreira, and A. Wallace, ‘Generalised theory of the brushless doubly-fed machine. part 1: Analysis,’ *IEE Proc.-Electric Power Applications*, vol. 144, pp. 111–122, March 1997.
- [3] B. Gorti, D. Zhou, R. Spée, G. Alexander, and A. Wallace, ‘Development of a brushless doubly-fed machine for a limited speed pump drive in a waste water treatment plant,’ *Proc. of the IEEE-IAS Annual Meeting*, pp. 523–529, Denver, Colorado, October 1994.
- [4] A. Broadway, ‘Cageless induction machines,’ *Proc. IEE.*, vol. 118, pp. 1593–1600, November 1971.
- [5] F. Liang, L. Xu, and T. Lipo, ‘D-q analysis of a variable speed doubly AC excited reluctance motor,’ *Electric Machines and Power Systems*, vol. 19, pp. 125–138, March 1991.
- [6] L. Xu and Y. Tang, ‘A novel wind-power generating system using field orientation controlled doubly-excited brushless reluctance machine,’ *Proc. of the IEEE IAS Annual Meeting*, Houston, Texas, October 1992.
- [7] F. Wang, F. Zhang, and L. Xu, ‘Parameter and performance comparison of doubly-fed brushless machine with cage and reluctance rotors,’ *IEEE Transactions on Industry Applications*, vol. 38, pp. 1237–1243, Sept/Oct 2002.
- [8] M.G. Jovanović, R.E. Betz, and J. Yu, ‘The use of doubly fed reluctance machines for large pumps and wind turbines,’ *IEEE Transactions on Industry Applications*, vol. 38, pp. 1508–1516, Nov/Dec 2002.
- [9] M.G. Jovanović and R.E. Betz, ‘Power factor control using brushless doubly fed reluctance machines,’ *Proc. of the IEEE-IAS Annual Meeting*, Rome, Italy, October 2000.
- [10] Y. Liao, L. Xu, and L. Zhen, ‘Design of a doubly-fed reluctance motor for adjustable speed drives,’ *IEEE Transactions on Industry Applications*, vol. 32, pp. 1195–1203, Sept/Oct 1996.
- [11] R.E. Betz and M.G. Jovanović, ‘Introduction to the space vector modelling of the brushless doubly-fed reluctance machine,’ *Electric Power Components and Systems*, vol. 31, pp. 729–755, August 2003.
- [12] L. Xu, L. Zhen, and E. Kim, ‘Field-orientation control of a doubly excited brushless reluctance machine,’ *IEEE Transactions on Industry Applications*, vol. 34, pp. 148–155, Jan/Feb 1998.

POSSIBILITIES OF TORQUE AND FLUX CONTROL USING DTC-8 METHOD

Andrzej Sikorski, Marek Korzeniewski*

Bialystok Technical University, Faculty of Electrical Engineering, Bialystok, Poland, * Bialystok Technical University, Faculty of Electrical Engineering, Bialystok, Poland

Abstract: A novel modified direct torque and flux method of control (DTC) to enable the flux and current vectors deformation with low motor speed elimination is presented in article. Correctness of this method is confirmed by laboratory investigations.

Key Words: DTC, optimization of DTC

1. INTRODUCTION

Direct torque control method proposed by Takahasi and Noguchi [1] in 1985 in spite of its disadvantages (flux and current distortion for small motor speed) is competitive to the flux oriented methods (FOC) of control. Methods of investigations of the current controlled AC motor and results proposed in paper [2] was applied to DTC method control analyze. Although in DTC method the current components are not controlled directly, the torque and flux control phenomenon is easy explained by the current components i_{sq} , i_{sd} changes. DTC method operation analysis to explain the flux and current distortion for the small speed of motor operation is discussed in the article.

2. DTC CONTROL ALGORITHM MODIFICATION

DTC method has some similarity to the FOC method. In the both methods flux and torque are controlled although in the FOC method indirectly by the current components i_{sd} - flux and i_{sq} - torque. So we can try to explain DTC method looking on current vector components behavior [3].

Possible directions (K_{xxx} - in Fig. 1a) of the current vector \underline{i}_s move for the particular inverter output voltage vector positions depending on conditions of motor work (motor current \underline{i}_s , electromotive force E which is proportional to ω_m) and motor parameters (stator resistance R_s and inductance L_s) are calculated by means of Eq.1 evaluated of the current derivative [2]. The investigations concern the rotational reference frame dq therefore the flux vector, current and voltage vectors are stationary and star composed by output voltage vector positions rotates.

$$L_s \frac{d}{dt} \underline{i}_s = -(\underline{E}_s + R_s \underline{i}_s^* + j\omega_o L_s \underline{i}_s^*) + \begin{cases} \frac{2}{3} U_d e^{j(k_s \frac{2}{3} - \omega_o t)} \\ "0" \end{cases} \quad (1)$$

Figure 1b presents method of command voltage vector \underline{U}_s^* evaluation to receive demanded for required angular motor speed (proportional to electromotive force

E) current components i_{sd} , i_{sq} . Directions of the \underline{i}_s vector move (K_{xxx}) for specified voltage vector \underline{U}_s^* corresponded to voltage vectors positions (110, 010, 001, 101, 111) in sector $N=1$ (tabl.1) are shown in Fig.1a. It means that particular voltage vectors cause the current vector and its component changes as it is shown in Fig.1a. For example, the voltage vector position 010 (K_{010}) causes the component i_{sq} increase (the torque increase) and component i_{sd} decrease (flux decrease). Remaining voltage vector positions cause presented in the Fig.1a directions of current components (torque and flux) changes. Influence of the others vector positions on the torque and flux changes are presented in table 1.

Table 1. Influence of converter output voltage vector positions on the torque and flux changes

	110	010	101	001	111
$i_{sq} \Rightarrow M$	↑	↑	↓	↓	↓
$i_{sd} \Rightarrow \Psi_M$	↑	↓	↑	↓	-

Results presented in table 1 concern position of the flux vector in the middle of sector $N=1$. Looking on rotating dq coordinates, according to equation 1, immobile flux, current and voltage vectors and rotating converter output voltage vector should be notice.

Conventional DTC method control scheme (without blocks signed in gray colour) is presented in Fig.2. The flux Ψ_M^* and electromagnetic torque M^* (output signal of the speed controller) set values are compared to the real values Ψ_M and M and the comparison errors are introduced in to the nonlinear controllers input (comparators). The optimal switching states of converter are determined by: three level of torque comparator state and two level of flux comparator state depending on the flux vector position actual sector $N(\pi/3)$ [1]. The angle between the stator flux vector Ψ_M and α axis in stationary reference frame $\alpha\beta$ is calculated using equation: $\varphi = \arctg(\Psi_{M\beta} / \Psi_{M\alpha})$. Table 2 contains assignation of the inverter transistor control pulses depending on values of torque M^* and flux Ψ_M^* in relation to its command signals M^* , Ψ_M^* for different sectors N where flux Ψ_M^* is located.

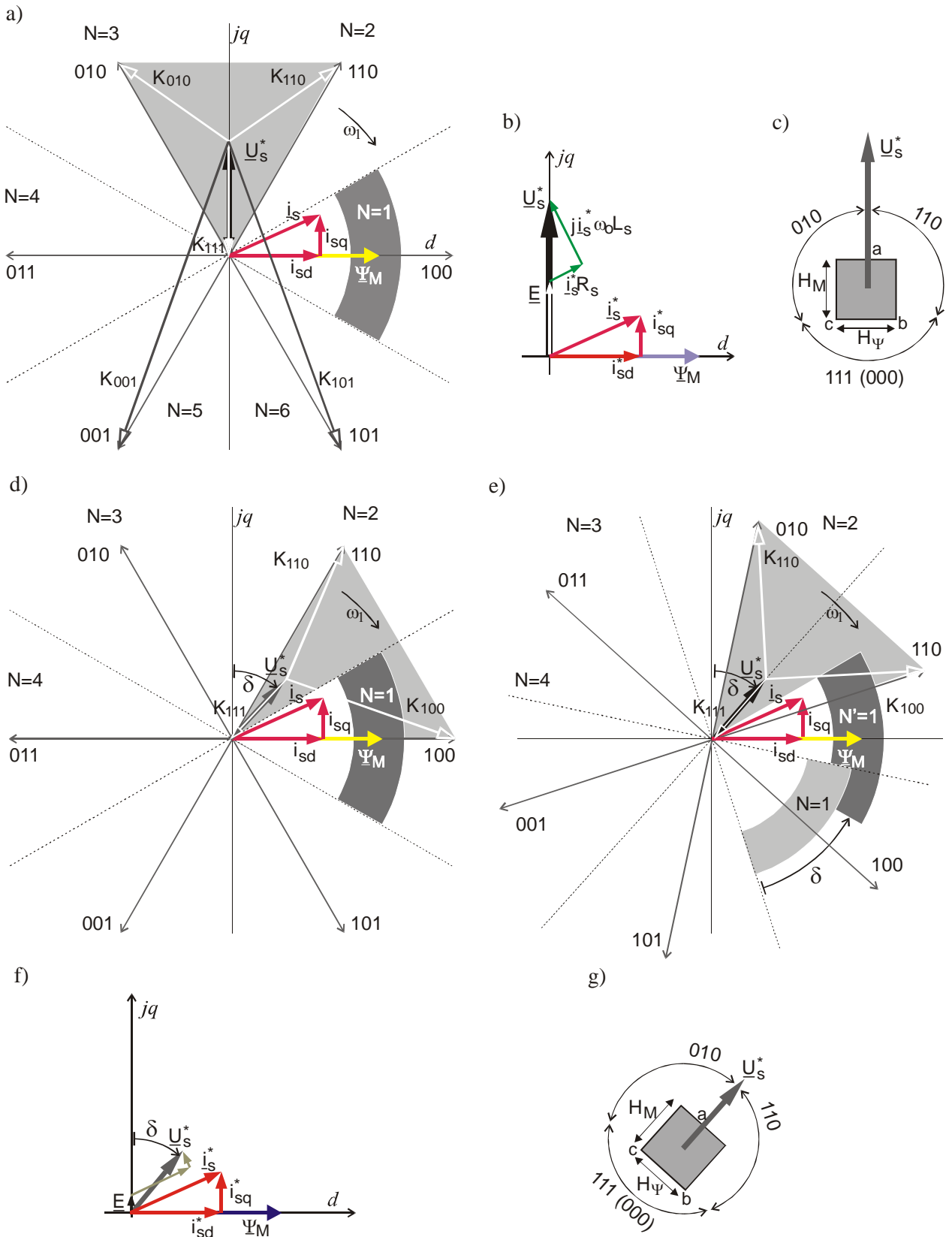


Fig.1. DTC method control analyze and modification in the rotational reference frame dq - graphical illustration of the current vector K_{xxx} direction move: high (a) and low (d) motor angular velocity for cassicall DTC method and modified DTC method (e), vectorial motor graph for sinusoidal (command value) waveforms for high (b) and low (f) angular velocity, command vector and error area positions for conventional DTC method and high motor velocity (c), modified DTC method and low motor velocity (g)

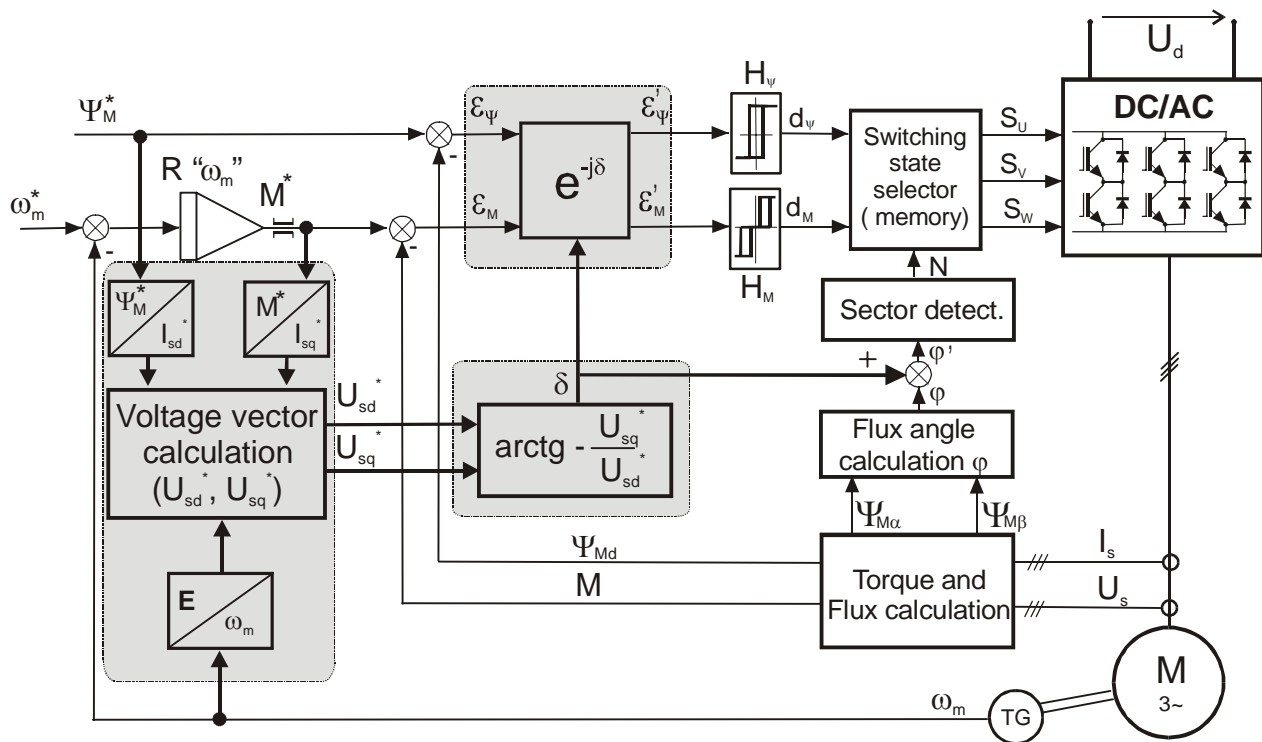


Fig.2. Block diagram of DTC and DTC- δ control methodes

Table 2. Table of the voltage vector selection for DTC control method

		N=1	N=2	N=3	N=4	N=5	N=6
$d\psi = 1$	$d_M = 1$	110	010	011	001	101	100
	$d_M = 0$	111	000	111	000	111	000
	$d_M = -1$	101	100	110	010	011	001
$d\psi = 0$	$d_M = 1$	010	011	001	101	100	110
	$d_M = 0$	000	111	000	111	000	111
	$d_M = -1$	001	101	100	110	010	011

In the steady state three voltage vector positions (010, 110, 000 or 111) in sector 1 (N=1) are used to enable moment and flux control depending on the errors values of the both control circuits [3]. Positions 010, 110 cause the torque increase when position 111 causes the torque decrease. The flux is decreased when position 010 is used and is increased with position 110. Additionally positions 001 and 101 are used in transient states to rapid torque changes during braking and reverse processes (the torque comparator state equal -1 means too large torque). In the steady state the errors of the torque control circuit (q -axis) and the flux control circuit (d -axis) form the error area rectangular in shape which dimensions are defined by hysteric H_M and H_ψ (Fig.1c). The error area may be square in shape when H_M is equal H_ψ . Table 2 shows which voltage vector position should be used to return the error inside the square when the error cross the square in any point. In the sector N=1 the vector positions 010, 110 and (111 or 000) are suitable, which are assigned to the error square periphery as it is shown in Fig.1c.

The following observation can be done looking on the DTC control method as voltage or current control. In DTC

methods it is assumed that command voltage vector is perpendicular to the flux vector (Fig.1a). It is shown in Fig. 1b where stator voltage command vector \underline{U}_s^* is formed as sum of the motor electromotive force E and voltage drops on the stator resistance R_s and leakage inductance L_s . From voltage control point of view we can observe that voltage vector \underline{U}_s^* (provoking current components responsible for torque and flux i_{sd} , i_{sq} changes) is formed by 010, 110 and zero positions it means the classical pulse width modulation of the \underline{U}_s^* voltage. Problems which occur in DTC control with small angular speed: flux hexagonal in shape and distorted current (Fig.3) can be explained by vectorial voltage control. In the Fig. If the voltage chart with small angular speed when electromotive force and voltage drop on the leakage inductance L_s are close to zero is presented. The feeding voltage \underline{U}_s^* is approximately equal to stator resistance voltage drop and is deviated from q -axis about angle δ . It means, that the voltage vector should be shaped using 110, 100 and 000 vectors positions (Fig. 1d). It leads to the switching table changes (instead 110 \rightarrow 100, instead 010 \rightarrow 110, etc.) or to the sectors N locations, in relation to inverter voltage vector positions, changes. As results this observations the method DTC scheme modification, as it is shown in Fig. 2e, 2g, is proposed. This new method requires of the angle δ identification (angle δ shows voltage vector \underline{U}_s^* deviation from the standard location). Need of δ identification is documented in Fig. 1f. The calculated current command components i_{sd}^* , i_{sq}^* are adequately proportional to the flux and torque command signals while signal proportional to the electromotive force E is recreated

on the base of mechanical pulsation ω_m . The angle δ is used to the two conversion (Fig. 2e, 2g). It is added to the angle φ , which define the sectors N borders. The sector changes from $N = 1$ to $N' = 1$ (after turning with angle δ) is shown in Fig. 2e. These changes allow to the voltage vector may be shaped using positions (110, 100 and 000 or 111) after flux vector move to the sector $N = 1$. It means that voltage vector \underline{U}_s^* is shaped using the standard switching table. Additionally the error area (Fig.1g) should be turned with angle δ , to maintain relation between the error area sections and assigned to him voltage vector positions. It means that vector position 110 causes of the error vector move to the inside area between a and b points, when vector position 010 – from section b and c etc (Fig.2g). In the paper [2] is shown that the turning of the error area with angle δ is adequate to the turning of the error vector with angle $-\delta$. This property is used to error vector $(\varepsilon_\psi + j\varepsilon_M)$ turning with angle $-\delta$ (in the scheme in the Fig. 2 multiplication by $e^{-j\delta}$).

3. EXPERIMENTAL RESULTS

The modified DTC control method was realized using ADSP-21061 processor and nonlinear hysteresis controllers type Δ with hysteresis width equal to zero and sampling time T_p equal $50\mu s$. Comparison of the results characterized classical and modified DTC methods is presented in the figures 3 and 4.

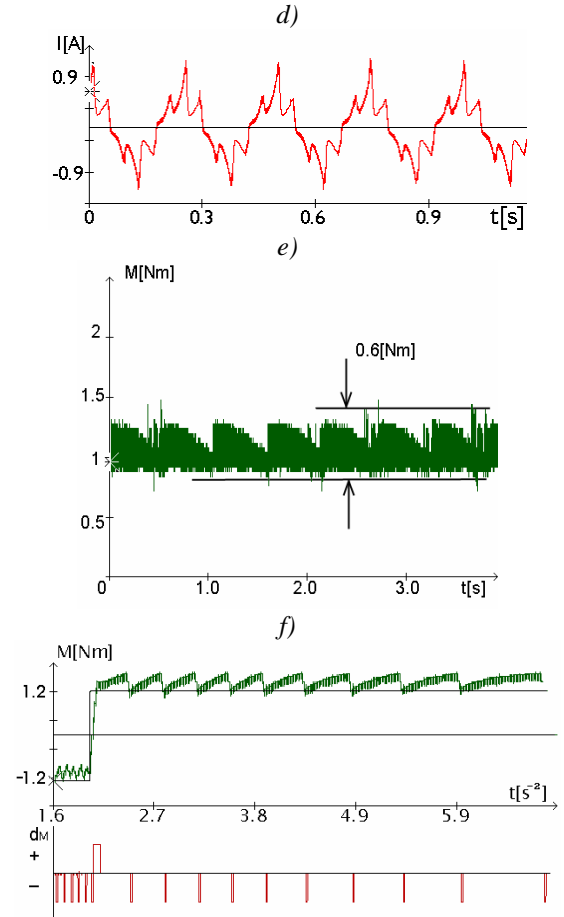
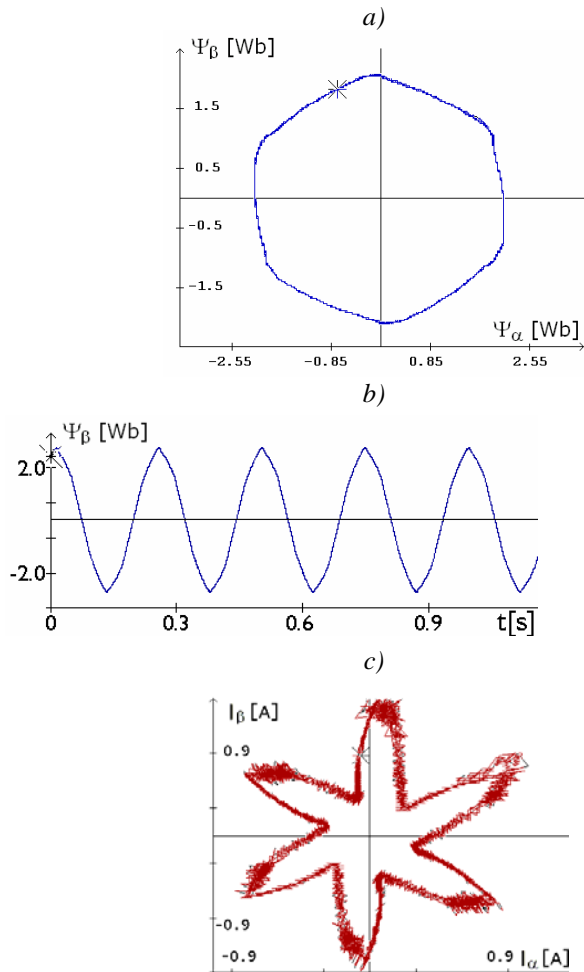


Fig.3. Results of conventional DTC method investigations: flux trajectory in $\alpha \beta$ coordinates (a), flux waveform (b), stator current vector trajectory in $\alpha \beta$ coordinates (c), current waveform (d), torque during steady state operation (e), torque during transient state operation (f)

These results concerns 5Hz frequency corresponded 0,1 value of the nominal rotor pulsation. The basic disadvantages of the conventional method: hexagonal flux and distorted motor current are evident, when the modified method is free from these disadvantages.

4. CONCLUSION

The proposed modified DTC method is free from the conventional DTC method disadvantages concerned: hexagonal shape of flux and distorted current (waveform Fig. 3ab and 4ab). The dynamical properties for the booth methods are comparable (fig.3d, 4d). The converter switching number for modified method is higher because the nonzero positions of the output converter voltage are used to shape the circular flux vector trajectory. It is important that in the modified method the conventional switching table is used.

a)

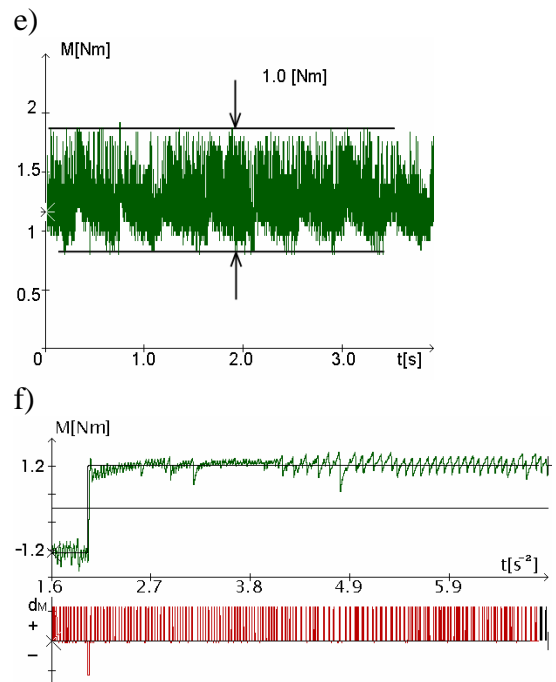
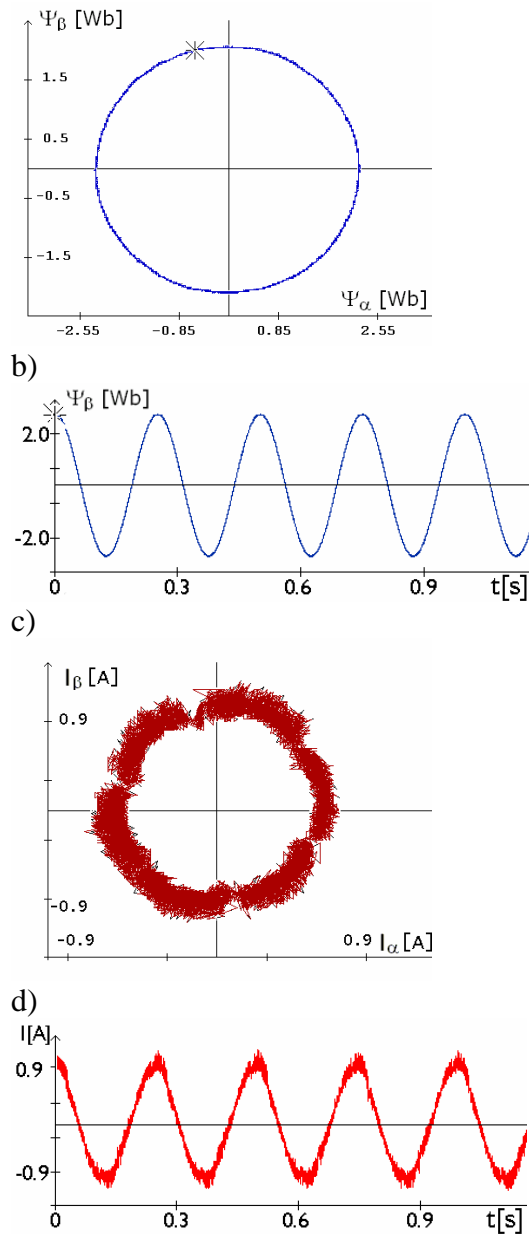


Fig.4. Results of modified DTC method investigations: flux trajectory in α β coordinates (a), flux waveform (b), stator current vector trajectory in α β coordinates (c), current waveform (d), torque during steady state operation (e), torque during transient state operation (f)

Investigations presented in this article were made as the KBN project 8 T10A 03/20.

5. REFERENCES

- [1] Takahashi I., Noguchi T.: "A new quick response and high efficiency control strategy of an induction motor", *IEEE Transactions on Industry Applications*, Vol. IA-22, No. 5, Sep/Oct 1986, pp. 820-827.
- [2] Sikorski A., Citko T.: "Current controller reduced switching frequency for VS-PWM invertet used with AC motor drive application", *IEEE Transactions on Industrial Electronics*, Vol. 45, No. 5, Oct. 1998, pp. 792-801.
- [3] Sikorski A., Korzeniewski M.: "Analysis of flux and torque control improvement of ac motor controlled by DTC method". 10th International Conference EPE-PEMC 2002, Dubrownik, Croatia, 2002.

LOW VOLTAGE SWITCHED CAPACITOR DC-DC CONVERTER FOR FUEL-CELL APPLICATIONS – PRELIMINARY DESIGN CONSIDERATIONS

Goce L. Arsov, Josif Kosev, Roberto Giral*, Faculty of Electrical Engineering - Skopje, Macedonia, * Departament d'Enginyeria Electrònica, Elèctrica i Automàtica, Escola Tècnica Superior d'Enginyeria, Universitat Rovira i Virgili, Tarragona – Spain

Abstract: This paper analyzes the possibilities for application of inductorless switched capacitor DC-DC converter in fuel cell application. It is shown that the ladder like SCC is capable to convert the voltage of a single fuel cell to 9-12 V with very high efficiency. The problems imposed by the high current through the switches of the first stage, as well as the start-up problems are discussed. The auxiliary circuit for producing the necessary supply to the gates at start-up is proposed.

Key Words: Switched capacitor DC-DC converter, fuel cell application, multi-step, geometric series

1. INTRODUCTION

Green power (renewable power) becomes increasingly more important due to global pollution problems. There exist many different types of green powertechnologies such as wind turbines, photovoltaic cells and fuel cells. Wind turbines and photovoltaic cells are well known and matured technologies but both have an obvious disadvantage: these technologies deliver only power when the wind blows/the sun is shining. Thus, these technologies cannot be used as primary power supply in the grid.

Fuel cells can produce power (electrical and thermal) when supplied with fuel and fuel cells(in some technologies)can have bidirectional power flow. In this case the fuel cell can therefore operate as an energy storage. A fuel cell system can also be used as an uninterruptable power supply for a house, a factory or a village.

Today, fuel cells have emerged as a promising alternative source of clean energy for applications ranging from automotive industry to residential and commercial installations. This has created a need for a class of specialized power converters geared to interface between the fuel cell device and the end-user appliance, often as a battery charger. Specifications for power conversion equipment depends on the fuel cell's physical properties and manufacturing economics.

The economics of fuel cells' manufacturing call for a relatively low output voltage, as the total output voltage is obtained by connecting in series a number of individual cells. Since increasing the cells' surface — which results in higher current capability and, consequently, higher power — is cheaper and less complex than increasing their number, a cost-optimized unit will have a high output current capability and a relatively low output voltage.

The cells' output voltage is dependent on the load; though nonlinear, it's approximately equivalent to a voltage source with series resistance. For a PEM (proton exchange membrane) cell, the voltage may drop from a no-load 1.23Vdc to below 0.5Vdc at full load. Consequently, a converter will have to work with a wide range of input voltages.

According to some authors the output voltage of a fuel cell can be expressed as:

$$E = E_0 - b \cdot \log(i) - R \cdot i - m \cdot e^{(n \cdot i)} \quad (1)$$

where: E_0 — the open circuit potential,
 b — tafel slope,
 R — resistance,
 m, n — mass transport,
(parameters are cathode pressure and temperature dependent).

The diagram showing the I/V characteristic of a fuel cell is shown in Fig. 1 [1].

A fuel cell stack could be catastrophically damaged if overloaded. Drawing excessive current from any one cell — more than its fuel delivery can produce — can lead to a cell reversal and membrane rupture. Therefore, a converter designed to work in these applications must be controlled based on input voltage and current, as well as output voltage and current — only fully digital control is practical.

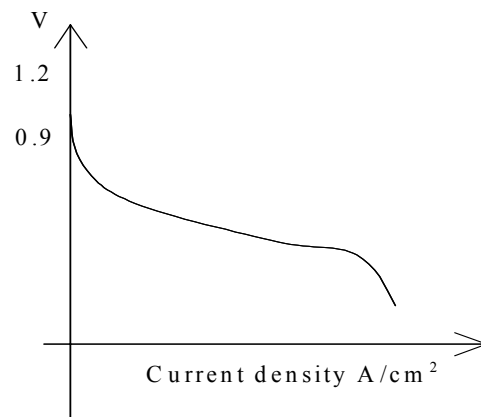


Fig. 1. Voltage vs. Current Density for a Fuel Cell [1]

Finally, due to the cost of generating power, converter efficiency is one of the most important parameters.

Up to now only very few configurations of low voltage fuel cell DC-DC converters have been found on the web and none in the conference or journal papers [1]-[3]. All of them give output power less than 2 W and only one gives output voltage greater than 5 V. In all proposed configurations the output voltage varies very much with the output power or with the changes of the input voltage. The maximal efficiency was reported to be from 75% to 90%. All configurations use more than one fuel cell in series to obtain the necessary input voltage for proper operation of the converter and higher efficiency. In [1] four level structure, using MAX857 low voltage converter, is proposed. The efficiency of 58% was reported for one level structure at output current of 0.68mA and output voltage of 3.3 V. Two fuel cells were connected in series so that the input voltage was 1.75 V. In this paper we propose a ladder like five step SCC for this purpose.

2. THE CONVERTER TOPOLOGY

In order to increase the output to input voltage ratio, the output power and the efficiency, using only one fuel cell, the

classical configuration of a ladder-like five-step inductorless DC-DC transformer (Fig. 2) is investigated using PSpice simulation program.

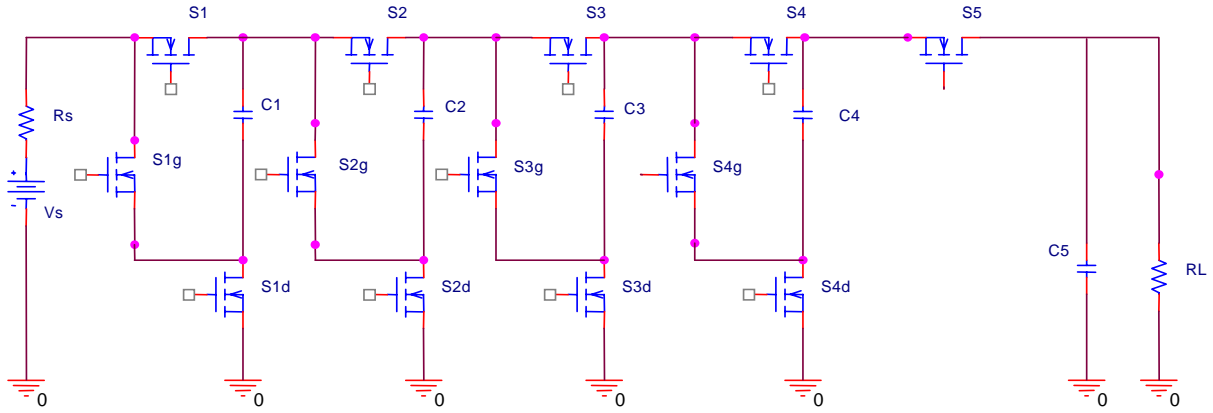


Fig. 2. Five-step SCC DC-DC converter

The fuel cell has been modeled as a voltage generator in series with resistance according to data in [4] for hydrogen PEM fuel cell at 300 kPa (In the approximately linear region the fuel cell has an output voltage of 0,8 V at 0,2 A/cm², and 0,5 V at 1,6 A/cm²). The switches are chosen to be low resistance MOSFETs IRF6607 and the switching frequency 25 kHz.

To improve the characteristics of the converter a geometric-series capacitance-ratio between the stages as described in [5] has been used ($k=2, C_5=220 \mu\text{F}$).

$$C_5 = C; C_4 = kC; C_3 = k^2C; C_2 = k^3C; C_1 = k^4C \quad (2)$$

Full analysis of the ladder like converter has been given in [5]. Some equations are rewritten here. The output voltage can be expressed with the following equation:

$$\bar{V}_L \approx V_{Lm} - \bar{I}_L \cdot R_O, \quad (3)$$

where V_{Lm} is the no-load output voltage,

$$V_{Lm} = 2^4 \cdot V_S, \quad (4)$$

and R_O , so-called switched-capacitor resistance:

$$R_O = \frac{1}{fC} \frac{43+11k+3k^2+k^3}{k^4}. \quad (5)$$

Here $f = 1/T$ is the switching frequency.

The DC-output efficiency expression follows directly from the previous equations:

$$\eta = \frac{\bar{V}_L \bar{I}_L}{V_S \bar{I}_S} = \frac{\bar{V}_L}{2^4 V_S} = 1 - \frac{\bar{I}_L R_O}{2^4 V_S} \quad (6)$$

To establish nearly constant current through the fuel cell the interleaving was used by connecting five converters and shifting the control pulses for each converter by 0,2 T. The timing diagrams for the switches of the first converter are given in Fig. 3.

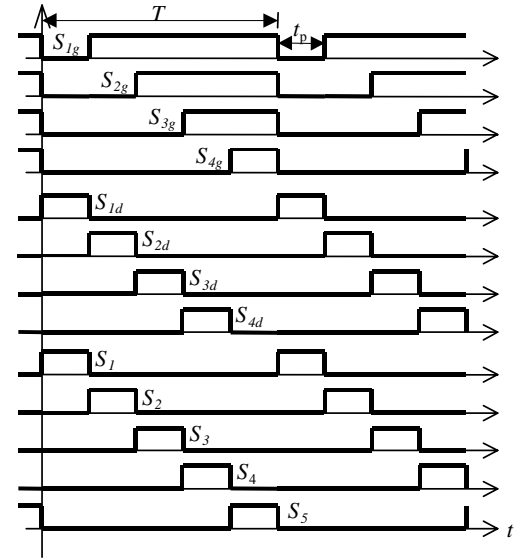


Fig. 3. Diagram of the states for the switches in the circuit of Fig. 2

The five operation steps of the converter together with the voltages of the capacitors at no load are shown in Fig. 4. The absolute current through C_1 is shown in Fig. 5. Each of the capacitors is charged during one of the steps consecutively, and discharged during the following steps. The ideal voltage ratio is 2^{n-1} , where n is the total number of capacitors. The last capacitor is used also as the filter capacitor that supplies the load during the first four steps and charges during the last (fifth) operation step.

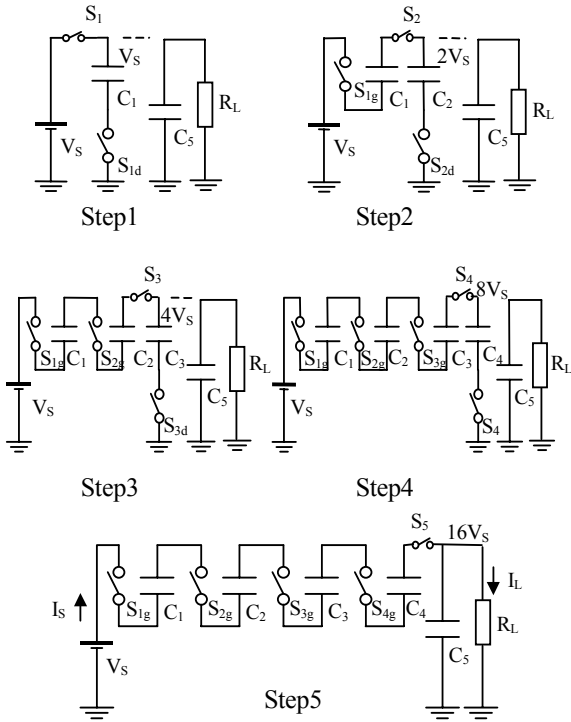


Fig. 4. Converter operation steps

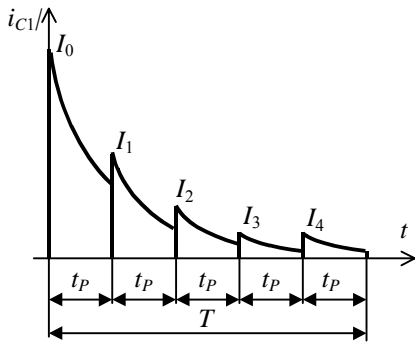


Fig. 5. Absolute current through C_1

3. SIMULATION RESULTS

Extensive simulations using Pspice simulation program were performed in order to examine the converter characteristics. The fuel cell was modeled following the data according to [4] and given above. For hydrogen PEM 25 cm^2 fuel cell the equivalent *emf*, in the linear region, was calculated to be 0.84 V and the internal resistance to be $7 \text{ m}\Omega$. The capacitors were chosen according to equation (2) with $k=2$ and $C_5=220 \text{ }\mu\text{F}$.

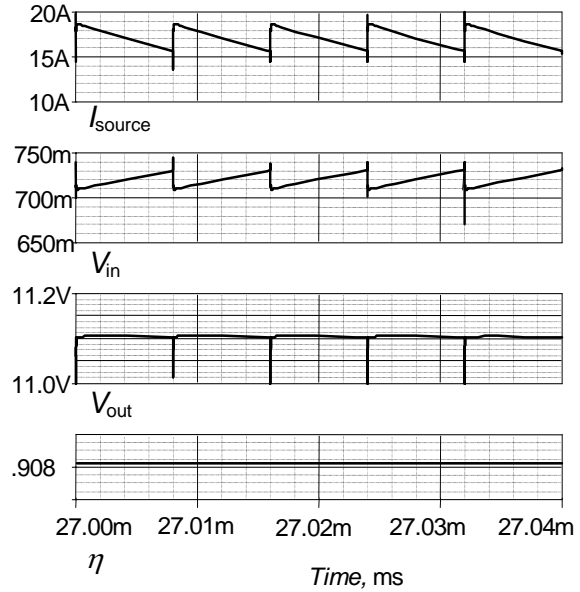


Fig. 6. Diagrams showing the current through the fuel cell, converter input voltage, converter output voltage and the efficiency for a resistive load of $11 \text{ }\Omega$ at steady state operation

The diagrams of the current through the cell, the voltage at the cell nodes, the output voltage with a resistive load of $11 \text{ }\Omega$, and the efficiency for steady state operation are shown in Fig. 6. The power delivered to the load was about 11 W. The start-up of the converter has been simulated under the worst case with the assumption that all capacitors are completely discharged. The diagrams of the current through the cell, the voltage at the cell output nodes and the converter output voltage are shown in Fig. 7.

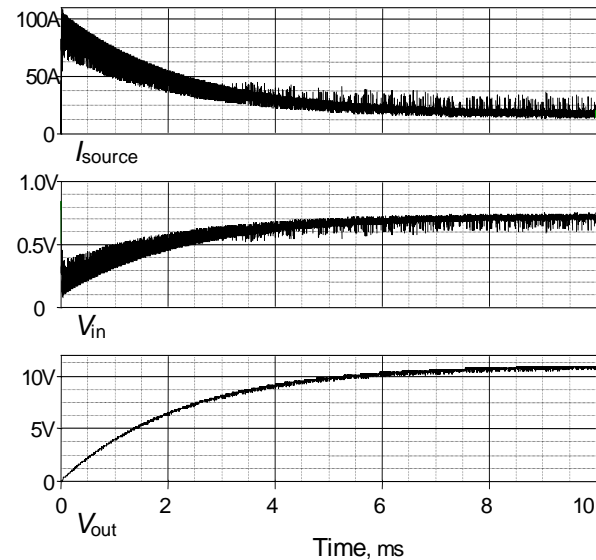


Fig. 7. Diagrams showing the current through the fuel cell, converter input voltage and converter output voltage at start-up

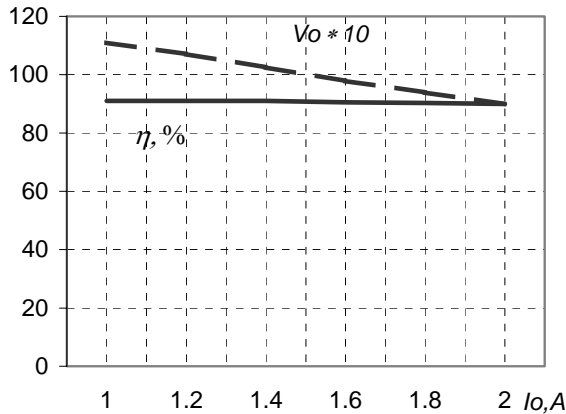


Fig. 8. Diagrams showing the dependencies $V_O = V_O(I_O)$ and $\eta = \eta(I_O)$

By variation of the load we have changed the load current from 1 to 2 A. The results for the output voltage and the efficiency (without regulation) are shown in Fig. 8. The variation of the output voltage is direct result of the fuel cell I/V characteristics. It can be seen that for a 25 cm² fuel cell the converter gives an output voltage of 9 V with a load current of 2 A. The efficiency was around 91%. For lower loads the control of the output voltage can be achieved by PWM. It should be noted, however, that the efficiency is very dependent of the output to input voltage ratio according to the equation (6).

We have compared these results with the results obtained for a classical boost converter using IRF6607 as a switch, inductance was 1 μ H, and the capacitance 200mF. The switching frequency was chosen to be 500kHz. For the same source characteristics and load resistance of 11 Ω , we have obtained output voltage of 9.74 V at duty cycle of .996 and with efficiency of less than 50% which is not far away from the results given in [1] for much lower output power.

4. DESIGN CONSIDERATIONS

Although the topology of the proposed converter is rather complex the converter itself shows very good behaviour. Yet, several problems have been detected during the analysis of the converter operation. The main reason for these problems is the low output voltage of a fuel cell. This means that high currents are expected at the input of the converter but also that this voltage may not be sufficient for gating and control purposes at start-up. One of the problems is induced by the variations of the fuel cell voltage. This will result in variations of the efficiency if the constant output voltage is needed at different loads.

4.1. Problems due to converter high input current

As the single fuel cell at the linear region has low output voltage (usually lower than 1 V), the converter input current, for the desired output power, will be significantly higher. In fact, to achieve output voltage of 12 V and load current of 2 A, we can expect the input current to be around 50 A (for input voltage of 0.55V and the converter efficiency of 90%). This means that we should expect significant voltage drops on the switches conducting during the first step of operation (Fig. 4). To minimize this voltage drop the switches should have very low on-resistance. In our

simulations we have used MOS switches IRF6607 with $R_{Dson} = 3.3 \text{ m}\Omega$, and we have got improved characteristics by connecting two MOSFETs in parallel for the switches S_1 and S_{1d} . Using the new Philips MOSFET PH2920 ($V_{DS} \leq 20\text{V}$, $V_{GS} \leq 20\text{V}$; $I_D \leq 60 \text{ A}$; $P_{tot} \leq 62.5 \text{ W}$; $R_{Dson} \leq 2.9 \text{ m}\Omega$; $I_{DM(pulse)} \leq 200 \text{ A/10ms}$ at $V_{DS} = 1 \text{ V}$), will give even better results. The paralleling of the switches may be imposed also by their current capabilities. It should be noted that during start-up the current through the switches is much higher for a short time interval.

4.2. Start-up problems

Two major problems were recognized during the start-up of the converter. First of all there is need of an auxiliary power supply for generating control pulses. In [1] low voltage converter MAX857 was used at about 1.75V input voltage. In some other applications an auxiliary battery is used for providing the power during the start-up. Another solution is to use an auxiliary low power self oscillating DC/DC converter. One possible circuit for this purpose is shown in Fig. 9. The circuit of Fig. 8 was examined by Pspice simulation. The output voltage at load resistance of 100k Ω was 11.6 V. The transistors were chosen to be Q2N2222A, the diodes – D1N4148 and the circuit component values are given in Table 1.

Table 1. Component values for the circuit given in Fig. 8

$L_{cc}, \mu\text{H}$	r_{cc}, Ω	$L_C, \mu\text{H}$	$L_B, \mu\text{H}$	$L_S, \mu\text{H}$	R_B, Ω
200	0.1	1.5	6	96	100

The output capacitors C_S are used as charge storage, and should supply the necessary charge to the gates of the MOS switches. We have calculated that for a start-up period of 10 ms the value of this capacitor should be around 1 mF to provide efficient control of total number of 75 MOS switches IRF6607 and to keep the supply voltage during start-up period above 10 V. In fact, as the total gate charge for an IRF6607 is 60 nC, the total charge for all switches will be 4.5 μC . At switching frequency of 25 kHz it gives average current of 112.5 mA. After the start-up period the converter output can be used for this purpose.

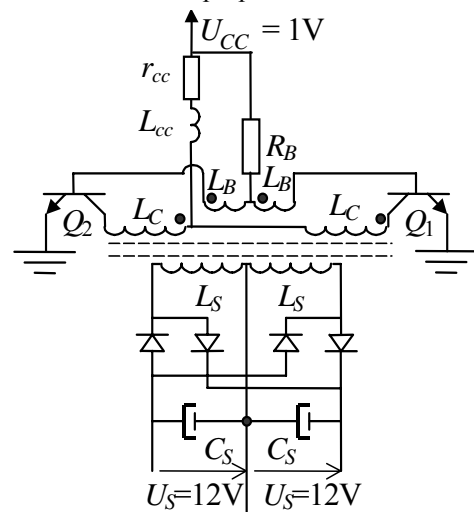


Fig. 9. Low power 1/12V DC/DC converter for start-up

The second problem, which should be taken in serious consideration, is very high initial current (Fig. 7). As mentioned above, a fuel cell could be catastrophically damaged if overloaded. This imposes the need of controlling the current through the cell during the start-up period. Also, the switches should be capable to withstand this transient current for a short period. One possibility is to control the current, rather than the duty ratio, through the switch S_1 , as described in [6]. As the input and output voltage of the converter does not change the expected conversion efficiency will not be affected [6].

5. CONCLUSIONS

This paper analyses the possibilities for application of inductorless switched capacitor DC-DC converter in fuel cell application. It is shown that the ladder like SCC is capable to convert the voltage of a single fuel cell i.e. from 0.6–0.8 V to 9-12 V. To establish nearly constant current through the fuel cell and to improve the efficiency at higher power levels, the interleaving was used by connecting five converters and shifting the control pulses for each converter by 0,2 T. Although the converter is more complex than those presented in [1] and [2], it is capable to convert much higher power, with high conversion efficiency.

The problems imposed by the high current through the switches of the first stage, as well as the start-up problems are discussed. One possible auxiliary circuit for producing the necessary supply to the gates at start-up is proposed. To prevent the possible damage of the cell during the start-up the measures for limiting the current should be taken into consideration.

Although the practical realization was not completed the simulation results show very good behaviour of the converter, small ripple of the output voltage, and efficiency higher than 90%.

6. REFERENCES

- [1] http://courses.ece.uiuc.edu/ece345/projects/spring2002/project37_final_paper.doc
- [2] http://www.fuelcellstore.com/products/ect/dc_converter.html
- [3] http://www.motorola.com/mot.doc/0/91_MotDoc.pdf
- [4] R.Stobart, "Fuel Cell Technology for Vehicles", www.sae.org
- [5] J. Kosev, G. L. Arsov, "Multistep inductorless DC-DC transformer with high voltage ratio", *ELECTRONICS*, vol 5, No 1-2, Dec. 2001, Fac. of Electrical Engineering, Banja Luka, RS – selected paper, pp 54-57
- [6] Chung, Hui, Tang, "Development of multistage current-controlled switched-capacitor step-down DC/DC converter with continuous input current", *IEEE Trans on circuit and systems – 1*, vol. 47, No. 7, July 2000, pp. 1017-1025

ELECTROMAGNETICAL COUPLING ON A DOUBLE CIRCUIT HIGH VOLTAGE 220 KV ELECTRICAL OVERHEAD LINES

Mariana Titihăzan^{}, Marian Greconici^{*}, Viorel Titihăzan^{*}, Dumitru Toader^{*}, Adrian Buta^{*}, Nicolae Chiosa^{**}, Valeriu Lazu^{**}, Florinel Sturza^{**}, Dragan Neşin^{**}, Marian Mihai^{**}*

^{} POLITEHNICA University of Timișoara, Romania, ^{**} TRANSELECTRICA Electrical National Company, S.T. Timișoara, Romania*

Abstract: *In the first part of this paper the analytical calculus, the modelling in PSPICE medium and the experimental measurements of the capacitive coupling voltages is analyzed. In the second part - analytical calculus and the experimental measurements of the inductive coupling voltages on the high voltage 220 kV overhead electrical lines with double circuit is analysed.*

Key Words: *Capacitive coupling voltage, Inductive coupling voltage, Electromagnetic compatibility, Numerical modelling*

1. ASPECTS OF THE ELECTROMAGNETICAL COMPATIBILITY OF THE ELECTROMAGNETICAL OVERHEAD ELECTRIC LINES

Overhead electric lines may produce electromagnetic disturbances – dangerous induced voltages – by capacitive and by inductive coupling. Capacitive coupling which is an electrostatic coupling, appears in any metallic circuit nearby by high voltage lines, if this passive circuit is insulated opposite earth. Capacitive coupling depends of the circuit geometry, but if the insulation resistance of the passive circuit is very great ($R_{ins} \rightarrow \infty$), induced potential U_p in this circuit may be calculate by coupling coefficient k_c [1]. The limit of the capacitive coupling influence may be obtain by following technical solutions:

- the distance increase between high voltage overhead electric line and telecommunication line – which are parallel placed;
- the utilisation of the telecommunication lines with two conductors;
- the screening of the telecommunication lines on the intersection portion or on parallelism with high voltage overhead electric line;
- the transposition of the phases so that for high voltage overhead electric line, so for telecommunication lines.

In the case of the three-phased high voltage overhead electric line with double circuit – at the removal under voltage of one of the three-phased circuit for repair, in the passive circuit may appear [1], [2], [3], [4]:

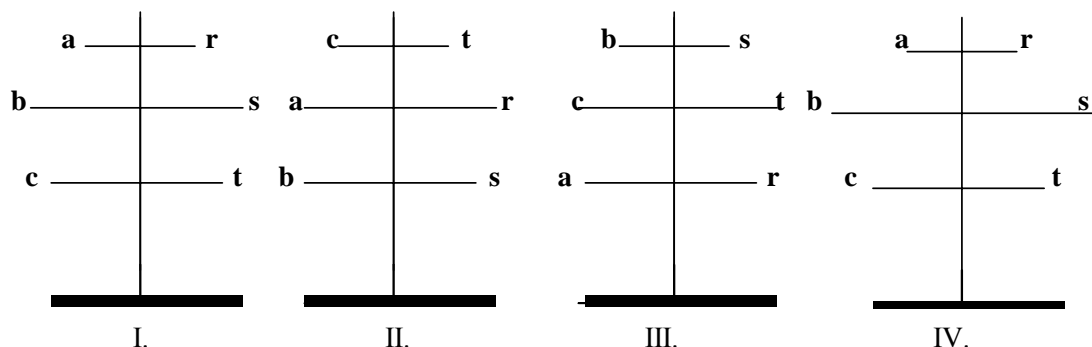


Fig.1. *The transposition phases overhead line 220 kV Double Circuit.*

- capacitive coupling voltages – in the situation of passive circuit is insulated to earth;
- inductive coupling voltages – proportional with the phase current value from inductor circuit, in the situation in which the three phases removed under voltage are short-circuited and connected to earth at least in one point - at an extremity.

Induced voltage in a passive phase depends of the mutual capacity values between analysed phase and the three inductor phase, as of the own capacity – to earth, of the analysed phase. The induced voltages by three-phased capacitive coupling will be phasorial summation.

2. THE ANALYTICAL CALCULUS OF THE INDUCED VOLTAGES BY CAPACITIVE COUPLING

The analysed electrical overhead line has 220 kV with double circuit and with four transposition tronsons of the phases. The conductors are by type Ol – Al 450 / 75 mm² having the radius

$r_o = 14.625$ mm. In Table 1 are presented the medium height H_j of every phase to earth, taking in consideration the transposition, which appeared (Figure 1).

In the Table 2 are presented the geometrical distances between the both phases of the three-phased inductor circuit (a, b, c) - and three-phased induced circuit (r, s, t).

Table 1. *Medium heights of the phases H_j ($j = r, s, t$).*

Transposition tronsons	H _r [m]	H _s [m]	H _t [m]
$l_{I} = 23.8$ km	25	18.5	12
$l_{II} = 45.3$ km	18.5	12	25
$l_{III} = 31.4$ km	12	25	18.5
$l_{IV} = 15.8$ km	25	18.5	12

Table 2 Distances between phases – for transpositions tronsons, for Tronson l_I .

Tronson l_I		Phase r	Phase s	Phase t
$l_I = 23.8$ km	Phase a	Dar = 9m	Das = 14.1m	Dat = 16.1m
	Phase b	Dbr = 14.1m	DBs = 16m	Dct = 14.53m
	Phase c	Dcr = 16.1m	Dcs = 14.53m	Dct = 10m

The own capacities of every phase $C_{(x, H_j)}$ was calculated for every transposition tronson $x = l_I$,

l_{II}, l_{III}, l_{IV} in the programming medium MathCad 5 for Windows. Induced voltages by capacitive coupling result

$$U_{ind r} = U_f \frac{C_{ar} - \frac{C_{br} + C_{cr}}{2}}{C_{ar} + C_{br} + C_{cr} + C_{ro}} = U_f \frac{C_{ech r}}{C_{ar} + C_{br} + C_{cr} + C_{ro}}$$

$$U_{ind s} = U_f \frac{C_{bs} - \frac{C_{as} + C_{cs}}{2}}{C_{as} + C_{bs} + C_{cs} + C_{so}} = U_f \frac{C_{ech s}}{C_{as} + C_{bs} + C_{cs} + C_{so}} \tag{1}$$

$$U_{ind t} = U_f \frac{C_{ct} - \frac{C_{at} + C_{bt}}{2}}{C_{at} + C_{bt} + C_{ct} + C_{to}} = U_f \frac{C_{ech t}}{C_{at} + C_{bt} + C_{ct} + C_{to}}$$

(1) from the calculus of the capacitive current circulation, the phase voltage being.

$U_f = 127$ kV. In Table 3 are given the mutual capacities and own capacities – summing the corresponding capacities of the four transposition tronsons :

The transpositions of the phases overhead line 220 kV having the total length 116.3 km conducted at a relative symetrisation of the electrical capacities and the of other parameters, having effect and on uniformisation and reducing of the induced voltage values by capacitive coupling.

Table 3. Mutual capacities and own capacities Phase r [nF] .

C_{ar}	C_{br}	C_{cr}	C_{ro}	$C_{ech r}$
970,9542	935,3294	934,5391	822,1624	36,0199

In Table 4 are comparative presented the induced voltages by capacitive coupling – by analytical calculus determined for:

- 220 kV overhead line double circuit with length $l_1 = 116.3$ km and with transposed phases;
- 220 kV overhead line double circuit with length $l_2 = 73.1$ km without the transpositions of the phases.

In the case overhead line double circuit without the transpositions of the phases resulted electric capacities with the greatest values for the phase r and with the least values for the phase s , and induced voltages by capacitive coupling also resulted with greater values and with a greater non-uniform grade.

Table 4. Induced voltages by capacitive coupling – by analytical calculus.

220 kV double circuit overhead line	Length	$U_{ind r}$ [kV]	$U_{ind s}$ [kV]	$U_{ind t}$ [kV]
With transpositions	$l_1 = 116.3$ km	1.24	1.33	1.58
Without transpositions	$l_2 = 73.1$ km	2.53	0.51	2.01

3. MODELLATIONS IN PROGRAMMING MEDIUM PSPICE OF THE INDUCED VOLTAGE BY CAPACITIVE COUPLING

The Microsim Corporation send up the program PSPICE (PC Simulation Program with Integrated Circuit Emphasis) for electronic circuits drawing, simulation and analyse [9], [10]. The application for behaviour simulation one high voltage circuits in transient regime – had like purpose a comparison about the obtained results by different methods and analyse about de parameters diagram influence upon induced voltages by capacitive coupling. The numerical modellation presents numerous advantages about oscilogrammes obtained so that for voltages, and so for currents from analysed circuits – for processing and comparative multiple analyse of the oscilogrammes.

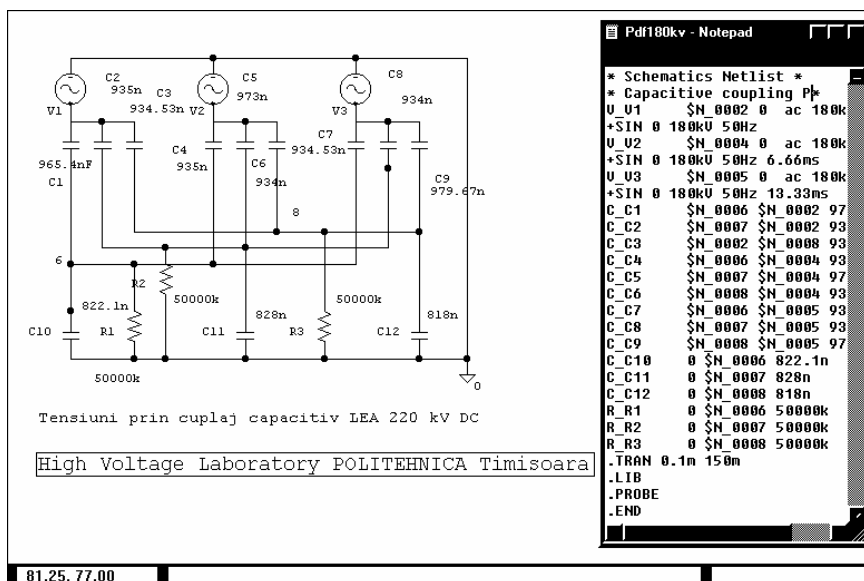


Fig.2. Cable diagram of tested high voltage circuit 220 kV.

In Figure 2 is given the cable diagram of the tested circuit, obtained with schematics editor SCHEMATICS. The diagram contains three sinusoidal voltage sources phasorial phase shifted, mutual capacities between phases and own capacities – of every phase to earth. In parallel with own capacities – of every phase, was introduced an insulating resistances $R_{ins} = 50 \text{ M}\Omega$ – in the nodes 6, 7 and 8. In the simulation program a standard transient analyse have effected between 0.01 ms and 60 ms.

In the Figure 3 are presented the induced voltages oscilogrammes by capacitive coupling in nodes 6 (phase r), 7 (phase s), 8 (phase t) and in nodes 2/10,

4/10, 5/10 with oscilloscope software PROBE obtained. In the first stage – theoretical case – in which the three-phased voltage system is not symmetrical due later s phase connection (at $t = 6.66\text{ms}$) and t phase connection ($t = 13.33 \text{ ms}$) – the induced voltages are great $U_{max} = 43 \text{ kV}_{max}$. After that voltage system of the three voltage sources become symmetrical ($t > 13.33 \text{ ms}$) the capacitive induced voltages values – substantial diminished and have approached values by the analytical calculated values.

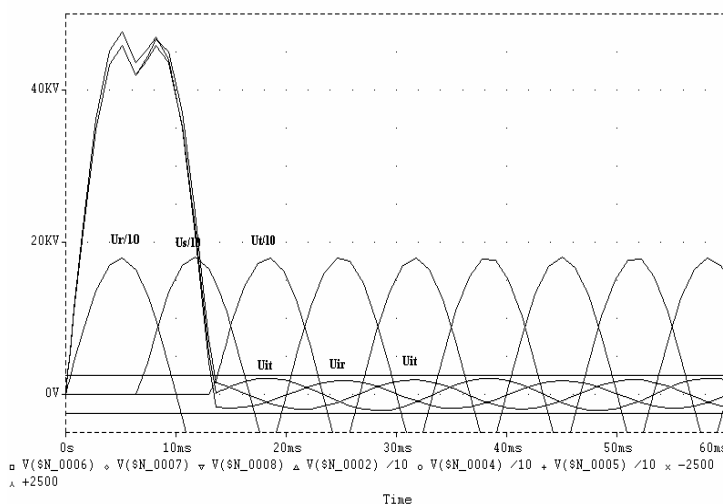


Fig.3. Oscilogrammes $U_{ind r}$ \$N_0006\$, $U_{ind s}$ \$N_0007,

4. EXPERIMENTAL MEASUREMENTS ABOUT CAPACITIVE COUPLING FOR OVERHEAD ELECTRIC LINES 220 KV WITH DOUBLE CIRCUIT

The research team composed by the professors - from the Electrotechnical Engineering Faculty of the Politehnica University Timisoara and specialist engineers in high voltages networks – from the Transelectrica National Company – Timisoara, have accomplished analytical and

$U_{ind t}$ \$N_0008\$, \$N_0002/10\$, \$N_0004/10\$, \$N_0005/10\$ experimental determinations about disturbances voltages – by capacitive coupling on a 220 kV double circuit electrical overhead line. In the Table 5 are centralized the calculated values and experimental

Measurements values for the capacitive coupling induced voltages. Experimental measurements by capacitive coupling of the voltages with an electrostatical high voltage voltmeters have effectuated.

Table 5. Induced voltages by capacitive coupling – centralization.

220 kV double circuit overhead line		U ind r [kV]	U ind s [kV]	U ind t [kV]
l _I = 116.3 km	Analytical values	1.24	1.33	1.58
	PSPICE modelling	1.55	1.28	1.38
With transpositions	Experimental values	2.4	2.5	2.7
l ₂ = 73.1 km	Analytical values	2.53	0.51	2.01
	PSPICE modelling	3.75	0.85	2.85

5. THE COMPLEX CALCULLUS OF THE INDUCED VOLTAGES ON A DOUBLE CIRCUIT ELECTRIC OVERHEAD LINES WITH 3 TRANSPOSITIONS

The analysed electrical line have Un = 220 kV with double circuit and with four tronsons with phases transpositions. By expressing inductor currents in complex:

$$I_a = I \quad I_b = I e^{-j 120} \quad I_c = I e^{+j 120} \quad (2)$$

The induced voltages by active phases a, b, c in passive phases r, s, t become:

$$\begin{aligned} U_{ir} &= j \omega I (M_{ar} + M_{br} e^{-j 120} + M_{cr} e^{j 120}) \\ U_{is} &= j \omega I (M_{as} + M_{bs} e^{-j 120} + M_{cs} e^{j 120}) \\ U_{it} &= j \omega I (M_{at} + M_{bt} e^{-j 120} + M_{ct} e^{j 120}) \end{aligned} \quad (3)$$

The mutual inductivities Mar ... Mct have been calculated for every transpositions tronson with known length l_k (k = I, II, III, IV), with these relations [1], [4]:

$$M_{ar} = \frac{\mu_o}{2\pi} l_k \ln \frac{R_p}{D_{ar}} \quad M_{ct} = \frac{\mu_o}{2\pi} l_k \ln \frac{R_p}{D_{ct}} \quad (4)$$

$$R_p = 550 \sqrt{\frac{\rho}{f}} \quad (5)$$

where Rp = 550 m the deeply of the return way by earth, ρ = 50 Ωm earth resistivity and f = 50 Hz.

For a load current I = 1 A results:

$$U_{ir} = (I_1 + I_{IV}) 33.15 e^{-j 102.5} + I_{II} 7.21 e^{-j 16.4}$$

$$+ I_{III} 27.28 e^{-j 78.2} = 0.193 - j 2.213$$

$$U_{is} = - 2.131 + j 0.881 \quad (6)$$

$$U_{it} = 2.185 + j 1.189$$

The induced voltages calculuss on every tronson – permits an induced voltages and induced current evaluation which can appear in the situation of the mounting in different points on overhead lines – short-circuits for the workers protection in the time of repair works. In Table 6 are centralised the effective values and initial phases of induced voltages – for every from four transposition tronsons, for an inductor current with unit value I = 1 A. In the case in which in inductor circuit pass symmetrical load current with value I₁ = 255 A and I₂ = 500 A, the induced voltages by inductive coupling – are calculated and presented in Table 7.

Table 6. Induced voltages U_{ir st} [V] for I = 1 A.

Tronson	Phase r	Phase s	Phase t
L _I = 23.8 km	0.7958 V α = - 102.65°	0.1732 V α = + 136.42°	0.6549 V α = 41.78°
l _{II} = 45.3 km	0.3247 V α = - 16.42°	1.2279 V α = + 161.78°	1.4922 V α = 17.34°
l _{III} = 31.4 km	0.8458 V α = - 78.22°	1.0279 V α = + 137.34°	0.2237 V α = 103.57°
l _{IV} = 15.8 km	0.5305 V α = - 102.65°	0.1545 V α = - 136.42°	0.4366 V α = 41.78°
l _Σ = 116.3 km	2.2222 V α = - 85°	2.3065 V α = + 157.53°	2.5899 V α = 32.44°

Table 7. Induced voltages U_{ir st} [V] for I₁ = 255 A and I₂ = 500 A.

Tronson	Phase r	Phase r	Phase s	Phase s	Phase t	Phase t
	I ₁ =255A	I ₂ =500A	I ₁ =255A	I ₂ =500A	I ₁ =255A	I ₂ =500A
l _I =23.8km	202.4	397	44.1	86.6	166.9	327.4
l _{II} =45.3km	82.8	162.5	313	613.9	380.5	746.1
l _{III} =31.4km	215.6	422.9	262	513.9	57.02	111.8
l _{IV} =15.8km	135.2	265.2	39.3	77.2	111.3	218.3
l _Σ =116.3km	566.7	1111.2	588.1	1135.2	660.4	1294.9

6. EXPERIMENTAL MEASUREMENTS ABOUT INDUCTIVE COUPLING FOR OVERHEAD ELECTRIC LINES 220 KV WITH DOUBLE CIRCUIT

In the first case – the 220 kV electrical line has l₁ = 116.3 km length and was projected with 3 transpositions of the phases – for the parameters symetrizing. In the second case of a shorter electrical line of l₂ = 73.1 km – without transpositions – was considered. In the Table 8 are centralised the calculated

values and experimental measurements values for the inductive coupling induced voltages. A relative dispersion of the analytical determination values and experimental determined values can be explain by some errors and disturbances which intervne in the diagrams and measurement apparatus, as the manner which was evaluated in calculus all geometrical distances. The geometrical distances of the line can have some fluctuation, in special zones of the overhead electric lines pass.

Table 8. Induced voltages by inductive coupling – centralisation.

220 kV Double Circuit overhead line		U _{i r} [V]	U _{i s} [V]	U _{i t} [V]
L ₁ = 116.3 km I _a =I _b =I _c = 255 A With transposition	Analytical values	566.7	588.1	660.4
	Experimental values	300	350	400
L ₂ = 73.1 km I _a =I _b =I _c = 300 A Without transpositions	Analytical values	725.5	158.2	593.3
	Experimental values	500	150	400

7. CONCLUSIONS

The induced voltages by capacitive coupling – measured and calculated - in medium limited – are similar with other values in technical specialty literature [6], [7], [8]. The transposition of the phases at a relative symetrisation of a overhead line parameters contributes – and of a diminish and a uniformization of the induced voltage.

The existence of a three-phased inductor voltages system reduces the induced voltage values by capacitive coupling. The induced voltages by capacitive coupling is canceled at a first earth connection of the respective phase – but presents a dangerous potential in the case of some tronsons which should remain insulated to earth – without any discharge point.

The induced voltages by inductive coupling – electromagnetic coupling, are less than induced voltages by capacitive coupling and depend by the phase current values from the inductor circuit (the circuit under voltage), by the length of the parallel tronsons, as well as by presence or absence of the closed loops – which can provoke screening effects. The transposition of the phases and respectively the acting with a symmetrical system of the inductor currents – have like effect the substantial reduction of the inductive coupling voltages. The transposition of the phases increase the cost of the high voltage overhead line and is recommended to apply for length greater than 100 km [6], [8].

For to respect the same succession of the phases at the entrance in the second electric substation – are necessary four tronsons with transpositions. The induced voltages determination by inductive coupling are important from the point of view of the Work Protection Normatives. Function by induced voltages values and by the earth electrode resistances from the extremity of the work areas – result the maximum voltages values on the earth electrodes. These voltage values cannot exceed for not create dangerous conditions for the technical personnel which execute repair works on the double circuit high voltage overhead electric lines.

8. REFERENCES

- [1] A. Buta “*Transportul și distribuția energiei electrice*“ vol. I + II, Universitatea Politehnica Timișoara, 1991.
- [2] V. Titihăzan “*Impactul rețelelor electrice asupra mediului și aspecte de compatibilitate electromagnetice*” Editura AGIR, Bucuresti, 2000.
- [3] V. Titihăzan, Mariana Titihăzan, D. Toader, M. Moga, N. Chiosa, I. Ardelean, D. Neșin “*Capacitive Coupling Voltage on a Double Circuit High Voltage 220 kV Electrical Overhead Lines*” 4th International Conference on Electromechanical and Power Systems, Chisinau, 26-27 sept. 2003, pg. 147-151
- [4] D. Radu, V. Titihăzan, A. Buta, Mariana Titihăzan, D. Toader, N. Chiosa, I. Ardelean, Verislava. Neșin, L. Popa “*Determination about Inductive Coupling Voltage on a Double Circuit High Voltage 220 kV Electrical Overhead Lines*” Proceedings of 6th International Conference on Applied Electromagnetics, Nis –3 June 2003, pg. 269-272
- [5] V. Titihăzan, A. Buta, Mariana Titihăzan, D. Toader, M. Moga, A. Pană, N. Chiosa, I. Ardelean, Verislava. Neșin “*PSPICE Modelling and Determination of the Capacitive Coupling Voltages on Double Circuit High Voltage 220 kV electrica ovehead lines*” Proceedings of 6th International Conference on Applied Electromagnetics, Nis –3 June 2003, pg. 273-276
- [6] A. Popescu, A. Cristovici, D. Necșulescu, F. Vatră “*Considerații privind implicațiile utilizării liniilor electrice multiplu circuit*” *Revista Energetica* 26, Nr.9, 1978, pg. 300 – 311.
- [7] C. Golovanov, M. Albu, N. Golovanov ș.a. “*Probleme moderne de măsurare în electroenergetică*” Editura Tehnică, București, 2001.
- [8] Normativ 3.RE – Ip 41 / 92 “*Instrucțiuni de proiectare și exploatare privind protecția împotriva influențelor datorate apropiierilor dintre liniile de energie electrică de înaltă tensiune*” ISPE București, 1995.
- [9] St. Andrei, “*PSPICE - Analiza asistată de calculator a circuitelor electronice*”, Editura ICPE București, 1996.
- [10] I. Sztojanov, S. Pașca – “*Analiza asistată de calculator a circuitelor electronice*”, Editura TEORA Bucuresti 1997. [Http:// www.microsim.com](http://www.microsim.com)

INFLUENCE OF VOLTAGE SAGS ON PERSONAL COMPUTERS AND PWM DRIVES

S. Ž. Djokić, J. V. Milanović, J. J. M. Desmet*, K. Stockman**, G. Vanalme*

Department of Electrical Engineering and Electronics, UMIST, Manchester, United Kingdom, * Department Provinciale Industriële Hogeschool, Hogeschool West-Vlaanderen, Kortrijk, Belgium, ** Department ESAT, Division ELECTA, Katholieke Universiteit Leuven, Leuven, Belgium

Abstract: This paper discusses the sensitivity of personal computers and PWM drives to voltage sags and short interruptions on the basis of extensive test results. The results of the following tests are presented in the paper: testing against various types of single-phase, two-phase and three-phase voltage sags and short interruptions, as well as testing with the ideal and non-ideal supply characteristics. Presented test results show that behavior of both equipment types in the general case cannot be described with the only one voltage-tolerance curve. Instead, families of voltage-tolerance curves should be used for description of the PCs and PWM drives sensitivity to voltage sags and short interruptions. Special attention is given to similarities in responses between these two types of equipment. Those similarities are discussed in detail in the paper.

Key Words: Short Interruptions, Voltage Sags, Power Quality, Equipment Sensitivity, Personal Computers, PWM Drives

1. INTRODUCTION

Both personal computers (PCs) and pulse-width modulation controlled voltage source inverter drives (in further text: PWM drives) are typical examples of recently emerged, widely used, rather complex and sophisticated non-linear electronic equipment. They are already reported as very sensitive to voltage sags and short interruptions (e.g., [1]-[3]). All the consequences of such a high sensitivity are additionally exacerbated because the PCs and PWM drives are usually utilised in a variety of commercial and industrial continuous processes. The PCs and PWM drives are often a critical piece of process equipment, since other equipment involved in the process is usually either controlled by them, or attached to them as a peripheral, or an auxiliary device. Accordingly, if a PC or PWM drive trips, the whole process will be stopped.

Based on the results of laboratory testing this paper shows that PCs and PWM drives have similarities in responses to voltage sags and short interruptions. They both utilise rectifier at the front end: full-wave single-phase diode switch-mode power supply is usually used for the PCs, and full-wave three-phase bridge diode rectifier is used for the PWM drives. Their ride through capabilities are mainly determined by the same three factors: a) dc link capacitance (i.e., stored energy that is used during the sag or interruption), b) power/current consumption of the load (i.e., energy demand of the rectifier's load) and c) undervoltage/overcurrent protection settings (i.e., allowed deviations in voltage/currents values during the energy conversion and transfer).

2. SENSITIVITY OF PERSONAL COMPUTERS

The sensitivity of personal computers to voltage sags is usually expressed with the only one voltage-tolerance curve, indentifying sags that yield to restarting/rebooting of the computer. However, test results presented in full in [2]

show that a voltage sag or short interruption might cause lockup of the actual operations performed by the computer and/or blockage of its operating system (OS) without restarting/rebooting of the computer. In other words, voltage-tolerance curves obtained only for restarting/rebooting malfunction criteria are not conservative. If only this voltage-tolerance curve is available, it may be misleading, especially in the case when a process controlled by the computer is of particular importance and interest (e.g., on-line processing, 24/7 Internet services, real-time data acquisition, the GUI, SCADA and other applications).

In the first part of testing, ideal supply characteristics were maintained before and after the application of rectangular voltage sags and short interruptions. It was found that voltage-tolerance curves of all tested PCs have the following three distinctive parts: a flat vertical part, a flat horizontal part, and a sharp "knee" between them. It was also found that different points on wave of voltage sag initiation and different phase shifts during the sag do not have any noticeable influence on the PCs behavior during the voltage sag. The detailed test results for one computer are shown in Fig. 1. There are significant differences between the three different voltage-tolerance curves that correspond to three different malfunction criteria.

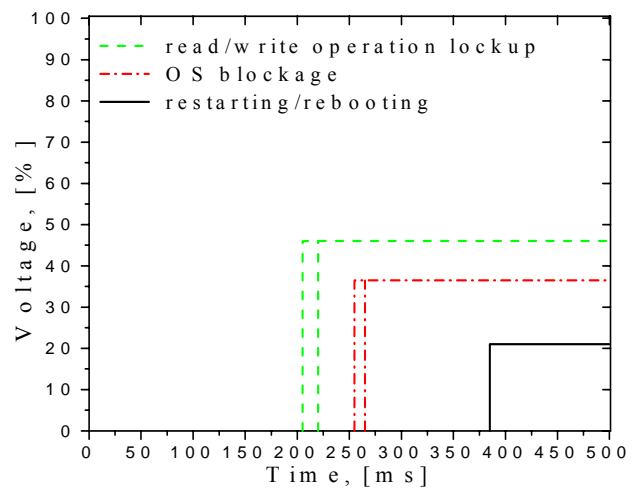


Fig. 1. Voltage-tolerance curves for one tested PC.

In Fig. 1, two software criteria (lockup of read/write operation and blockage of computer OS) result in a wider vertical part (a family of vertical lines whose boundaries are shown in Fig. 1) than the hardware (restart) criterion. This is a consequence of different power consumption conditions related to different stages of operation, or different OS execution states (i.e., different loading conditions). The hardware criterion results in a single vertical line because it is related to the (undervoltage) limit of the switch mode power supply. There are also significant differences in the horizontal parts of these voltage-tolerance curves. The difference in the sensitivity thresholds between the curves obtained using the first software criterion (lockup of read/write operation) and the hardware criterion

(restarting/rebooting) is almost a 100% for the duration and more than a 100% for the voltage magnitude. These differences indicate the range of possible errors if ride-through capabilities of the computer were assessed only on the basis of the hardware malfunction criterion.

The rectifier dc voltage (5V dc output) was monitored during the tests. It was found that it starts to decay at about 200ms after the initiation of the voltage sag. The voltage sags and interruptions shorter than 200ms therefore, will not have influence on the behavior of computer. This happens because there is enough energy stored in a dc link capacitance to maintain correct operation of dc voltage regulator, i.e. correct operation and functioning of computer.

Results for all six tested computers are shown in Fig. 2. The voltage sag magnitude thresholds for tested computers vary between 20-65% of rated voltage, and duration thresholds vary between 40-400ms.

The ITIC [4] and SEMI F47 [5] power acceptability curves are also plotted in Fig. 2 (with thick solid and thick dashed line, respectively). It can be seen that all tested PCs satisfy the ITIC power acceptability curve, but all of them except one, violate the most recent SEMI F47 standard.

During the second stage of testing, the PCs were supplied from the non-ideal voltage source. Deviations from the ideal supply characteristics were within the following limits: voltage magnitude variations up to $\pm 10\%$ of the rated voltage, frequency variations up to $\pm 2\%$ of the rated frequency, and different harmonic content (3^{rd} , 5^{th} and 7^{th} harmonic) superimposed to the fundamental frequency waveform with the THD not exceeding 20%. The above disturbances were applied both separately and simultaneously, in order to assess their individual and cumulative effect on the PC's operation during the sags and interruptions.

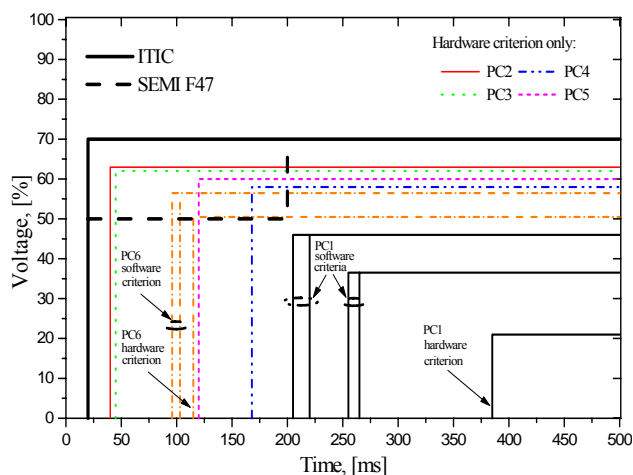


Fig. 2. Voltage-tolerance curves for six tested PCs.

As an example, cumulative effects of both voltage magnitude variations and presence of the third harmonic is illustrated in Fig. 3. The third harmonic has the biggest influence and it is also the dominant harmonic in the "harmonic spectrum" emitted by the personal computers during the normal operation. It can be seen that the simultaneous variations of the pre-sag voltage magnitude and the harmonic content have a significant effects on the computer sensitivity to voltage sags.

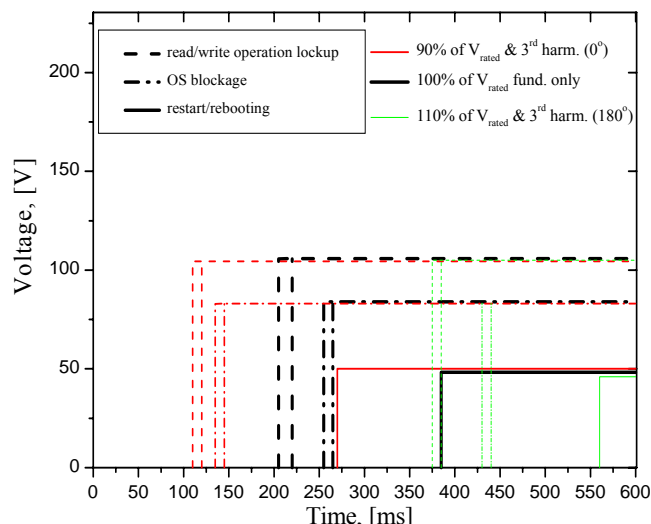


Fig. 3. Cumulative influence of non-ideal supply ($\pm 10\%$ voltage magnitude and 3^{rd} harmonic with 20% THD).

3. SENSITIVITY OF PWM DRIVES

The voltage-tolerance curves of the PWM drives identified in tests have several characteristics very similar to the voltage-tolerance curves of computers. The voltage-tolerance curves of the PWM drives also have three distinctive parts: a flat or slightly inclined vertical part, a slightly inclined horizontal part, and a smooth "knee" between them. As with the PCs, it was found that different points on wave of sag initiation and different phase shifts during the sag do not have influence on the drive behavior.

Three different load types were used in tests: a) constant power load, b) constant torque load, and c) quadratic torque load. Very small differences are identified between the voltage-tolerance curves for these three load types, and a constant torque load type was used in further tests.

The PWM drives are three-phase equipment and different combinations of the three phase voltages during the sags have different effects on their operation. However, not all combinations of phase voltages during the voltage sags and short interruptions are likely to occur in power systems. It was assumed in testing that sags and interruptions caused by different fault types (line to ground, double-line to ground, line-to-line and three-phase faults) propagate in a power systems in such a way that at least two phase voltages during the sag have equal (similar) magnitudes. Thus, testing of the PWM drives was conducted with the following three types of voltage sags:

1. Three-phase balanced voltage sags, i.e., during-sag voltage magnitudes in all three phases are equal.
2. Generalized two-phase voltage sags, i.e., during-sag voltage magnitudes of two sagged phases are equal; voltage in the third, "unsagged" phase is used as a parameter, and it can be either rated or below the rated.
3. Generalized single-phase voltage sags, i.e., during-sag voltage magnitude of one (sagged) phase is below the rated value; voltage magnitudes in two other phases are used as a parameter - they are always equal and rated, or equal and below the rated value.

Obtained test results show that the sensitivity of the PWM drives also cannot be described with only one voltage-tolerance curve [3]. In fact, the PWM drives have a more

complex sensitivity pattern, resulting in a greater number of voltage-tolerance curves than in the case of personal computers. Each voltage-tolerance curve obtained in drive testing corresponds to one particular voltage sag type, one particular load type, one particular value of loading torque and one particular value of motor speed. Furthermore, in tests performed with generalized single-phase and two-phase sags, additional parameter was voltage magnitude in the unsagged phase(s), which resulted in additional sets of voltage-tolerance curves. Each voltage-tolerance curve from these additional sets corresponds to one particular value of voltage magnitude in the unsagged phase(s). Figures 4-6 show families of voltage-tolerance curves identified in tests with the three different sag types, constant torque load types, rated motor speed and rated loading torque.

For all three sag types, significant influence of actual loading torque value and adjusted motor speed on drive sensitivity was identified in tests. These two parameters (torque and speed) actually present different loading conditions of the drive. Voltage-tolerance curves for one PWM drive obtained in tests with balanced three-phase sags and different torques and speeds are shown in Figures 7 and 8, respectively. Similar behaviour (i.e., better ride-through capabilities for lower torque and lower speed) were also identified in testing with generalized two-phase and single-phase sags and interruptions.

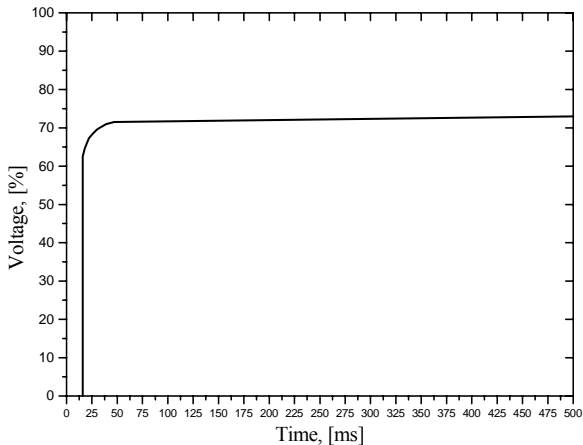


Fig. 4. Voltage-tolerance curve of PWM drive for balanced three-phase sags and interruptions.

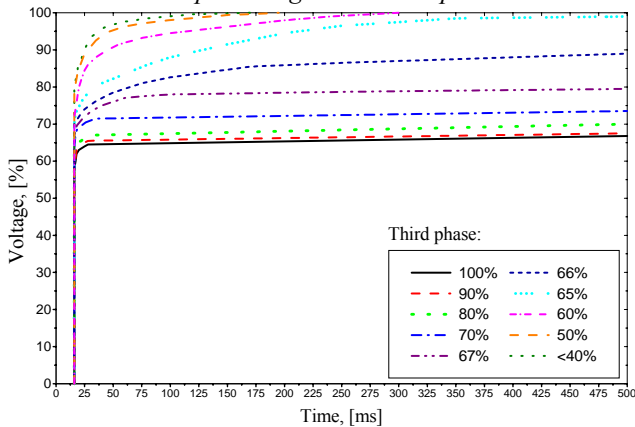


Fig. 5. Voltage-tolerance curves of PWM drive for generalized two-phase sags and interruptions.

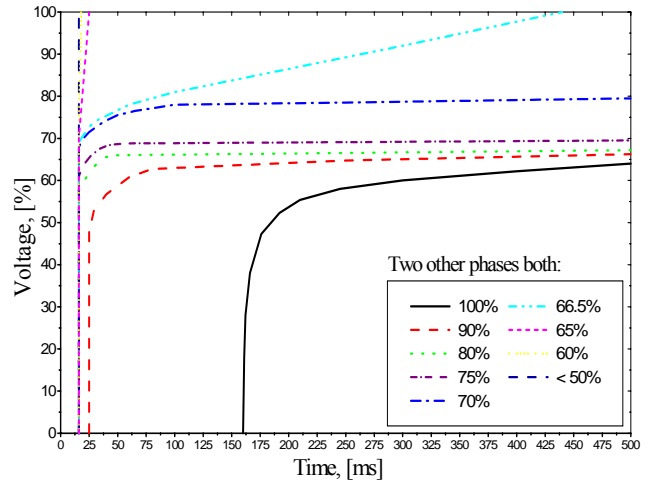


Fig. 6. Voltage-tolerance curves of PWM drive for generalized single-phase sags and interruptions.

As in testing of the personal computers, drives were also tested for a non-ideal power supply conditions present before and after the initiation of balanced rectangular three-phase sags and interruptions.

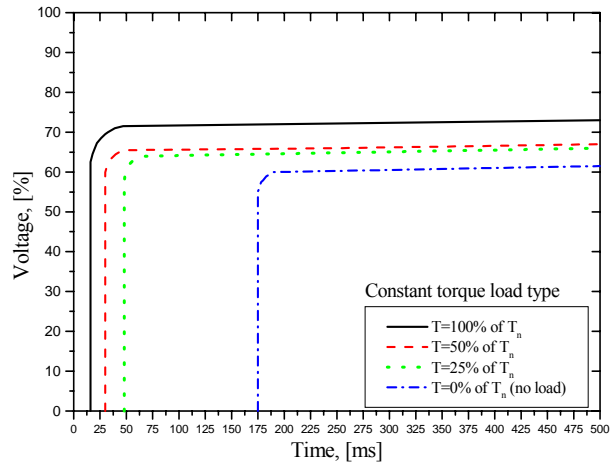


Fig. 7. Influence of different torque values on PWM drive sensitivity to balanced three-phase sags and interruptions.

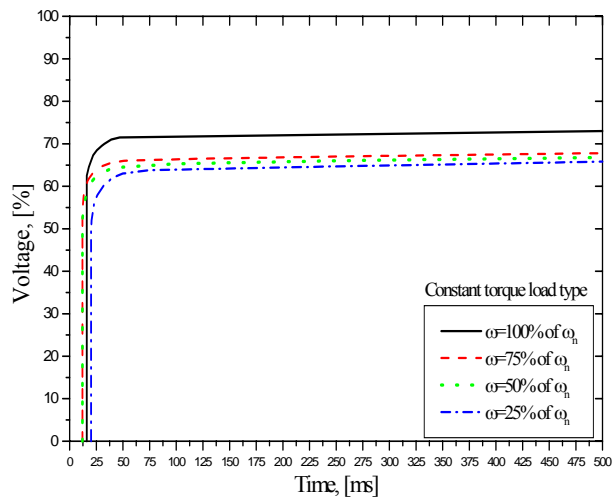


Fig. 8. Influence of different motor speeds on PWM drive sensitivity to balanced three-phase sags and interruptions.

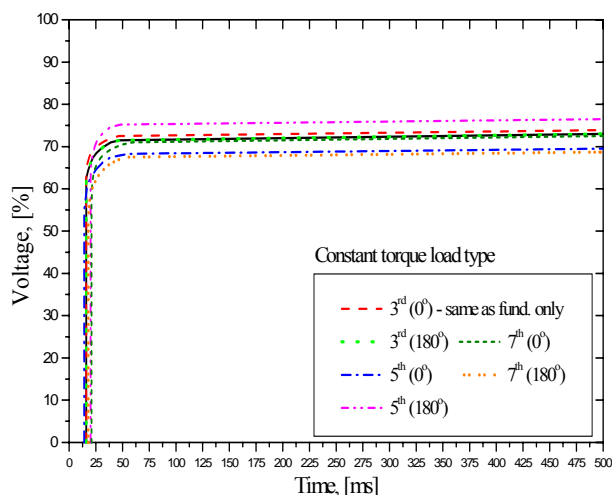


Fig. 9. Sensitivity of PWM drive to balanced three-phase sags regarding the variations in harmonic contents of pre-sag and post-sag supply voltage.

Applied deviations in non-ideal supply characteristics were the same as in tests of computers. It was found that drives have similar responses to the non-ideal power supply conditions, even regarding the response to different harmonic contents.

The highest influence on drive sensitivity was identified for the fifth harmonic, again the dominant harmonic in “harmonic spectrum” emitted by the drive during the normal operation Figure 9.

4. CONCLUSIONS

The PCs and PWM drives are both recently emerged, widely used, very sophisticated (power) electronic devices, that utilise the rectifier at the front end. They are very sensitive and often a critical piece of equipment in continuous processes in which are involved. Besides these general similarities, results presented in this paper show that they also have similar responses to voltage sags and short interruptions.

The behaviour of both PCs and PWM drives cannot be described with only one voltage-tolerance curve. Instead, families of voltage-tolerance curves should be used for full description of their sensitivity to voltage sags and short interruptions. Both PCs and PWM drives have similar shapes of voltage-tolerance curves: this shape is rectangular for PCs, and almost rectangular for PWM drives. Only difference in voltage-tolerance curve shapes is presence of a smooth “knee” for PWM drives.

Point on wave of voltage sag initiation and phase shift during the sag, as the additional sag parameters, do not have influence on their sensitivity.

The sensitivities of both PCs and PWM drives vary significantly with the different loading conditions. With decreasing of the power/current consumption, their sensitivities decrease.

The non-ideal supply conditions also have similar effects on their behaviour during the sags and interruptions. Specifically, regarding the different harmonic contents, both PCs and PWM drives have the highest change in sensitivity for harmonics that are dominant in their spectra during the normal operation (the third harmonic for the PCs and the fifth harmonic for the PWM drives).

For both PCs and PWM drives, drop in ac voltage of the power supply during the sag is essentially seen as the drop in dc voltage at the output of the rectifier. Thus, maintenance of a continuous dc link voltage is crucial for normal operation of computers and PWM drives. The same three factors have the greatest influence on their dc link voltage and determine their overall sensitivity and ride-through capabilities: a) dc link capacitance, b) power/current consumption during the operation and c) undervoltage/overcurrent protection settings.

The same two protection systems are responsible for disconnection/tripping of both PCs and PWM drives during the sags and interruptions: the undervoltage and overcurrent protection systems.

After passing a particular magnitude and duration thresholds, the PCs and PWM drives both have the same characteristic in their responses to voltage sags and short interruptions (vertical part of their voltage-tolerance curves influence that there are no differences in tripping time between the sags and interruptions). The magnitude and duration thresholds are mainly determined by the settings of the undervoltage and overcurrent protection systems.

Due to the small power consumption, the ride-through capability of the PCs can be improved with a relatively small sag mitigation equipment (e.g., with a small uninterruptible power supply - UPS). For PWM drives however, their power consumption ranges influence the costs of adequately rated mitigation equipment which can be much higher.

5. REFERENCES

- [1] M. H. J. Bollen, “Understanding power quality problems: Voltage sags and interruptions”, IEEE Press, Series on Power Engineering, New York, 2000.
- [2] S. Ž. Djokić, J. Desmet, G. Vanalme, J. V. Milanović, K. Stockman: “Sensitivity of Personal Computers to Voltage Sags and Short Interruptions” (submitted for publication in IEEE Trans. on Power Delivery).
- [3] S. Ž. Djokić, K. Stockman, J. V. Milanović, J. Desmet, R. Belmans: “Sensitivity of AC Adjustable Speed Drives to Voltage Sags and Short Interruptions” (submitted for publication in IEEE Trans. on Power Delivery).
- [4] Information Technology Industry Council: “ITI (CBEMA) curve and Application note”, Washington, 1998, 2000. (<http://www.itic.org/technical/iticurv.pdf>)
- [5] Semiconductor Equipment and Materials International: “SEMI F47-0200, Specification for semiconductor processing equipment voltage sag immunity”, San Jose, 1999/2000. (<http://www.semi.org/pubs/semipubs.nsf>)

DISTORTED POWERS OF SOME POWER ELECTRONIC EQUIPMENTS

Ioan Şora, Alexandru Hedeş, Dan Nicoară, "POLITEHNICA" University of Timișoara, Faculty of Electrical Engineering, Timișoara, Romania

Abstract: The work presents the results of an experimental investigation on the harmonic distorted state determined at the electrical grid interface by some modern power sources, incorporating power electronics: a single-phase arc welding inverter, and an ultrasonic generator. Based on up-to-date definitions for powers associated with nonsinusoidal waveforms, there are presented and discussed the components of power measured at the grid interface of these equipments with power electronics.

Key Words: Harmonic Distortion, Power Measurement, HF Power Converters

1. INTRODUCTION

The new and high performance electrotechnologies require an accurate control of power processing. Power electronics is nowadays recognized as the "heart" of the power processing in various electrotechnologies. Two of these applications are the well-known arc welding and the ultrasonic processing of materials. The modern arc welding inverters and the electronic generators of electro-ultraacoustical equipments belong to static power converters, which represent - in electrical terms - nonlinear loads and hence, distorted power sources for the electric power system, Fig. 1, [1,2].

The large spread of electrical equipments incorporating power electronics and the current spotlight on power quality has reinforced the need for harmonic studies as a standard component of power system analysis and equipment design activities, [3,4].

In the circumstances of proliferation of high nonlinear and distorting loads for electrical low voltage networks, a large effort has been focussed on the definitions of powers associated with non-sinusoidal waveforms, based on theoretical considerations and on experimental measurements performed with modern and high accuracy power analyzers, [5].

The present work try to reveal, based on experimental investigations, how the various amount of distorted powers are presented at the electric grid interface of some equipments incorporating power electronics, designed for two electrotechnological applications: arc welding and ultrasonic cleaning, respectively.

In Fig. 1, is presented - as an example of a HF power converter - a HB topology with electrical isolation.

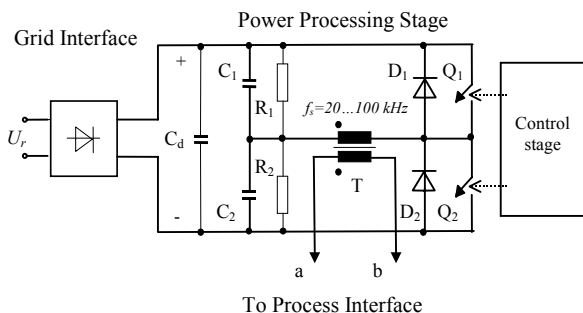
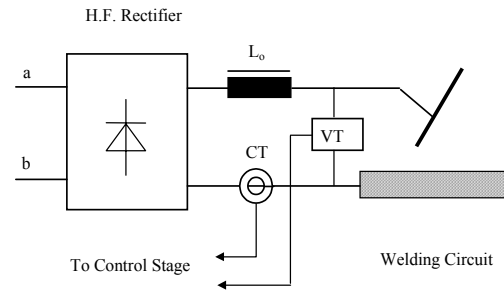


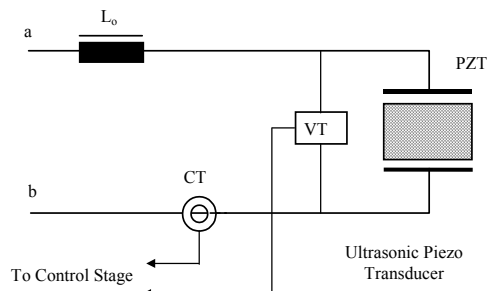
Fig. 1. The HB converter scheme of a HF power processing equipment

The switching frequency of the converter is in the range of 20 ... 100kHz.

The process interfaces, associated with the two above mentioned electrotechnologies, are presented in Fig. 2.



a. Arc welding equipment



b. Ultrasonic equipment

Fig. 2. The process interfaces for a HF power converter.

The goal of the experimental study is to determine the input harmonic spectra of: voltage, current and active power, the input distorting powers, and the distorting state indicators. The equipments under test have not been provided with filtering devices (passive or active) at the interface with the supply electrical network.

2. DEFINITIONS FOR POWERS IN SINGLE-PHASE SYSTEMS

In order to describe quantitatively the distorting state, various definitions of powers, and/or criteria for the quality of electric power have been proposed, [3,4].

In power terms, the distorting state is characterized by the presence of a so-called "distortion power", D , as defined by the general relationship:

$$S^2 = P^2 + Q^2 = S_1^2 + D^2 = P_1^2 + Q_1^2 + D^2 \quad (1)$$

where: P represents the total active power; Q - total reactive power, S_1 - fundamental apparent power with its components: fundamental active, P_1 , and reactive power, Q_1 . The term D represents a non-fundamental apparent power and consists of three components:

$$D^2 = S^2 - S_1^2 = (U_1 \cdot I_d)^2 + (U_d \cdot I_1)^2 + (U_d \cdot I_d)^2 \quad (2,a)$$

or, in other terms:

$$D^2 = D_i^2 + D_u^2 + D_{ui}^2 \tag{2,b}$$

where:

U_1, I_1 , are the fundamental of rms voltage and current;
 U_d, I_d , represent the rms values of the deforming residues of voltage and current.

The terms of the distortion power, in expressions (2), are respectively: D_i , the current distortion power; (usually the dominant term); D_u , the voltage distortion power; D_{ui} , the harmonic apparent power.

The relationships (2) suggest a geometrical model of powers in non-sinusoidal state, as represented in Fig. 3. This model consists of four rectangular triangles of powers, as follows, [6]:

- triangle of fundamental powers: $V_1 V_2 V_3$;
- triangles of distorted powers: $V_3 V_4 V_5$, and $V_3 V_5 V_6$; they are coplanar with the triangle $V_1 V_3 V_6$;
- triangle of total apparent power: $V_1 V_3 V_6$.

Based on the above definitions of powers, some power factors can be defined, as follows, [3]:

- the “total distortion power factor”:

$$k_{pd}^2 = \left(\frac{D}{S_1}\right)^2 = \left(\frac{I_d}{I_1}\right)^2 + \left(\frac{U_d}{U_1}\right)^2 + \left(\frac{U_d \cdot I_d}{U_1 \cdot I_1}\right)^2 = k_{di}^2 + k_{du}^2 + (k_{di} \cdot k_{du})^2 \tag{3}$$

- the “harmonic apparent power factor”:

$$k_{pdh} = \frac{D_{ui}}{S_1} = \frac{U_d \cdot I_d}{U_1 \cdot I_1} = k_{du} \cdot k_{di} \tag{4}$$

In the relationships (3) and (4), $k_{di}=I_d/I_1$, $k_{du}=U_d/U_1$, represent the harmonic distortion factors for current and voltage respectively. These power factors represent useful indicators for describing the distorted state determined by the non-linear electric loads in electrical network.

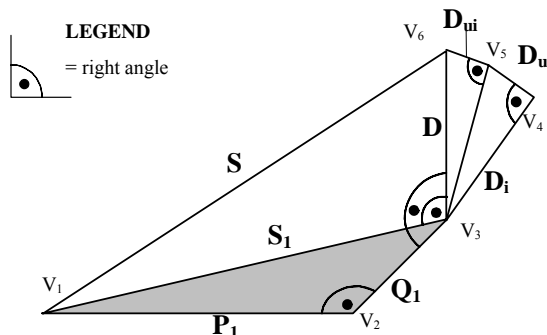


Fig. 3. The geometrical model of powers

3. EXPERIMENTAL RESULTS

3.1. The case of an arc welding inverter

The high performances of the arc welding inverter power source are strongly related to the high-frequency power processing. An uncontrolled single/tri-phase rectifier, with a capacitive filter, supplies the inverter power source from the electric network. The presence of the diode rectifier

at the interface with the electric network, and the high-frequency switching operation of the inverter, result in a substantial current harmonic pollution and electromagnetic interference (EMI), at the input of the arc welding inverter power source, [6].

The experimental study was performed on a single-phase inverter power source designed for Manual Metal Arc (MMA) and Wolfram Inert Gas (WIG) welding, with a 5...150A output current range, [7].

The input current harmonic spectra, at three levels of welding current, and the corresponding input harmonic active power spectra are presented in Fig. 4, and in Fig. 5, respectively.

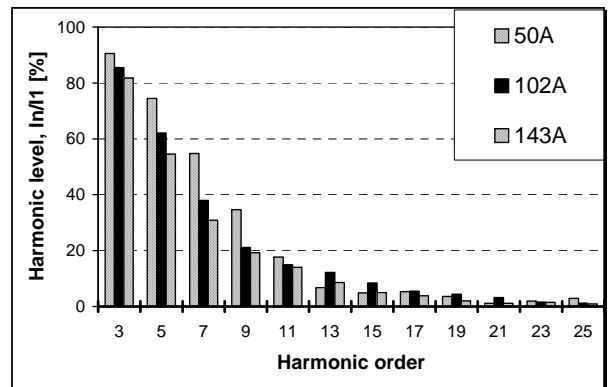


Fig. 4. The current harmonic spectra at the input of the arc welding inverter power source.

The harmonic level is defined as, $\gamma=I_n/I_1$, where: I_n , represents the r.m.s value of the n^{th} harmonic current.

As can be seen from Fig. 4 and Fig. 5, the arc welding inverter represents a serious distorting load for the electric network. The current harmonic levels decrease with the output load level of the power source.

The large scale spread of this type of welding equipment, imposes the application of harmonic mitigation methods, in order to reduce the harmonic currents up to the limits stipulated in harmonic standards, such as NF EN 61000-3-2, [2].

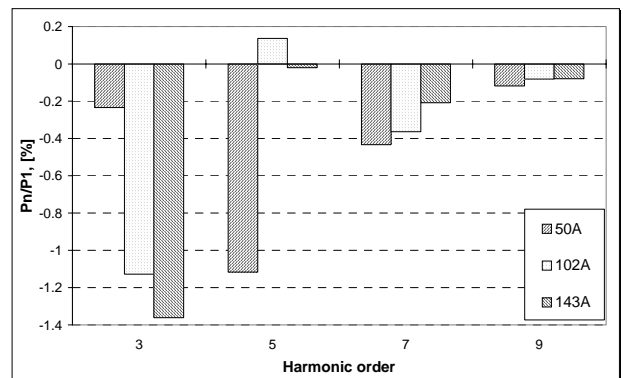


Fig. 5. The active power harmonic spectra at the input of the arc welding inverter power source

The measured and some calculated results are summarized in Table 1.

Table 1. Determinations for the arc welding inverter

Parameter	Welding current		
	50A	102A	143A
U [V]	223,93	221,88	218,26
U_i [V]	223,44	221,68	218,04
U_d [V]	14,81	9,42	9,80
THD_u	0,066	0,042	0,045
I [A]	8,78	25,03	32,24
I_i [A]	5,12	16,29	22,74
I_d [A]	7,13	19,00	22,86
THD_i	0,812	0,759	0,709
S [kVA]	1,967	5,553	7,038
P [kW]	1,131	3,408	4,472
Q [kVar]	1,609	4,384	5,434
D [kVA]	1,600	4,218	4,994
S_i [kVA]	1,143	3,612	4,959
P_i [kW]	1,130	3,446	4,671
D_u [VA]	75,75	153,46	222,81
D_i [kVA]	1,595	4,211	4,984
D_{ui} [VA]	105,69	178,93	223,93
Power Factor	0,575	0,614	0,636
k_{pd}	1,399	1,168	1,007
k_{pdh}	0,092	0,049	0,045

The measured total harmonic distortion of the voltage and current (THD) are given by the relationships:

$$THD_u = \frac{\sqrt{U^2 - U_1^2}}{U}; \quad THD_i = \frac{\sqrt{I^2 - I_1^2}}{I} \quad (5)$$

Based on the results from table 1, the following remarks can be made:

- the current harmonic distortion THD_i is much greater than the voltage harmonic distortion THD_u , i.e. the current distortion power D_i is much greater than the voltage and the harmonic distortion powers, D_u , and D_{ui} , respectively;
- the current harmonic distortion THD_i decreases with the increasing of the load current, and the total power factor increases with the increasing of the load current;
- the total distortion power factor, k_{pd} , and the harmonic apparent power factor, k_{pdh} , decrease with increasing of the load current;
- the total active power is not equal to the fundamental active power, due to the harmonic active powers.

3.2. The case of a power generator for ultrasonic cleaning

The characterization of an electronic power source dedicated to excitation of electro-acoustic transducers, in terms of the behaviour at the interface with the supply electrical network, must be made in conjunction with the evaluation of the output parameters of the power source, especially those concerning the excitation at the resonance of the ultrasonic transducer.

The equipment under investigations was an ultrasonic cleaning bath [8]. In Fig. 6, is presented the harmonic

spectrum of the input current, and in Fig. 7, the input active power harmonic spectrum. The values of the parameters, resulted from experimental investigation, are presented in Table 2.

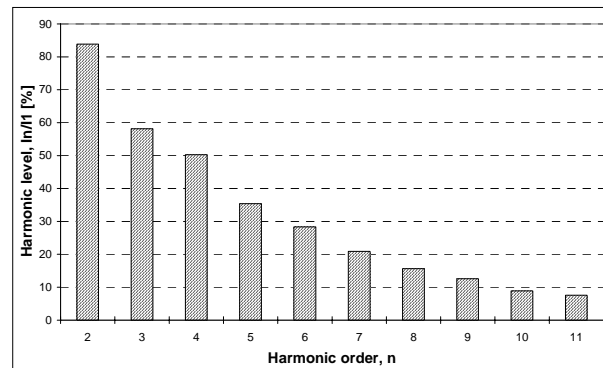


Fig. 6. The current harmonic spectrum at the input of an ultrasonic power generator.

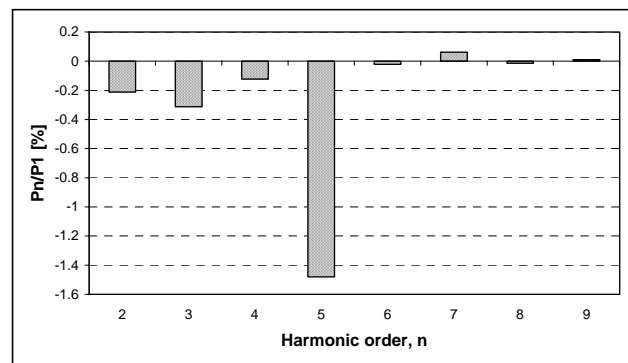


Fig. 7. The active power harmonic spectrum at the input of an ultrasonic power generator.

The harmonic spectra, experimentally determined, spotlight the “pure” behaviour of this type of equipments, that is characterized by the following aspects:

- the current harmonic spectrum shows a significant harmonic level ($>10\%$), for harmonic order less than 10;
- for the ultrasonic bath, the input current harmonic spectrum shows comparable harmonic levels between the odd and even current harmonics, that denotes a “hard” distortion of the input current (current distortion factor $K_{di}=0,7758$); this is in fact the result of the sequential operation of the generator, by piloting the pulses at 50Hz;
- the active harmonic powers, for a rated ultraacoustic load operation, are mainly odd and negative ones (except the 7th), thus being injected into the electrical network by the nonlinear receiver;
- the voltage harmonic spectrum shows a relative higher level (2,79%) for the 5th voltage harmonic, the others harmonics being much smaller, that correspond to a distortion factor less than 5%.
- based on the experimental results, the main conclusion that can be drawn is that the electro-ultraacoustical equipments can be included in the family of harmonic and distortion sources for the public supply electrical network, accordingly to IEC 1000-3-2, class D standard.

Table 2. Determinations for the ultrasonic generator

Parameter	Value	Parameter	Value
U [V]	226,44	Q [VAr]	135,406
U_1 [V]	226,229	D [VA]	115,069
U_d [V]	9,759	S_1 [VA]	93,474
THD_u	0,043	P_1 [W]	62,267
I [A]	0,655	D_u [VA]	4,032
I_1 [A]	0,413	D_i [VA]	114,891
I_d [A]	0,508	D_{iii} [VA]	4,956
THD_i	0,776	Power Factor	0,407
S [VA]	148,254	k_{pd}	1,231
P [W]	60,369	k_{pdh}	0,053

In the tables 1 and 2, the quantities marked with *italics* are measured, the other ones, are calculated.

4. CONCLUSIONS

The main conclusions that can be drawn from the experimental investigation are:

- the measurement of powers represents a useful tool to investigate the behaviour of the non linear loads supplied from the electricity network;
- based on the power measurements, it can be defined some power factors that describe quantitatively the distortion components of the total apparent power;
- the arc welding inverter power source and the power generator for ultrasonic processing represent today some exponents of the new generation of high frequency power processing equipments widespread in various applications;
- the distorting state indicators are comparable in both situations, except the total power factor, that is less in the case of ultrasonic generator;
- the arc welding inverter and the power generator for ultrasonic cleaning are both distorting non-linear loads for the electric network, being in need for application of harmonic mitigation techniques, [2].

5. REFERENCES

- [1] D. Nicoară, "Researches concerning the utilization of electro-ultraacoustical equipments on the enhancement of some technological processes in liquid media". Ph. D. Thesis, "Politehnica" University of Timișoara, 2000 (in Romanian language).
- [2] Șora I., Hedeș A., Nicoară D., "Experimental Evaluation of Harmonic Passive Filters for an Inverter Arc Welder", Proceedings of the 10th Symposium on Power Electronics, Ee'99, Novi-Sad, (YU), October, 1999, pp. 95-100.
- [3] * * * "Practical Definitions for Powers in Systems with Nonsinusoidal Waveforms and Unbalanced Loads: A Discussion", IEEE Working Group on Nonsinusoidal Situations: Effects on Meter Performance and Definitions of Power, IEEE Trans. Power Delivery, Vol. 11, No. 1, Jan. 1996, pp. 79-87.
- [4] Hyosung K., Blaabjerg F., Bak-Jensen Brigitte, "Unified Definition of Powers in Single-Phase Systems and Three-Phase Systems", Proceedings of EPE 2001, Graz, CD-ROM Version.
- [5] Bezold H., Lampl R., "Power Analysis with Distorted Wave Forms", PCIM Europe Magazin, No. 5, 1997, pp. 270-274.
- [6] Hedeș A., Șora I., "From the Welding Arc to the Mains Supply via the Inverter Power Source", Official Proceedings of the 7th European Power Quality Conference, June 19-21, 2001, Nürnberg, Germany, PQ 2.3, pp. 57-62.
- [7] * * * REHM Schweißtechnik – *Der Maßstab für modernes Schweißen: BOOSTER 150* – Inverter des Jahres, 1997.
- [8] * * * COLE-PARMER Instruments Co, Lab Products, Illinois, USA, 1999.

REGULAR PAPERS

DESIGN OF CAN CONTROLLER BY PETRI NETS TECHNIQUE

Blagomir Donchev, Krassimira Philipova, Andrey Popov
Technical University of Sofia

Abstract: This paper represents an implementation of Petri Nets in modeling and analysis of a CAN (Controller Area Network) interface. The major automats in the controller are first modeled with Petri Nets (PN). The CAN controller with a simple bus line connection performs all the functions of the physical and data-link layers. The application layer is provided by a microcontroller, to which the CAN controller connects through general purpose non-multiplexed parallel 8-bits bus. The description of the automat is transferred to very high level descriptive language (VHDL) after analyzing the properties of Petri Nets

Keywords: Petri Nets, CAN controller, VHDL

1. INTRODUCTION

The CAN architecture that is widely applied in modern in-car communication systems [1] defines the lowest two layers of the model: the data link and physical layers. The application levels are linked to the physical medium by the layers of various emerging protocols, dedicated to particular industry areas plus any number of propriety schemes defined by individual CAN users.

The physical medium consists of a twisted-pair with appropriate termination. In the basic CAN specification [2], it has a transmission rate from 20KBaud up to 250 KBaud whilst full CAN runs up to 1 MBaud.

The physical and data link layers will normally be transparent to the system designer and are included in any component that implements the CAN protocols. There are some microcontrollers with integral CAN interfaces, for example, the 8051-compatible Siemens C505C processor and the 16-bit SAB-C167CR. The 81C91 is a standalone CAN controller which directly interfaces many microcontrollers.

Modeling with Petri nets is based on the interaction between events and conditions. The event is an action in the system, and the condition is a logical description of the systems state. The growing use of Petri nets is due to their strong mathematical description allowing the properties of the modeled system to be checked by analyzing the Petri net and its basic properties: *reachability tree*, *safeness*, *boundedness*, *liveness*, and *conservativeness*.

In this paper we first study the applicability of Petri nets for modeling of CAN protocol based systems, then we introduce the models being used for description by VHDL code and verified by simulation. Next the timing properties of the protocol are introduced and studied in order to enable proper timing simulation.

2. MODELING OF TRANSMITTER AND RECEIVER BLOCKS WITH PETRI NETS

According to the description of CAN protocol PNs are made of the main finite state automats – Transmitter block (Figure 1) and Receiver block (Figure 2). Each state of the automat is represented with a place in the PN.

Reachability tree is used in order to determine specific properties of the Petri net. Some of the more important properties that can be determined include safeness, boundedness, liveness, and conservativeness. The reachability tree begins with the initial marking M_0 . From this marking, a new marking is created for each enabled transition from that marking. Subsequently, a new marking is created for each enabled transition from the reached markings. Once a marking is found that is already present in the tree it need not be added to the tree for a second time. Once all possible markings have been found, the tree is complete. The completed reachability tree shows all of the possible markings that can be obtained from the initial marking given every possible sequence of transition firings.

The reachability tree of TXBL is shown by matrixes on Figure 3. On Figure 4 are shown the relevant matrixes for RXBL.

The columns in RM represents Reachable Markings and A represents adjacency matrix ($A(i,j)$ means oriented arc from vertex i to vertex j). Value of $A(i,j)=p$ means that marking in column RM(j) could be reached from place i by

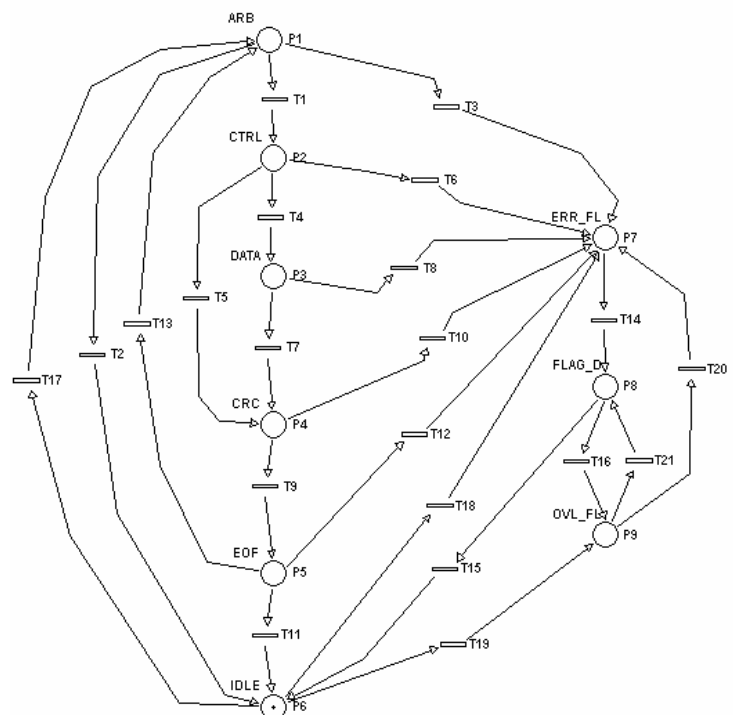


Fig. 1: Petri net description of transmitter block

firing transition p. The PN of the TXBL is safe, because there is only one token in the PN in all reachable markings. Properties boundedness and conservativeness are derived from property safeness. TXBL PN is live, because there is no deadlock. This property is important quality for the TX

automat, because it guarantees that the communication protocol will have proper operation in all possible conditions.

Similar analysis is made for the PN of the Receiver: the PN is safe and live. On the ground of that results the description of both Petri Nets is transferred to VHDL [3-4], by describing the states and the conditions for transition from one into another.

3. IMPORTANCE AND FUNCTIONAL DESCRIPTION OF CAN CONTROLLER

In real-time control systems, usually, many wiring connectors are used for various switches, sensors and actuators. The extreme example is automobile electronics, where the wiring became not only expensive, but also unreliable. In order to solve this problem and interconnect all devices efficiently, using multiplex transmission communication technology, a small scale LAN (Local Area Network) is constructed, resulting in data communication among devices using common lines. The communication format (protocol) is adapted by the Society of Automotive Engineers (SAE) in United States and referred to as SAE-J1850 [5]. However, the more popular and widely spread protocol name is CAN.

The importance of CAN introduction can be seen through the changes it brought in automotive electronics [6]. Figure 5 summarizes the state-of-the-art automotive application area. Its main characteristic is networking of electronic systems. The sub-systems must share data in real-time manner [7] and thus perform control in a more intelligent way. The best example for networking benefit is the coordination of the data generated by the braking, steering and suspension systems. Also, the technique of 'second guessing' becomes possible. It is a practice to use data from one system as a back-up for the other system under certain conditions. Thus, the wheel speed and vehicle direction information, already used in a stability management

system, could be used to back-up the navigation system, especially if the GPS (Global Positioning System) signal is lost.

Five distinct main communication systems are usually implemented, as shown in Figure 5. Very high speed network is in charge of processing of the external signals and requires high processing power. Body electronics is distributed in two networks according to speed requirements. Critical safety control functions (braking, steering, suspension) are grouped on a redundant network in order to meet fault tolerance criteria. Thus, only safety critical information is allowed on these buses. Due to becoming more and more robust, the airbag system is usually implemented as an

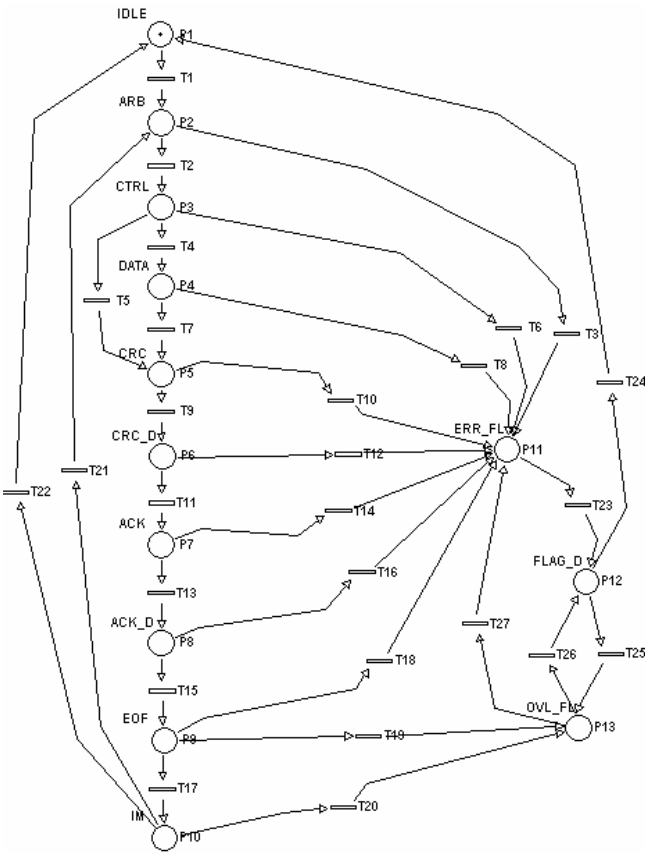


Fig. 2: Petri net description of receiver block

$$A_{TX} = \begin{bmatrix} 0 & 17 & 18 & 19 & 0 & 0 & 0 & 0 & 0 \\ 2 & 0 & 3 & 0 & 1 & 0 & 0 & 0 & 0 \\ 0 & 0 & 0 & 0 & 0 & 14 & 0 & 0 & 0 \\ 0 & 0 & 20 & 0 & 0 & 21 & 0 & 0 & 0 \\ 0 & 0 & 6 & 0 & 0 & 0 & 4 & 5 & 0 \\ 15 & 0 & 0 & 16 & 0 & 0 & 0 & 0 & 0 \\ 0 & 0 & 8 & 0 & 0 & 0 & 0 & 7 & 0 \\ 0 & 0 & 10 & 0 & 0 & 0 & 0 & 0 & 9 \\ 11 & 13 & 12 & 0 & 0 & 0 & 0 & 0 & 0 \end{bmatrix}$$

$$RM_{TX} = \begin{bmatrix} 0 & 1 & 0 & 0 & 0 & 0 & 0 & 0 & 0 \\ 0 & 0 & 0 & 0 & 1 & 0 & 0 & 0 & 0 \\ 0 & 0 & 0 & 0 & 0 & 0 & 1 & 0 & 0 \\ 0 & 0 & 0 & 0 & 0 & 0 & 0 & 1 & 0 \\ 0 & 0 & 0 & 0 & 0 & 0 & 0 & 0 & 1 \\ 0 & 0 & 0 & 0 & 0 & 0 & 0 & 0 & 0 \\ 1 & 0 & 0 & 0 & 0 & 0 & 0 & 0 & 0 \\ 0 & 0 & 1 & 0 & 0 & 0 & 0 & 0 & 0 \\ 0 & 0 & 0 & 1 & 0 & 0 & 0 & 0 & 0 \end{bmatrix}$$

Fig. 3: Matrix description of transmitter block

$$A_{RX} = \begin{bmatrix} 0 & 1 & 0 & 0 & 0 & 0 & 0 & 0 & 0 & 0 & 0 & 0 & 0 \\ 0 & 0 & 2 & 3 & 0 & 0 & 0 & 0 & 0 & 0 & 0 & 0 & 0 \\ 0 & 0 & 0 & 6 & 4 & 5 & 0 & 0 & 0 & 0 & 0 & 0 & 0 \\ 0 & 0 & 0 & 0 & 0 & 0 & 23 & 0 & 0 & 0 & 0 & 0 & 0 \\ 0 & 0 & 0 & 8 & 0 & 7 & 0 & 0 & 0 & 0 & 0 & 0 & 0 \\ 0 & 0 & 0 & 10 & 0 & 0 & 0 & 9 & 0 & 0 & 0 & 0 & 0 \\ 24 & 0 & 0 & 0 & 0 & 0 & 0 & 0 & 25 & 0 & 0 & 0 & 0 \\ 0 & 0 & 0 & 12 & 0 & 0 & 0 & 0 & 0 & 11 & 0 & 0 & 0 \\ 0 & 0 & 0 & 27 & 0 & 0 & 26 & 0 & 0 & 0 & 0 & 0 & 0 \\ 0 & 0 & 0 & 14 & 0 & 0 & 0 & 0 & 0 & 0 & 13 & 0 & 0 \\ 0 & 0 & 0 & 16 & 0 & 0 & 0 & 0 & 0 & 0 & 0 & 15 & 0 \\ 0 & 0 & 0 & 18 & 0 & 0 & 0 & 0 & 19 & 0 & 0 & 0 & 17 \\ 22 & 21 & 0 & 0 & 0 & 0 & 0 & 0 & 20 & 0 & 0 & 0 & 0 \end{bmatrix}$$

$$RM_{RX} = \begin{bmatrix} 1 & 0 & 0 & 0 & 0 & 0 & 0 & 0 & 0 & 0 & 0 & 0 & 0 \\ 0 & 1 & 0 & 0 & 0 & 0 & 0 & 0 & 0 & 0 & 0 & 0 & 0 \\ 0 & 0 & 1 & 0 & 0 & 0 & 0 & 0 & 0 & 0 & 0 & 0 & 0 \\ 0 & 0 & 0 & 1 & 0 & 0 & 0 & 0 & 0 & 0 & 0 & 0 & 0 \\ 0 & 0 & 0 & 0 & 1 & 0 & 0 & 0 & 0 & 0 & 0 & 0 & 0 \\ 0 & 0 & 0 & 0 & 0 & 1 & 0 & 0 & 0 & 0 & 0 & 0 & 0 \\ 0 & 0 & 0 & 0 & 0 & 0 & 1 & 0 & 0 & 0 & 0 & 0 & 0 \\ 0 & 0 & 0 & 0 & 0 & 0 & 0 & 1 & 0 & 0 & 0 & 0 & 0 \\ 0 & 0 & 0 & 0 & 0 & 0 & 0 & 0 & 1 & 0 & 0 & 0 & 0 \\ 0 & 0 & 0 & 0 & 0 & 0 & 0 & 0 & 0 & 1 & 0 & 0 & 0 \\ 0 & 0 & 0 & 0 & 0 & 0 & 0 & 0 & 0 & 0 & 1 & 0 & 0 \\ 0 & 0 & 0 & 0 & 0 & 0 & 0 & 0 & 0 & 0 & 0 & 1 & 0 \\ 0 & 0 & 0 & 1 & 0 & 0 & 0 & 0 & 0 & 0 & 0 & 0 & 0 \\ 0 & 0 & 0 & 0 & 0 & 0 & 1 & 0 & 0 & 0 & 0 & 0 & 0 \\ 0 & 0 & 0 & 0 & 0 & 0 & 0 & 0 & 1 & 0 & 0 & 0 & 0 \end{bmatrix}$$

Fig. 4: Matrix Description of receiver block

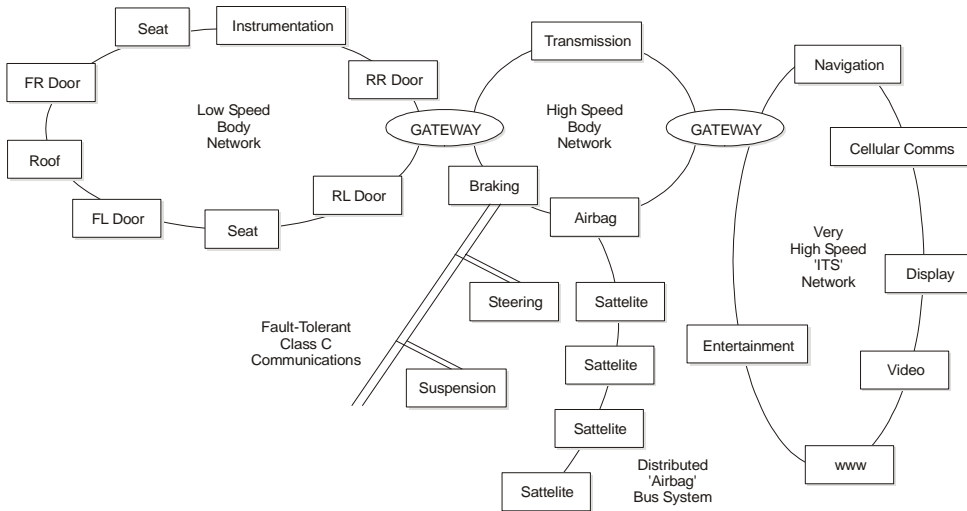


Fig. 5: On-vehicle electronic systems

independent network. Between the networks there are ‘gateways’ to share information across the boundaries when necessary.

In all five networks only two wires, CAN TX (Transmitting pull-up) and RX (Receiving pull-up) lines, are main communication carriers. Besides CAN, low speed (< 20Kbit/sec) modules (door, seat, roof) communicate with their sensors and actuators using LIN (Local Interconnect Network) [8-9], while newly the extremely fast applications (navigation, multimedia) turn to FlexRay [10-11] network (> 1Mbit/sec).

The represented CAN controller (MBCAN - this is abbreviation of current design.) contains all the necessary hardware for controlling the serial communication flow through the area network using the CAN-protocol. The MBCAN conforms to the CAN specification 2.0 part B. The MBCAN fully supports the Standard Format frames and it acts as a passive node for the frames in Extended Format.

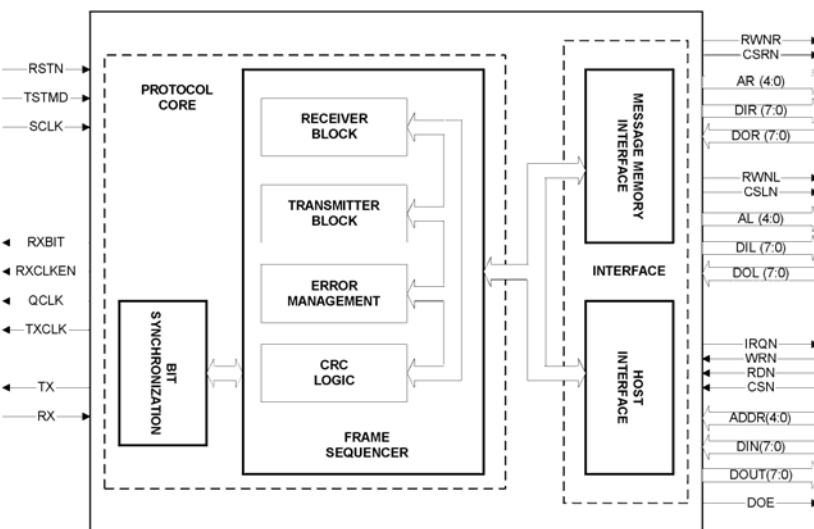


Fig. 6: Block diagram of the CAN controller

That means the MBCAN can be connected in a network that makes use of Extended Format as well as Standard Format. Messages in Extended Format are only received - the MBCAN doesn't corrupt them but sends acknowledge if they are correct. Messages with extended identifier cannot be

accepted (i.e. the host CPU is not notified) nor can the MBCAN send a frame in Extended Format.

The MBCAN must be linked to the physical transfer medium through an appropriate bus transceiver according to ISO/DIS 11898 or modified RS-485 transceivers. The MBCAN connects to this transceiver using one logic-input and one logic-output line. These are RX and TX correspondingly.

The MBCAN can be partitioned in two blocks – the *Protocol Core* accomplishing all the CAN rules [12], and the *Interface* block that provides the

ability to control the *Protocol Core* using a general microprocessor bus (Figure 6).

The *Frame Sequencer* is responsible for realizing the frame serialization, coding, decoding, error detection and signaling, and bus monitoring. The *Transmitter* and the *Receiver* incorporate the corresponding state machines needed for the transmission and for the reception of correct frames.

The *Error Management* unit performs the error confinement according to the CAN-protocol. It comprises of two error counters and additional logic, in order to define the bus/error status of the MBCAN.

The *CRC (Cyclical Redundancy Check) Logic* takes care of CRC generation during transmission of a message, and of a CRC check at the end of a received message.

The *Bit Synchronization* block controls the bit duration and bus sampling point, and derives information for synchronizing with the serial data stream. The internal logic of this block is able to lengthen/shorten the bit timing so that a correct sampling of the CAN-bus may be performed.

The MBCAN operates with three message buffers. They are realized in a dedicated external Dual Port RAM (DPRAM), called message memory. The *TX Message Buffer* takes 10 bytes of that memory into which the host writes the message that is to be transmitted. There are two *RX Message Buffers*. Each of them occupies 10-bytes of the message memory for storing the incoming message. In this way the host is able to process one message while another is being received. When both of the RX buffers are full, overload frames are generated until the host clears at least one of them. The interface signals to the DPRAM are elaborated inside the *Message Memory Interface*.

The *Host Interface* accomplishes a general purpose, non-multiplexed, parallel interface through which any control device (implementing the application layer of the protocol)

can access control and status information, as well as read and write the message buffers.

4. HOST INTERFACE

There are two types of accesses that might be performed into the internal registers.

The host initiates *read access* by first issuing valid ADDR (register address on address bus) and CSN (active low chip select signal). Internal address decoding is done when CSN is low. The data output bus DOUT becomes valid after the internal address decoding. When the host asserts RDN (Read control signal active low) LOW, the DOUT bus is already stable. The DOE (Data Output Enable) signal is set to HIGH when both the RDN and CSN are LOW. The DOE should enable the three-state on the system level. Therefore the CPU can sample the DOUT at any time while RDN is LOW.

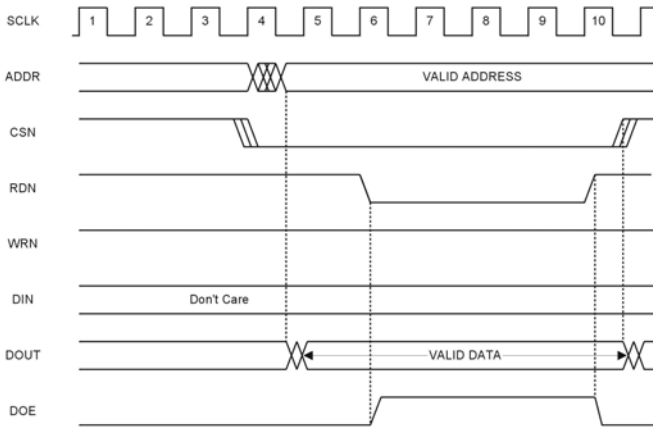


Fig. 7: Read access

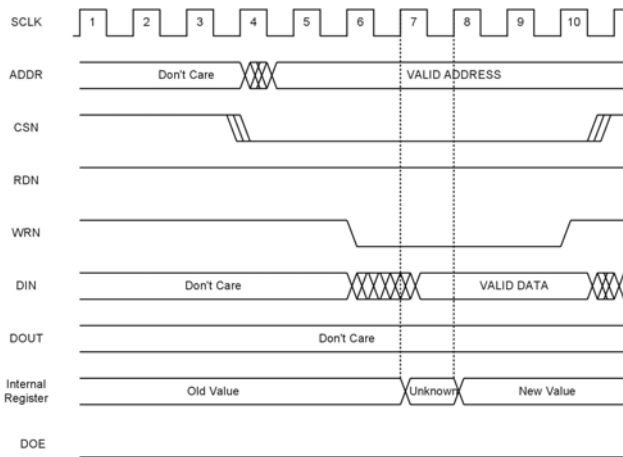


Fig. 8: Write access

The host initiates *write access* by first issuing valid ADDR and CSN. When these become stable, the host asserts WRN LOW. While the WRN signal is LOW, the MBCAN updates the accessed register at every rising edge of the SCLK (cycles 7, 8, 9 and 10). The host CPU must provide valid (stable) data over the DIN (Input Data) bus prior to set the WRN (Write control signal active low) HIGH. The internal register being target of the current access is updated more than once, but the last update is always performed at the end of a valid write operation (SCLK (System Clock)

cycle 10). Thus the register effectively stores meaningful information. In the case of a write access to the *Command Register* the commands are executed once only, after the host has finished the operation (WRN is set to HIGH) and the valid data have already been latched.

5. CAN BIT TIMING

A bit period is built up from a number of time quanta as defined by the CAN protocol. The time quantum T_Q is a fixed unit of time derived from the system clock (oscillator) by the means of a prescaler. The nominal bit period is the result of the addition of the programmable time segments TS1 and TS2 and the fixed length duration synchronization segment SYNCSEG (shown at Fig.9). SYNCSEG, TS1 and TS2 determine the location of the sample point (following equations, (1), (2), (3), (4) and (5) are valid).

$$T_{TS1} = T_Q(8TS1.3 + 4TS1.2 + 2TS1.1 + TS1.0 + 1) \quad (1)$$

$$T_{TS2} = T_Q(4TS2.2 + 2TS2.1 + TS2.0 + 1) \quad (2)$$

$$T_{SYNCSEG} = T_Q \quad (3)$$

$$T_Q = T_{SCLK}(32PSC5 + 16PSC4 + 8PSC3 + 4PSC2 + 2PSC1 + PSC0 + 1) \quad (4)$$

$$RSJW = T_Q(RSJ + 1) \quad (5)$$

Bit timing is controlled through the value of bit timing registers, BT0 and BT1. They are composed with 8 bits in the following order:

BT1 = -, TS2.2, TS2.1, TS2.0, TS1.3, TS1.2, TS1.1, TS1.0
 BT0 = RSJ, -, PSC5, PSC4, PSC3, PSC2, PSC1, PSC0

Accordingly, BT1 decides the length of time segments TS1 and TS2, while BT0 contains prescaler settings (PSC bits), dividing machine clock, and controls the resynchronization jump width (RSJW) through RSJ bit.

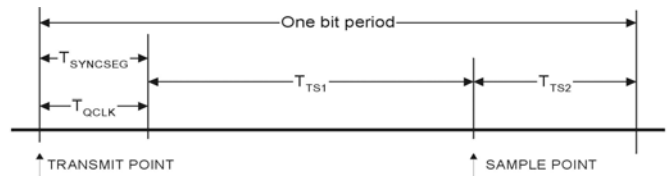


Fig. 9: Bit period as implemented in the MBCAN

Therefore the contents of the BT0 and BT1 registers define the nominal bit-rate of the transmitted and received messages.

A typical case is 1Mb/s with 8 quanta per bit with the sample point at the end of the 5th quantum and maximum of 2 quanta per resynchronization jump. Thus the SCLK should be 16 MHz, the contents of the BT0 register must equal hex (80) and BT1 register must be hex (23).

6. CAN COMMUNICATION PROTOCOL

The MBCAN bus controller supports the four different CAN-protocol frame types for communication: Data Frame, to transfer data; Remote Frame, to request data; Error

Frame, globally signals a (locally) detected error condition; Overload Frame, to extend delay time of subsequent frames.

There are two logical bit representations used in the CAN-protocol: A recessive bit on the bus-line appears only if all connected MBCAN send a recessive bit at that moment. Dominant bits always overwrite recessive bits i.e. the resulting bit level on the bus-line is dominant.

◆ Data Frame

A Data Frame carries data from a transmitting MBCAN to one or more receiving MBCANs. A Data Frame is composed of seven different bit-fields: Start-Of-Frame, Arbitration Field, Control Field, Data Field, CRC Field, Acknowledge Field, End-Of-Frame.

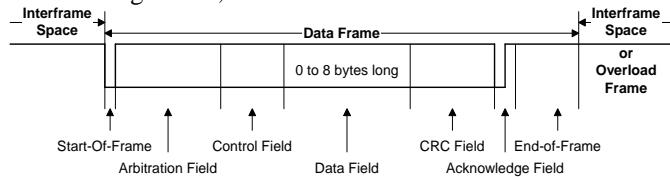


Fig. 10: Data Frame Format

◆ Remote Frame

An MBCAN, acting as a receiver for certain information may initiate the transmission of the respective data by transmitting a Remote Frame to the network, addressing the data source via the Identifier and setting the RTR (Remote Transmission Request) bit HIGH (remote; recessive bus level). The Remote Frame is similar to the Data Frame with the following exceptions: RTR bit is set HIGH, Data Length Code is ignored, No Data Field Contained.

◆ Error Frame

The Error Frame consists of two different fields. The first field is accomplished by the superimposing of Error Flags contributed from different MBCANs. The second field is the Error Delimiter. There are two forms of an Error Flag: Active Error Flag, Passive Error Flag.

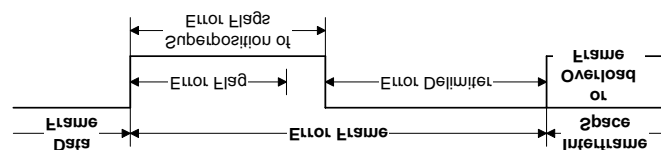


Fig. 11: Error Frame Format

◆ Overload Frame

The Overload Frame consists of two fields, the Overload Flag and the Overload Delimiter. There are two conditions in the CAN-protocol, which lead to the transmission of an Overload Flag: Receiver circuitry requires more time to process the current data before receiving next frame; Detection of a dominant bit during Intermission Field.

7. CONCLUSION

In this paper design of CAN controller was discussed. It is ideal for any situation where microcontrollers need to communicate either with each other or with remote peripherals. In its home environment, the car, CAN was originally used to allow mission-critical real time control systems such as engine management systems and gearbox controls to exchange information.

Petri nets were proven to be a concept exceptionally suitable for modeling of control systems. It allows for a mechanisms to analyze all possible states of realization for CAN controller. According to that, an attempt was done, described in this paper, to implement Petri nets for modeling of a CAN protocol. As a results of Petri nets design was an incident matrix with all possible matrix's invariants. It gives considerable advantages concerning the effectiveness of the synthesis for CAN controller.

The models developed will be applied as fundamental concepts in much bigger and more complex simulation tasks within the car communication system. All that being part of a designing tools development for CAN technology.

8. REFERENCES

- [1] CAN Description, *Siemens*, 1997.
- [2] CAN Specification,, *Robert BOSCH GmbH*, 1991.
- [3] C. Holmes and M. Willoughby, "VHDL Language Course", *Rutherford Appleton Laboratory*, 1997.
- [4] S. Mazor and P. Langstraat, "A Guide to VHDL", *Synopsys Inc.*, 1992.
- [5] Class B Data Communications Network Interface, SAE J1850 Standard, *SAE Vehicle Network for Multiplexing and Data Communications Standards Committee*, Revision May 1994
- [6] R. Jurgen, "Automotive Electronics Handbook", *McGraw-Hill*, 1995
- [7] D.Marsh , "CANbus ICs marry mechanics with electronic supervision and control", *EDN Magazine*, March, 1997
- [8] J. Quinn, "Digital Data Communication", *Prentice Hall*, 1995
- [9] www.lin-group.org – LIN Homepage
- [10] J. Berwanger et al., "FlexRay – the communication system for advanced automotive control systems", *SAE 2001 World Congress*, Detroit, April 2001, paper No. 2001-01-0676
- [11] www.flexray.com - FlexRay Homepage
- [12] J. Rushby, "Bus Architectures for Safety-Critical Embedded Systems", *EMSOFT 2001 – First Workshop on Embedded Software*, Lake Tahoe CA, October 2001
- [13] D. Smith, "HDL Chip Design", Doone Publication, *Madison* , 1996.
- [14] Ehrig H., Padberg J., "Petrietze: Modellierung, Strukturierungund Kompositionalitat", Berlin, 1998 .
- [15] Reisig W., "Elements of Distributed Algorithms: Modelling and Analysis with Petri nets", Springer- Verlag, 1998
- [16] Rozenberg G., Agha G., Cindio F., "Concurrent Object-Oriented Programming and Petri Nets", Springer-Verlag, Berlin,2001.
- [17] Billington J., Diaz M., Rozenberg G., "Application of Petri Nets to Communication Networks, LNCS", v.1605, Springer-Verlag, 1999.

- [18] Lavagno L., Blunno I., "Deriving Signal Transition Graphs from Behavioral HDL", IEEE Comp.Soc.Press, 2000.

REAL-TIME HUMAN FACE TRACKING WITH AN ACTIVE CAMERA USING BLOCK MATCHING TECHNIQUE

¹Nikola Teslić,²Vladimir Radenković,¹Dragan Kukulj,¹Miroslav Popović

¹Chair for Computer Engineering, Faculty of Technical Sciences, University of Novi Sad, Trg Dositeja Obradovica 6, 21000 Novi Sad, Serbia and Montenegro e-mail nikola.teslic@krt.neobee.net

²Television Novi Sad, Sutjeska1, 21000 Novi Sad, Serbia and Montenegro, e-mail vradenkovic@tvns.co.yu

Abstract: The paper presents an algorithm for the human face tracking using moving camera. Initially, detection of human silhouette is made, using difference of frames with and without moving object. Face region on selected silhouette is determined according to colour criterion. The block matching algorithm with reduced number of pixels is used for further tracking of selected block from face region. In that way, computational complexity is reduced and algorithm is capable to operate in real time regime. Moving vector of the selected block is moving vector of the whole figure in same time. The connection between a moving vector and a camera angle is calculated by pinhole algorithm, while camera speed is obtained using predicted moving vector of the next frame.

Keywords: Real Time tracking, block matching technique, moving object

1. INTRODUCTION

Problem of detection and tracking of moving object in video sequence is explored a lot in literature recently. Those algorithms are highly employed in: robotics, video surveillance, compression of video streams, traffic control, video conferencing, etc [1]-[3]. Some of these algorithms are used in systems for human silhouette tracking [4]. This is one of the most complex and demanding problems. Human silhouette is not rigid body, it means shape of tracing object is changed from frame to frame; environment-background is also changing shape, chrominance and luminance.

Requirements put in front of developed algorithm are even more demanding, because in the scene it is possible to have similar moving objects (human silhouette) and algorithm should provide stable tracking of selected object [6]. One more dimension of complexity of this problem is camera on moving robot platform [7].

First step in human face/head tracking is separation of moving object from background. Characteristics of background are not static: luminance, chrominance and movement. Outdoor as well as indoor there are ambience changes which depend on period of the day, changes in light etc. Those changes in comparison with changes introduced by moving object are slow; therefore in initialization phase background (without tracking algorithm) is analyzed. This approach gives ambience characteristics as result [2],[4],[6]. Next step is moving object separation from background in real sequence. Pixels which fulfil equation (1) are part of background.

$$|B_i(x, y) - F_i(x, y)| < D_i(x, y) \quad (1)$$

where:

$$B_i(x, y) = \frac{\sum_{j=i-N}^{i-1} F_j(x, y)}{N} \text{ is mean value of luminance}$$

on (x,y) coordinates in N consecutive frames of scene without tracking object (background);

$F_i(x, y)$ is value of luminance on (x,y) coordinates in current field;

$$D_i(x, y) = \frac{\sum_{j=i-N}^{i-1} |F_j(x, y) - F_{j-1}(x, y)|}{N} \text{ is mean}$$

value of difference between two successive frames on (x,y) coordinates.

Removing pixels that belong to the background from video sequence with moving object results in silhouette of moving object. Next step is to establish a region of interest, in our case position of face/head inside extracted silhouette. In literature [12], most common criterion is colour, anyhow there are no hard criteria which precisely define attributes of face/head, namely there is no exact colour coordinate of human face. Usually for this purpose HSI instead of RGB coordinate system is used, in case of HSI colour representation, face colour is defined with H axis [12],[13]. Value of coordinate H in most cases is in range from 0 to 50 degrees (between red and yellow).

Leading idea for this paper is to find optimal method for real time human face tracking. In this paper three methods are evaluated and compared: (1) tracking based on chrominance, (2) tracking based on chrominance and movement and (3) tracking based on block matching algorithm. Both methods, (1) and (2) show lower performance than block matching method, in cases of rotating tracking object and overlapping with near similar objects.

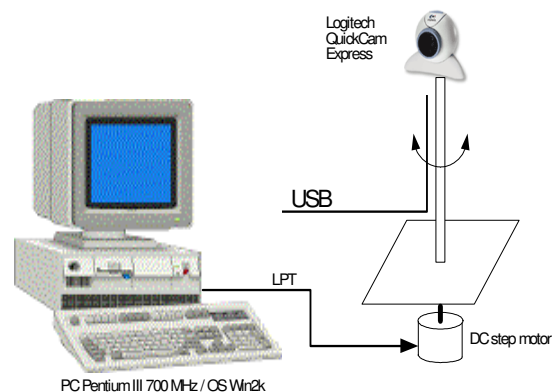


Figure 1. Rotation platform block diagram.

Evaluation platform for algorithm development is PC based work station (Intel PIII – 700MHz, OS Win2k) equipped with Logitech QuickCam Express USB colour web camera. Algorithm works in real time with 15 frames per second. Additionally, to make algorithm development as close as possible to target application (semiautonomous robot, which use developed algorithm for tracking of master) hardware module is developed. Block diagram of rotation platform (with rotation angle +/- 180 degrees) is shown on Figure 1, on top of the platform camera is mounted. Platform is equipped with step motor controlled through PC LPT port.

In following paragraphs, previously referenced (steps 1-4) algorithms will be separately analyzed, with clear statements what advantages and what drawbacks of each technique are.

2. DESCRIPTION OF THE SIMILAR METHODS

2.1. Color Based Tracking Algorithm

Extraction of the TO is realized in RGB colour space. First, silhouette is separated from background (step 2). Inside the silhouette pixels that belong to face are marked. In the first frame threshold value is experimentally determined, and pixels that are in range +/-20 from threshold value are marked to belong to the TO. Mean value of marked pixels in RGB colour space is calculated, this becomes a threshold for the next frame. In the next frame only pixels that are in range of new threshold +/-20 are marked as part of TO. Criteria for marking one pixel must be satisfied in all three coordinates (RGB). Equation that shows criterion when pixel belongs to the TO (when is marked) is given in (2).

$$C(x, y) = \begin{cases} 1, & |R(x, y) - R_{thr}| < 20 \text{ and } |G(x, y) - G_{thr}| < 20 \text{ and } |B(x, y) - B_{thr}| < 20 \\ 0, & \text{otherwise} \end{cases} \quad (2)$$

In field application TO colour is changed due to different ambient luminance. Threshold should be updated from frame to frame. The same approach like in the first frame is used. Mean value of marked pixels in RGB coordinate space is calculated and used as threshold for the next frame. As tracking object, circumrectangle around marked pixels is used. Orthocenter of circumrectangle is assigned as center of the TO.

Additionally, to reduce algorithm complexity one more simplification is done. Tracking human on relatively short distance has a consequence that x-y movement is small (in number of pixels). Having this in mind processing area in the next frame can be reduced to circumrectangle + maximal expected movement. Successfully separated TO using colour criterion in RGB coordinate space is shown in Figure 2. Disadvantage of using colour criteria are in sequences where human figure rotates (turnaround), namely when face turns away from the camera. To remove this artefact, algorithm described in the next paragraph is developed.



(a) input frame (b) marked pixels

Figure 2. Separation of TO using colour criteria.

2.2 Combined Motion and Color Based Tracking Algorithm

For separation of moving object, algorithm often used in TV application for motion detection is employed. This algorithm is realized in YUV colour space, where motion detection is performed only in Y domain, using interlaced model of image sequence representation (i.e. fields, consisting of only odd or even lines alternate in time). Presence of motion could be detected using equation given in (3), taking pixel from current frame $Y_i(x, y)$, and two pixels above $Y_{i-1}(x, y-1)$ and below $Y_{i-1}(x, y+1)$, from previous frame. If amplitude of middle pixel (from current frame) is not between amplitude of pixels above and below from previous frame, it is highly probably that there is movement. Determination of the moving region is made using equation (3) on previously formatted black-white picture $M(x, y)$.

$$M(x, y) = \begin{cases} 1, & Y_i(x, y) = \max(Y_{i-1}(x, y-1), Y_i(x, y), Y_{i-1}(x, y+1)) \text{ or} \\ & Y_i(x, y) = \min(Y_{i-1}(x, y-1), Y_i(x, y), Y_{i-1}(x, y+1)) \\ 0, & \text{otherwise} \end{cases} \quad (3)$$

Inside marked area (circumrectangle around pixels where motion is detected) colour criteria described in previous paragraph is applied. In Figure 3 results for motion detection are given.

Motion estimation (estimation of motion vector) is done based on a movement of orthocenter between two successive frames. Position of orthocenter is calculated according to equations given in (4) and (5).

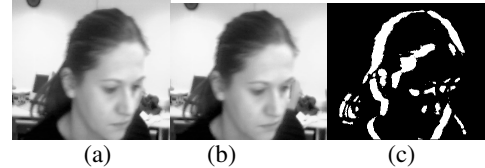


Figure 3. Motion detection results (a) i-1 frame, (b) i frame, (c) results of motion detection.

$$T_x = \left(\sum_{i=1}^W NW_i \cdot i \right) / N, \quad (4)$$

$$T_y = \left(\sum_{i=1}^H NH_i \cdot i \right) / N, \quad (5)$$

where W is picture width, H is picture height; NW_i and NH_i are numbers of pixels in i-th column and row where motion is detected. N is total number of pixels where motion is detected.

3. BLOCK MATCHING BASED TRACKING ALGORITHM

The proposed block matching algorithm consist four step as follows:

Step 1. In initialization phase the background without tracking object is analyzed;

Step 2. In working mode the first step is to separate object from a background using motion criteria between scenes with and without TO (tracking object);

Step 3. As a result of previous step human silhouette is extracted, and face localization is done. Colour criterion is used for selection of starting block which will be used as reference block for next frame;

Step 4. Finally, for tracking, adapted block matching algorithm is used.

Block matching is well known technique in digital image processing [14],[15] especially image compression. Rectangular block is compared with block of the same size in the next frame. The best match is on position where difference between reference block and compared block is minimal. Difference is calculated using mean absolute errors (MAE) criterion. On the beginning of the procedure, the center (A) of the initial region corresponding to face colors is determined, and block of dimension 40x40 pixels with center in point A is selected. Size of the block (40x40) and searching window (80x80) are experimentally determined.

Searching window is area with high probability that reference block in the next frame will be located in it. Orthocenter of reference block coincides with orthocenter of searching window.

Application of MAE is adjusted for image in RGB representation. This technique is usually applied on YUV images, where matching is done on Y pixels (luminance) only. RGB → YUV format conversion is CPU demanding processing block, and usually is realized in hardware. Modification of block matching algorithm for RGB colour space consists of calculating differences for all three coordinates according formula (6).

$$MAE(x, y) = \sum_{j=-\frac{RBH}{2}}^{\frac{RBH}{2}} \sum_{i=-\frac{RBW}{2}}^{\frac{RBW}{2}} |R_{i-1}(x+i, y+j) - R_i(x+i, y+j)| + |G_{i-1}(x+i, y+j) - G_i(x+i, y+j)| + |B_{i-1}(x+i, y+j) - B_i(x+i, y+j)| \quad (6)$$

where MAE is mean absolute error, while RBH and RBW are height and width of the block. When the best match is located, calculated MAE value should be checked additionally. Threshold value is MAE value calculated for two blocks taken from the same positions (reference and compared) in background sequence (recorded in initialization phase – step 1). If MAE value is below calculated threshold, compared block becomes reference block and vector between orthocenter of reference block and orthocenter of compared block is motion vector. Using additional threshold, false motion estimation in areas with uniform luminance is avoided.

In Figure 4 position of reference blocks with regards to the TO is shown. Experiments shown in this figure were done with fixed camera.

To speed up BM algorithm, calculation is performed on decimated picture, decimation by factor two is used (every second pixel in reference and in compared block are used for calculation).



Figure 4. Illustration of block matching based tracking algorithm with fixed camera.

4. CAMERA CONTROL

For camera movement standard step motor is used (1.8° per step, unipolar), platform with camera has freedom of +/-180° movement in horizontal plane. Based on motion estimation, calculated motion vector is used as input for control of the camera rotation.

Rotation angle is determined according to pinhole model [16]. The vertical projection of the model is presented on Figure 5, where meanings of symbols are: O – camera focus, D – object distance in point B, H – horizontal movement of an object, A_v and B_v – vertical object projections in points A and B, respectively, C_vD_v – horizontal component of moving vector, p – angle of camera movement, and d – focus distance from image plane.

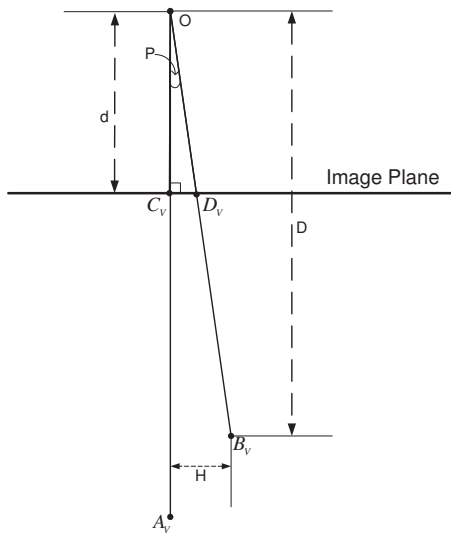
The camera movement is estimated according to formula (7):

$$\text{tg } p \sim p = C_v D_v / d, \quad (7)$$

where variable d is experimentally determined.

There are two control signals: one for rotation direction (0 – clockwise and 1 – counter clockwise), and the second for number of rotation steps. Frequency of second signal defines rotation speed. Speed of the camera [17] is determined by distance between the calculated moving vector in current p(t) and next frame p(t+1), or Camera Speed = S (p(t+1) - p(t)) / Δt, where S is a scaling factor and Δt is the time interval between the consecutive frames.

Due to closed loop in the system and possible instability (oscillations, which occurred in experimental phase during algorithm development), a PI control algorithm is used for motor control. Proportional control action is calculated as difference of the horizontal component of the TO orthocenter in two successive frames, divided by normalizing factor. In our case, for the given picture resolution and resolution of motor rotation, normalizing factor is eight. Integral control action is average of the last ten successive normalized P actions. Final PI control action presents sum of these two values. In Figure 6 the block matching tracking algorithm with rotating camera is illustrated.



INSTRUCTION FOR AUTHORS

Name of the author/s, Affiliation/s

Abstract: *Short instruction for authors is presented in this paper. Works that are to be printed in the review "Electronics" should be typed according to this instruction.*

Keywords: *Review Electronics, Faculty of Electrical Engineering in Banjaluka, Instruction for authors.*

1. INTRODUCTION

In the review "Electronics", we publish the scientific and professional works from different fields of electronics in the broadest sense like: automatics, telecommunications, computer techniques, power engineering, nuclear and medical electronics, analysis and synthesis of electronic circuits and systems, new technologies and materials in electronics etc. In addition to the scientific and professional works, we present new products, new books, B. Sc., M. Sc. and Ph.D. theses.

In order to enable the unification of the technical arrangement of the works, to simplify the printing of the review "ELECTRONICS", we are giving this instruction for the authors of the works to be published in this professional paper.

2. TECHNICAL DETAILS

2.1. Submitting the papers

The works are to be delivered to the editor of the review by the E-mail (elektronika@etfbl.net) or on floppy (or CD) by post mail to the address of the Faculty of Electrical Engineering (Elektrotehnicki fakultet, Patre 5, 78000 Banja Luka, Republic of Srpska, Bosnia and Herzegovina).

2.2. Typing details

The work has to be typed on the paper A4 format, 8.27" width and 11.69" height (21.0x29.7 cm), upper margin of 1" (2.54 cm) and lower margin of 0.59" (1.5 cm), left and right margins of 1.57" (2 cm) and 0.39" (1cm) (mirrored margins). The header and footer are 0.5" (1.27cm) and 57" (2 cm). The work has to be written in English language. Our suggestion to the authors is to make their works on a PC using the word processor MS WORD 97/2000, and for the figures to use the graphic program CorelDraw, if the graphs are not going from the original programs, i.e., from the programs received (like MATLAB).

The title of the work shall be written on the first page, in bold and 12 pt. size. Also, on the first page, moved for one line spacing from title, the author's name together with the name of his institution shall be printed in the letter size (10pt, *Italic*). The remaining parts of the manuscript shall be done in two columns with 0.5cm distance. The work shall be typed with line spacing 1 (Single) and size not less than 10 pt (like as this instruction). After the title of the work and the name of the author/s, a short content in English language follows, written in italics. The subtitles in the text shall be written in bold, capital letters of the size as in the text (not less than 10 pt.). Each work shall, at the beginning, comprise a subtitle INTRODUCTION, and, at the end, the subtitles CONCLUSION and BIBLIOGRAPHY / REFERENCES.

The operators and size marks that do not use numerical values, shall be written in common letters. The size marks that can use numerical values shall be written in italics. The equations shall be written in one column with right edge numeration. If the breaking of equations or figures is desired, those may be placed over both columns.

Illustrations (tables, figures, graphs etc.) may be wider than one column if necessary. Above a table there shall be a title, for instance: Table 2. *The experimental measuring results*. The same applies to figures and graphs but the accompanying text comes underneath the figure of graphs, for instance: Fig.3: *Equivalent circuit diagram...*

The work should not be finished at the beginning of a page. If the last manuscript page is not full, the columns on that page should be made even. Number of pages should not go over 6.

3. CONCLUSION

This short instruction is presented in order to enable the unification of technical arrangement of the works.

4. REFERENCES

At the end of work, the used literature shall be listed in order as used in the text. The literature in the text, shall be enclosed in square brackets, for instance: ...in [2] is shown ...

ELECTRONICS

Vol. 7, No. 2, December 2003.

PREFACE AND BIOGRAPHIES OF GUEST EDITORS	1,2
<i>Selected papers from the Symposium POWER ELECTRONICS 2003</i>	
THIRTY YEARS OF SYMPOSIUM	3
Vladan Vučković	
HIGH PRECISION CALIBRATION OF AC CURRENT TO VOLTAGE CONVERTERS.....	6
Petar Miljanić	
VECTOR - CONTROLLED MULTI PHASE MULTI - MOTOR DRIVE SYSTEMS WITH A SINGE INVERTOR SUPPLY	9
Emil Levi, Atif Iqbal, Slobodan N. Vukosavić	
LOSS FUNCTION ON - LINE IDENTIFICATION FOR THE INDUCTION MOTOR DRIVES	21
Slobodan N. Vukosavić, Emil Levi, Veran Vasić	
POWER QUALITY: STATE OF THE ART AND FUTURE TRENDS.....	32
J. V. Milanović	
AN OVERVIEW OF CURRENT TRENDS IN AUTOMOTIVE POWER ELECTRONICS	38
Dušan Graovac, Friedrich Schwamm	
THREE PHASE ZCS FREQUENCY CONVERTER.....	43
Vladislav Damec, Jan Dudek, Petr Chelebiš	
G - SERIES CONVERTER STABILIZED WIND TURBINE WITH PERMANENT MAGNET SYNCHRONOUS GENERATOR	46
Stevan Grabić, Nikola Čelanović, Vladimir Katić	
A NOVEL POWER INVERTER FOR SWITCHED RELUCTANCE MOTOR	50
Željko Grbo, Slobodan N. Vukosavić	
DESIGN AND SIMULATION OF WORKING IN PARALLEL TRANSISTOR INVERTERS	54
Georgi Kunov, Elissaveta Gadjeva	
STEADY - STATE ANALYSIS OF POWER CONVERSION SYSTEMS	59
Armando Bellini, Stefano Bifaretti, Stefano Constantini	
COMPARATIVE ANALYSIS ON TWO MODELS OF RELUCTANCE MOTOR	64
Alecsandru Simion, Leonard Livadaru, Sergiu Calugareanu, Emanuel Romila	
RESULTS RECURRENCE ON GENETIC ALGORITHM ESTIMATION OF THE INDUCTION MOTOR EQUIVALENT SCHEME PARAMETERS.....	68
Zdravko Andonov, Borislav Jeftenić, Slobodan Mircevski	
SENSORLESS VECTOR CONTROL OF INDUCTION MOTOR WITH NEURAL NETWORK	72
Martin Kuchar, Pavel Brandstetter, Martin Kaduch	
PHASE ANGLE STANDARD.....	76
Zoran Mitrović	
CONTROL STRATEGY FOR OPTIMISED COMPOUND SET OF SUPERCAPS AND ELECTROCHEMICAL BATTERIES FOR ROAD VECHICLES	80
Salvatore D' Arco, Diego Iannuzzi, Enrico Pagano	
DIGITAL SLIDING MODE CONTROL OF X - RAY APPARATUS ELECTRICAL DRIVES	85
Čedomir Milosavljević, Darko Mitić, Boban Veselić, Milić Pejović	
PRINCIPLES OF OPERATION AND CONTROL OF DOUBLY FED RELUCTANCE MACHINES.....	90
Milutin G. Jovanović	
POSSIBILITIES OF TORQUE AND FLUX CONTROL USING DTC - δ METHOD	95
Andrej Sikorski, Marek Korzeniewski	
LOW VOLTAGE SWITCHED CAPACITOR DC - DC CONVERTER FOR FUEL - CELL APPLICATIONS - PRELIMINARY DESIGN CONSIDERATIONS	100
Goce L. Arsov, Roberto Giral	
ELECTROMAGNETICAL COUPLING ON A DOUBLE CIRCUIT HIGH VOLTAGE 220 KV ELECTRICAL OVERHEAD LINES	105
Mariana Titihazan, Marian Greconici, Viorel Titihayan, Dumitru Toader, Adrian Buta, Nicolae Chiosa, Valeriu Lazu, Florinel Sturza, Dragan Nesin, Marian Mihai	
INFLUENCE OF VOLTAGE SAGS ON PERSONAL COMPUTERS AND PWM DRIVES	110
S. Ž. Đokić, J. V. Milanović, J. J. M. Desmet, K. Stockman, G. Vanalme	
DISORTED POWERS OF SOME POWER ELECTRONIC EQUIPMENTS	114
Ioan Sora, Alexandru Hedes, Dan Nicoara	
<i>Regular papers</i>	
DESIGN OF CAN CONTROLLER BY PETRI NETS TECHNIQUE	119
Blagomir Donchev, Krassimira Philipova, Andrey Popov	
REAL - TIME HUMAN FACE TRACKING WITH AN ACTIVE CAMERA USING BLOCK MATCHING TECHNIQUE	124
Nikola Teslić, Vladimir Radenković, Dragan Kukulj, Miroslav Popović	